NASA Contractor Report 4642

Development of a Multicomponent Force and Moment Balance for Water Tunnel Applications, Volume II

Carlos J. Suárez , Gerald N. Malcolm, Brian R. Kramer,
Brooke C. Smith, Bert F. Ayers
Eidetics International, Inc
Torrance, California

Prepared for
NASA Dryden Flight Research Center
Contract NAS2-13571

National Aeronautics and
Space Administration

Office of Management

Scientific and Technical
Information Program

1994

TABLE OF CONTENTS

LIST OF FIGURES

ABSTRACT VOL. 2

The principal objective of this research effort was to develop a multi-component strain gauge balance to measure forces and moments on models tested in flow visualization water tunnels. Static experiments (which are discussed in Volume I of this report) were conducted, and the results showed good agreement with wind tunnel data on similar configurations. Dynamic experiments, which are the main topic of this Volume, were also performed using the balance. Delta wing models and two F/A-18 models were utilized in a variety of dynamic tests. This investigation showed that, as expected, the values of the inertial tares are very small due to the low rotating rates required in a low-speed water tunnel and can, therefore, be ignored. Oscillations in pitch, yaw and roll showed hysteresis loops that compared favorably to data from dynamic wind tunnel experiments. Pitch-up and hold maneuvers revealed the long persistence, or time-lags, of some of the force components in response to the motion. Rotary-balance experiments were also successfully performed. The good results obtained in these dynamic experiments bring a whole new dimension to water tunnel testing and emphasize the importance of having the capability to perform simultaneous flow visualization and force/moment measurements during dynamic situations

NOMENCLATURE

Co	Root chord
$\bar{c}$	Mean aerodynamic chord
b	Wing span
α, AOA	Angle of attack, deg
α_o	Mean angle of attack, deg
α_s	Starting angle of attack, deg
α_f	Ending angle of attack, deg
β	Sideslip angle, deg
ϕ	Roll angle, deg
Q_∞	Free stream dynamic pressure
V_∞	Free stream velocity
M	Mach number
Re	Reynolds number
C_N	Normal force coefficient
C_m	Pitching moment coefficient (body axis)
C_Y	Side force coefficient (body axis)
C_n	Yawing moment coefficient (body axis)
C_l	Rolling moment coefficient (body axis)
f	Oscillation frequency, Hz
k	Reduced frequency, $\frac{\pi f \bar{c}}{V_\infty}$
ω	Angular velocity, deg/sec
ω_{max}	Maximum angular velocity, deg/sec
a	Acceleration, deg/sec^2
q	Pitch rate, deg/sec
q_o	Non-dimensional pitch rate, $\frac{q \bar{c}}{2 V_\infty}$
$\dot{\phi}$, ϕdot	Roll angular velocity, deg/sec
$\ddot{\phi}$, ϕddot	Roll acceleration, deg/sec^2
Ω	Non-dimensional rotation rate, $\frac{\omega\,[\text{rad} / \text{sec}]\, b}{2 V_\infty}$

DEVELOPMENT OF A MULTI-COMPONENT FORCE AND MOMENT BALANCE FOR WATER TUNNEL APPLICATIONS

Volume II - Dynamic Water Tunnel Tests

1.0 INTRODUCTION

Water tunnels have been utilized in one form or another to explore fluid mechanics and aerodynamics phenomena since the days of Leonardo da Vinci. Many studies (Refs. 1-6) have shown that the flow fields and the hydrodynamic forces in water tunnels are equivalent to the aerodynamic flow fields and forces for models in wind tunnels for the incompressible flow regime (i.e., Mach numbers less than 0.3). Only in recent years, however, have water tunnels been recognized as highly useful facilities for critical evaluation of complex flow fields on many modern vehicles such as high performance aircraft. Water tunnel testing is attractive because of the relatively low cost and quick turn-around time to perform experiments and evaluate the results. Models are relatively inexpensive (compared to wind tunnel models) and can be built and modified as needed in a relatively short time period. The response of the flow field to changes in model geometry can be directly assessed in water tunnel experiments with flow visualization. Detailed flow visualization also is an excellent means of understanding the physics of the flow. Understanding the flow structure and how the flow field interacts with the aircraft surfaces is extremely valuable in making configuration changes to solve specific aerodynamic problems.

While flow visualization is very valuable and is the primary reason for the existence of many water tunnels, there are some limitations, as there are for all experimental facilities. One of the principal limitations of a water tunnel is that the low flow speed, which provides for detailed visualization, also results in very small hydrodynamic (aerodynamic) forces on the model, which, in the past, have proven to be difficult to measure accurately. In most cases where force and moment information is essential, wind tunnel tests (usually with a different model) eventually have to be performed. The advent of semi-conductor strain gauge technology and devices associated with data acquisition such as low-noise amplifiers, electronic filters, and digital recording has made accurate measurements of very low strain levels feasible. If the water tunnel could also determine forces and moments to some level of accuracy simultaneously with the flow visualization, there would be a definite saving in time and cost in the selection and creation of the proper model to be constructed for sub-scale wind tunnel tests. Knowledge of the cause and effect of the complex flows and resulting non-linear aerodynamics at high angles of attack requires the capability to correlate what we see with what we measure in terms of airframe loads.

The increasing interest in flying at very high angles of attack (post-stall) to improve fighter aircraft agility and maneuverability dictates a pronounced emphasis in developing testing techniques to investigate dynamic situations in this flow regime. On a single maneuver, an advanced fighter aircraft can encounter attached flows, vortex and burst vortex flows, and totally separated flows. In particular, these vortical and highly separated flows are very sensitive to unsteady or time variant effects. The understanding of these flows is extremely important in the design or improvement of this type of aircraft, and the water tunnel force/moment balance may also provide a capability for quantitative dynamic experiments. The fact that flow visualization and force measurements can be performed simultaneously with relative simplicity in the water tunnel can be of significant importance to obtain a direct correlation between the changes in the flow field and the response of the forces and moments. Another advantage of conducting dynamic tests in a water tunnel is related to the motion and data acquisition rates. The high flow speed typical of wind tunnel tests requires rapid movement of the model in order to simulate a properly scaled dynamic maneuver and the motions are mechanically difficult to implement. The fast model movement also places demanding requirements on the response of the data acquisition system to acquire data at high sample rates. In contrast, the flow speed of water tunnel tests is typically

much lower (two orders of magnitude or more), and consequently, the model motion required to simulate a dynamic maneuver is also very slow. Thus, the response rates for data acquisition required for force and moment measurements during transient and dynamic situations in a water tunnel are less demanding than in a wind tunnel. This phase of the research program was focused not only in developing the force/moment balance, but in developing the hardware, software and techniques or procedures that allow obtaining meaningful dynamic data in a water tunnel.

The Phase I of this SBIR contract showed promising results with a three-component water tunnel balance, and therefore, the effort to develop, construct and test a multi-component water tunnel balance was clearly justified. This final report, which is divided into two Volumes, summarizes the results of the Phase II research program. Volume I provides a detailed description of the balance, calibration procedure and data acquisition/reduction hardware and software, and presents results of the calibration and of the static water tunnel tests performed on several models. Volume II describes the improvements on the water tunnel model support required to perform dynamic tests (computerized motions, new roll mechanism, rotary balance rig, etc.) and discusses the dynamic tests performed, including methodology, results and comparisons, when possible, to wind tunnel tests.

2.0 PHASE II TECHNICAL OBJECTIVES AND APPROACH

The overall objective of the Phase II research program was to design, develop and test a five-component force and moment strain gauge balance and perform both static and dynamic experiments to verify its performance. In addition to the basic balance, a complete calibration system and data acquisition hardware and software were developed and integrated. The balance needed to be capable of measuring forces and moments on 3-dimensional aircraft models that are sting mounted from the rear, similar to typical wind tunnel mounting techniques. Of special interest during this phase of the contract was the use of the balance to perform dynamic experiments, including rotary balance tests. The Eidetics water tunnel model support system, which had the capability for model motions in pitch and yaw, was expanded to perform high-fidelity dynamic motions in three axes (pitch, yaw, and roll). A roll mechanism and a rotary rig were designed and built, and the existing motors and electronics of the model support were improved. The unique capability of performing simultaneous force measurements and flow visualization during dynamic situations was of primary importance in this project.

The long-term goal of the contract was to create and demonstrate a comprehensive test capability in the Eidetics water tunnel for static and dynamic tests including a complete and stand-alone force/moment data acquisition and reduction system. To accomplish this, the specific technical objectives of the proposed program were the following:

1. Design and build a 5-component force/moment balance compatible with the Eidetics water tunnel or similar.

2. Design and build a suitable calibration rig and related hardware and software to perform an accurate balance calibration.

3. Design, purchase and assemble the necessary data acquisition system components to acquire and process the data into engineering units for display, printing and plotting. Write the required software to process, display and plot the balance data and reduced aerodynamic coefficients along with the model position and motion time history as required.

4. Perform static force and moment measurements on generic configurations (delta wings) and on an F/A-18 model, and compare results to existing wind tunnel data.

5. Increase the test capability of the Eidetics water tunnel model support system from the present two axes of motion (pitch and yaw) to three axes (pitch, yaw, roll) and modify the model support drive control system to produce high-resolution motions in all three axes to acquire "dynamic" force and moment time-history data.

6. Develop a technique for conducting dynamic tests. Perform tests using the same models and measure time-lag response of the forces and moments to forced motions such as high-amplitude pitch-ups and body-axis roll. If possible, perform and display flow visualization and force measurements simultaneously.

7. Develop an apparatus for producing a "coning" motion, or a roll motion about the velocity vector with fixed angle of attack and sideslip, commonly performed in wind tunnel tests on a rotary-balance apparatus. Perform tests on the F/A-18 model to evaluate the test capability and compare the results to the rotary-balance data on the F/A-18 obtained by Eidetics in the Ames 7 x 10-ft wind tunnel under another SBIR Phase II contract.

The approach to developing the test capabilities outlined in the specific objectives focused on designing, building, assembling and testing a complete operational system that is tailored to the needs of a typical water tunnel user. The balance and data acquisition system were designed to be as versatile as possible in order to accommodate a wide variety of water tunnel applications. The main goal was to be able to provide a complete balance and data acquisition system that the user can install in his/her water tunnel facility without having to commit significant time and money to make it operational. The balance and the calibration equipment are the heart of the system; the remaining components, consisting of the appropriate signal conditioning and amplifying equipment, data acquisition hardware, and desktop computer are available off-the-shelf. A complete and user-friendly software package to process the balance and tunnel-related information was developed using LabView (Version 3.0), a popular and widely used graphical programming language. All the improvements to the model support and hardware designed and built to conduct the dynamic tests, despite being customized for the Eidetics water tunnel, can be slightly modified and adapted for use in any other tunnel.

A five-component balance, a calibration rig and a copy of the data acquisition/reduction software are delivered to NASA Dryden along with this final report. Again, discussions related to the first four objectives are presented in Volume I of this final report. Results of this research effort regarding the dynamic tests in objectives 5-7 are the main subjects of this Volume.

3.0 WATER TUNNEL MODEL SUPPORT IMPROVEMENTS

3.1 UPGRADE FOR DYNAMIC FORCE/MOMENT MEASUREMENTS

The computer-controlled feature of the existing water tunnel model support system allowed the model to be driven open loop through specific motions of the user's choice, as long as the rotational velocity did not exceed 15 deg/sec. While this provided sufficient capability to visualize the flow field of a model in motion, it did not provide the precision required for accurate motion time histories for measuring forces and moments. The model motion must be very smooth or large inputs to the balance will be generated from vibration and noise. The challenge was to smooth out the drive system both mechanically and electronically to better provide a high-fidelity motion history.

The primary upgrade to produce high-resolution motions with minimum vibration or undesirable unsteadiness was to include position feedback in the motor drive controller. The original motors used in the pitch and yaw axes were replaced with GLOBE DC permanent magnet planetary gear motors with HP incremental optical encoders. This 24 Volt motor, which is also

used in the new roll mechanism, has a gear ratio of 36:1 and can provide a maximum speed (no load) of 5,700 rpm and a maximum continuous torque of 102 oz. in. These specifications totally satisfy the requirements for performing the dynamic experiments. The HP encoder, which has a resolution of 512 CPR (cycles per revolution), provides the required position feedback to obtain accurate motions in the three axes. The new motors installed in the model support are shown in Fig. 1.

3.2 COMPUTERIZED DRIVER AND CONTROLLER

The DC motors are driven and controlled with an off-the-shelf system manufactured by nuLogic. The nuDrive is a complete power amplifier and system interface unit for up to three axes of servo or stepper motion control (Fig. 2). For servo motors, nuDrive utilizes PWM amplifiers with a 10 Amp peak output current rating and a 48 Volt DC bus, and it provides everything needed to interface motors, encoders, limit switches and motion hardware to the motion control board, nuControl. The nuControl board is a fully programmable, three-axis motion controller that plugs directly into any NuBus Apple Macintosh II computer. Each axis can be programmed for velocity, acceleration and position control in both continuous and point-to-point motion. Closed loop servo performance is fully programmable via a time samples digital filter control loop. A Macintosh Quadra 700 computer is used for both data acquisition/reduction and for motion control.

3.3 MOTION SOFTWARE

The software used in this project, developed specifically for this application, was written using National Instrument's LabView (Version 3.0), a graphical programming language. A library with virtual instruments that handle basic motion commands was provided by nuLogic, the manufacturer of the controller and drive system used. These virtual instruments were integrated into a program that allows moving the model with single commands or more complicated, prescribed trajectories in any of the three axes (the "Multi-Axis" feature is still under development). The software section for the motion control can be opened by clicking on the "Move Model" button of the main front panel (Fig. 3a). Within this sub-panel (Fig. 3b), the model can be moved with different angular rates or accelerations in any of the three axes. Three meters indicate the position of the model in degrees. The "Re-Initialize or Calibrate" sub-panel provides the features illustrated in Fig. 3c. The "Initialize" panel is used to specify the motor and encoder characteristics for each of the axes. With the "Re-Zero Position" button, the indicators can be re-zeroed at any time; this is very useful when leveling the model in the tunnel. A bubble is used to level the model in pitch and roll; dye streamlines are used to align the model in yaw. After the model is leveled, the indicators are re-zeroed and the encoder will provide the position referenced to that zero location. In order to read degrees directly, the user can specify different "gearing constants" (two per axis). These constants convert the DC motor revolutions into degrees of motion of the model support for the particular axis. With the hardware utilized in this investigation, the gearing constants are 36 for the gearmotor in each axis, and then 44, 30 and 40 for the pitch, yaw and roll axes, respectively. These last set of constants are the gear/track ratios for the C-strut and turntable (pitch and yaw), and the ratio between worm and worm-gear in the roll mechanism. The "Settling Time" feature was not used for these tests.

In addition to these "single command" motions, pre-programmed trajectories can be specified in any axis. These motions include ramp-hold, saw-tooth and sine wave approximations, as shown in Fig. 3d, and the user can specify the amplitude, velocity, acceleration, number of cycles, etc. The panel for commanding a Ramp-Hold motion is depicted in Fig. 3e, and inputs for this example include starting angle (deg), ending angle (deg), velocity (deg/sec) and acceleration (deg/sec^2).

3.4 ROLL MECHANISM DESCRIPTION

The existing model support used with the Eidetics Water Tunnel was capable of generating motions in the pitch and yaw axes. The pitch motion is provided by a motor-driven C-strut in the vertical plane and the yaw motion is generated with a motor-driven turntable in the horizontal plane. In order to provide the versatility of varying the model attitude in any of the three axes, it was proposed to add a mechanism to roll the model.

The roll mechanism, shown in Fig. 4, consists of one main stainless steel support that attaches to the C-strut. Side, top and bottom aluminum plates conform a "box" that provides housing to all the hardware. Three bulkheads, with stainless steel bearings, support the shaft. The motion is transmitted from the motor to the shaft by means of a worm gear. The motor is located on top, outside the tunnel, on a bracket attached to the C-strut. Since both the roll mechanism and the motor are attached to the C-strut, the angle of attack can be varied from 0° to 50° without modifying the relative position of the components. A 0.64 cm (1/4") rod connects the motor and the roll mechanism, with the worm gear providing the 90° motion transmission. The gear and worm gear combination proved very smooth and no backslash problems were noticed. The different components of the roll mechanism are shown in more detail in Fig. 5.

3.5 ROTARY RIG DESCRIPTION

The water tunnel rotary rig is very similar to the apparatus developed for the F/A-18 wind tunnel experiments at the NASA Ames 7 x 10-ft wind tunnel. One difference, of course, in the wind tunnel apparatus, is that the model can be rotated continuously since the electrical signals from the balance can be carried across the rotating interface with electrical sliprings and there are no dye tubes to be concerned about. Since no sliprings were used ("submersible" electrical sliprings were not available), the water tunnel rig can only be rotated for 3-4 revolutions in each direction and large service loops in the dye tubes and the balance wires are provided to avoid excessive twisting.

The rig consists of an aluminum C-strut that attaches to the roll mechanism by means of a special adapter (Fig. 6). The angle of attack is changed manually by sliding the arm along the C-strut, allowing testing at angles of attack between 0° and 60°. Once the desired α is obtained, the arm is fixed in position with two screws. Sideslip can be varied by rotating the sting in the adapter located at the end of the arm. Figure 7 shows an assembly drawing of the rotary rig, with the arm and sting at both angle of attack extremes ($\alpha = 0°$ and 60°).

4.0 EXPERIMENTAL SETUP

4.1 WATER TUNNEL

All experiments were conducted in the Eidetics 2436 Flow Visualization Water Tunnel. The facility is a continuous horizontal flow tunnel with a test section 0.91 m (3 ft) high x 0.61 m (2 ft) wide x 1.83 m (6 ft) long. The tunnel speed can be varied from 0 to 30 cm/sec (1 ft/sec). The model is mounted inverted, and it is possible to test at angles of attack between 0° and 65°, at sideslip angles between -25° and 25°, and at any roll angle.

4.2 MODELS

Flat plate delta wings with 70° and 80° sweep angles were used for these experiments. The delta wings, which are shown in Fig. 8, have a main chord of 38.1 cm (15"), have a double-beveled leading edge and are made of aluminum. The balance is located at the model centerline and

the reference center is at the C/3 position, or 50% of the mean aerodynamic chord $\bar{c}$ ($\bar{c}$ is defined as 2/3C). Two fiberglass fairings (top and bottom) covered the entire balance.

Additional dynamic experiments were performed on a 1/32nd-scale F/A-18 model, seen in Fig. 9. The plastic model is equipped with dye ports for flow visualization, and the balance is attached to an internal aluminum plate. Control surfaces were fixed at 0° throughout the entire set of experiments (leading edge flaps were fixed at 34°). Moments are referenced to the 25% $\bar{c}$ location, except when indicated.

The rotary balance experiments were performed on a 1/48th-scale F/A-18 due to size constraints in the water tunnel. The width of the test section (24 inches) did not allow the use of the 1/32nd-scale F/A-18 model utilized for the other dynamic experiments. The smaller plastic model, which has a span of 24.7 cm (10.1 inches), is depicted in Fig. 10.

4.3 INSTRUMENTATION

The heart of the instrumentation is the five-component water tunnel balance, which allows measuring all forces and moments except for the axial component. Semi-conductor strain gauges are used to obtain the desired sensitivity. Since the balance operates under water, the strain gauges, connectors and wires were water-proofed. The balance was carefully calibrated using a custom built calibration rig. Results of the calibration revealed linear response in the primary sections, low component interactions and no hysteresis. A detailed description of the balance and calibration procedures and results can be found in Volume I of this final report.

A multi-channel system for generating conditioned high-level signals from strain gauge inputs was used. The eight-channel system is a MEASUREMENT GROUP Model 2100 strain gauge conditioner and amplifier. During all the dynamic experiments, the excitation voltage was 5 Volts and the external gain was 200 in all channels. Five (one per channel) 100 Ω external potentiometers are used to balance each bridge under any loading condition when the internal potentiometer of the signal conditioner does not provide the required range.

The output lines for each channel are routed both to the digital display of the signal conditioner and to the A/D board inside the Macintosh Quadra 700 computer (by means of a ribbon cable). The board is a National Instruments NB-MIO-16XL, which is a high-performance multi-function analog, digital and timing I/O board for Macintosh NuBus computers. Features of this board include: fast 16-bit ADC, 16 single-ended or 8 differential channels, programmable gains, guaranteed rates up to 55 ksamples/sec, etc. The high sampling rate capability of the A/D board proved extremely useful for the dynamic experiments.

4.4 DATA ACQUISITION/REDUCTION SOFTWARE

As mentioned in Section 3.3, the software for the motion control and data acquisition/reduction system was written using LabView. The goal was to provide software that is user friendly, easy to use and modify as needed for specific applications, and is versatile in its ability to reduce and display the balance and tunnel condition data efficiently and effectively. The basic methodology for the data reduction system, particularly the treatment of the balance equations, was initiated using the same approach used for typical wind tunnel data reduction schemes. The data acquisition/reduction software allows to perform a full balance calibration, as well as the static and dynamic experiments. The main front panel of the program was already seen in Fig. 3a. As was done in Volume I, a brief description of each "sub-panel" will be provided in different sections in this report (where that particular panel or software feature is utilized). Of

particular interest is the specialized software for acquiring/reducing the rotary balance data (see Section 8.2)

5.0 DYNAMIC EXPERIMENTS IN PITCH

Experiments in pitch were conducted using the 70° delta wing and the 1/32nd-scale F/A-18 models. The tests included pitch-up/pitch-down and hold maneuvers and oscillations at different amplitudes and frequencies.

5.1 METHODOLOGY AND INERTIAL TARES

The first step in performing the dynamic experiments in pitch was to obtain a weight (static) tare throughout the angle of attack range, in a similar manner as the "alpha" tare taken during static tests. This tare will account for the change in the model weight as the angle of attack increases or decreases. As in the static tests, the balance channels are zeroed before each run and a static zero data point is acquired (tunnel off, $\alpha = 0°$, $\beta = 0°$, $\phi = 0°$).

One of the unknowns in dynamic water tunnel experiments was the model inertia effects on the data, i.e., the effect of the resistance to motion due to the model mass moment of inertia in pitch, I_{yy}. Before actually performing the experiments, it was calculated that the inertia contribution to the aerodynamic values to be measured would be small, because of the low motion rates used in the water tunnel. It should be noted that the pitch rates selected for experiments in the water tunnel should, of course, be scaled properly to represent the correct relationship between rotation rate, scale, and free stream velocity. As an example, assume that a full-scale aircraft with a 3.5 m (138 in.) mean aerodynamic chord $\bar{c}$ pitches at 60 deg/sec at M = 0.2 (V_∞ = 61 m/sec = 200 ft/sec). In a water tunnel, the model $\bar{c}$ is approximately 11 cm (4.3 in.) and the tunnel velocity is 15.2 cm/sec (0.5 ft/sec). The parameter that should be matched is the non-dimensional pitch rate $q_0 = \frac{q\,\bar{c}}{2\,V_\infty}$. From the above numbers, the angular pitch rate q for the water tunnel would be approximately 4.8 deg/sec. The aerodynamic moment is the component that is to be measured. It must be determined from the total moment felt by the balance by subtracting out the contributions from the mass moment of inertia. The inertia effects are determined by measuring the time-variant moment recorded by the balance with the model in motion with the tunnel velocity at zero. The motion must have the identical motion time history as the motion generated with the tunnel on ($V_\infty > 0$). The aerodynamic contribution is determined by subtracting the measured moment at $V_\infty = 0$ from the moment measured at $V_\infty > 0$.

Results indicate that the inertial contribution is, indeed, very small. Figure 11 shows the measured normal force on the 70° delta wing during a pitch-up and hold maneuver from 15° to 60° angle of attack. The value of the normal force N (lbs) measured during the pitch-up motion when the water tunnel is off ($V_\infty = 0$) is almost negligible, approximately 1% of the value measured with tunnel speed. Also included in this plot is the value of the normal force measured during the specified motion with no water in the tunnel. The value of N throughout the dynamic maneuver under the "no water" condition is very similar to the $V_\infty = 0$ case, indicating that there are no major "virtual mass effects" (resistance of the surrounding water to being displaced by the moving model). Similar results were obtained during pitch oscillations, both for the 70° delta wing and the F/A-18 models, as seen in Figs. 12a and b, respectively. Therefore, depending on the quality of the data required, the inertia effects can be ignored, facilitating the testing and the data reduction process.

The data are corrected for blockage effects at high angles of attack with the same technique utilized during the static water tunnel experiments (see Vol. I and Ref. 5 for boundary correction equations).

5.2 SOFTWARE

The software handles the entire data acquisition/reduction and model motion processes. The "Dynamic Data W/Motion" panel, shown in Fig. 13a, is used for conducting most of the dynamic experiments that involve model movement. An "alpha" weight tare, performed statically throughout the desired angle of attack range, has to be loaded before opening this panel, in the same manner as during the static tests. The user starts selecting the type of motion to be performed (ramp and hold, saw-tooth or sine wave approximation) and the axis of motion, and then the parameters for the desired motion are specified (the "Real Time Plot Setup" is not implemented yet). For a "Ramp and Hold" maneuver (pitch-up or pitch-down), the user specifies the starting and ending angles (in degrees), and the velocity (in deg/sec) and acceleration (in deg/sec^2). The model will accelerate until the desired velocity is reached, and then it will hold the speed constant until it starts to decelerate to reach the ending angle with zero speed. The "Saw-Tooth" inputs are the same with the addition of the number of cycles. The way the parameters are defined for the sine wave approximation is slightly different than in the other motion cases. Different breakpoints along the sine wave can be selected. The position, velocity and acceleration at each particular point have to be calculated and specified; the larger the number of breakpoints, the better the approximation.

After all the motion parameters are loaded, the data sampling parameters have to be defined, using the "Dynamic Data Rate" button. The "Dynamic Data Rate" panel (Fig. 13b) is independent from the setup used for the calibration and the other experiments. In order to synchronize the model motion with the data acquisition, the software uses the following logic. An encoder reading is acquired, then the balance channels are read at the specified sampling number and rate and a final encoder reading is acquired. The average of each balance channel is assigned to the position given by the average of the two encoder readings. The combination of the high sampling rate A/D board and the low motion rates in the water tunnel permits acquiring a large number of samples during very small model displacements, giving an adequate density of data points along the model trajectory. The user has to specify not only the sampling number per channel and the sampling rate (10,000 samples per second maximum), but the number of encoder-reading/data-reading/encoder-reading loops as well (Number of cycles in Fig. 13b). A static zero has to be acquired before the tunnel is started.

Additional buttons in the "Dynamic Data W/Motion" panel deal with model motion ("Move to Level" and "Go to Start"). Once the motion and data acquisition are initialized, and the zero point is taken, the tunnel is set at the desired speed and the "Move and Record Dynamic Data" button starts the motion and data acquisition processes simultaneously. As in the previous cases, the signals from each channel are displayed in the x-y plot. By using the "Display Type" switch, the motion signals can also be displayed.

5.3 EFFECT OF DATA SAMPLING RATE AND FILTERING

Preliminary experiments were conducted to evaluate the quality of the data obtained while the model is moving. The main purpose of these tests was to determine the effects of sampling rate and to determine if the data needed to be heavily filtered, as in the case of most dynamic wind tunnel experiments. As explained in the previous section, the software takes an encoder reading, then acquires the balance data, takes a second encoder reading and assigns the balance values to the average of the two encoder readings. The number of balance samples acquired between each encoder reading can be varied, and the final value for each channel is the arithmetic average of the

samples taken. As expected, the larger the number of samples acquired, the better the quality of the data. Figure 14 shows the normal force coefficient during a ramp-hold maneuver (pitch-up) performed with the 70° delta wing. For the cases in which a small number of samples are taken, the normal force coefficient presents large fluctuations, therefore making the use of these data almost impossible. However, by increasing the number of samples to 800-1,000 per channel, the data obtained are very smooth and repeatable, requiring no post-processing and clearly indicating the value of the force/moment at the particular model location. Since the A/D board used allows acquiring data very fast (10,000 samples per second), it is possible to take a large number of samples per channel and still get an adequate density of points (again, the low motion rates required in the water tunnel facilitate these experiments).

Since LabView has many built-in filters (Bessel, Butterworth, etc.), it was decided to experiment with some of these filters. It was found that the quality of the data was not significantly improved with the use of different digital filters at various cut-off frequencies. Figure 15 shows data during a pitch-up and hold motion from 15° to 60° angle of attack. The data sets are not smoother than for the simple "average" case and results depend strongly on the cut-off frequency used.

The results from these preliminary experiments dictated that most of the dynamic tests were conducted at 10,000 samples per second, acquiring 1,000-2,000 samples per channel, and without the use of an external filter.

5.4 70° DELTA WING RESULTS

5.4.1 Pitch-Up/Hold and Pitch-Down/Hold Maneuvers

Figures 16a and b show the variations in the normal force and pitching moment coefficients during a pitch-up and hold (α = 15° to 65°) motion, for non-dimensional pitch rates q_o from 0.0069 to 0.055. The motion is such that the model accelerates with a constant acceleration (1 deg/sec^2) until the desired pitch rate is reached, and then it holds the pitch rate constant until it decelerates so it gets to the final angle of attack with zero speed. The overshoots in normal force and pitching moment are strongly dependent on rate. For the highest non-dimensionalized pitch rate, the normal force coefficient at 55° angle of attack has almost twice the value of the static case at that particular angle of attack. One interesting characteristic is observed for the pitching moment curve corresponding to q_o = 0.0550. For angles of attack between 15° and 35°, the dynamic curve indicates an undershoot with respect to the static case. Figures 16c and d show the angle of attack and the C_N and C_m time histories for two of these maneuvers: q_o = 0.0069 and 0.0550. It is evident that for the fastest case, the sampling rate during the pitch-up was not adequate (due to hardware limitations) and that could be responsible for the "undershoot" in C_m observed in the previous figure.

The pitch-down and hold of the delta wing from 65° to 15° angle of attack produces changes in the longitudinal characteristics that are presented in Fig. 17. Changes in C_N are small for angles of attack between 65° and 50°; however, for α's between 50° and 15°, the data reveal an undershoot in the normal force that is again strongly dependent on rate. It should be noted that, in this case, both the magnitude of the undershoot and the angle of attack at which the value of C_N reaches the static value are functions of q_o (α = 30° for q_o = 0.0069, α = 22° for q_o = 0.0138 and α = 15° for q_o = 0.0290 and 0.0550). The pitching moment results reveal an undershoot starting at α = 45°.

The effect of changing the acceleration in a pitch-up and hold motion is illustrated in Fig. 18. In this case, the non-dimensionalized rate was left constant ($q_0 = 0.020$), and the acceleration during the start and the end of the motion was varied. As the data indicate, the effect of changing the acceleration on the longitudinal characteristics is minimum. The overshoots for C_N and Cm are very similar for all the different cases. A reason for this could be the fact that the time periods in which the angular rate is changing are relatively small. Figure 19 presents data for pitch-up and hold motions starting at different angles of attack and stopping at 45°. The effect of starting angle of attack is negligible, both in terms of the overshoot and the overall shape of the curve.

5.4.2 Pitch Oscillations

Additional experiments with this delta wing model included pitch oscillations at different reduced frequencies k, amplitudes and motion profiles. The first set of experiments consisted of large-amplitude pitch oscillations about a mean angle of attack α_0. The purpose of these tests was to directly compare the water tunnel data to results from wind tunnel tests conducted at NASA Langley by Brandon and Shaw, where a 70° wing was investigated for forces and moments produced by these large-amplitude pitch motions (Ref. 7). Figure 20a presents changes in the normal force coefficient produced by oscillating the delta wing ±18° about different α_0's with a reduced frequency k = 0.0376. This k value corresponds to a maximum full-scale pitch rate of approximately 60 deg/sec for a typical fighter aircraft at $V_\infty = 200$ ft/sec. The hysteresis loops are evident in the force measurements, with all the cases producing similar values of C_N overshoot. Results from the wind tunnel tests in Ref. 7 are revealed in Fig. 20b, and the similarities in the two data sets can be clearly identified. The level of C_N is slightly lower in the wind tunnel test, especially above 25°, but the shape of the dynamic loops and the relative increments are very similar in both plots. The motion profile for the water tunnel tests, which is an approximation of a sine wave, is depicted in Fig. 21. Also included in this figure are time histories of the normal force and the pitching moment coefficients. Even thought the models in the two experiments rotated about a different reference point (50% $\bar{c}$ for the present investigation and 40% $\bar{c}$ for the wind tunnel test), the behavior of the pitching moment is very similar in both tests. As the angle of attack is increasing (Fig. 22), the lag in the burst point of the vortex produces a destabilizing increment in C_m at high angles of attack. The difference in the location of the burst point at the same angle of attack between static and dynamic conditions was clearly shown by the flow visualization. When the model reverses direction, a negative C_m increment is produced for the higher α_0 cases. This increment, produced by a lag in the flow reattachment, is very small for the $\alpha_0 = 22°$ and 27° cases; the dynamic C_m curves follow the static curve very closely. As in the normal force case, the sizes of the hysteresis loops in pitching moment increase as the mean angle α_0 increases.

Figure 23 reveals results of similar oscillations performed at lower reduced frequencies, k = 0.0226 and 0.0075. The decrease in the frequency produces a reduction in the C_N overshoot and in the sizes of the hysteresis loops. Data from different runs permitted evaluating the effect of the reduced frequency on the dynamic overshoot in C_N (Fig. 24a). The percentage increase in the normal force coefficient over the maximum static value during this dynamic situation agrees very closely with the wind tunnel data from Ref. 7, as seen in Fig. 24b. This clearly demonstrates that dynamic experiments can be successfully conducted in the water tunnel with this balance, with the advantage that the tests are inexpensive and easier to perform, and motion and data acquisition rates are much less demanding than in the wind tunnel. It should be noted also that the water tunnel data presented for these cases have not been curve-fitted or smoothed, while the wind tunnel data had to go through a heavy filtering and curve-fitting process.

The 70° delta wing model was also used for investigating the effect of the motion profile (period, rate, acceleration, etc.) on the response of the forces and moments measured. Figure 25 presents results of pitch oscillations from 19° to 55° angle of attack at a reduced frequency $k = 0.0376$. The motion profiles varied from a sine wave approximation (low acceleration) to a saw-tooth (high acceleration), but the period of the motion was kept constant (Fig. 25b illustrates the motions with the lowest and highest accelerations). As the data indicate, the changes in the normal force coefficient caused by the different motion profiles are similar, especially in terms of the overshoot and the shape of the loop. The very small acceleration case produces a slightly larger undershoot, but, in general, no major differences are observed. The next plots (Figs. 26 and 27) show motions with the same maximum angular velocity but different accelerations. In the first case (Fig. 26a, $\omega_{max} = 0.56°/sec$), no major differences in the hysteresis loops are observed. The same experiment was conducted with a higher maximum angular velocity and the effects are larger (Fig. 27a, $\omega_{max} = 1.12°/sec$). The acceleration change does not affect the overshoot in C_N significantly, but it definitely affects the undershoot, with the smaller accelerations presenting a larger undershoot and, therefore, a larger loop. It should be noted that by increasing or decreasing the acceleration, the reduced frequency k is also changed, especially for the high angular velocity case. It is very difficult to isolate and modify one parameter in this type of motion without affecting the others. Changing the maximum angular velocity and leaving the acceleration constant produces the largest variations in the force and moment outputs. This was expected because the variation in the angular velocity produces drastic changes in the motion profiles and it affects the reduced frequency considerably. Therefore, it is not surprising that the hysteresis loops shown in Figs. 28 and 29 are strongly dependent on ω_{max}. Both the overshoot and undershoot in the normal force coefficient vary considerably with angular velocity. These simple experiments appear to indicate that, in the water tunnel, the type of motion profiles do not affect significantly the response of the forces and moments, as long as the major parameters of the profile (peak-to-peak amplitude and reduced frequency) are kept constant.

Very large amplitude oscillations (from $\alpha = 16°$ to 64°) at different reduced frequencies were also performed and the results in normal force and pitching moment coefficients are seen in Fig. 30. These tests were conducted to obtain a direct comparison with results from another water tunnel data set from experiments described in Ref. 5. Comparisons in Figs. 31a and b for $k = 0.0265$ and 0.0742, respectively, indicate that the loops obtained in the present study are shifted up slightly, with a larger overshoot occurring at lower angles of attack, and a smaller undershoot. The agreement, in general, can be considered quite good taking into account possible slight differences in models, motion profiles and water tunnels.

5.5 F/A-18 RESULTS

5.5.1 Pitch-Up/Hold and Pitch-Down/Hold Maneuvers

Experiments on the 1/32nd-scale F/A-18 model started with pitch-up/down and hold maneuvers. Figure 32 presents results for pitch-up and hold motions from 15° to 65° angle of attack for different non-dimensional pitch rates q_o. The normal force and pitching moment data show a dependency on pitch rate, as reported by Brandon and Shaw in Ref. 8. In general, there is an increase in C_N and a decrease in C_m over the entire range of motion. As discussed in Ref. 8, the induced angle of attack in the horizontal tails and the lag in the separation and vortex formation are mainly responsible for the negative C_m increment at angles of attack lower than 55°. At higher angles of attack, the lag in the breakdown of the LEX vortex becomes dominant, generating a positive C_m increment. The static tests described in Volume I revealed that the vortex flow field of the F/A-18 presents a large asymmetry at angles of attack greater than 50°, with the associated non-zero C_Y and C_n at zero sideslip. For the dynamic case, the flow stays symmetric for some time

even when the model has passed $\alpha = 55°$, i.e., it takes some time for the vortex asymmetry to fully establish. The yawing moment curves show less sensitivity to changes in the pitch rate, even though it appears that the time it takes for the asymmetry to establish decreases slightly as the pitch rate is increased. The motion profiles for two of these runs, along with the variation of some of the forces and moments with time, are illustrated in Fig. 33 . The "persistence" in normal force, defined as the time it takes the force to reach its steady or static value from the moment the motion stopped, is clearly observed in Fig. 33a. This phenomenon of persistence will be discussed in more detail at the end of this section.

The effect of the starting angle on a pitch-up and hold maneuver was also investigated. Results for normal force and pitching moment for motions starting at different angles of attack and ending at $\alpha = 65°$ are presented in Fig. 34. The non-dimensional pitch rate for these experiments was kept constant at 0.0184. For $\alpha_s = 15°$, 20° and 30°, the curves reveal similar trends and overshoots in C_N. When the maneuver is started at $\alpha_s = 40°$, with the wings stalled and the LEX vortex burst point close to the LEX apex, the overshoot in C_N is slightly smaller. This is probably due to the fact that the burst point quickly move to the LEX apex and therefore, it generates a slightly smaller C_N increment. Less effect on the response of the forces and moments was observed when the final angle of attack was varied. The pitch-up and hold motions at $q_0 = 0.0182$ started at $\alpha = 15°$ and the final angle of attack was varied from 55° to 65° (Fig. 35). The data show very similar trends and values, indicating that the effect of the ending angle of attack, at least in this α range, is almost negligible.

As in the 70° delta wing case, the effect of the acceleration on this type of dynamic maneuvers is minimum. The test was conducted keeping the maximum pitch rate constant and changing the value of the acceleration. The curves of C_N and C_m versus angle of attack (Figs. 36a and b) reveal small differences for the three cases, with the low acceleration showing a slight decrease in the values of the C_N overshoot and the C_m undershoot.

In order to complete this set of experiments, pitch-down and hold maneuvers at different rates were performed. The maneuver consisted of pitching down the F/A-18 model from 65° to 15° angle of attack, and the response of the normal force and the pitching moment are presented in Figs. 37a and b. The data show an undershoot in C_N that is independent of rate at the beginning of the motion (from 65° to 50° angle of attack). Between 50° and 15° angle of attack, the high rate motion generates a larger undershoot. Figure 37c illustrates the motion profiles and the change in the normal force coefficient versus time. It is very interesting to notice that, contrary to the behavior observed during the pitch-up maneuvers in terms of persistence, by the time the model stops after the pitch-down, the value of the normal force is almost the same as the static value, denoting a very small or almost zero persistence. The persistence in C_N, in terms of convective time units, is compared to data from the wind tunnel experiments (Ref. 8) in Fig. 38. A convective time unit is the time it takes one particle in the free stream to travel a distance equal to the mean aerodynamic chord on the model. The similarities between the results from the two experiments are quite evident, indicating similar flows and dynamic force/moment responses. The small discrepancies in the value of persistence observed in each test can be attributed to the difference in motions. While the pitch-up and pitch-down motions from the present test were between 15° and 65° angle of attack, those performed in Ref. 8 were between 0° and 75°. Results from the same investigation indicated that the persistence is a strong function of not only the non-dimensional pitch rate, as the water tunnel test indicates, but of the ending angle of attack as well. Limitations in the water tunnel model support did not allow for reproducing the same motion.

The effect of the starting angle of the pitch-down maneuver appears to be more pronounced than in the pitch-up case, especially in pitching moment (Fig. 39). By starting the pitch-down maneuver at $\alpha = 55°$, a considerably larger positive increment in C_m is generated for angles of attack between 55° and 40°.

5.5.2 Pitch Oscillations

Oscillations in pitch were also performed with the F/A-18 model. The first set of experiments consisted of relatively small amplitude oscillations (peak-to-peak amplitude of 20°) about several mean angles of attack α_o. The oscillations were conducted at reduced frequencies $k = 0.04$ (Fig. 40) and $k = 0.06$ (Fig. 41). The data show hysteresis loops in the normal force and pitching moment coefficients. The size of the loops and the overshoot in normal force are similar for these particular reduced frequencies. The traditional mechanism responsible for the C_N loops is the lag in breakdown and reformation of the LEX vortices during an oscillation cycle. The pitching moment data show counter-clockwise hysteresis loops, i.e., a nose-down C_m increment occurs during the pitch-up and a nose-up C_m increment occurs during the pitch-down portion of the oscillation. At the low angle of attack range, the primary mechanism responsible for these loops appears to be the pitch damping provided by the horizontal tails. Vortical behavior also contributes to the formation of the dynamic loops; during the pitch-up portion, the LEX vortex burst is aft of the location observed during static conditions, and thus a nose-down pitching moment is generated. During the pitch-down, the lag in the flow delays the loading of the aft portions of the model, producing a nose-up increment.

Larger amplitude oscillations (15° to 55° angle of attack) were conducted to investigate the effect of the reduced frequency. Figures 42a and b present C_N and C_m data for different k values, from 0.01 to 0.06. As observed in the experiments performed with the 70° delta wing model, the shape of the hysteresis loops and the overshoot and undershoot in both normal force and pitching moment are strongly dependent on reduced frequency. The angle of attack and C_N time histories for the low and high frequency values shown in Fig. 42c illustrate the drastic differences in the response of the force. The percentage of C_N overshoot with respect to the static case and as a function of the reduced frequency is summarized in Fig. 43.

The last set of pitch oscillations were conducted at higher angles of attack, in a region that is dominated by large asymmetries in both the forebody and LEX vortices. The peak-to-peak amplitude was 40° and the mean angle of attack α_o varied from 35° to 45° (Fig. 44). The hysteresis loops in C_N present the expected shapes and the overshoot is not dependent on α_o. Significant changes appear in C_m; the shape of the counter-clockwise loop starts deteriorating and a highly non-linear behavior is observed as the mean angle of attack is increased. For the last case ($\alpha_o = 45°$), a clockwise loops appears between 55° and 65° angle of attack. In general, the results of the dynamic tests conducted with the F/A-18 model agree well with tests at the Langley 12' wind tunnel (Ref. 8).

A very interesting loop is observed in yawing moment (Fig. 45). In general, no hysteresis effects were observed in the lateral-directional characteristics during pitch oscillations where the maximum angle of attack did not exceed 55°. The asymmetric vortex flow field at $\alpha = 55°$ and higher is responsible for the hysteresis loop observed in yawing moment for the oscillation between $\alpha = 20°$ and 60°. The flow tries to stay symmetric in the dynamic case up to 60° angle of attack, until the asymmetric vortex flow field finally gets established, overshooting the static C_n value. During the pitch-down, the yawing moment shows an undershoot until it reaches again the static value corresponding to the lower angles of attack.

6.0 DYNAMIC EXPERIMENTS IN YAW

These experiments, consisting of monitoring the flow field and the response of the forces and moments during a dynamic sideslip angle change, were performed with the 1/32nd-scale F/A-18. The free stream velocity during these tests was 12.7 cm/sec (0.42 ft/sec).

6.1 METHODOLOGY

The methodology and procedures for conducting these tests are very similar to those utilized for the pitch experiments. Since the tests were performed in a horizontal tunnel, the weight component does not change with sideslip angle, and therefore, a "beta" weight tare is not needed.

6.2 SOFTWARE

The "Dynamic Data W/Motion" front panel, described in Section 5.2, is used for these experiments.

6.3 RESULTS

The dynamic tests in the yaw axis were limited to oscillations between 0° and 20° sideslip angle, at $\alpha = 30°$, and at two reduced frequencies k (0.04 and 0.06). The motion profiles and the response of the yawing and rolling moments with time are presented in Fig. 46.

The hysteresis in the longitudinal characteristics is minimum; the values follow the static case very closely, as Fig. 47a indicates for C_N. The major changes are observed, as expected, in the lateral-directional characteristics (Figs. 47b, c and d). The yawing moment and rolling moment data present hysteresis loops with opposite directions. The loops for C_n are clockwise, while the loops for C_l are much larger and counter-clockwise. While the principal mechanism for the loops in yawing moment is probably the yaw damping produced by the vertical tails, the primary mechanism responsible for the loops in C_l is the lag in the LEX vortex burst and reformation.

7.0 DYNAMIC EXPERIMENTS IN ROLL

Two types of experiments in roll were conducted: free-to-roll (wing rock) tests and forced-to-roll tests. In order to perform the wing rock investigation, the worm gear from the roll mechanism was removed, leaving the sting "free-to-roll", supported by the three ball bearings.

7.1 METHODOLOGY

During the free-to-roll experiments, the roll angle was measured with a rotational displacement transducer located above the tunnel, attached to the C-strut of the model support. The motion was transmitted from the sting to the shaft of the transducer by means of a rubber belt. The raw output was acquired and then post-processed with the appropriate constants to obtain the roll angle in degrees. It should be noted that the aerodynamic forces that induce the limit-cycle oscillation in roll known as "wing rock" are very small in the water tunnel because of the low flow speeds. Because of this, friction and interference have to be kept to a minimum, and it was decided not to measure forces during these experiments to avoid the interference from the wire bundle coming from the balance.

As in the pitch tests, the first step in performing the forced-to-roll experiments was to obtain a weight (static) tare. This "phi" tare will account for the change in the model weight as the balance is rotated. The model is rotated throughout the roll angle range of interest and static

readings are taken at several roll angles. The values from this "phi" tare will be subtracted out from the raw data at the appropriate roll angle. It is important to note that, in this case, the balance channels are zeroed at the specific angle of attack. A static zero data point is acquired before moving the model (tunnel off, $\phi = 0°$).

The inertia effects in roll are also negligible, and the data are corrected at high angles of attack with the same technique utilized during the static water tunnel experiments.

7.2 SOFTWARE

The "Dynamic Data" front panel is utilized during the free-to-roll (wing rock) tests. This panel permits acquiring dynamic data but does not have any model motion capability, which is not needed during the wing rock experiments.

The "Dynamic Data W/Motion" front panel, described in Section 5.2, is used for the force-to-roll experiments. The procedure is similar to the one used for the dynamic experiments in pitch. The only difference is that a "phi" weight tare has to be performed at each angle of attack. The "zero point" must also be acquired with the model at the desired angle of attack.

7.3 WING ROCK EXPERIMENTS

The 80° delta wing was utilized in these experiments, since it is well known that this delta wing exhibits a strong wing rock. The phenomenon of wing rock is a moderate and high angle of attack dynamic motion manifested primarily in a limit-cycle oscillation in roll, with in some cases, a coupled oscillation in yaw. Results shown in this section are obtained from a thorough analysis of the roll angle history.

Figure 48 shows the roll angle history of the wing rock motion at $\alpha = 35°$ and $V_\infty = 23.9$ cm/sec = 0.78 ft/sec. The delta wing presents a limit-cycle oscillation from -20° to 24° roll angle; this amplitude is smaller that the amplitude reported in Ref. 9 during a similar water tunnel test. However, the data from this investigation agree very well with results obtained in a wind tunnel test by Levin and Katz (Ref. 10). The wind tunnel model used in this study has a balance fairing similar to the fiberglass fairing used in the water tunnel model, and that could be responsible for the smaller peak-to-peak amplitude obtained in the present water tunnel test (compared to water tunnel data from Ref. 9). The wing rock frequency observed in this test is approximately 0.40 Hz, which corresponds to a reduced frequency k = 1.34. The reduced wing rock frequency reported in Ref. 10 was approximately 0.21 at the same angle of attack. The discrepancy in reduced frequencies between water and wind tunnel tests is not surprising and it is due to the difficulty in inertially scaling the models for the air and water mediums. In order to match the reduced frequency of the two experiments, either the inertia of the wind tunnel model must be substantially smaller or the water tunnel model inertia must be substantially larger. Increasing or decreasing the test velocity has no effect on $\omega b/2V_\infty$, because ω is directly proportional to V_∞. If V_∞ is changed, ω is changed by the same factor. Another characteristic revealed in Fig. 48 is the fact that the wing rock motion is established completely in approximately 3 cycles.

The analysis of the motion obtained during the free-to-roll experiments provides the means to estimate the roll angular velocity $\dot{\phi}$ and the roll acceleration $\ddot{\phi}$. The roll angle data obtained with the transducer were smoothed graphically (Fig. 49a) and then differentiated numerically, yielding $\dot{\phi}$. The angular velocity data were smoothed and differentiated again, and the roll acceleration was obtained. This acceleration $\ddot{\phi}$ is proportional to the total aerodynamic rolling moment coefficient.

Plots of roll angle, roll rate and roll acceleration for one cycle of the wing rock motion can be seen in Figs. 49b and c.

The plots of $\dot{\phi}$ and $\ddot{\phi}$ versus ϕ are commonly referred to as phase plots. Depicted in Fig. 50 are phase plots for one cycle of the wing rock motion at $\alpha = 35°$. The roll angular velocity $\dot{\phi}$ (phidot, in deg/sec) shows the expected behavior: starting at $\phi = 0°$, the angular velocity is maximum. As the model moves right-wing-down, the angular velocity decreases to zero when the model is at the maximum roll angle. The motion reverses its direction and the velocity starts to increase (negatively), reaching the maximum negative magnitude when the model is at $\phi = 0°$ again. The roll angular acceleration $\ddot{\phi}$ (phiddot, in deg/sec^2), which closely represents rolling moment, yields the typical wing rock hysteresis loops when plotted as a function of roll angle. In this graph, a clockwise loop denotes an area where energy is being added to the system, i.e., the oscillations are being driven (destabilizing). The counter-clockwise loops near the maximum roll angle represent areas where the system is consuming energy, and therefore the motion is being damped (stabilizing). The $\ddot{\phi}$ versus ϕ plot reveals that the areas contained within the destabilizing and stabilizing loops are about equal, indicating an energy balance which is required to sustain the limit-cycle wing rock. The cross points in this plot are roll angles at which the total roll damping goes to zero, and for this particular case, these roll angles are -11° and 14°.

7.4 FORCED-TO-ROLL EXPERIMENTS

7.4.1 80° Delta Wing Model Results

The main idea behind this investigation was to obtain the roll angle history from the free-to-roll experiments and then reproduce the exact motion with the roll mechanism and the computerized motion system. Forces and moments can therefore be measured during the specified motion without the problems associated with extra friction or interference. However, the roll rates encountered during the wing rock experiments were fairly large due to the inappropriate inertia scaling of the model (a much heavier model would be necessary for these water tunnel experiments). The hardware utilized for the forced oscillation experiments did not allow for obtaining those high rates, and, therefore, forced oscillations were performed matching the amplitude of the limit cycle oscillations observed, but at much lower frequencies.

Oscillations were performed with the 80° delta wing model between -20° and 24° (as in the free-to-roll case) at four different frequencies, corresponding to k values of 0.10, 0.24, 0.48 and 0.90. The reduced frequency of 0.48 was the maximum allowed by the hardware used in the model support at the same velocity of the free-to-roll experiments, significantly smaller than the reduced frequency observed during the wing rock tests. In order to obtain the higher value of $k = 0.90$, the free stream velocity was decreased to 12.7 cm/sec (0.42 ft/sec). A further decrease of V_∞ would have taken the reduced frequency closer to the wing rock test value of $k = 1.34$, but at the same time, it would have worsened the resolution of the balance because of the reduced dynamic pressure.

Of primary importance was the response of the rolling moment to the body axis roll. Figs. 51 to 54 present the roll angle history and the change in rolling moment coefficient for the four different k values. The rolling moment coefficient is plotted versus time and also versus roll angle, in order to evaluate the shape of the hysteresis loops obtained in each motion. The shape of the hysteresis loops is strongly dependent on frequency. For the low frequency case ($k = 0.10$), the data reveal two counter-clockwise loops. In a typical wing rock hysteresis loop, such as the one presented in Fig. 50, these counter-clockwise loops represent areas where the motion is being damped (stabilizing loop). As the frequency increases, the shape of the loops change. For the

case of k = 0.24, one central clockwise loop and two small counter-clockwise loops near the roll angle extremes are clearly defined. These loops resemble those seen in the free-to-roll case, but the area within the central (destabilizing loop) is much larger than the areas within the two counter-clockwise loops. It should be noted that the data from these experiments were smoothed in order to facilitate the visualization of trends or general characteristics. As indicated in Figs. 52c and d (one cycle at k = 0.24), the smoothing routine applied does not change the data significantly, but it removes some of the irregularities that make it difficult to visualize, for example, the directions of the loops near the roll angle extremes. For the two high frequency cases (k = 0.48 and 0.90), only one clockwise (destabilizing) loop is observed.

Figure 55 shows the relationship between the roll angle and the angular rate and acceleration for the motion at k = 0.90. The phase plots, especially the $\ddot{\phi}$ versus ϕ, reveal the limitations of the hardware, both in terms of obtaining the rates required to match the free-to-roll frequency, and generating a variable acceleration that will produce the hysteresis loops seen in the wing rock experiments. These differences in the motion are undoubtedly affecting the force/moment responses.

Results indicate that the body-axis oscillations produce variations not only in rolling moment but in all the other balance components as well. Figs. 56 to 58 show the changes in the normal and side forces, and in the pitching and yawing moments for the roll oscillations at k = 0.10, 0.48 and 0.90, respectively. The normal force oscillates at twice the motion frequency. Changes in pitching moment are negligible, and variations in C_Y and C_n are as expected. Interesting hysteresis loops in normal and side forces are observed (Figs. 59 to 61 for the same three frequencies). In the C_N versus roll angle plots, it is clearly seen that the direction of the loops are opposite for the low frequency motion compared to the two higher frequency cases. The behavior of the side force coefficient is similar; the direction of the loop is clockwise for the low frequency case and counter-clockwise for the two higher frequency motions. Moreover, the shape of the C_Y loops is significantly affected by the frequency, with the area of the loops increasing as the frequency is increased. This difference in behavior was also observed earlier in the rolling moment data. The reason for the change in the loop direction with frequency of oscillation must be a function of the time lags in the flow field response to the forced motion of the model. An important question, which remains unanswered because of the difficulty in matching free-to-roll and forced-to-roll frequencies, is whether the lead-lag relationship between the model and flow field is the same for the same oscillation frequency.

7.4.2 1/32nd-Scale F/A-18 Model Results

Forced-to-roll experiments were also conducted using the 1/32nd-scale F/A-18 model. The approach for the first set of experiments was to match the free-to-roll motion obtained in the wind tunnel test performed in Ref. 11. In that investigation, a 2.5%-scale model of the F-18 presented a wing rock motion for angles of attack between 30° and 50°, with a maximum peak-to-peak amplitude of 44° at $\alpha = 45°$. The wing rock amplitude was found to be independent of Reynolds number for Re higher than 40,000. However, at lower Re, the amplitude of the oscillation decreases significantly as Re decreases. At $\alpha = 40°$, the F-18 oscillates between -13° and 13° at Re = 20,000, and from -18° to 18° at Re = 50,000. Even thought the present water tunnel tests are conducted at low Reynolds number (Re = 12,500 when running at V_∞ = 12.7 cm/sec = 0.42 ft/sec), it was decided to investigate both amplitude cases at $\alpha = 40°$.

The five components of the forces and moments measured with the balance during a body-axis roll (between -13° and 13°) at three different frequencies (k = 0.025, 0.050 and 0.10) are presented in Figs. 62, 63 and 64, respectively. The smallest frequency matches the reduced

frequency observed in the wind tunnel test performed in Ref. 11. Variations in normal force and pitching moment are small, but the changes in C_m produced by the rolling motion are larger than those observed on the 80° delta wing. Changes in directional characteristics are significant, as expected, with noticeable differences from the delta wing case. While in the delta wing case the variations in C_Y and C_n followed the roll angle, i.e., positive C_Y and C_n for positive ϕ and vice versa, the opposite occurs with the F/A-18. Positive changes in C_Y and C_n are seen for negative roll angles. The rolling moment behaves as expected, and the shape of the hysteresis loops are strongly dependent on the frequency. Figure 65 shows C_l plotted versus roll angle for the three cases discussed before; different shape hysteresis loops are revealed for each of the motions. It appears that by increasing the frequency, the central clockwise loop (destabilizing) starts decreasing, until it disappears completely for the high frequency oscillation. For this case, a single counter-clockwise loops is observed.

The peak-to-peak amplitude of the limit cycle oscillation was increased from -13° to 13° to -18° to 18°, and results for the rolling moment coefficient are presented in Fig. 66. The hysteresis loop in C_l shows similar characteristics to the loop observed previously at the same frequency ($k = 0.025$). The angular roll rate and acceleration were obtained from the roll angle history and they are presented in Fig. 67. It is important to remember again that the motion used is a sine wave approximation, so differences in the phase plots (Figs. 67c and d) with respect to free-to-roll experiments and thus in the force/moment response can be expected.

The last set of "body-axis roll" experiments performed on the F/A-18 consisted of high amplitude oscillations (-40° to 40°) at different angles of attack. Results for the rolling moment coefficient at $\alpha = 0°$, 20° and 40° are presented in Fig. 68. A very large counter-clockwise loop is seen for the three motions, with the shape changing especially for the 40° angle of attack case. The response of some of the other balance components at $\alpha = 20°$ are revealed in Fig. 69. Interesting loops are observed in C_Y and C_n (Figs. 69b and c).

8.0 ROTARY BALANCE WATER TUNNEL TESTS

Another important maneuver for present and future aircraft is "loaded roll" or rolling around the velocity vector at medium to high angles of attack. In the wind tunnel, rotary balances are used to acquire force and moment data from an internal balance with the model rotating around the velocity vector at varying rotation rates. With the addition of the balance, the water tunnel provides a limited version of the same type of test capability with the added benefit of observing the behavior of the flow at the same time.

8.1 METHODOLOGY

Because of the complexity associated with a hydraulic slip-ring for the dye and with an electric (submersible) slip-ring for the balance, the number of revolutions in the water tunnel experiments is limited. Since the model rotates around the velocity vector continuously, the balance wires and dye tubes need to have sufficient length and flexibility to accommodate up to 3 revolutions in each direction without twisting beyond the point of disconnecting or unacceptable tension. Once the 3 revolutions have been accumulated, the model coning motion is reversed. This affects the data acquisition/reduction scheme utilized. In wind tunnel rotary-balance tests, data are usually acquired and averaged over a large number of cycles. Because of the large number of cycles, it is not crucial if the last is not a full cycle. In the water tunnel, data must be averaged over exact cycles. In order to accomplish this, a data clipping routine is utilized. This routine basically "chops" the data over the desired range (for example, from -360° to 360° roll angle if data are to be averaged over two revolutions) and discards the rest of the data.

As in the other dynamic experiments, it was found that the inertial effects on the data were negligible, and thus, the rotary tare can be performed at any rotation speed. These particular rotary-balance experiments were performed for non-rotational rates $\Omega = \frac{\omega b}{2 V_\infty}$ up to ±0.15 and the rotary tares were always conducted at rates corresponding to $\Omega = 0.10$.

Data were acquired and averaged over exactly 2 revolutions. Results are presented for non-dimensional rotation speeds of up to ±0.15. Data from the water tunnel rotary-balance tests correspond to runs at 0.42 ft/sec and/or 0.58 ft/sec (Reynolds number of 8,200 and 11,500, respectively). These data are compared to results from a rotary-balance test performed by Eidetics on a 6%-scale F/A-18 in the NASA Ames 7x10' wind tunnel (Ref. 12), and from a test of a 1/10-scale F-18 model at the Langley Spin Tunnel (Ref. 13).

8.2 SOFTWARE

The software for performing rotary-balance experiments is a variation of the "Dynamic Data W/Motion" panel. The first step in conducting these experiments is to load or to perform a rotary tare. In order to perform a rotary tare, the "Create New Rotary Tare" panel has to be used. Before showing the main panel, the software will automatically open a panel to define the motion and the data clipping (Fig. 70a). The motion, of course, will take place in the roll axis, and the starting and ending angles, velocity and acceleration have to be specified. The rotation should be a constant speed motion, thus the value of the acceleration is not very important (10 deg/sec^2 is adequate). After the motion is started, the rig will accelerate until the desired speed is reached, and then it will hold the speed constant until it decelerates to reach the ending angle with zero speed. The data clipping also helps discarding the data that are not acquired at constant speed (beginning and ending of motion). As an example, if data are to be averaged over exactly two revolutions, the inputs in the data clipping panel are -360° for start angle and 360° for ending angle. In the motion definition, the inputs are -380° for start angle and 380° for ending angle. This ensures constant speed data over the entire clipping range. After the tare is created, it has to be loaded with the "Load Old Rotary Tare" button.

The "Rotary Balance" panel is the same as the rotary tare main panel (Fig. 70b). The procedure for loading the motion and clipping parameters is as explained in the above paragraph. The logic for defining the data sampling parameters is the same as in the "Dynamic Data W/Motion" panel. The "EU data" file created provides the average of the five channels for each point acquired (actual forces/moments and coefficients).

8.3 RESULTS

Before showing the results for the rotary-balance experiments, the static characteristics of the 1/48th-scale F/A-18 model are presented and compared to those of the 1/32nd-scale model in Fig. 71. The small model presents a lower value of C_N for angles of attack up to 40°, especially for the low Reynolds number case. Reynolds number effects are negligible for Re greater that 12,250. This difference in the magnitude of the normal force is attributed to small differences in geometry between the two models. Except for the low Re case, the agreement in pitching moment is good. The lateral-directional characteristics present similar trends, with only some small differences in the magnitude of the vortex asymmetries observed (denoted by the non-zero value of C_Y and C_n at high angles of attack). The models present opposite asymmetries in rolling moment.

The first set of rotary-balance force/moment measurements results, presented in Fig. 72, corresponds to experiments at $\alpha = 30°$. The normal force coefficient obtained in the water tunnel test presents again a lower value than in the other two tests, as it was seen during the static

experiments. In general, the normal force decreases slightly with rotation rate. There is a discrepancy in pitching moment, with the water tunnel data showing a positive C_m. The pitching moment at $\Omega = 0$ is different to the pitching moment measured under static conditions with the standard sting support, thus it appears that the difference in model support might be responsible, in part, for the discrepancy in pitching moment. There is also the possibility that the center of pressure is very close to the reference center, and thus any minor disturbance or support interference can produce a center of pressure shift, changing the pitching moment characteristics significantly. The agreement in the other coefficients is fairly good; positive rotations produce negative yawing moments and vice versa. Figure 73 shows flow visualization performed on the 1/48th-scale F/A-18 model at $\alpha = 30°$ and at three conditions: static, and positive and negative rotations ($\Omega = \pm 0.15$). For the static case, the forebody vortex flow field is symmetric, as observed during the static tests performed with the 1/32nd-scale F/A-18 model. The positive rotation (clockwise, pilot's view), causes the burst point of the leeward vortex (blue/left) to move forward significantly. The windward vortex (red/right) is lifted up slightly and it can be seen interacting with the vertical tail. Almost a "mirror" image is observed during negative rotations.

Similar flow visualization and force/moment results are presented in Figs. 74 and 75, respectively, for the case at $\alpha = 50°$. For the static case, the forebody vortex flow field is symmetric. The positive rotation causes that the windward vortex gets lifted up from the body. A "right-vortex-high" asymmetry is created, with the associated negative side force and yawing moment. The opposite occurs when the model is rotated at $\Omega = -0.15$, i.e., a "left-vortex-high asymmetry is produced. Force/moment measurement results reveal that the normal force coefficient has similar behavior in all the tests, i.e., a slight increase with rotation rate. The pitching moment shows a slightly negative increment with rotation rate. There is a slight C_m difference between the two water tunnel runs, indicating that the location of the center of pressure is probably changing as the free stream speed increases. The offset in C_m between the water and wind tunnel results indicates a more aft center of pressure for the wind tunnel model and the reason for this is unknown. The agreement in the lateral/directional coefficients is quite acceptable. Evidently, the forebody vortex flow fields in the water and wind tunnel experiments present opposite asymmetries, as indicated by the side force value at $\Omega = 0$, but the anti-spin slope is similar in both tests. The yawing moment coefficient obtained in the water tunnel presents a smaller slope than that revealed by the wind tunnel results, especially for negative rotations, denoting again a possible slight shift in the center of pressure. The anti-spin behavior, however, is still present. The rolling moment presents positive slopes in both tests, and it is the component that shows the larger Reynolds number effects in the water tunnel tests.

Results at $\alpha = 60°$ are shown in Fig. 76. The longitudinal characteristics present similar trends as those observed at the other angles of attack, i.e., the water tunnel data show similar behaviors with rotation speed but different magnitudes. Again, the pitching moment of the present test reveals a relatively large offset with respect to the other data. It should be noted that in this case, there is a difference also between the two wind tunnel data, especially for negative rotation speeds. The lateral/directional characteristics compare very well for non-dimensional rotation speeds not greater than 0.1. At higher speeds, these coefficients reveal a reversal which is not seen in the wind tunnel data. This could be due to the fact that, at 60° angle of attack, the rotation brings the model very close to the side tunnel walls and the blockage probably increases. Also, this is the most "unbalanced" configuration and some vibrations were noticed during the test that could have definitely affected the quality of the data at the high rotation speeds.

In general, results from these experiments can be considered quite encouraging, especially in terms of having the capability of performing flow visualization and F/M measurements to assess spin characteristics during the preliminary design phase.

9.0 CONCLUSIONS

A five-component balance was designed, built and tested in the Eidetics water tunnel. The balance was calibrated and results of static experiments (discussed in detail in Volume I of this Final Report) were quite satisfactory, showing good correlation with wind tunnel data of similar configurations (delta wing and F/A-18 models).

This phase of the contract focused on using the balance to perform dynamic experiments in the water tunnel. The model support of the Eidetics' water tunnel was improved, and both a new roll mechanism and a rotary rig were designed and built to assess the performance of the balance under different types of dynamic situations. Among the advantages of conducting dynamic tests in a water tunnel are less demanding motion and data acquisition rates than in a wind tunnel test (because of the low-speed flow) and the capability of performing flow visualization and force/moment measurements simultaneously with relative simplicity. Also important is the fact that this investigation showed that the values of the inertial tares (the effect of the resistance to motion due to the mass model of inertia) are very small due to the low rotation rates required in a low-speed water tunnel. Depending on the accuracy of the data required, these tares can be ignored, simplifying testing and the data reduction process.

Initial dynamic experiments consisted of oscillations and ramp-hold maneuvers in the three axes: pitch, yaw and roll. Oscillations in pitch showed that the responses of the forces and moments are not very sensitive to the motion profile, as long as the important parameters (amplitude and frequency) are kept constant. The hysteresis loops obtained in these tests were compared to data from dynamic wind tunnel experiments; both data sets showed loops with similar shapes and similar dynamic increments over the static values. Ramp-hold maneuvers in pitch revealed the long persistence of some of the force components that has been observed in other investigations (35-45 convective time units). Oscillations in the yaw axis (dynamic sideslip angle change) showed interesting hysteresis loops in the lateral-directional characteristics. Free-to-roll and forced-to-roll experiments were also performed. Forces and moments were not measured during the free-to-roll motions, but a thorough analysis of the roll angle history of wing rock provided the typical phase plots and hysteresis loops. The forced-to-roll tests revealed the behavior of the forces and moments during the body-axis roll maneuver.

The last set of dynamic experiments consisted of rotary balance tests and results from these experiments are very satisfactory. Forces and moments measured in the water tunnel showed the same trends and spin behavior as the wind tunnel tests, and the flow visualization revealed several interesting characteristics to complement the F/M measurements, such as vortex asymmetries and interactions, support interference, etc.

Whenever possible, flow visualization and force measurements were performed simultaneously to obtain a direct correlation between the dynamic change in the vortex flow field and the response of the forces and moments. A video that shows flow visualization and plots of force/moment coefficients displayed simultaneously in the same screen for different dynamic maneuvers was created and is part of this final report. This video clearly shows examples of the different dynamic experiments that can easily be performed in a water tunnel and the usefulness of having flow visualization and F/M measurements displayed at the same time. In general, results obtained in this contract should encourage the use of water tunnels for a wider range of quantitative and qualitative experiments, especially during the preliminary phase of aircraft design.

10.0 ACKNOWLEDGMENTS

This study was supported by the NASA Dryden Flight Research Center under SBIR Phase II Contract No. NAS2-13571. The technical monitor was Mr. John Del Frate. We would also like to acknowledge Mr. Mel Heier and Mr. Patrick Mc Farland from PSI-TRONIX for the technical support and assistance during and after the balance gauging.

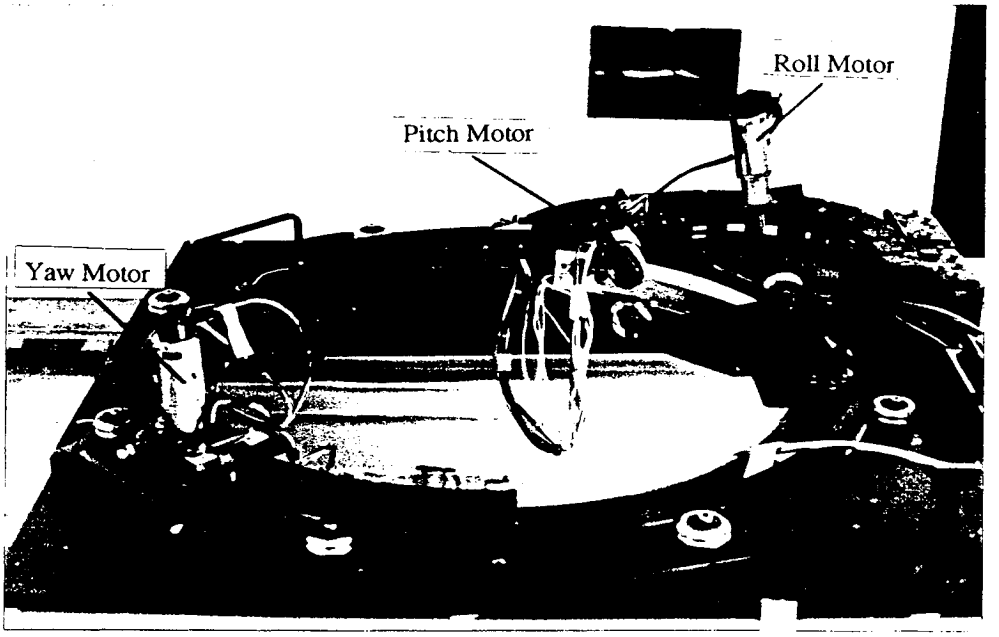

Figure 1 - Water Tunnel Model Support

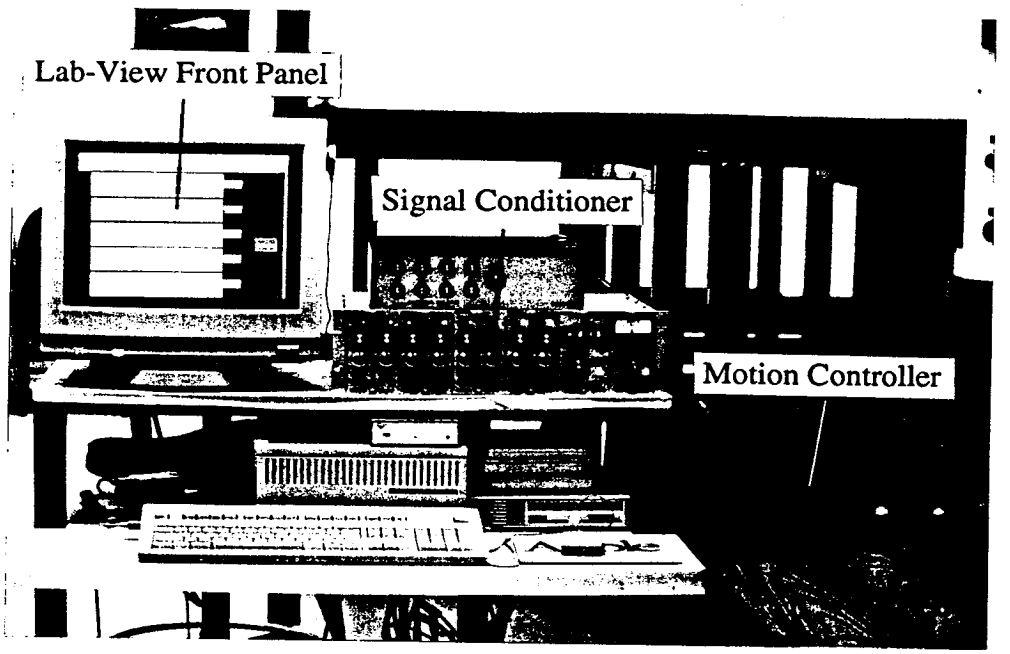

Figure 2 - Data Acquisition/Reduction System and Motion Driver/Controller

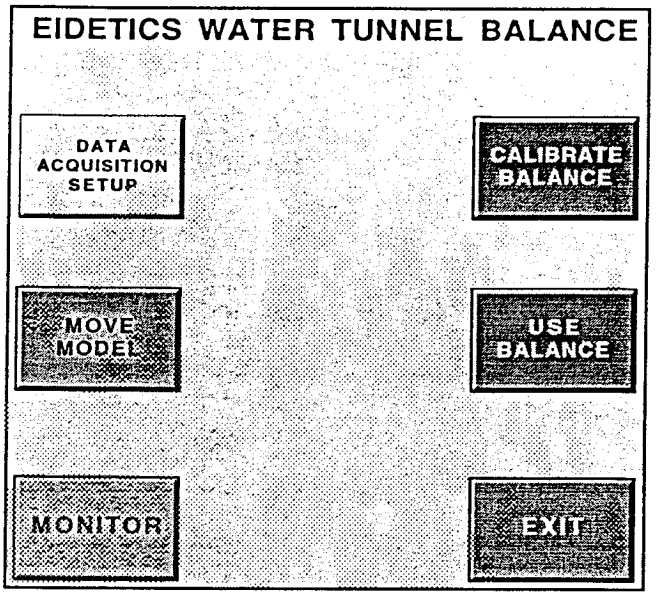

a) "Main" Front Panel

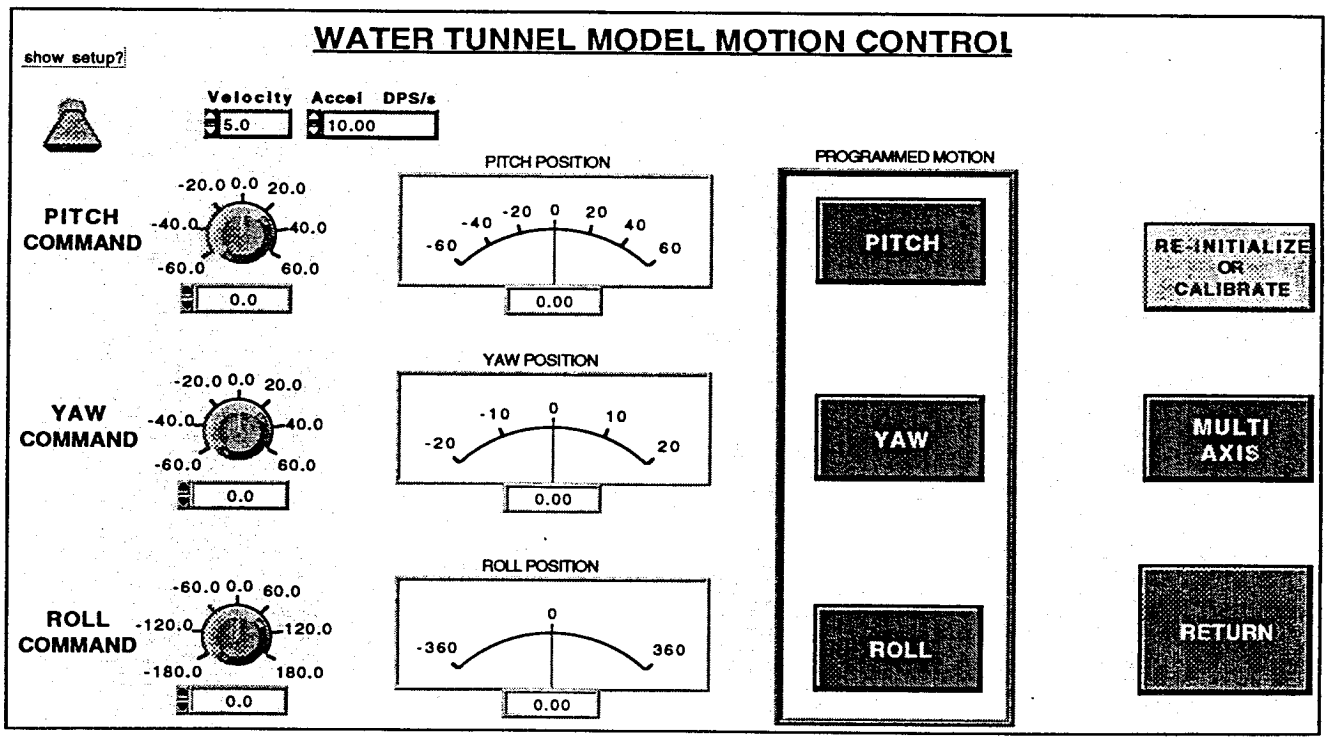

b) "Move Model" Panel

Figure 3 - Software Front Panels

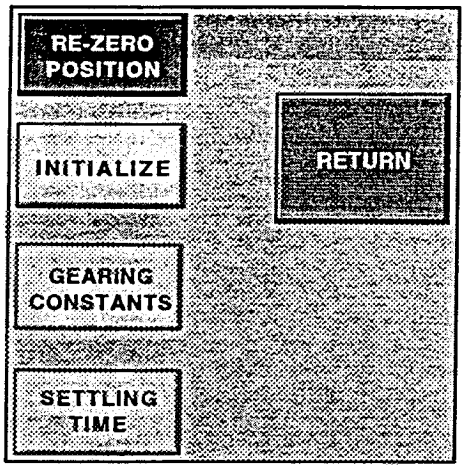

c) "Re-Initialize or Calibrate" Panel

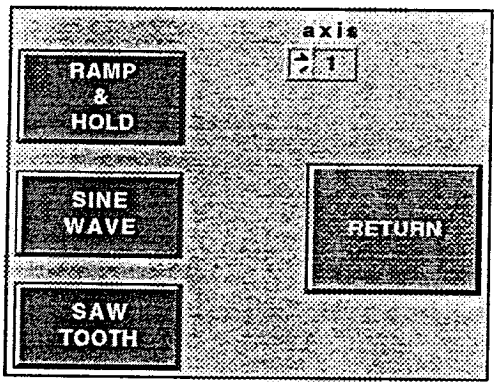

d) "Pitch Programmed Motions" Panel

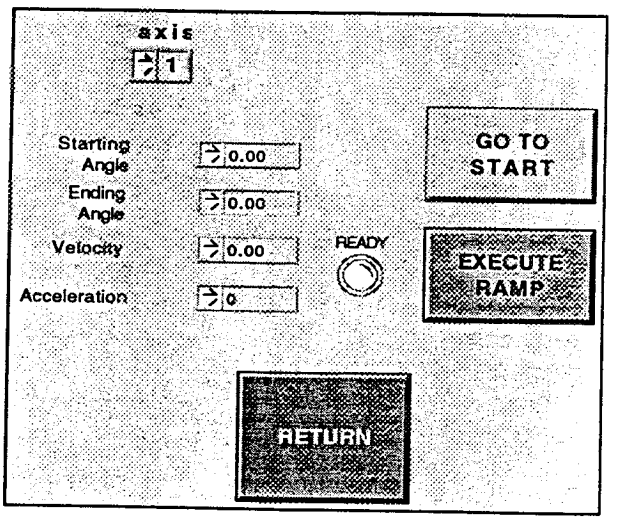

e) "Ramp and Hold" Panel

Figure 3 - Concluded

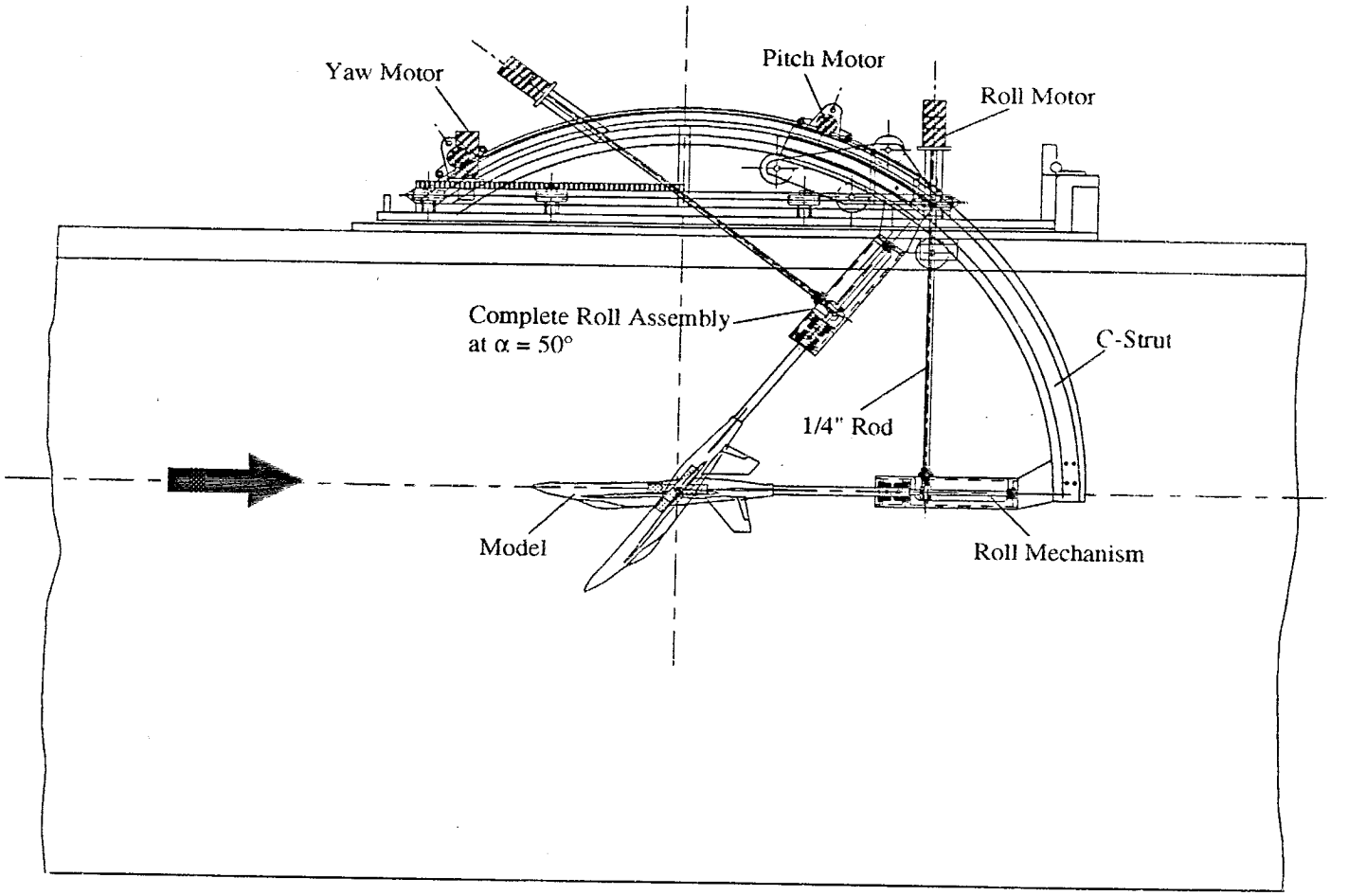

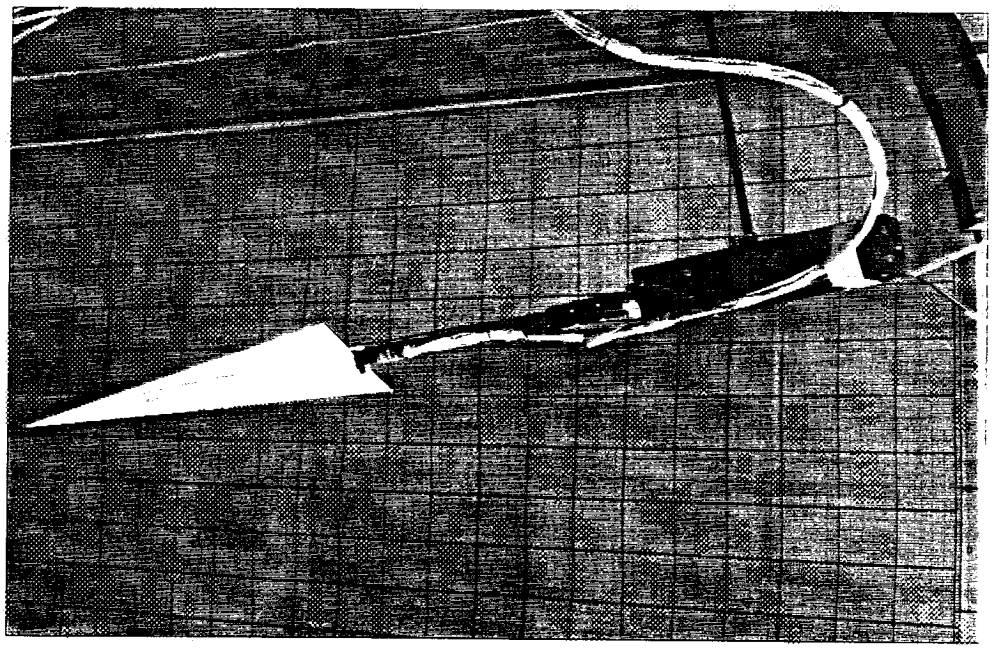

Figure 4 - Schematics and Photograph of the Water Tunnel Roll Mechanism

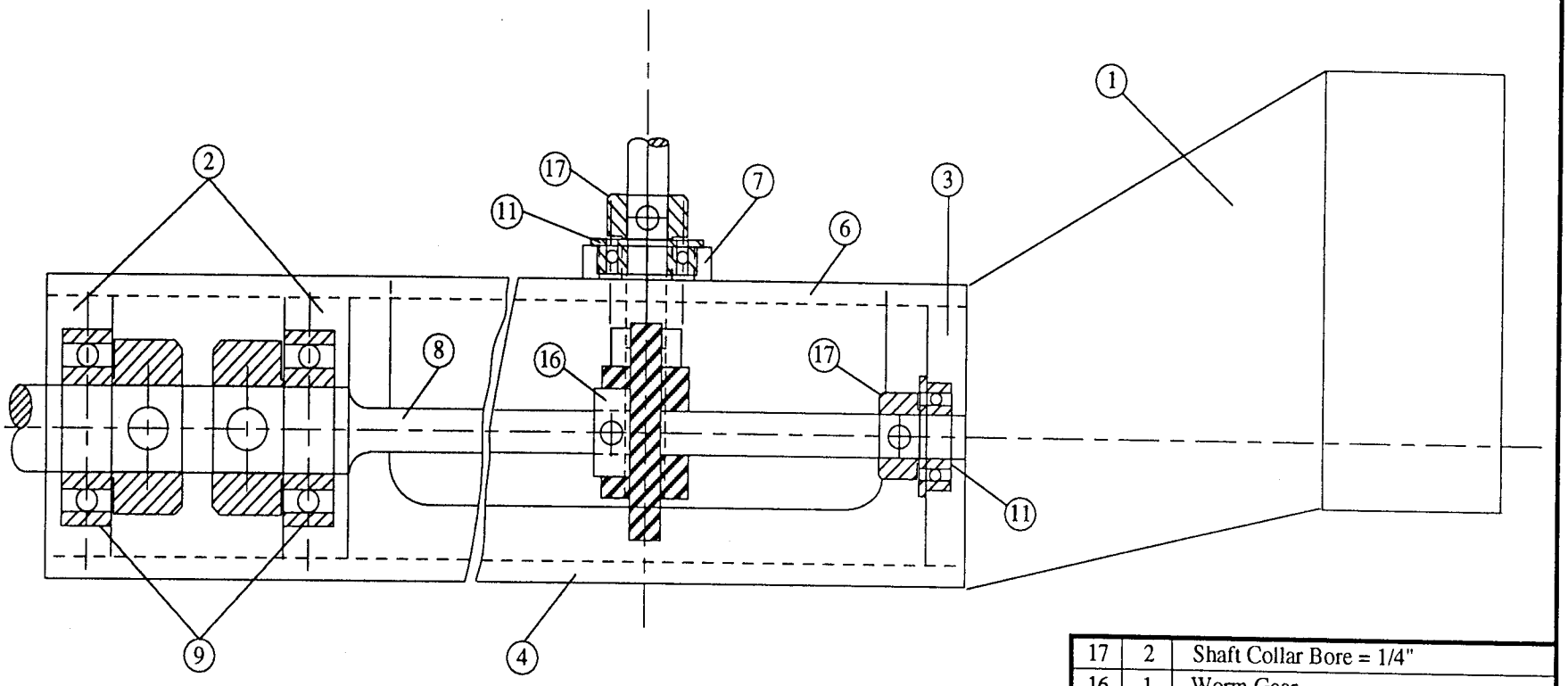

COMPLETE ASSEMBLY - SIDE VIEW

Item	Qty.	Description
17	2	Shaft Collar Bore = 1/4"
16	1	Worm Gear
11	2	Bearing Bore = 1/4"
9	2	Bearing Bore = 1/2"
8	1	Shaft
7	1	Top Bearing Support
6	1	Top Plate
4	1	Bottom Plate
3	1	Rear Bearing Support
2	2	Front Bearing Support
1	1	Main Support

EIDETICS INTERNATIONAL

ROLL MECHANISM
ASSEMBLY (SIDE VIEW)

Material : Stainless Steel/Aluminum

Tolerances (unless noted) : x.xxx +/- 0.005

Designed : CJS	Drawn : CJS	Date : 8/13/93
Scale : FULL	All dimensions in inches (unless noted)	Drawing # 030 Rev. -

NOTES:
DIMS ARE ON SURFACE OF PART
BREAK ALL SHARP EDGES
FINISH 0.8 µm (32 µin) IN RMS

Figure 5 - Roll Mechanism Assembly

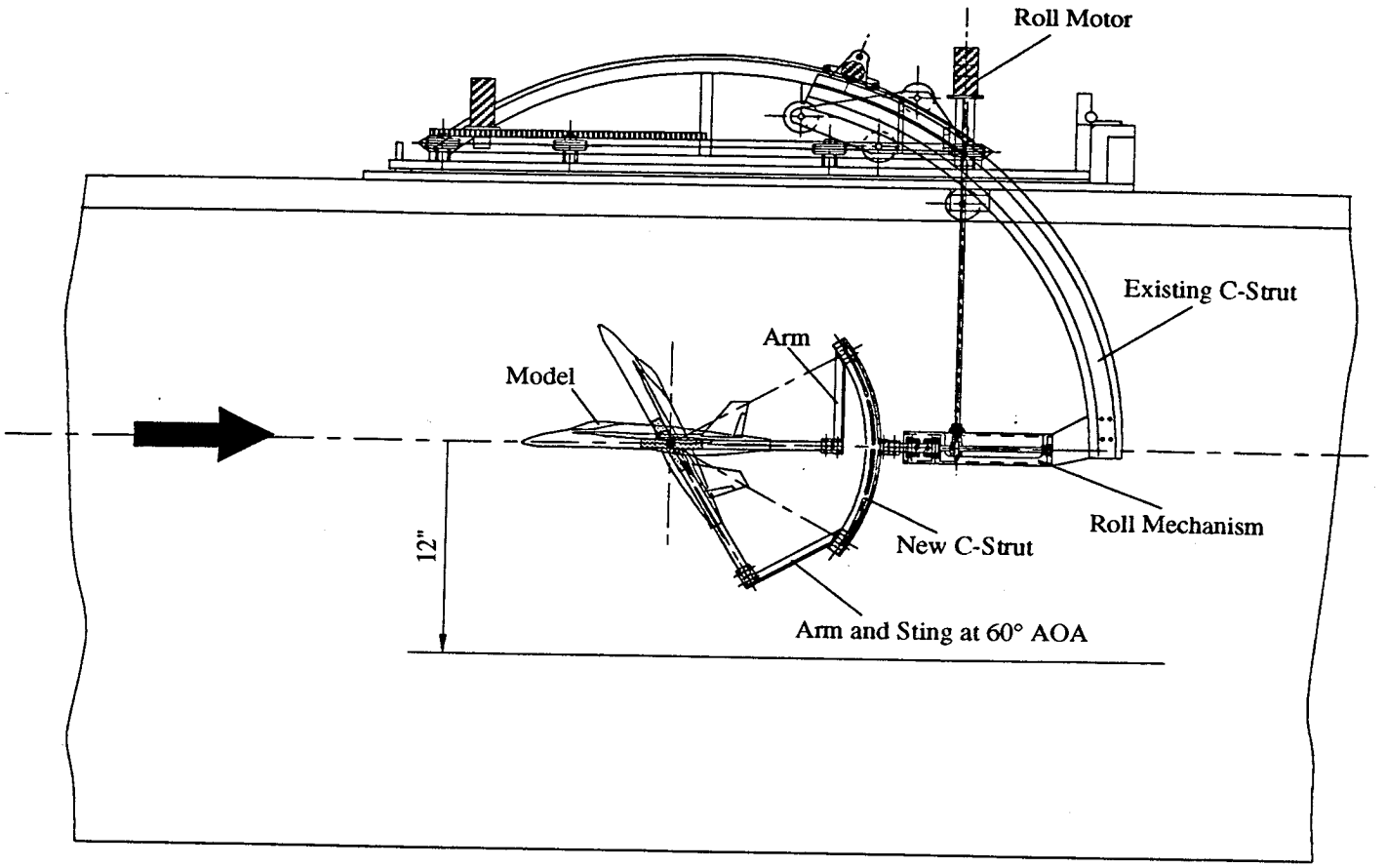

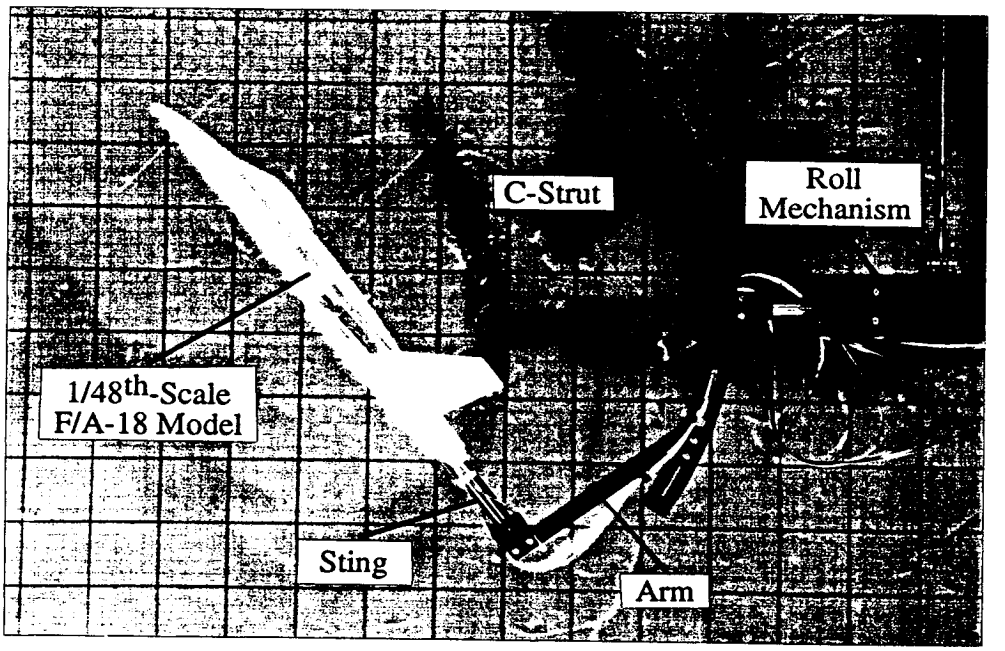

Figure 6 - Schematics and Photograph of the Water Tunnel Rotary Rig

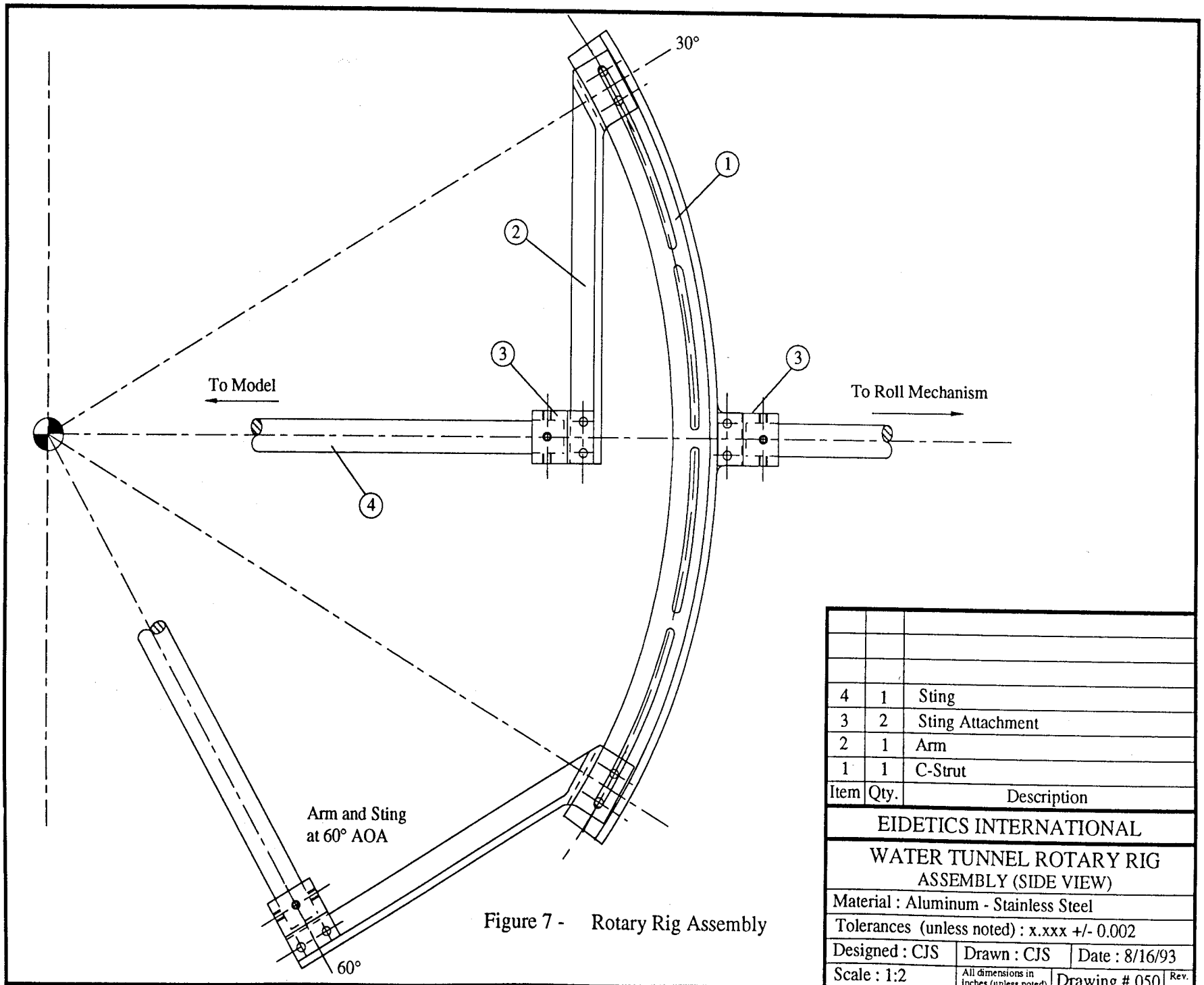

4	1	Sting
3	2	Sting Attachment
2	1	Arm
1	1	C-Strut
Item	Qty.	Description

EIDETICS INTERNATIONAL

WATER TUNNEL ROTARY RIG
ASSEMBLY (SIDE VIEW)

Material : Aluminum - Stainless Steel		
Tolerances (unless noted) : x.xxx +/- 0.002		
Designed : CJS	Drawn : CJS	Date : 8/16/93
Scale : 1:2	All dimensions in inches (unless noted)	Drawing # 050 Rev. -

Figure 7 - Rotary Rig Assembly

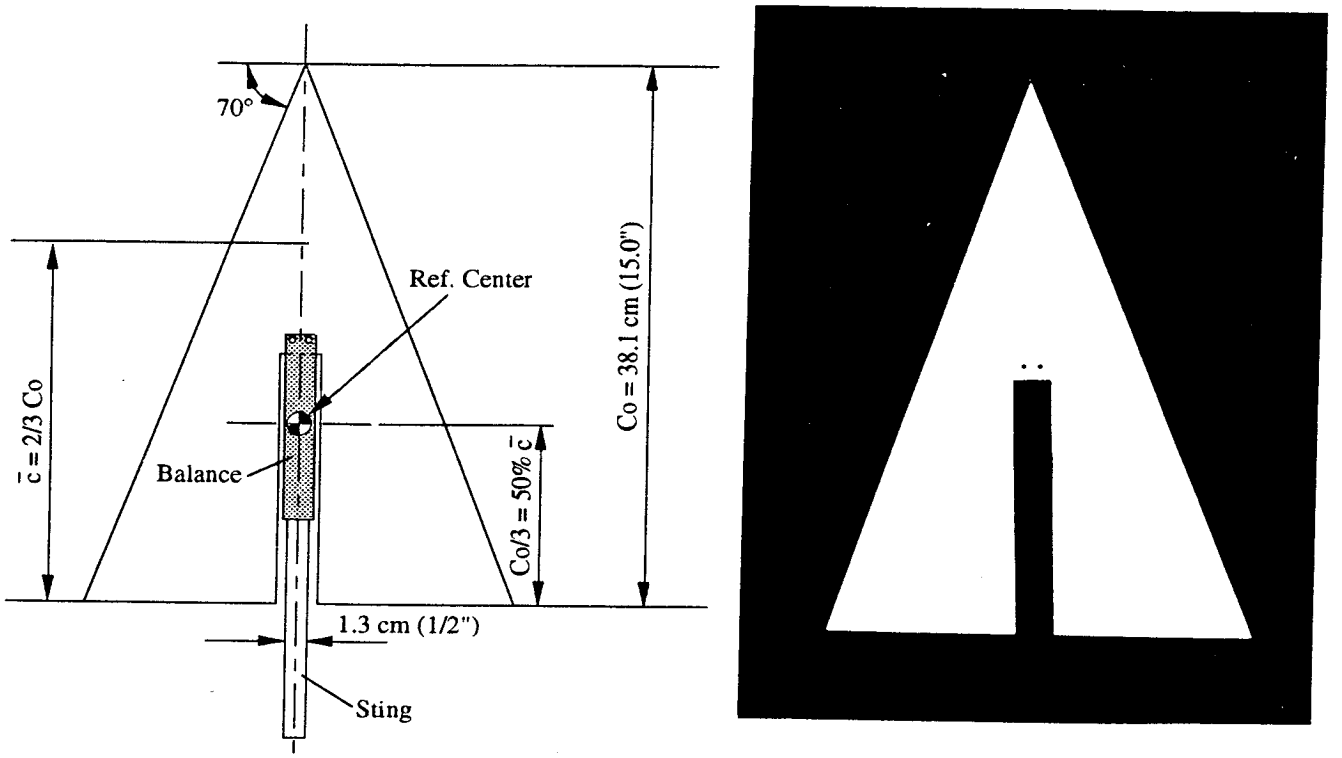

a) 70° Delta Wing

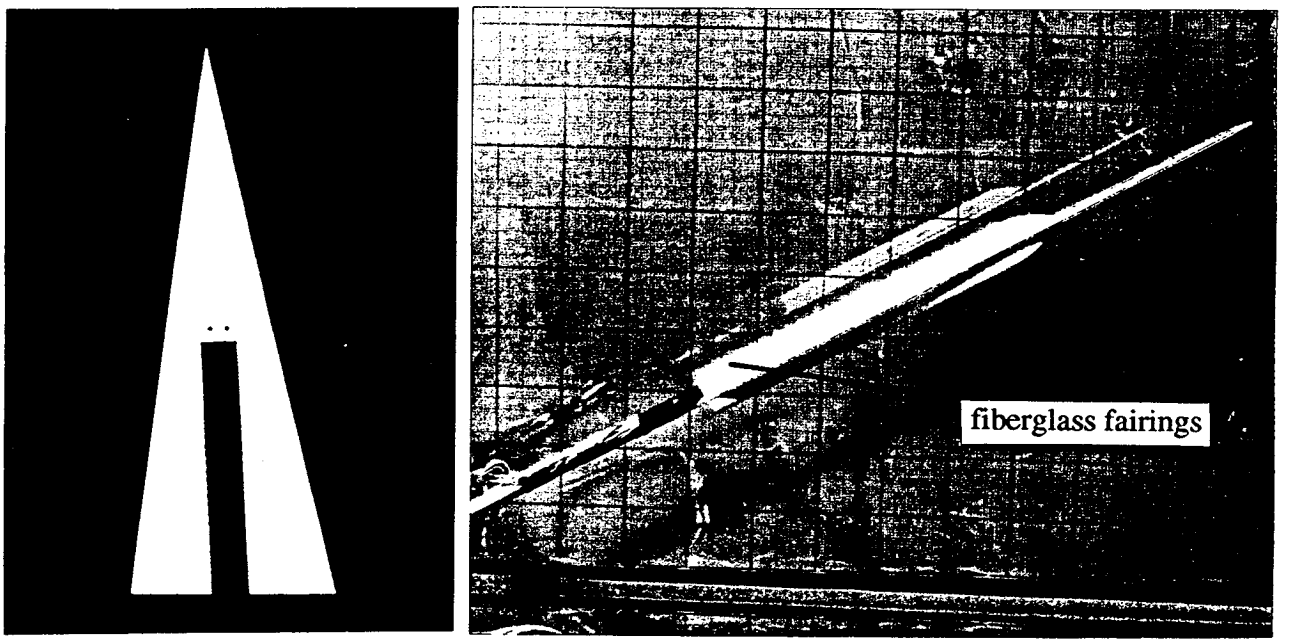

b) 80° Delta Wing

Figure 8 - Delta Wing Models

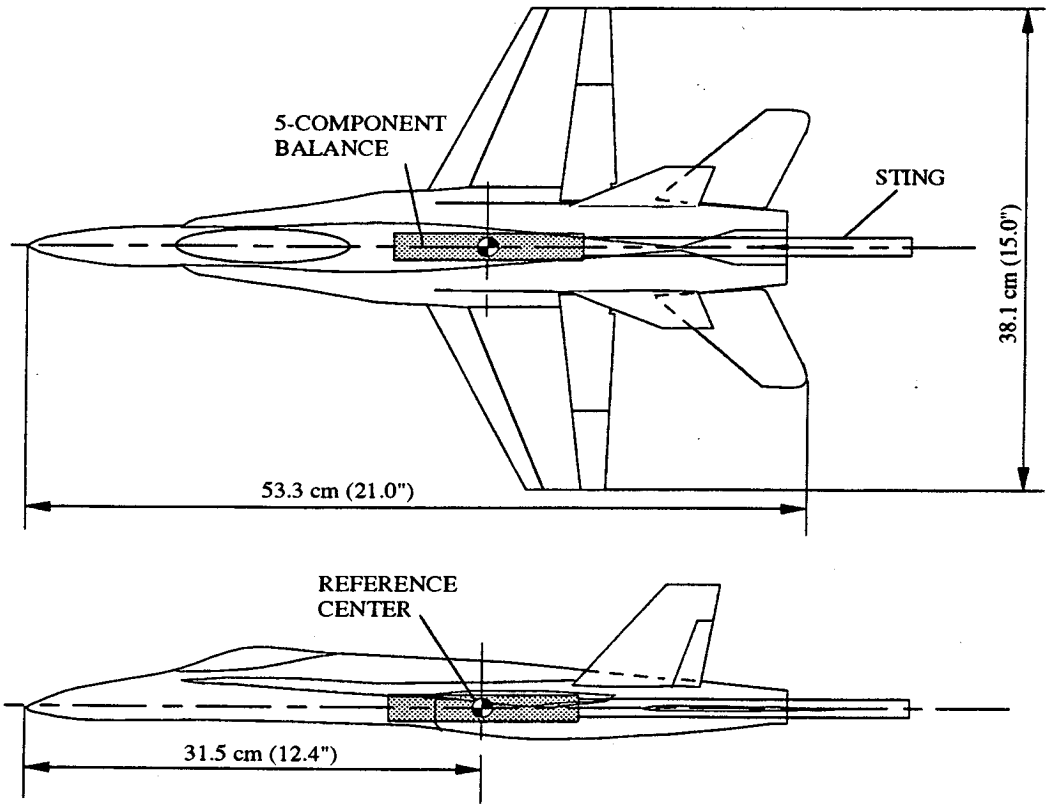

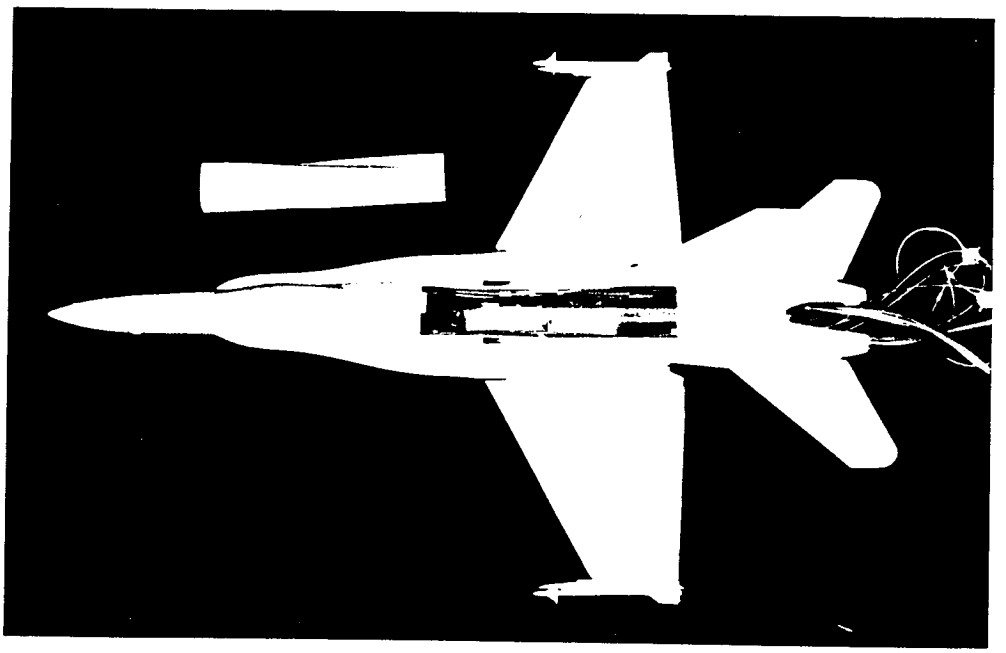

Figure 9 - 1/32nd-Scale F/A-18 Model

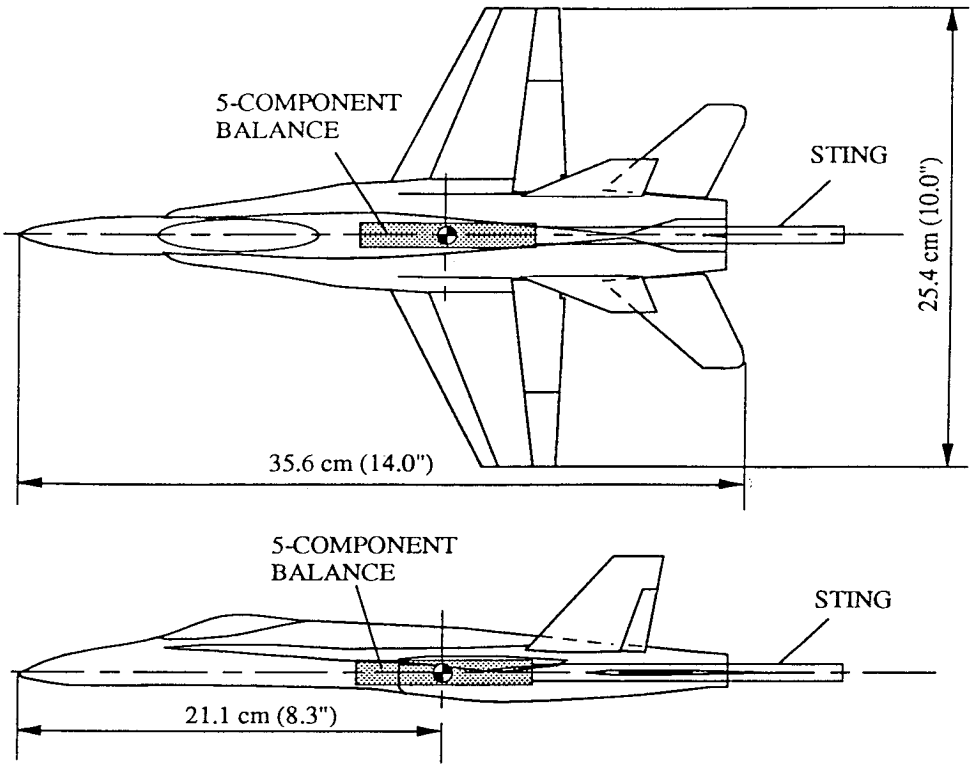

Figure 10 - 1/48th-Scale F/A-18 Model

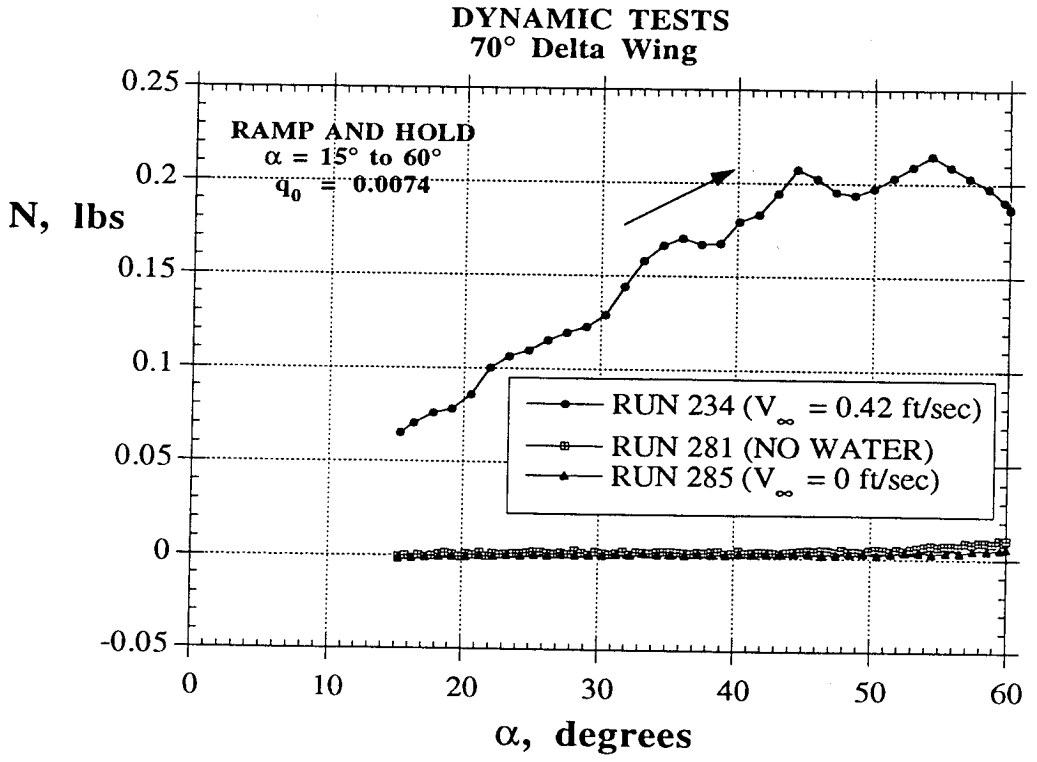

Figure 11 - Inertial Tares During a Pitch-Up and Hold Maneuver (70° Delta Wing)

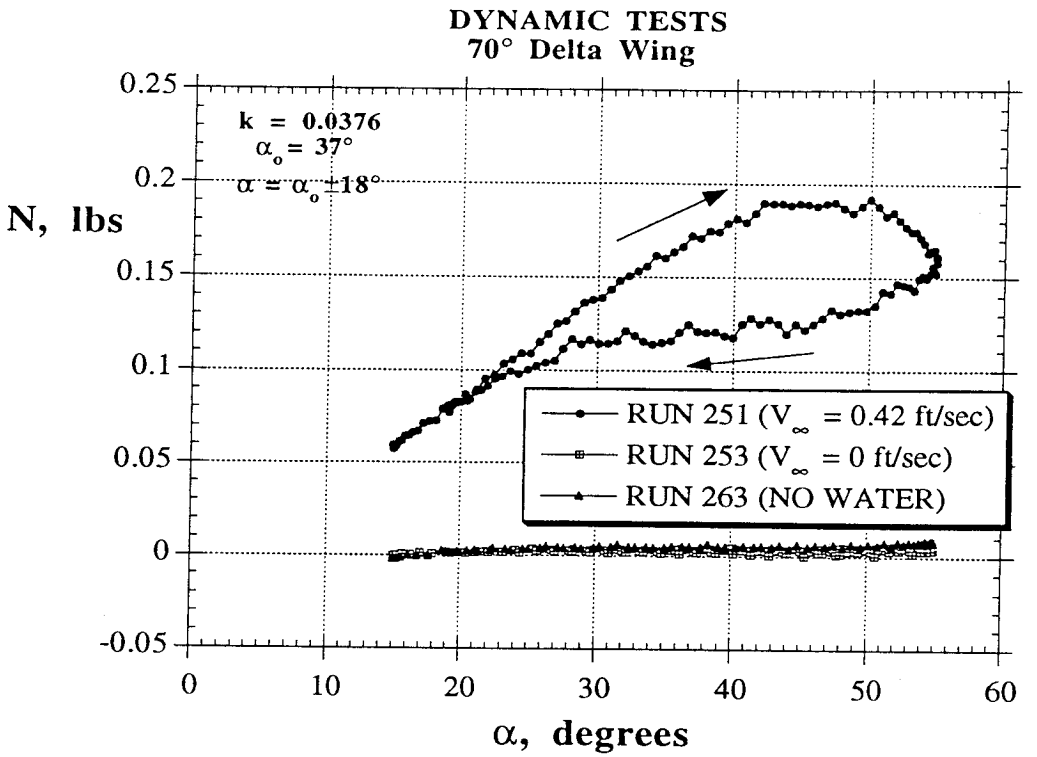

a) 70° Delta Wing

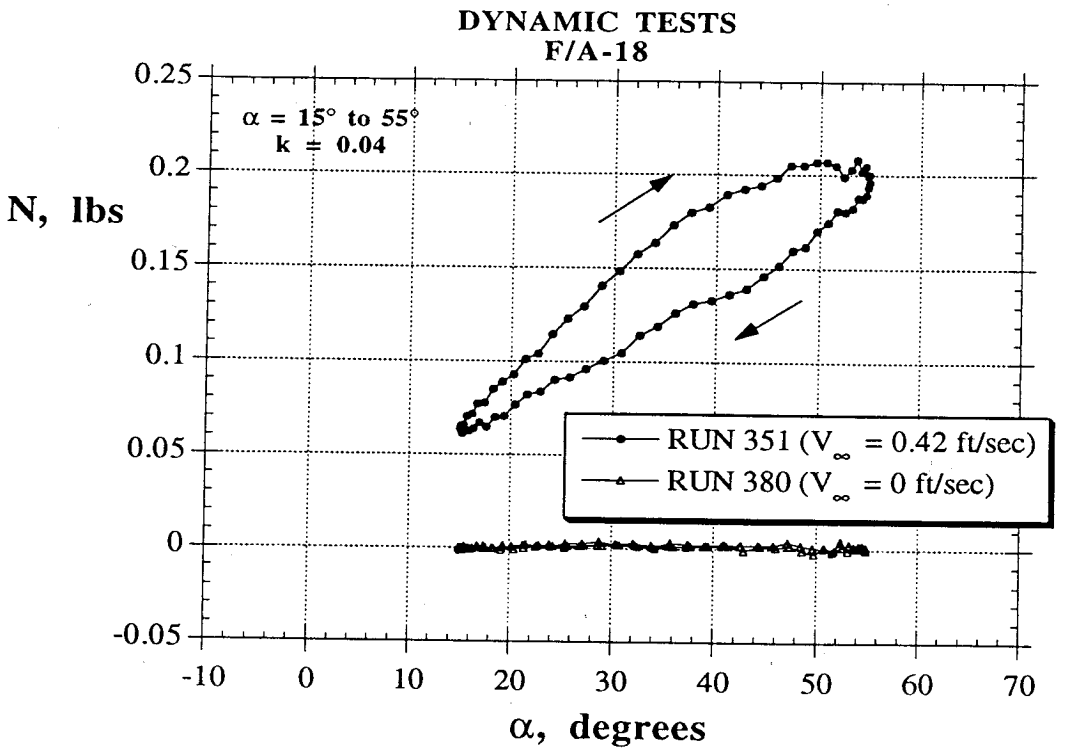

b) 1/32nd-Scale F/A-18

Figure 12 - Inertial Tares During Pitch Oscillations

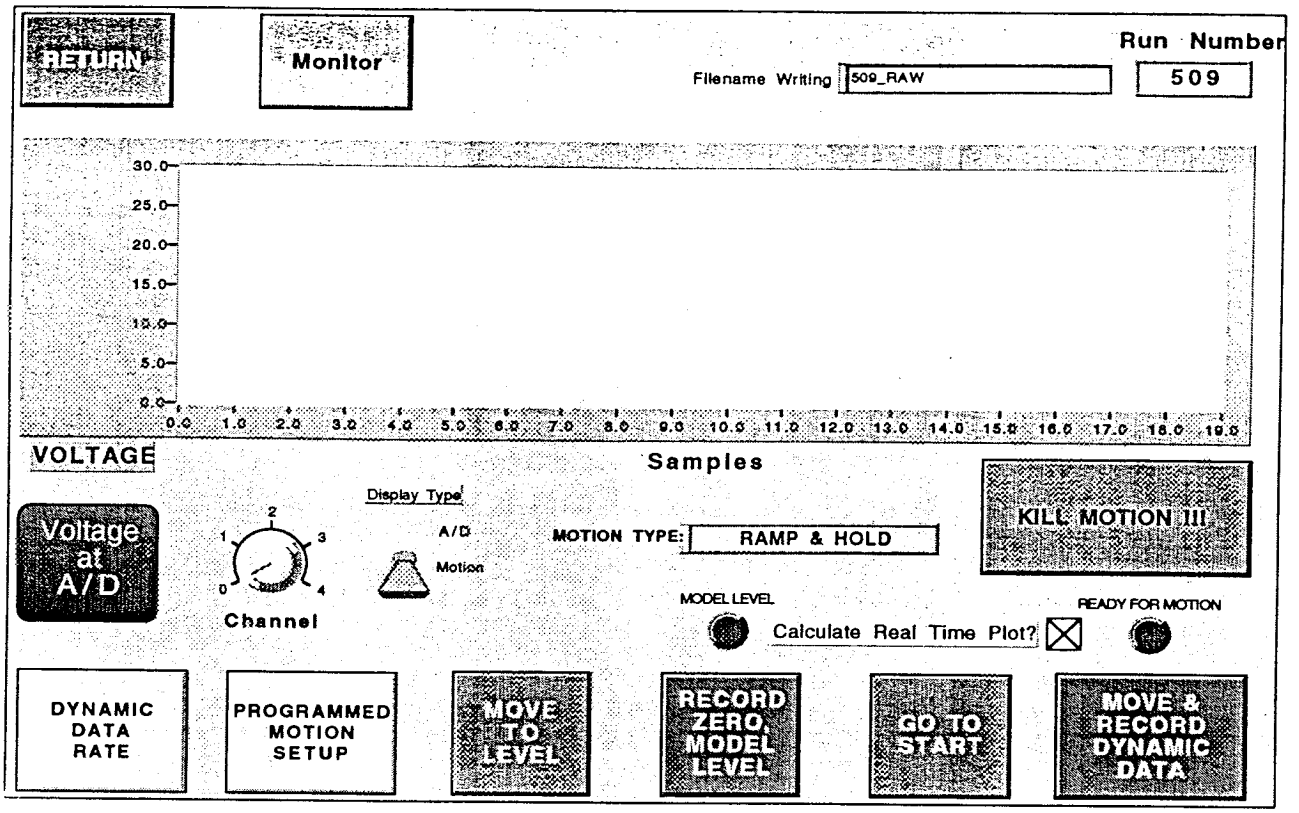

a) "Dynamic Data W/Motion" Panel

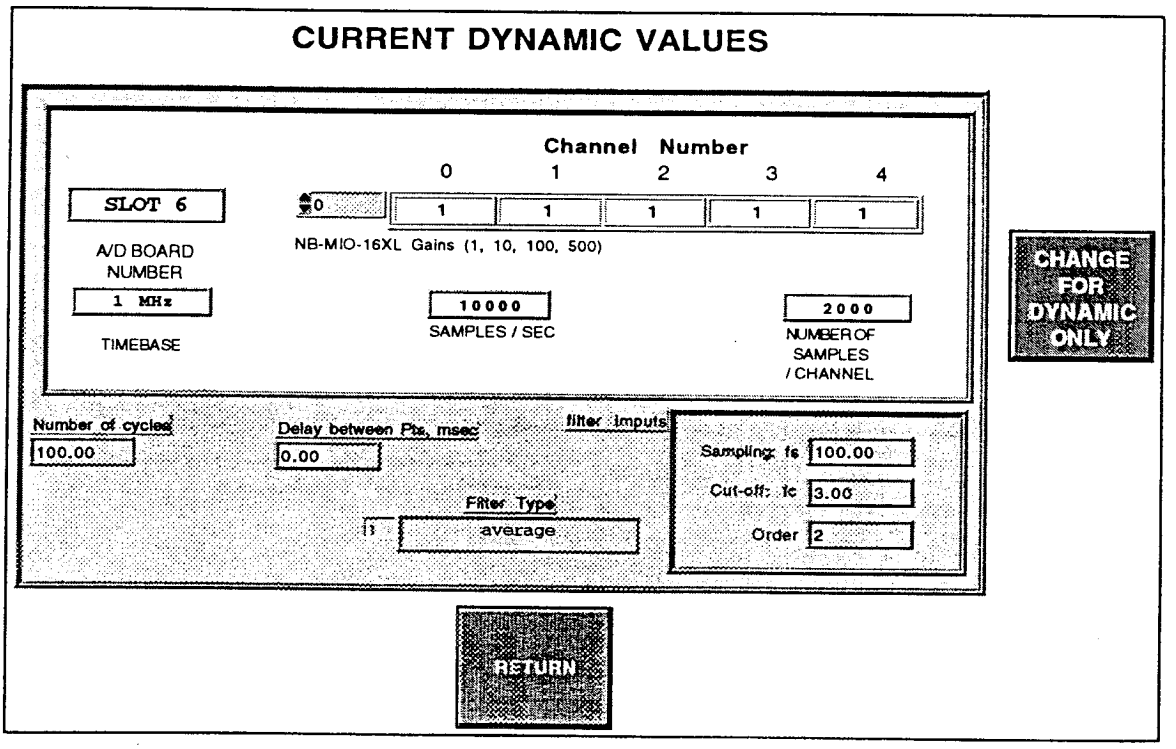

b) "Dynamic Data Rate" Panel

Figure 13 - Software Front Panels Used During Dynamic Tests

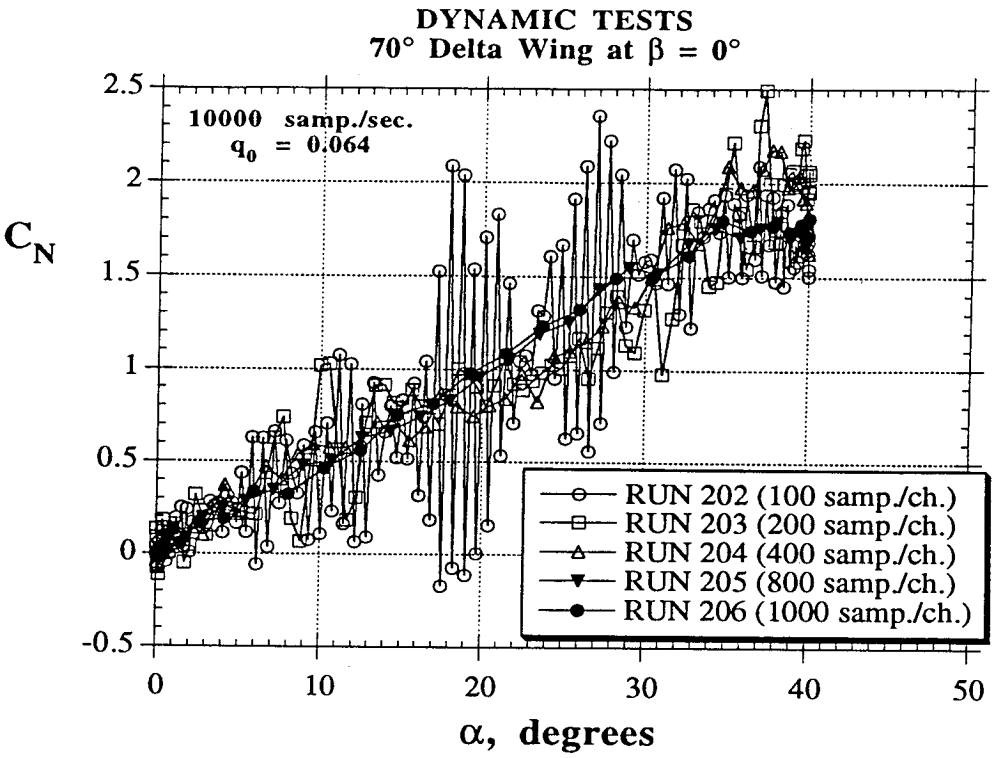

Figure 14 - Effect of Sampling Number on Dynamic Data

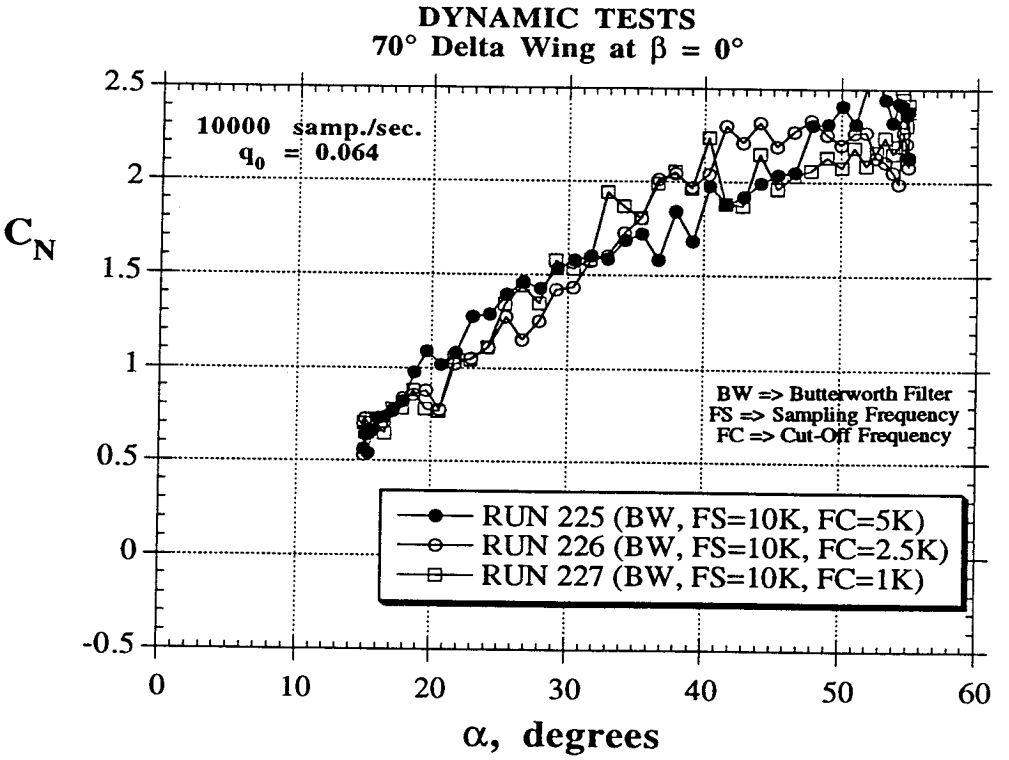

Figure 15 - Effect of Digital Filter (Butterworth) on Dynamic Data

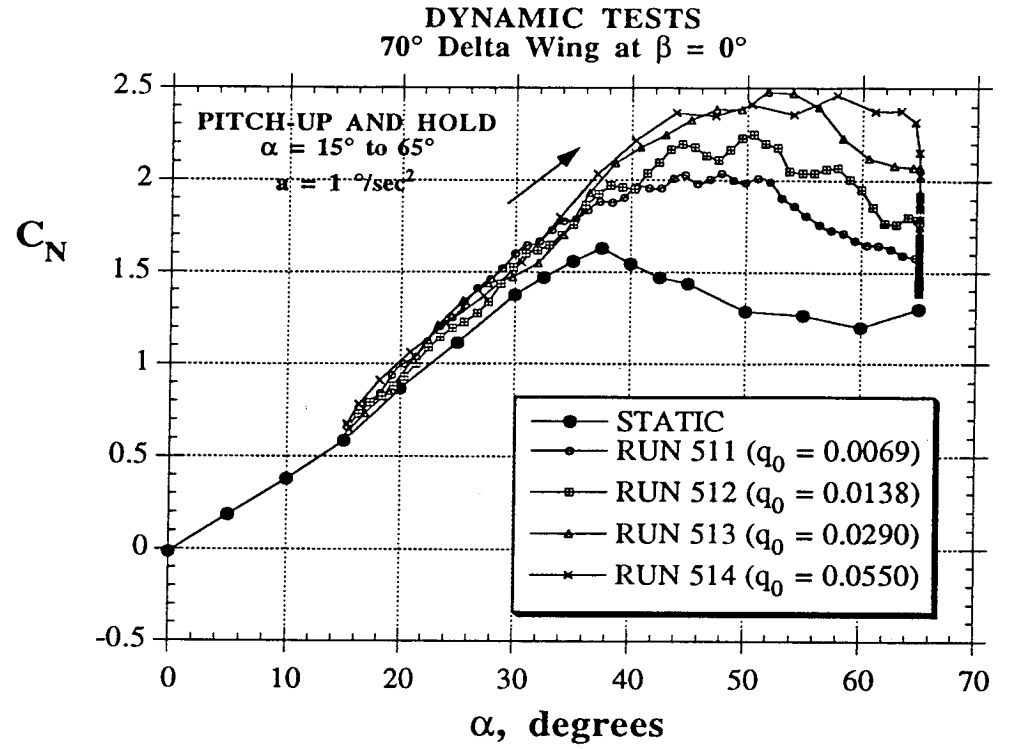

a) Hysteresis Loops in C_N

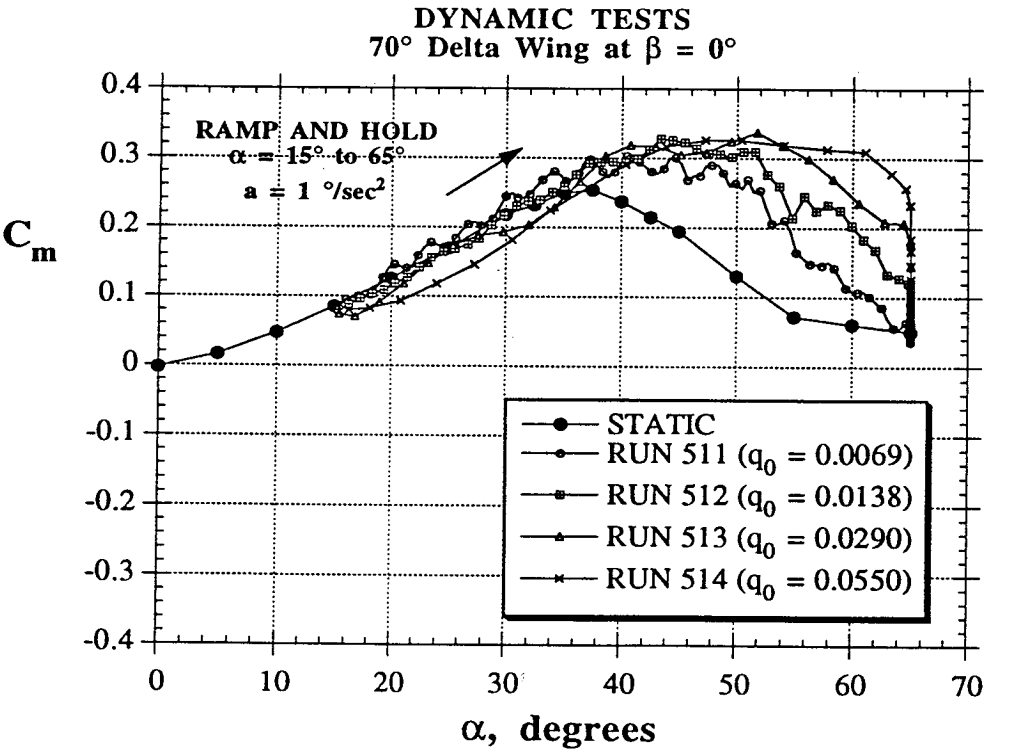

b) Hysteresis Loops in C_m

Figure 16 - Effect of Pitch Rate on the Longitudinal Characteristics of the 70° Delta Wing During a Pitch-Up and Hold Maneuver

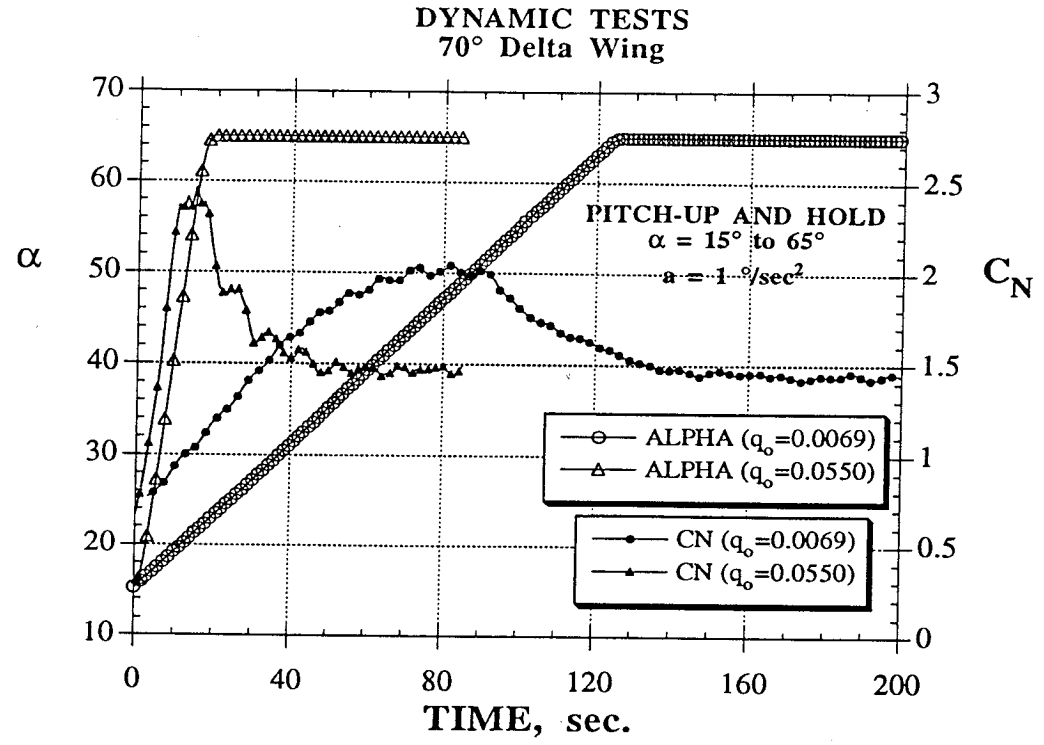

c) Angle of Attack and C_N Time Histories

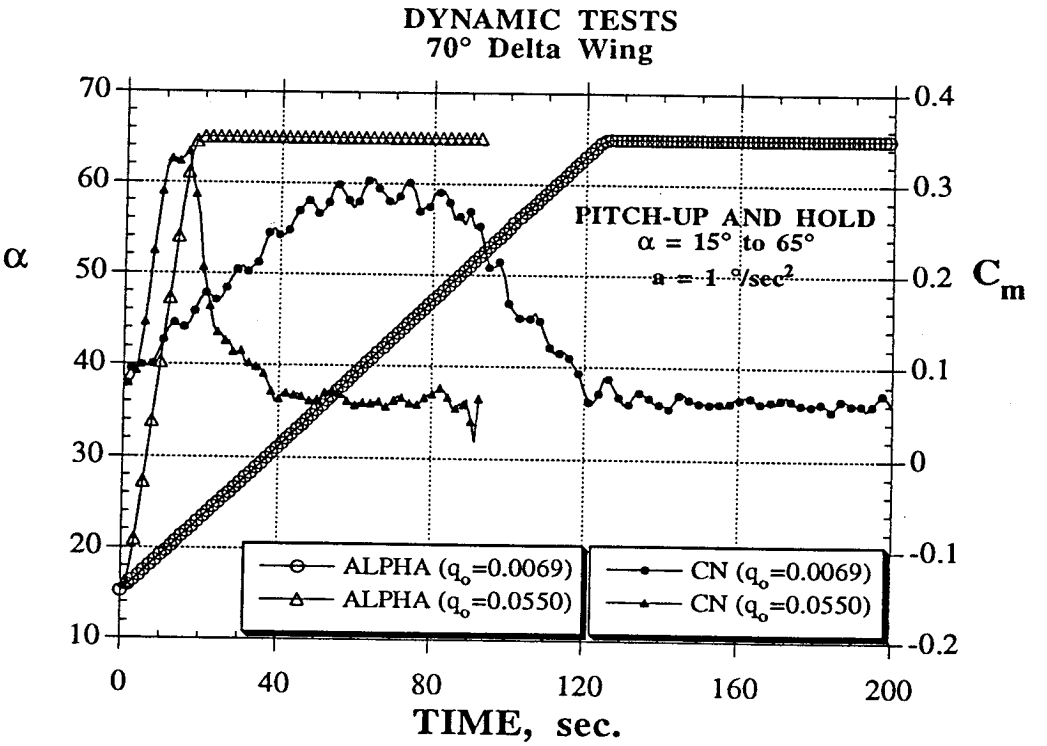

d) Angle of Attack and C_m Time Histories

Figure 16 - Concluded

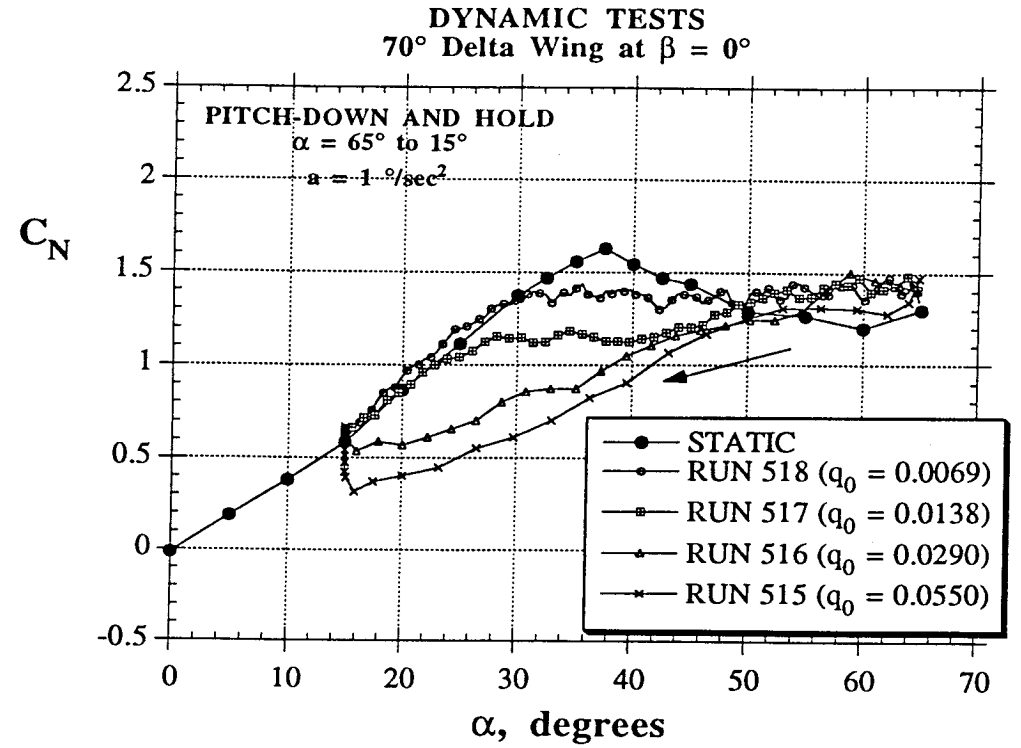

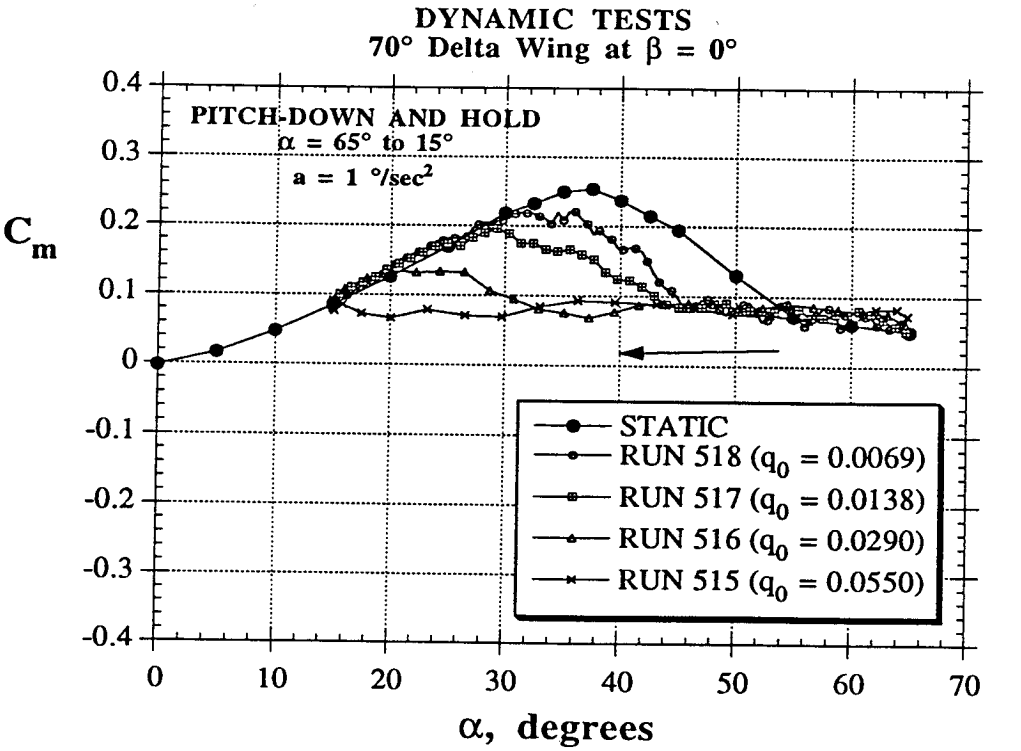

Figure 17 - Effect of Pitch Rate on the Longitudinal Characteristics of the 70° Delta Wing During a Pitch-Down and Hold Maneuver

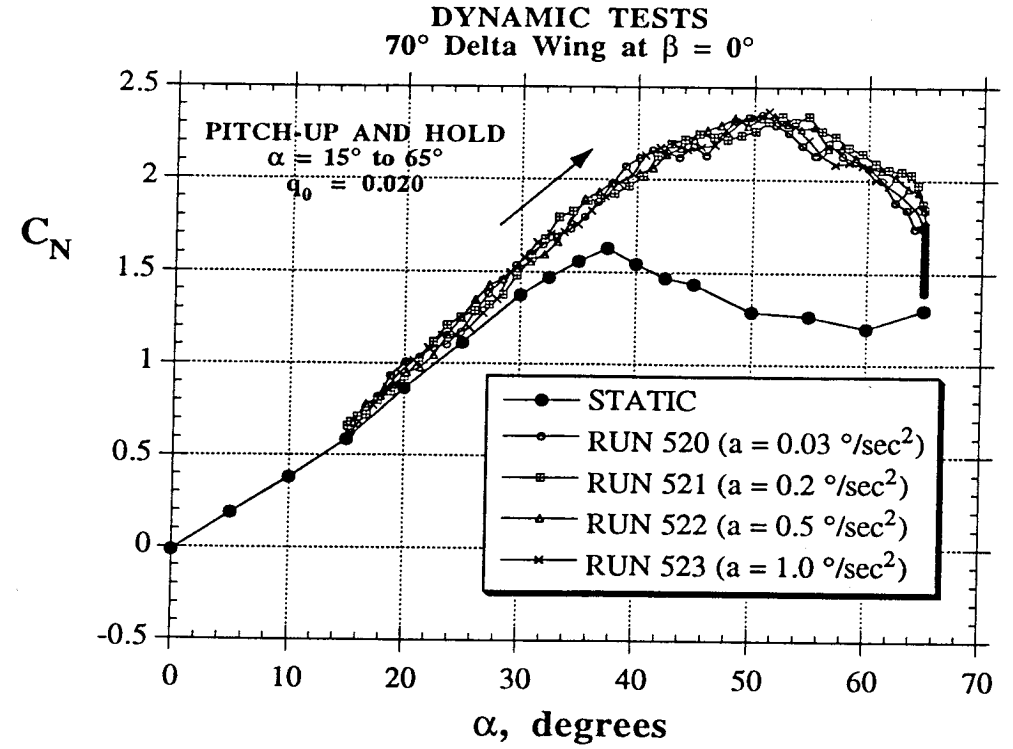

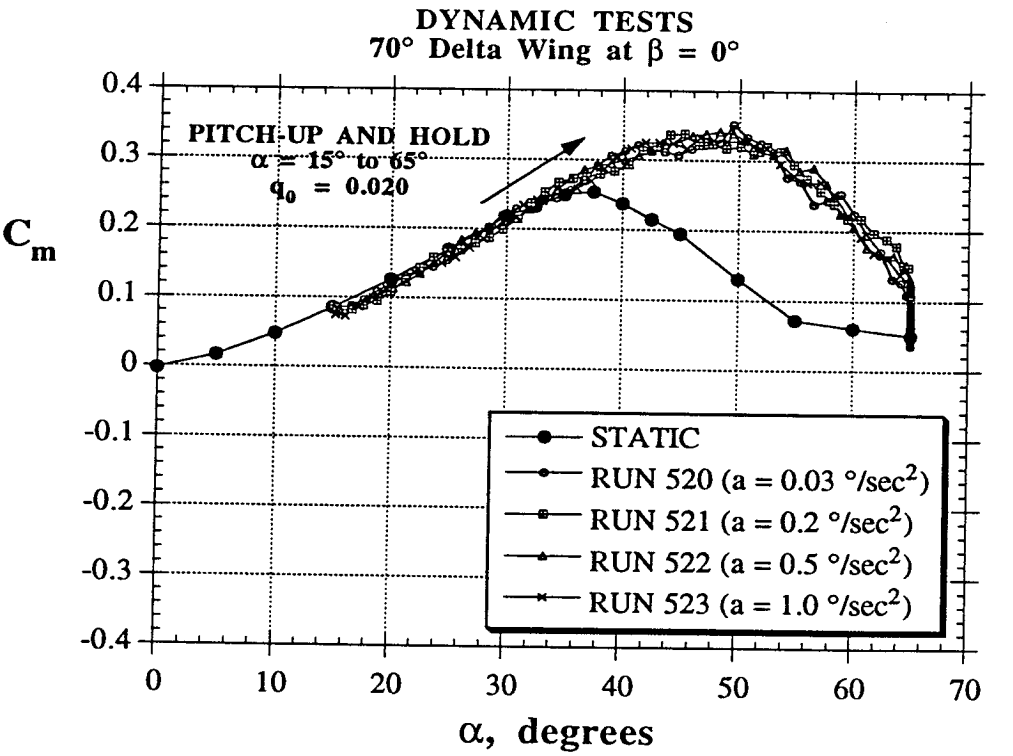

Figure 18 - Effect of Acceleration on the Longitudinal Characteristics of the 70° Delta Wing During a Pitch-Up and Hold Maneuver

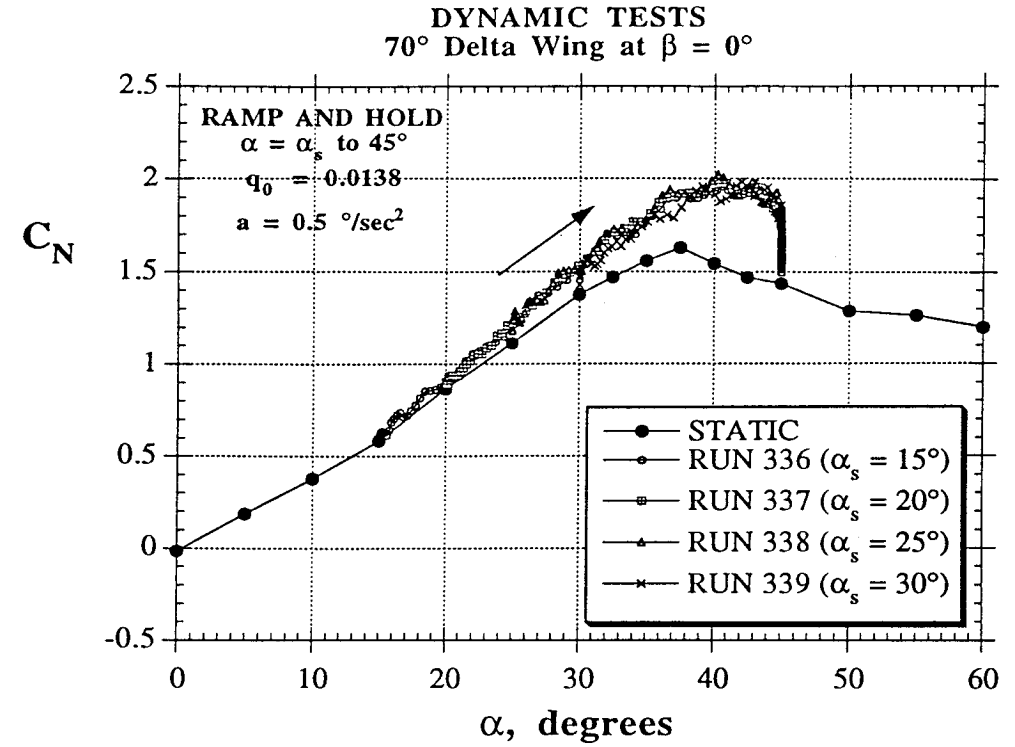

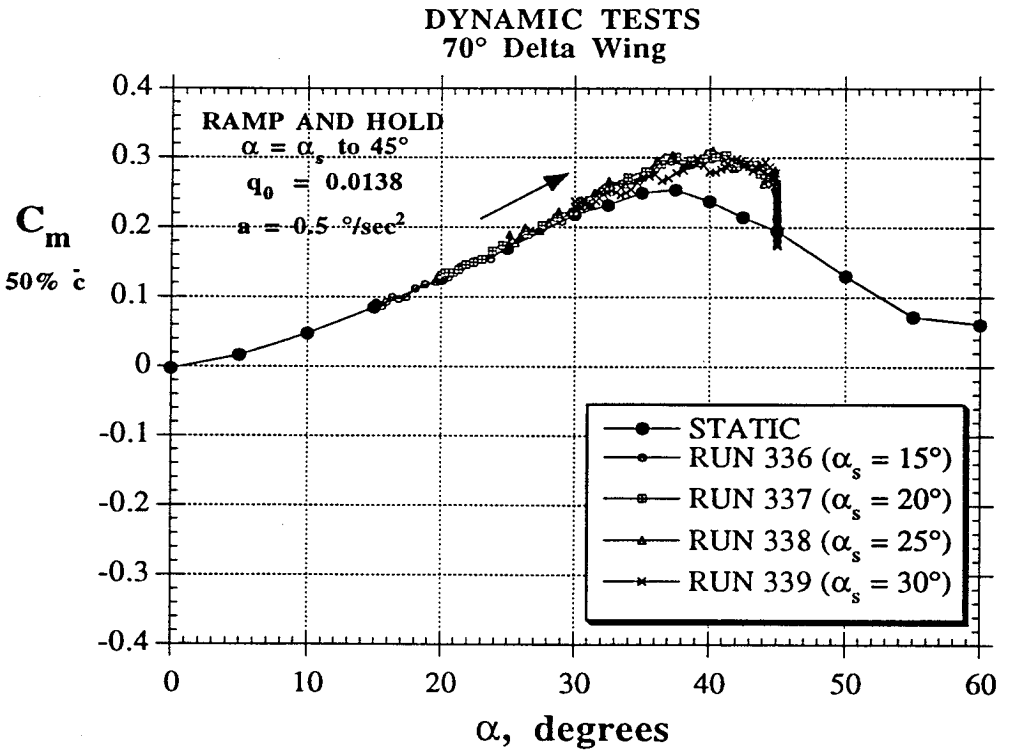

Figure 19 - Effect of Starting Angle of Attack on the Longitudinal Characteristics of the 70° Delta Wing During a Pitch-Up and Hold Maneuver

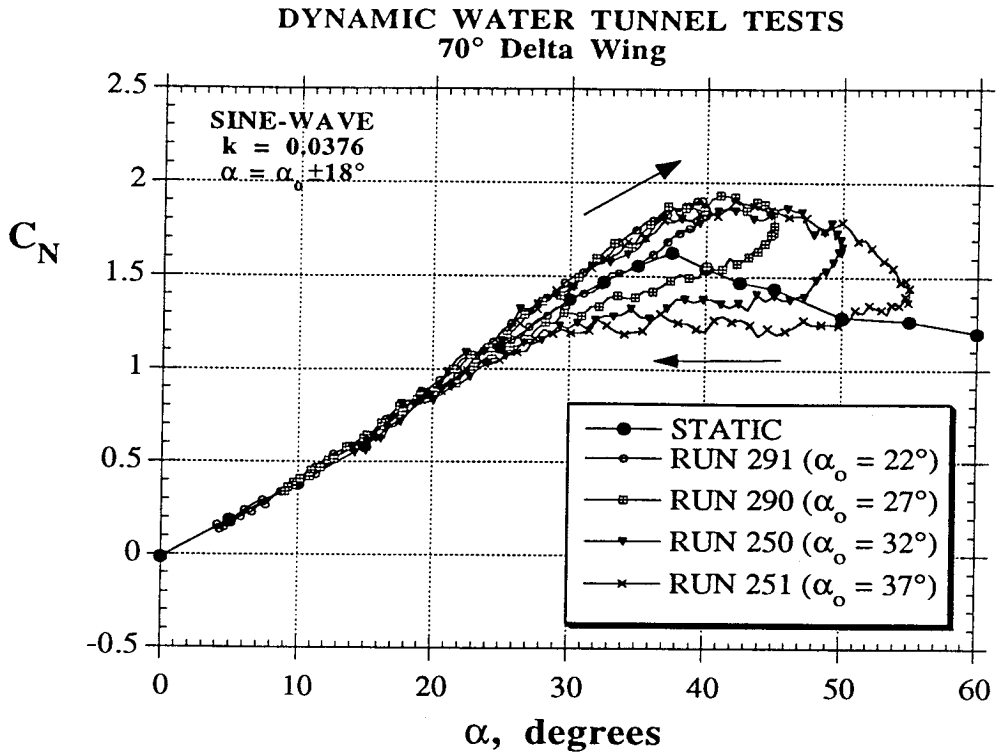

a) Water Tunnel Test

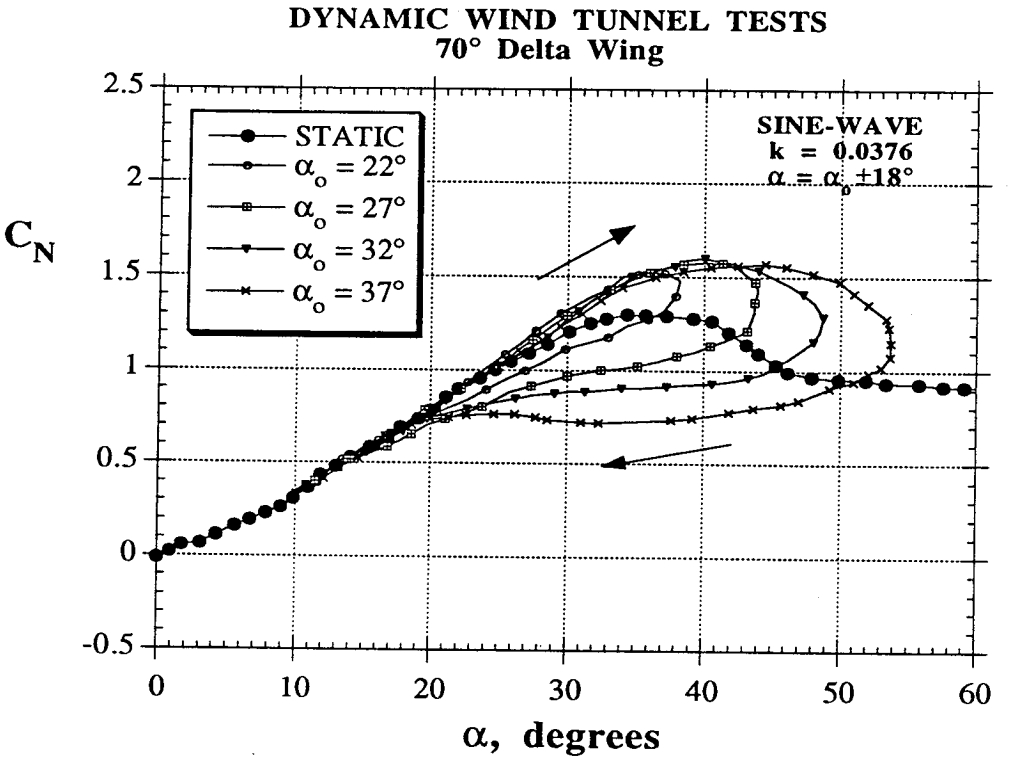

b) Wind Tunnel Test (Ref. 7)

Figure 20 - Normal Force Variations During Pitch Oscillations about Different Mean Angles of Attack α_o at k = 0.0376 (70° Delta Wing)

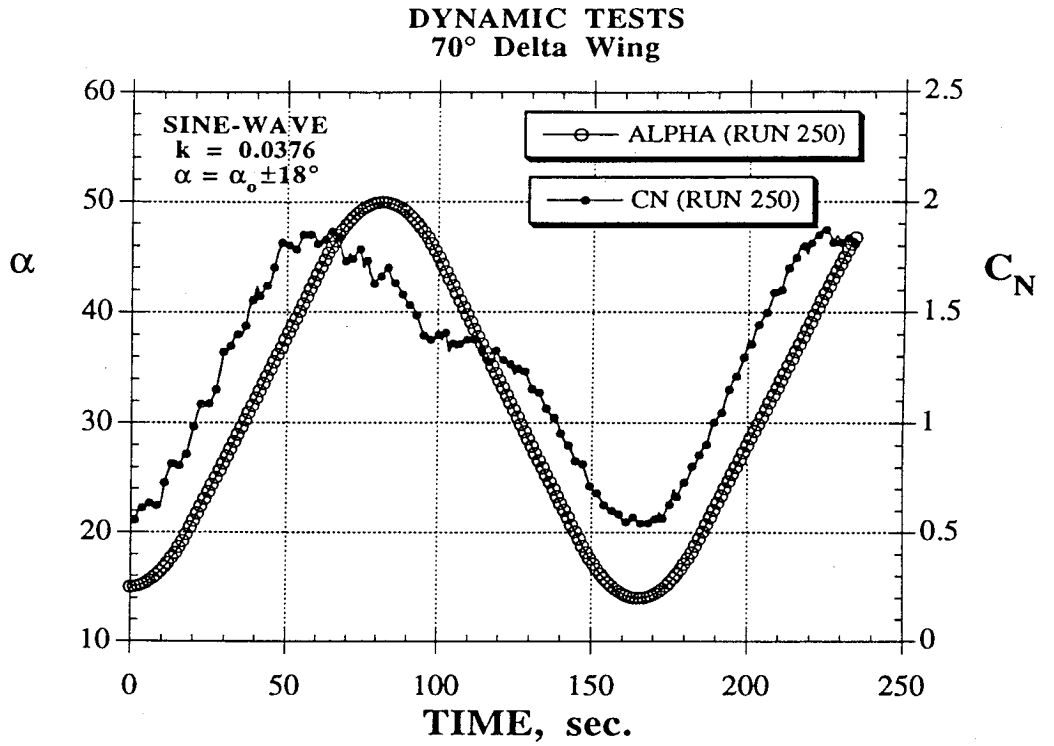

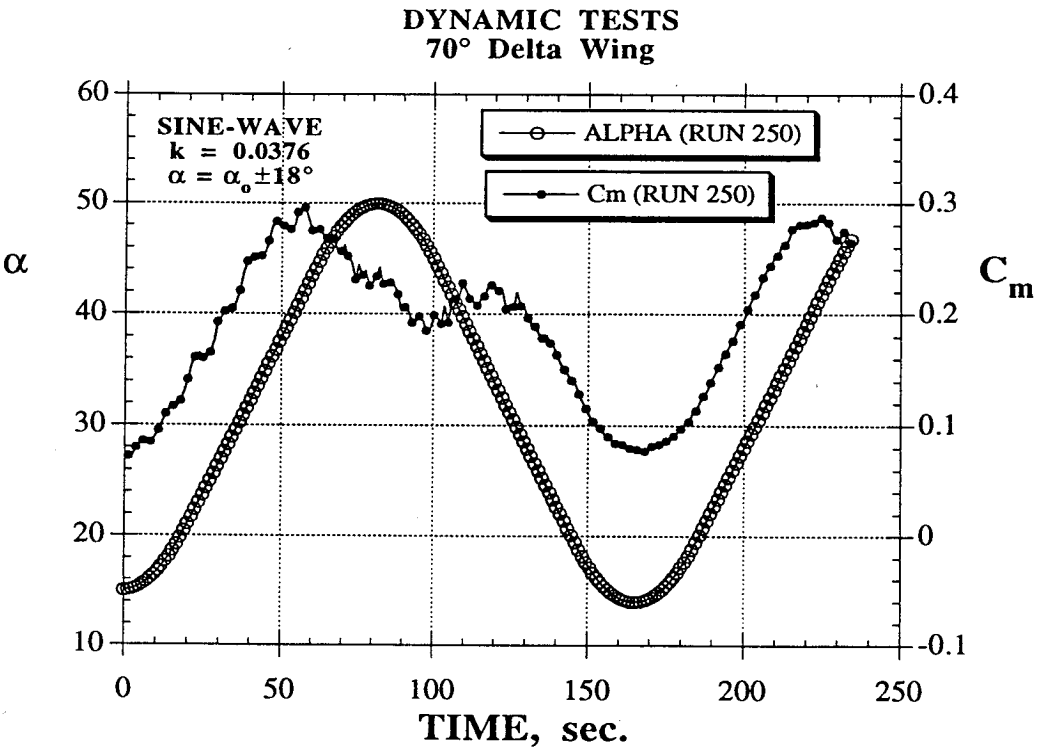

Figure 21 - Angle of Attack, C_N and C_m Time Histories During a Pitch Oscillation From $\alpha = 14°$ to 50° at $k = 0.0376$ (70° Delta Wing)

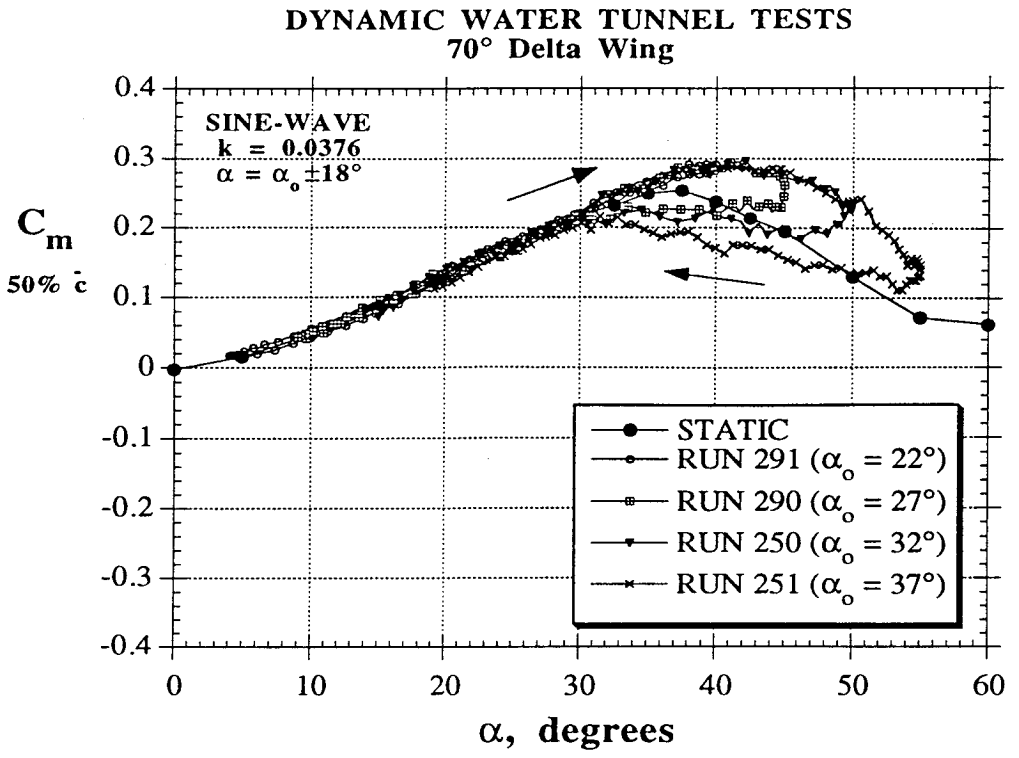

a) Water Tunnel Test (50% $\bar{c}$)

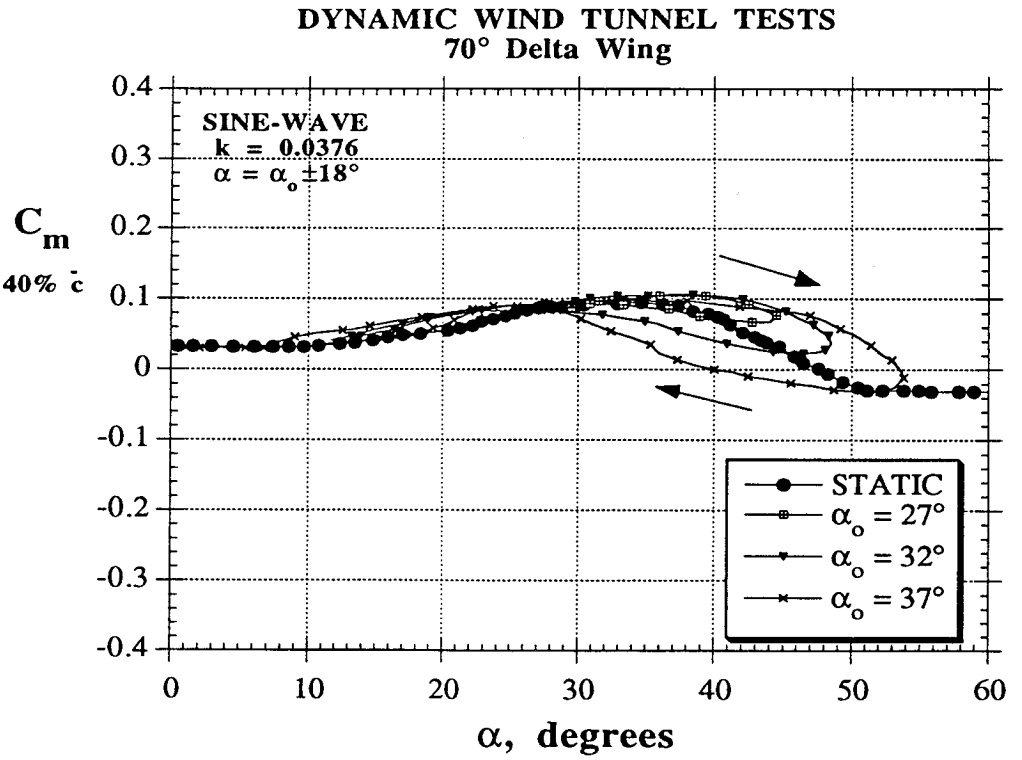

b) Wind Tunnel Test (40% $\bar{c}$, Ref. 7)

Figure 22 - Pitching Moment Variations During Pitch Oscillations about Different Mean Angles of Attack α_0 at k = 0.0376 (70° Delta Wing)

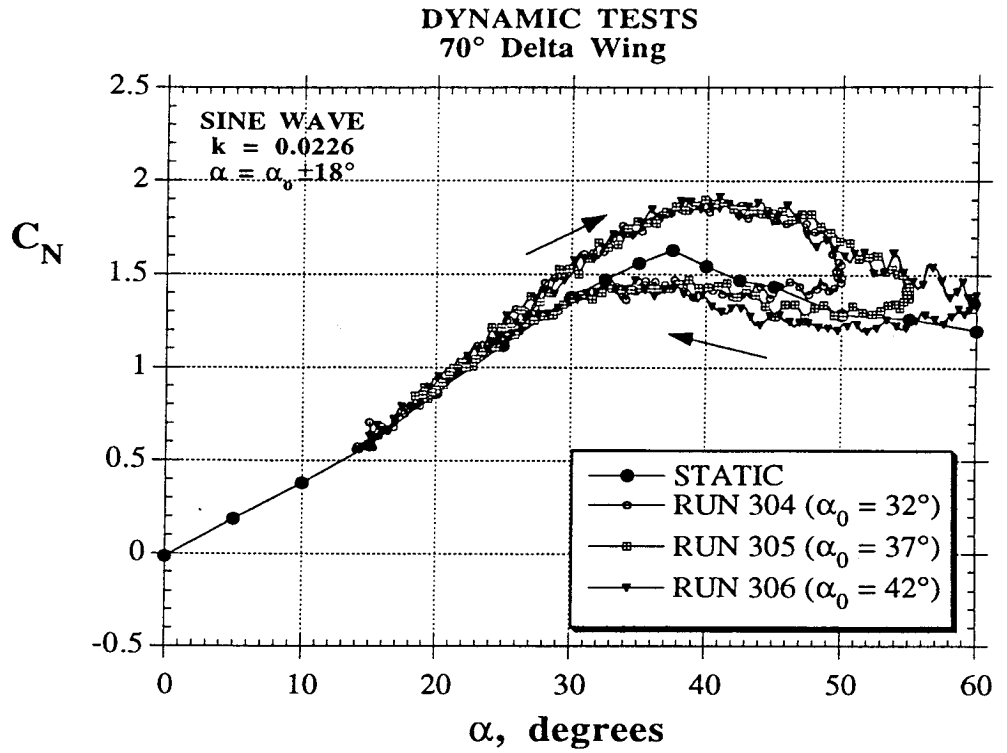

a) k = 0.0226

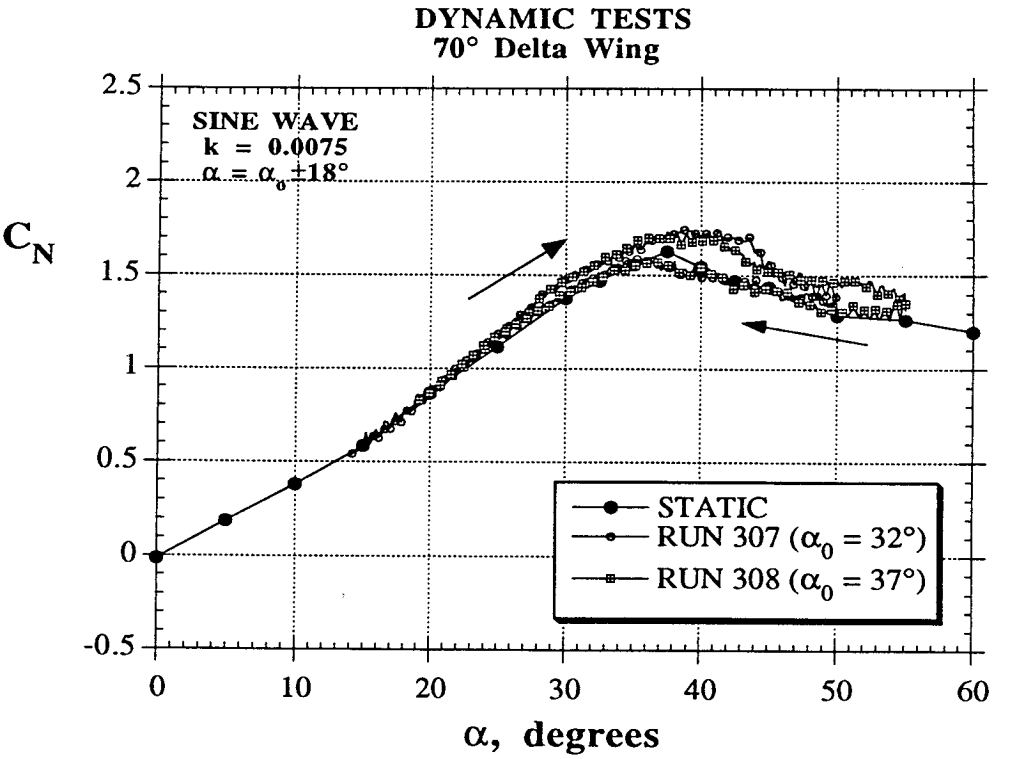

b) k = 0.0075

Figure 23 - Effect of Frequency on the Normal Force During Pitch Oscillations about Different Mean Angles of Attack α_0 (70° Delta Wing)

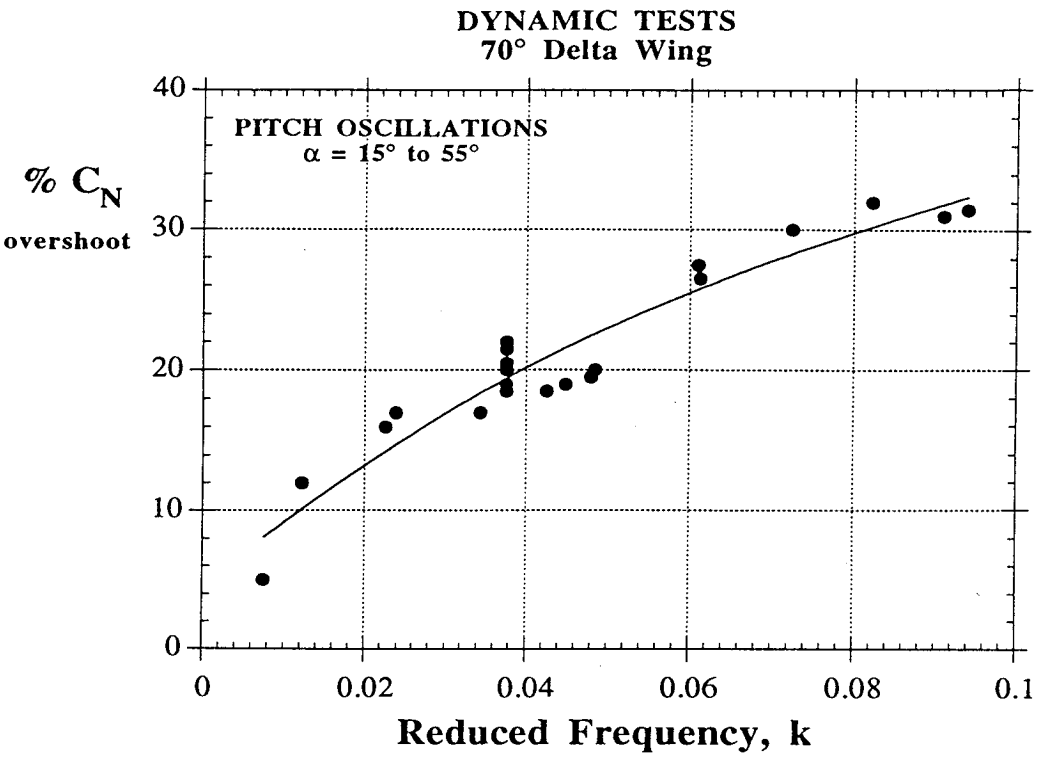

a) Water Tunnel Test

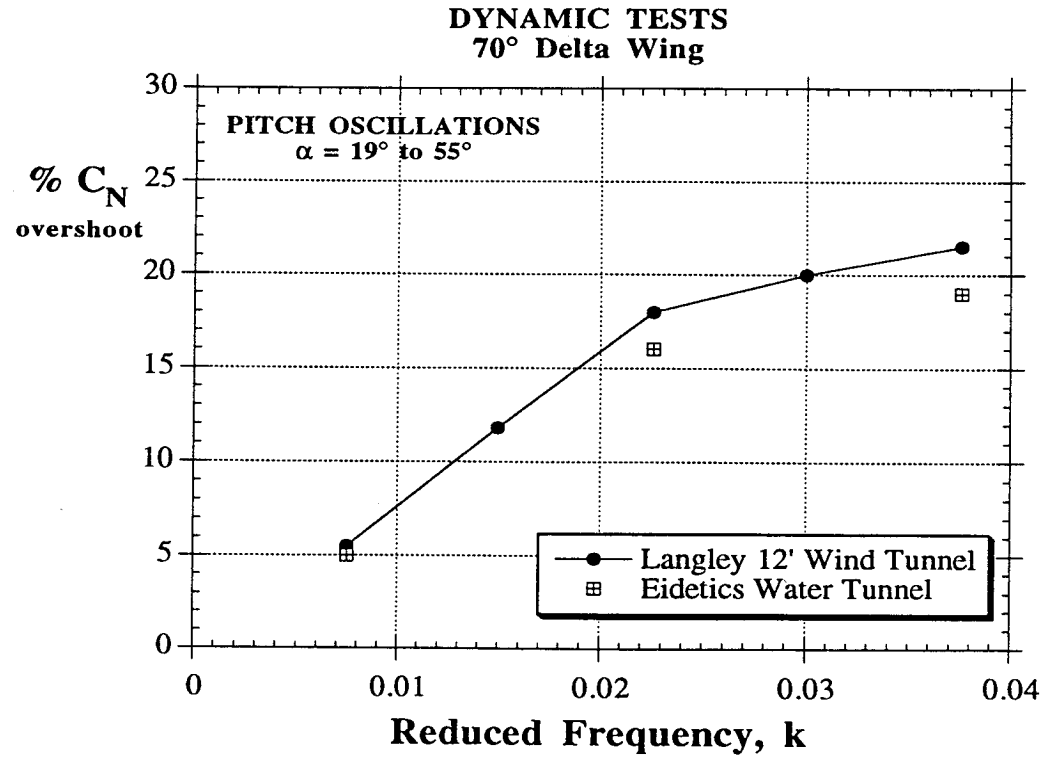

b) Comparison to Wind Tunnel Test (Ref. 7)

Figure 24 - Percentage of Normal Force Overshoot During Pitch Oscillations at Different Frequencies (70° Delta Wing)

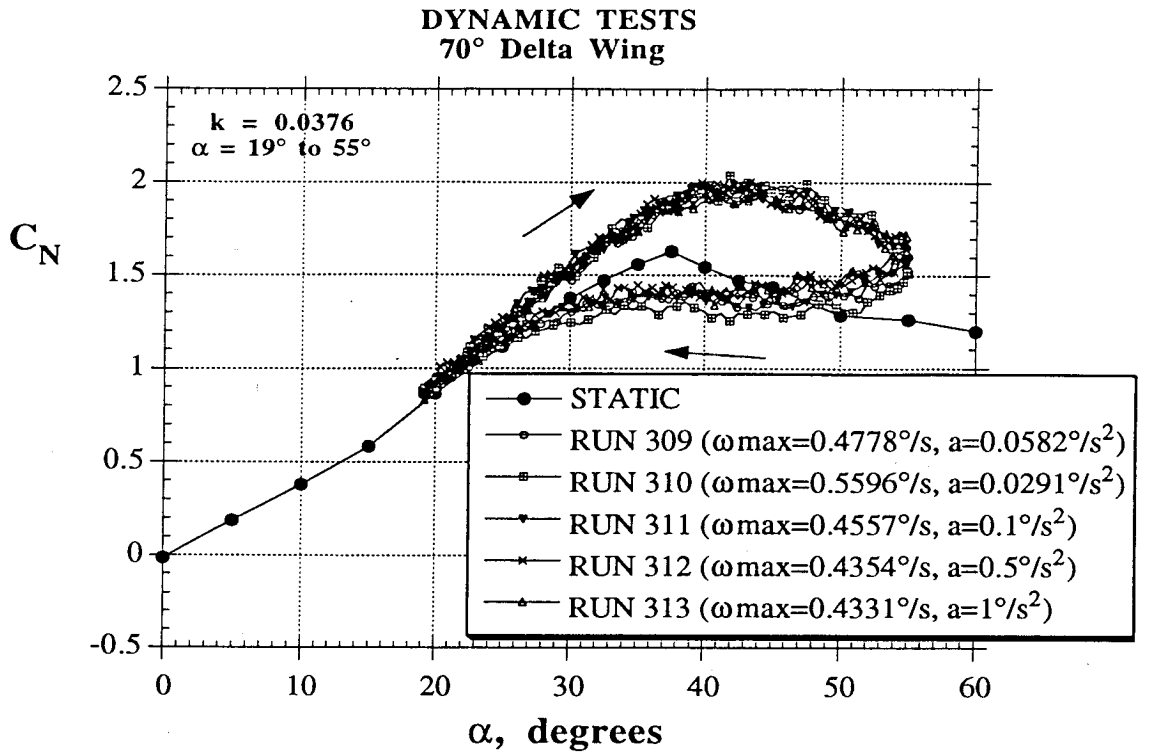

a) C_N Hysteresis Loops

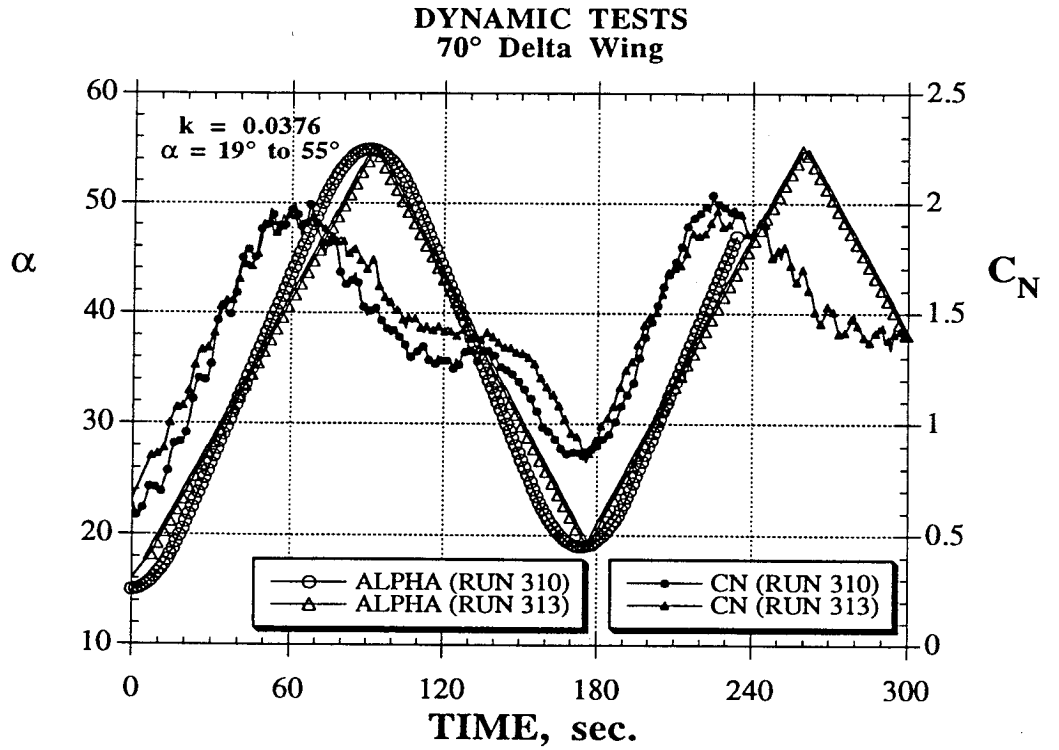

b) Angle of Attack and C_N Time Histories

Figure 25 - Constant Period Pitch Oscillations at k = 0.0376 (70° Delta Wing)

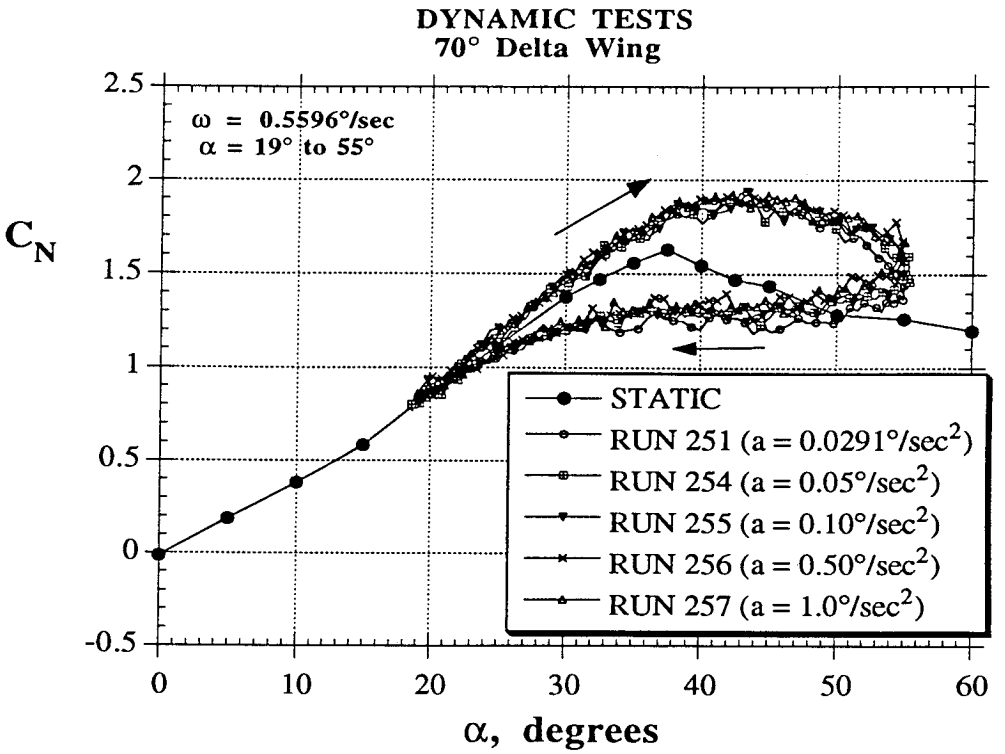

a) C_N Hysteresis Loops

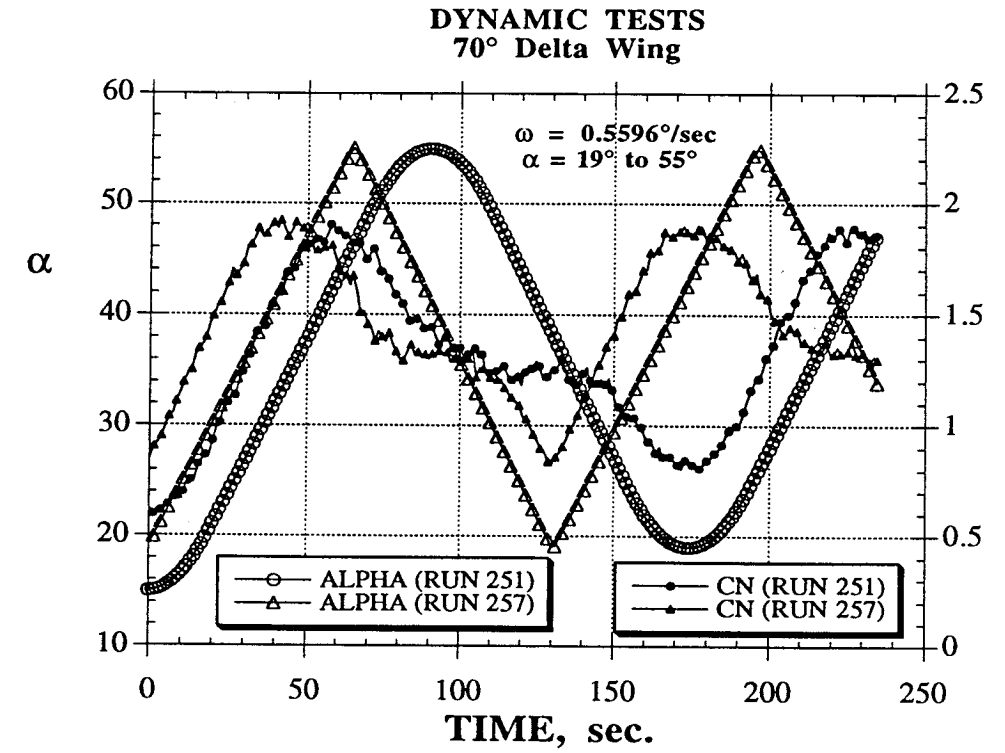

b) Angle of Attack and C_N Time Histories

Figure 26 - Effect of Acceleration During Pitch Oscillations (70° Delta Wing, ω_{max} = 0.56 deg/sec)

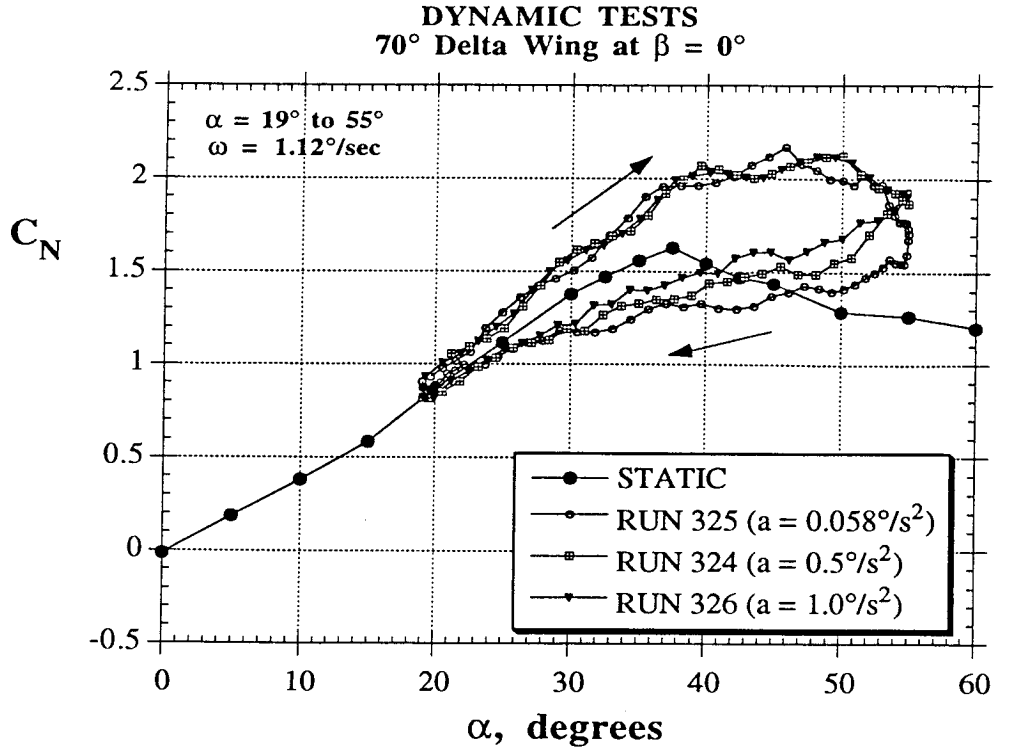

a) C_N Hysteresis Loops

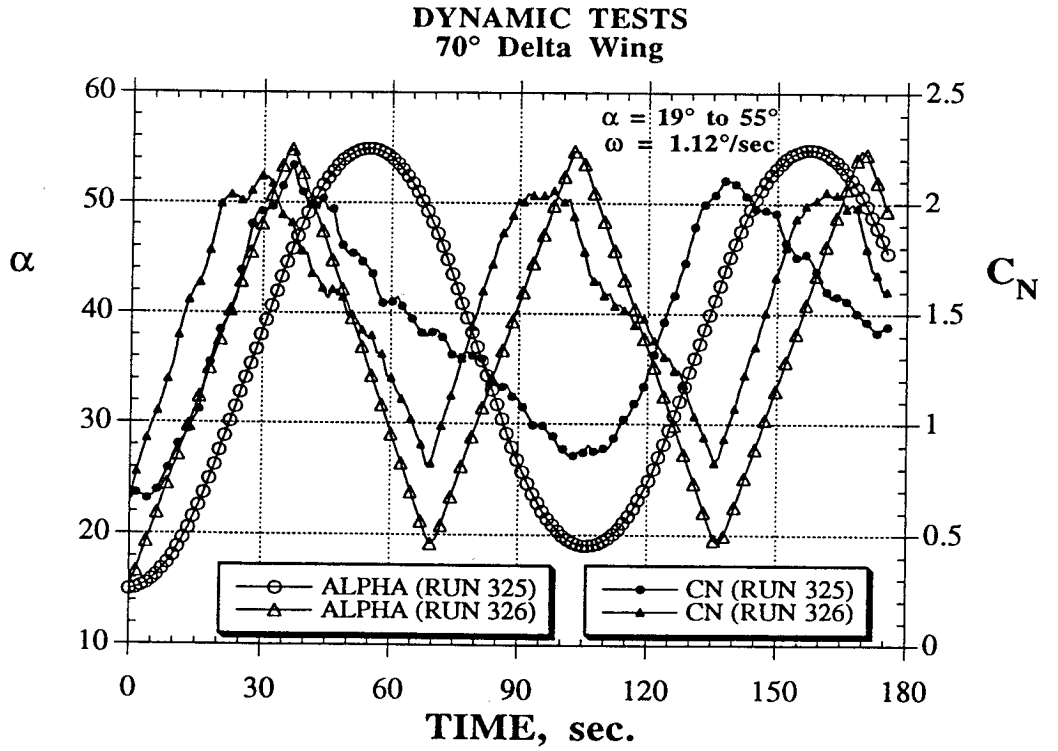

b) Angle of Attack and C_N Time Histories

Figure 27 - Effect of Acceleration During Pitch Oscillations (70° Delta Wing, ω_{max} = 1.12 deg/sec)

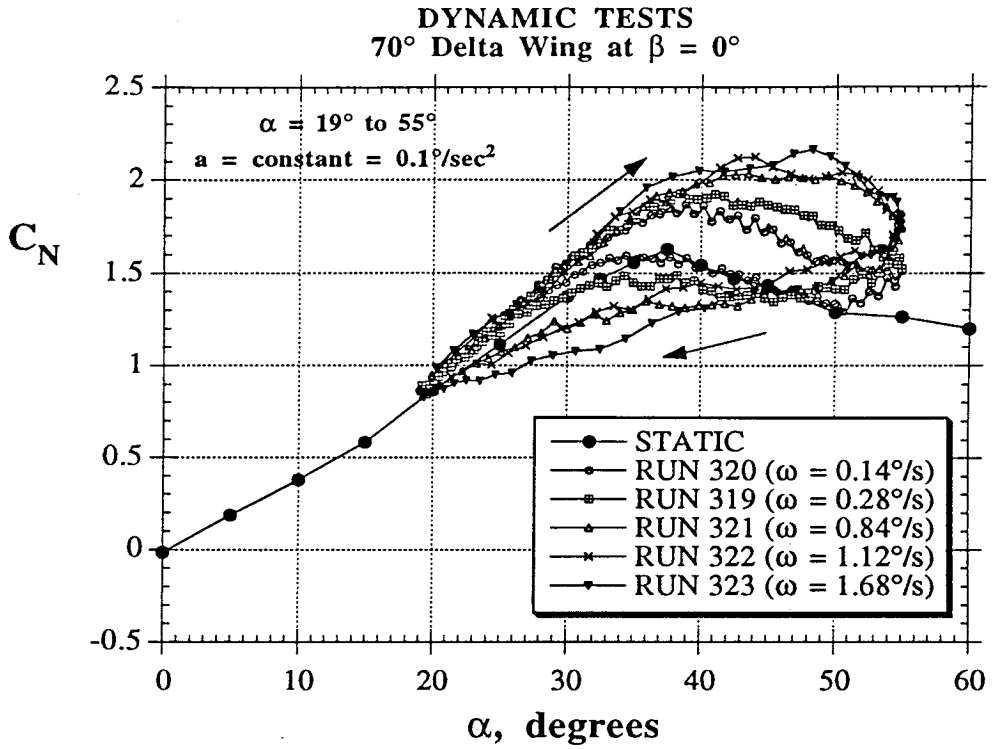

a) C_N Hysteresis Loops

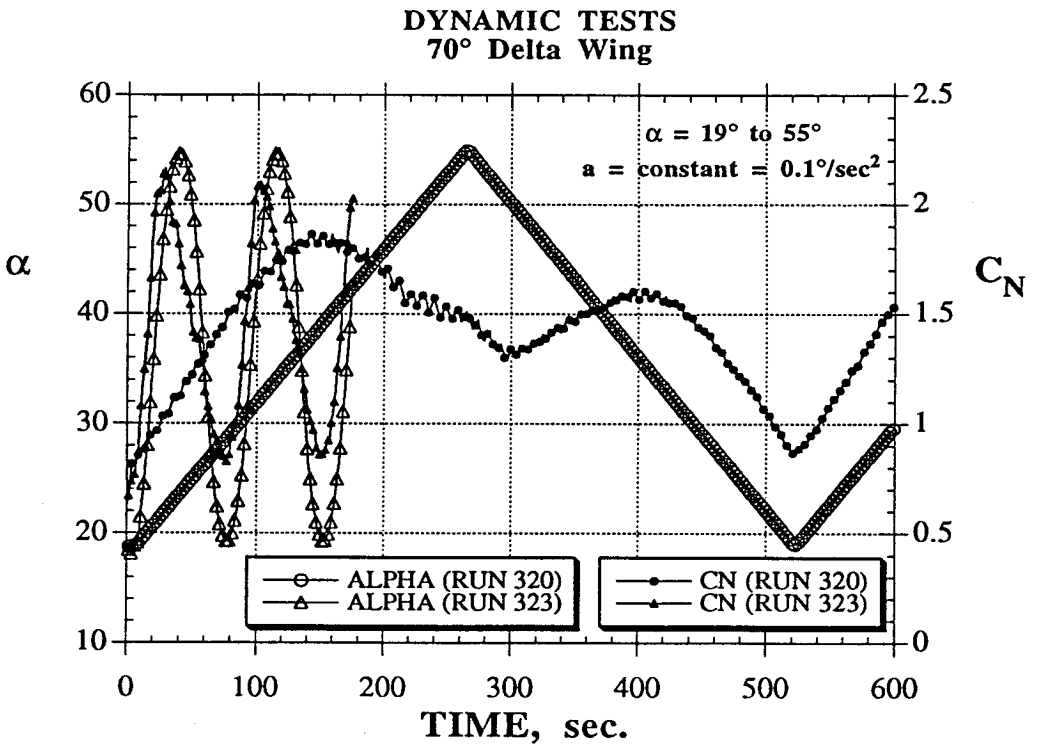

b) Angle of Attack and C_N Time Histories

Figure 28 - Effect of Maximum Angular Velocity During Pitch Oscillations (70° Delta Wing, a = 0.1 deg/sec^2)

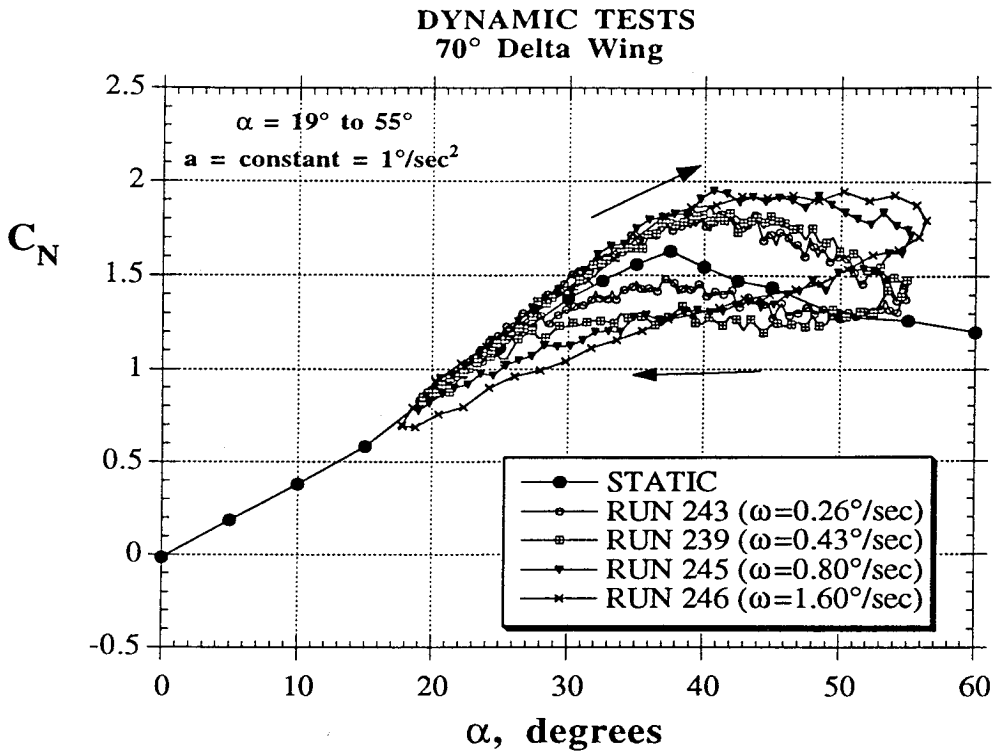

a) C_N Hysteresis Loops

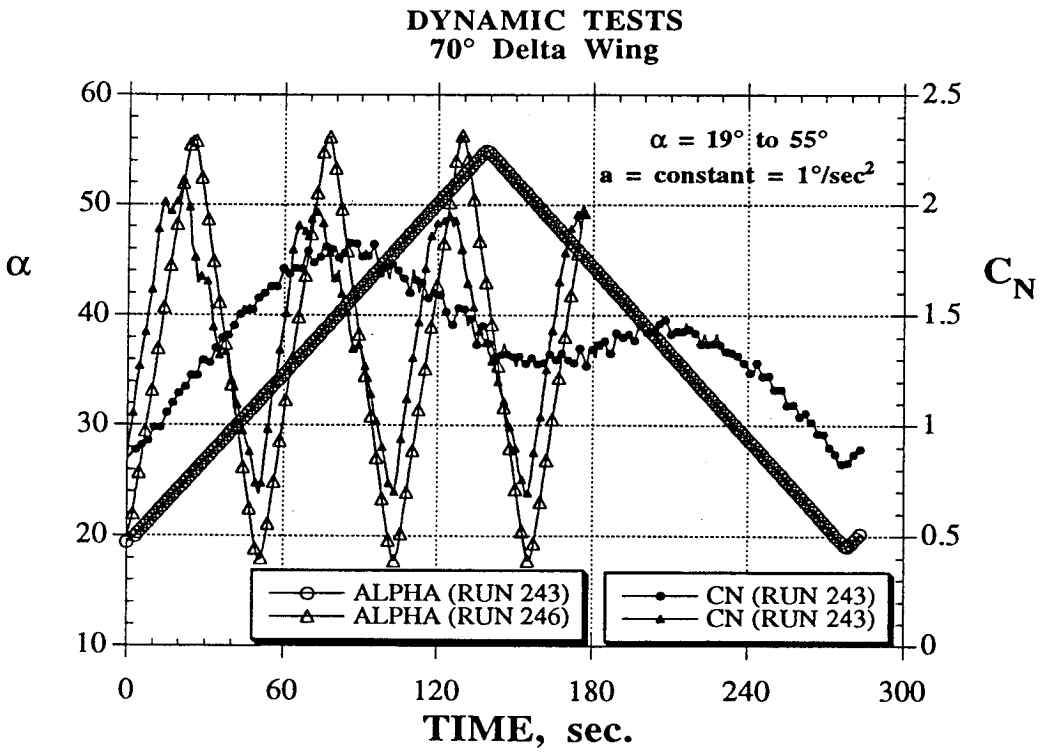

b) Angle of Attack and C_N Time Histories

Figure 29 - Effect of Maximum Angular Velocity During Pitch Oscillations (70° Delta Wing, a = 1.0 deg/sec^2)

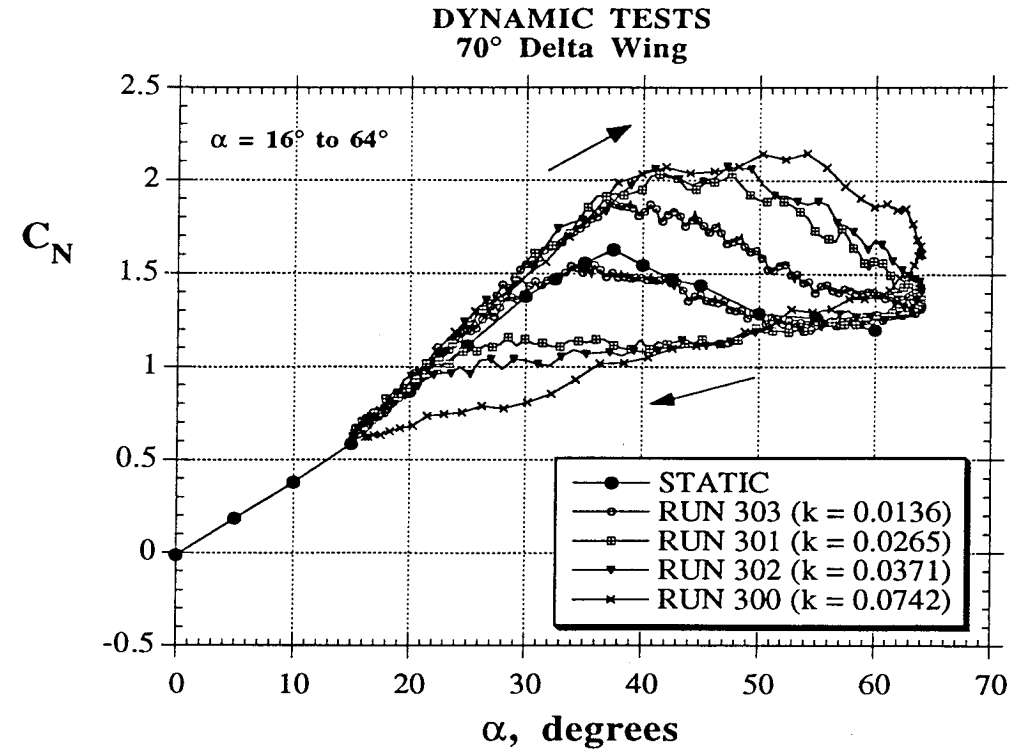

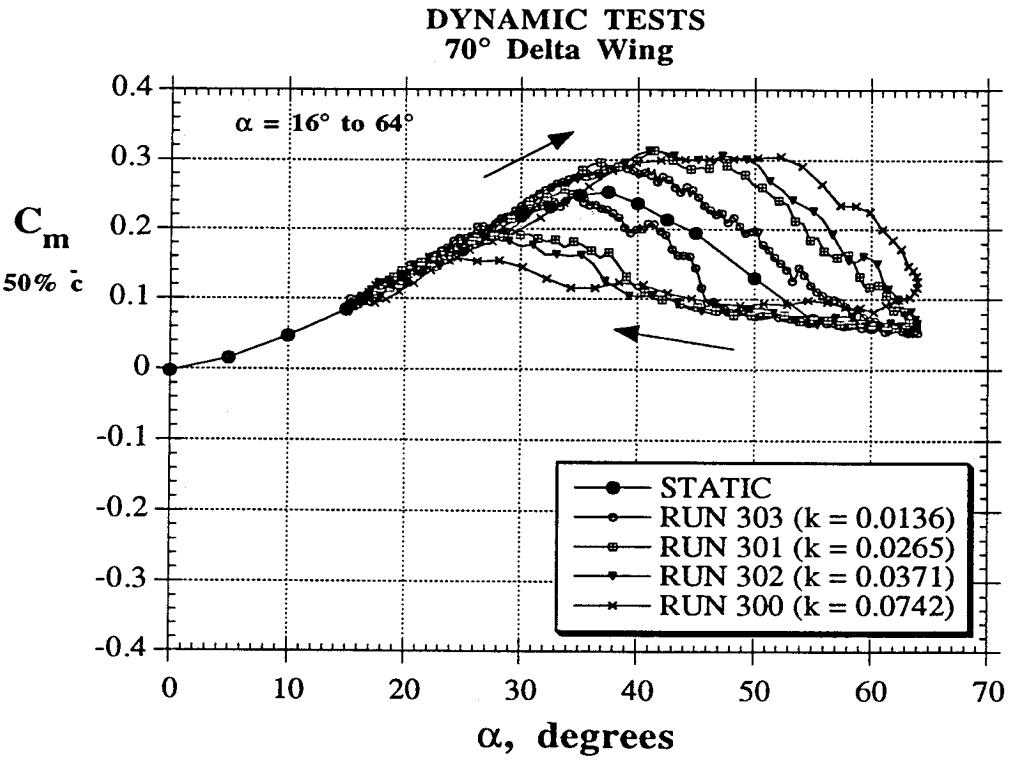

Figure 30 - Effect of Frequency on the Longitudinal Characteristics During Large Amplitude (α = 16° to 64°) Pitch Oscillations (70° Delta Wing)

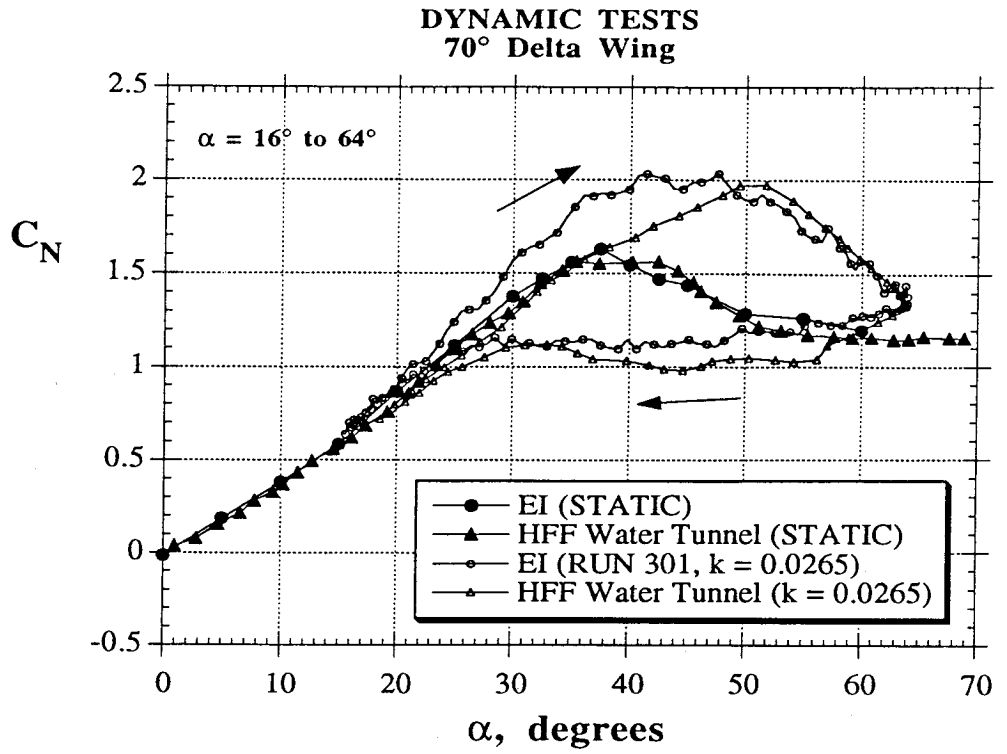

a) k = 0.0265

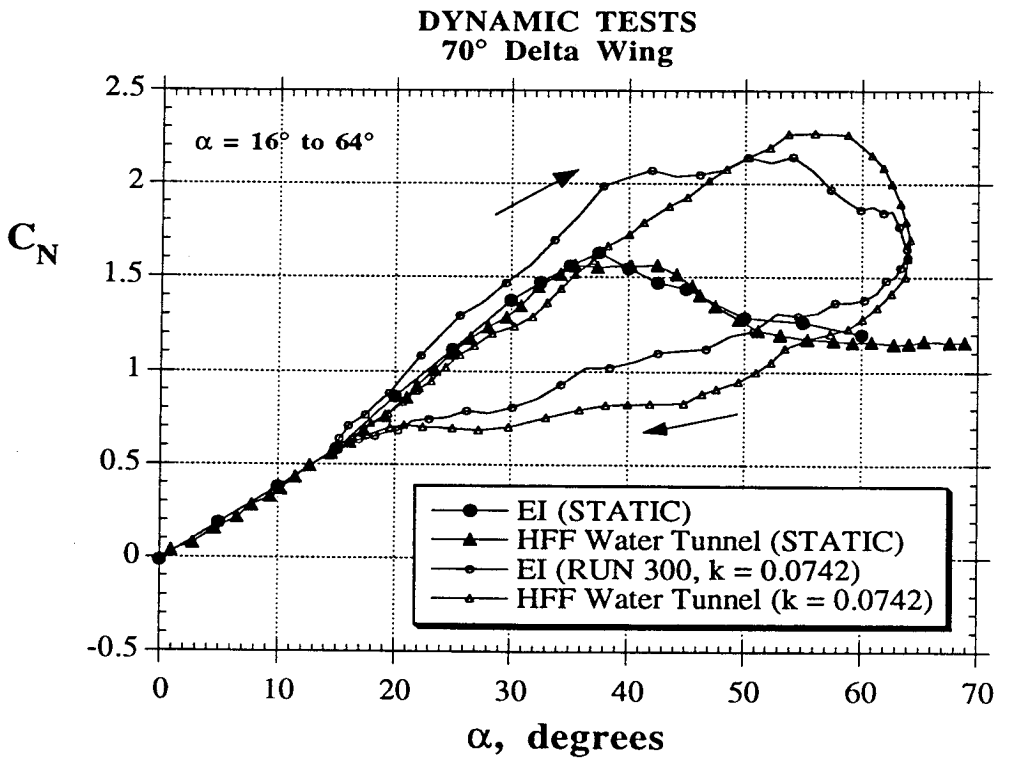

b) k = 0.0742

Figure 31 - Comparison of Water Tunnel Data to Results from Ref. 5 for Large Amplitude Pitch Oscillations (70° Delta Wing)

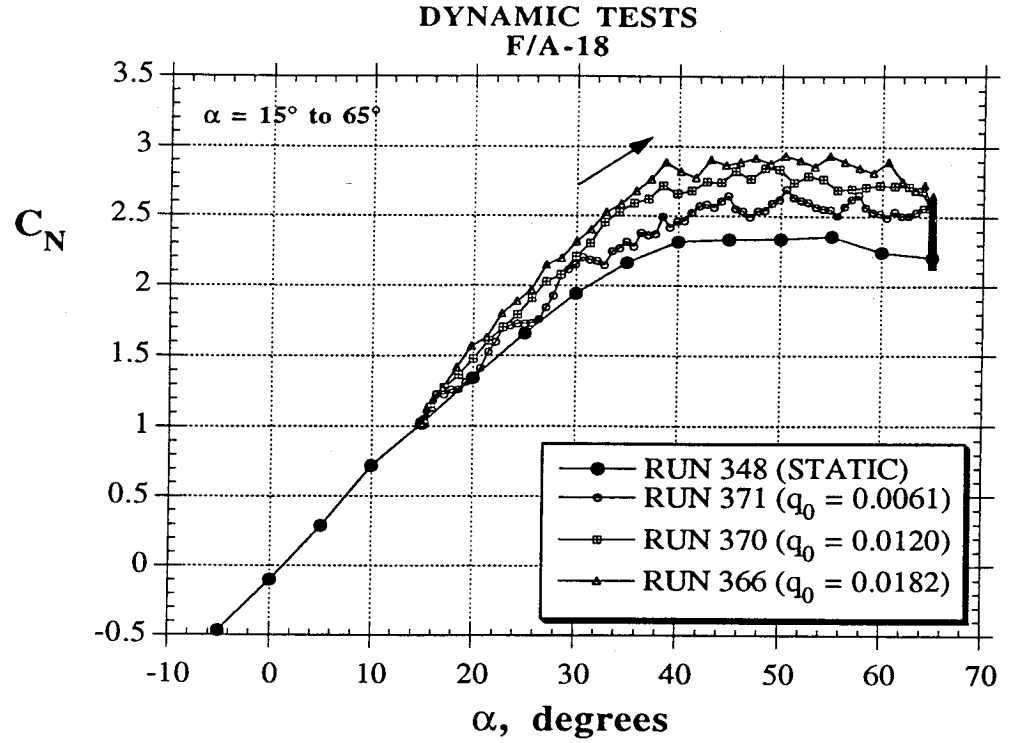

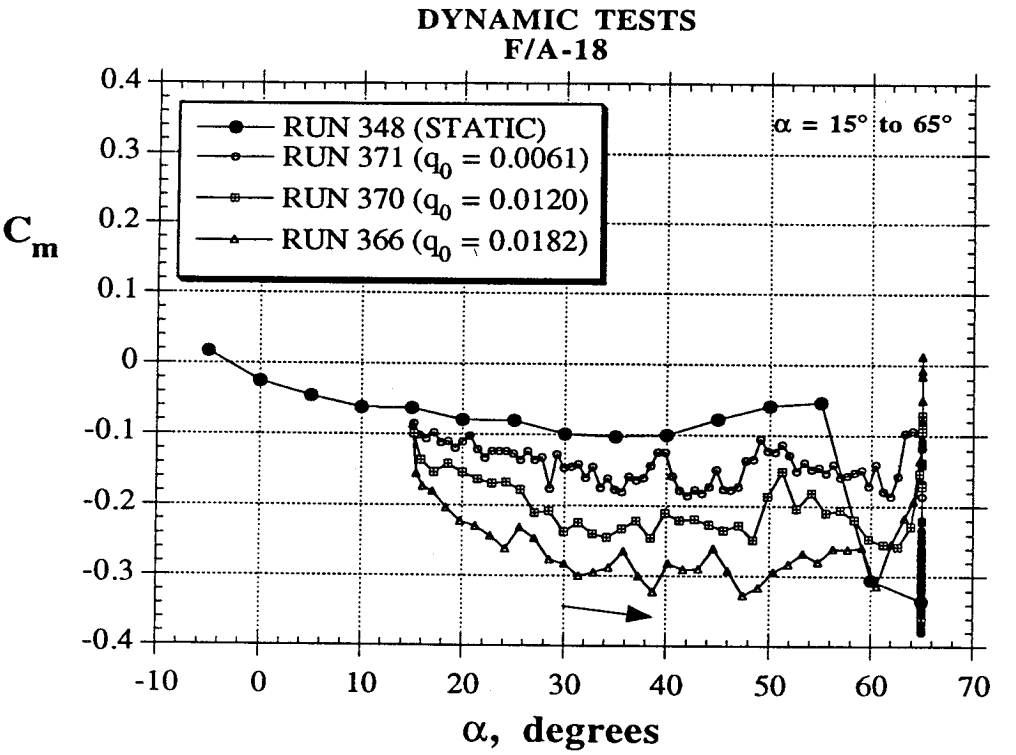

Figure 32 - Effect of Pitch Rate on the Normal Force and Pitching and Yawing Moments During a Pitch-Up and Hold Maneuver (F/A-18)

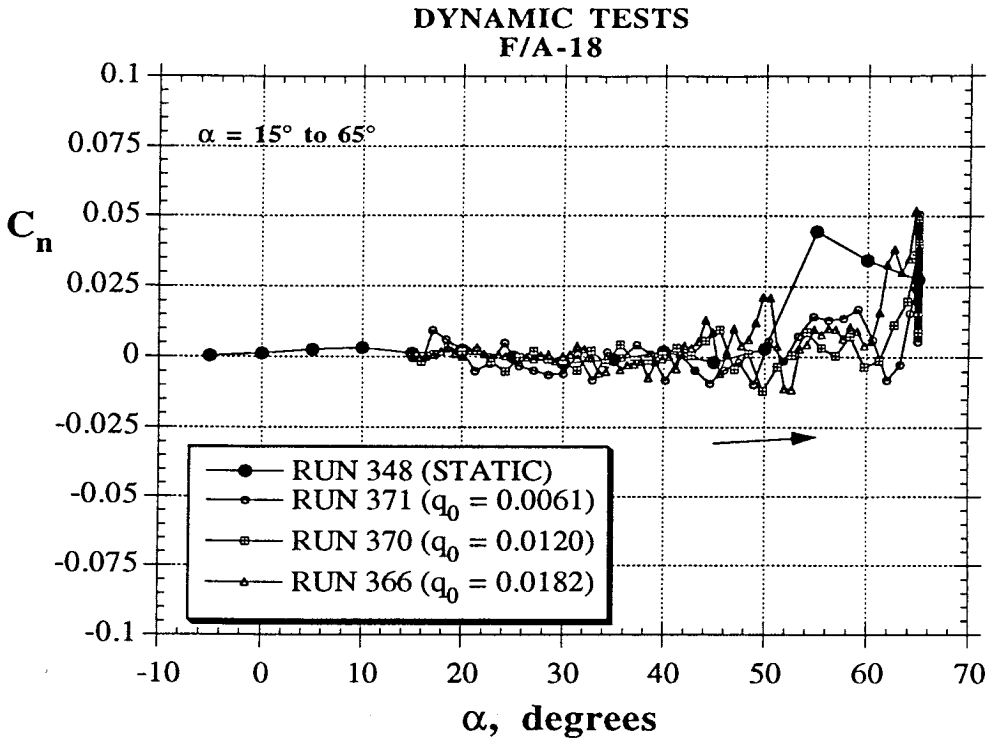

Figure 32 - Concluded

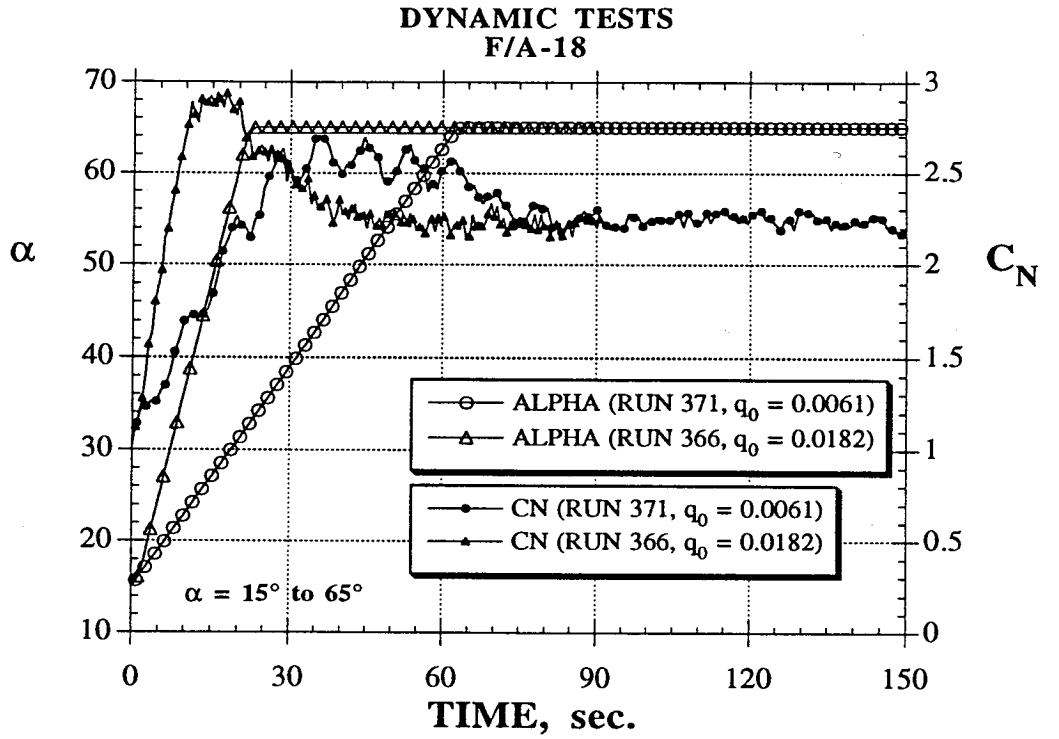

a) Angle of Attack and C_N

Figure 33 - Force/Moment and Angle of Attack Time Histories During a Pitch-Up and Hold Maneuver (F/A-18)

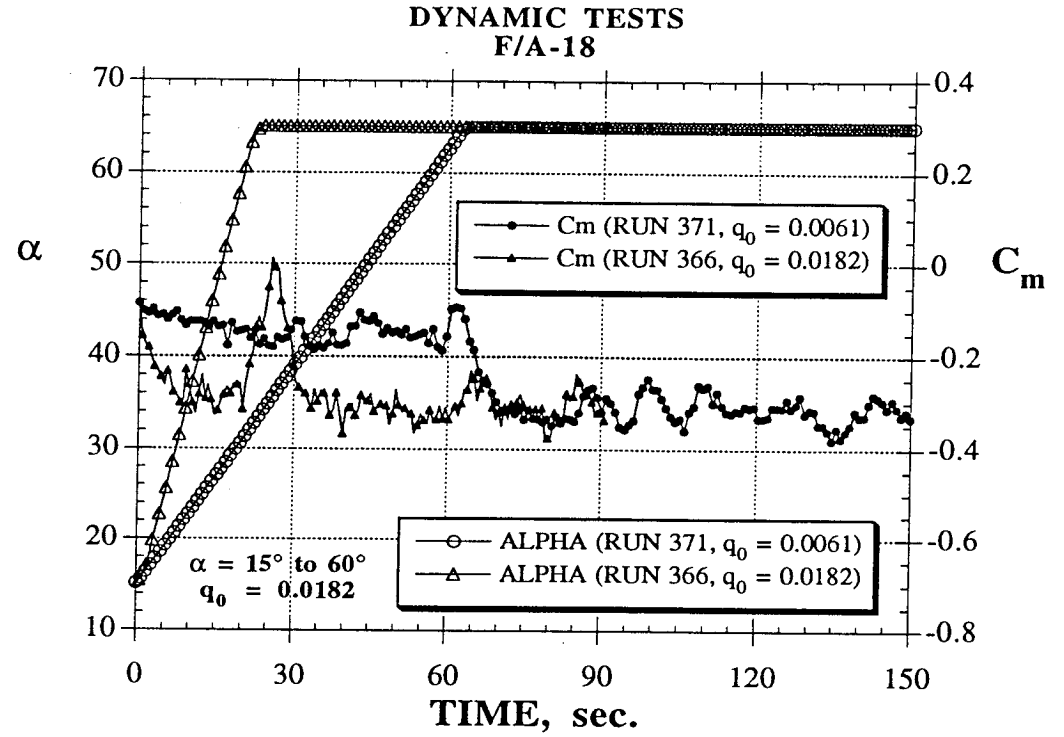

b) Angle of Attack and C_m

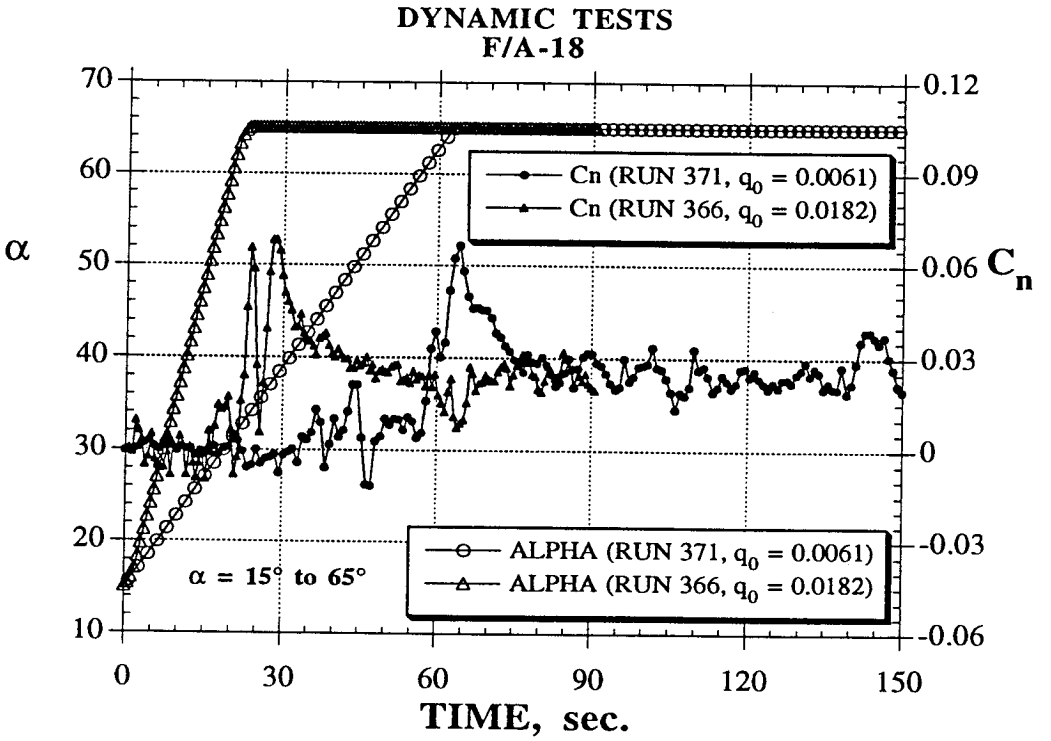

c) Angle of Attack and C_n

Figure 33 - Concluded

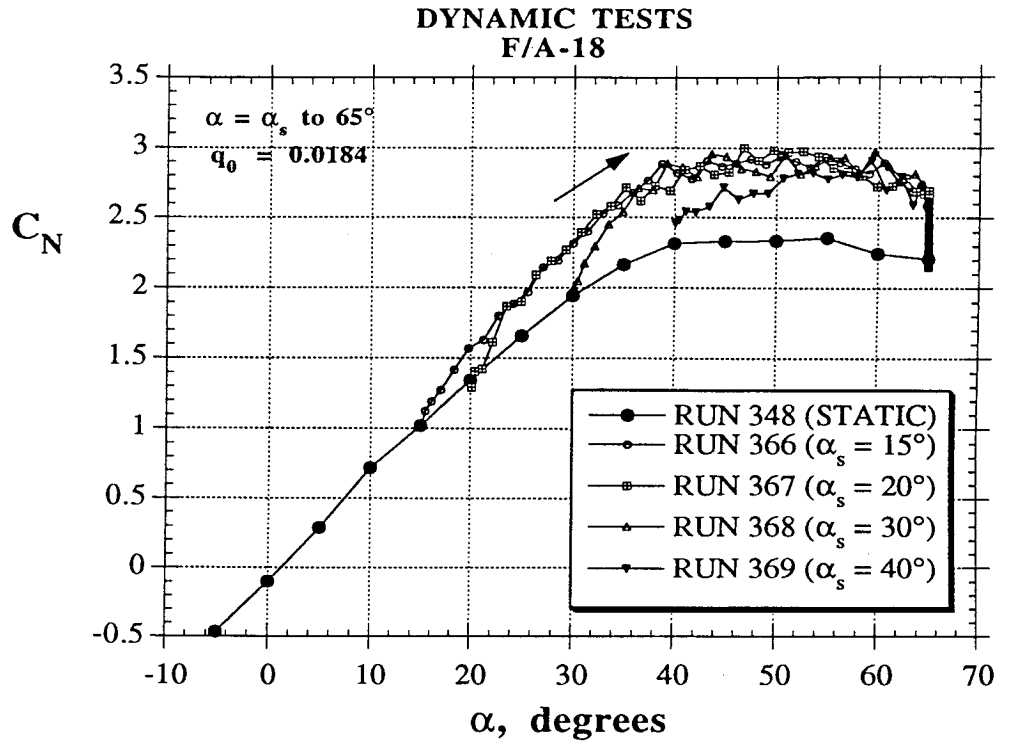

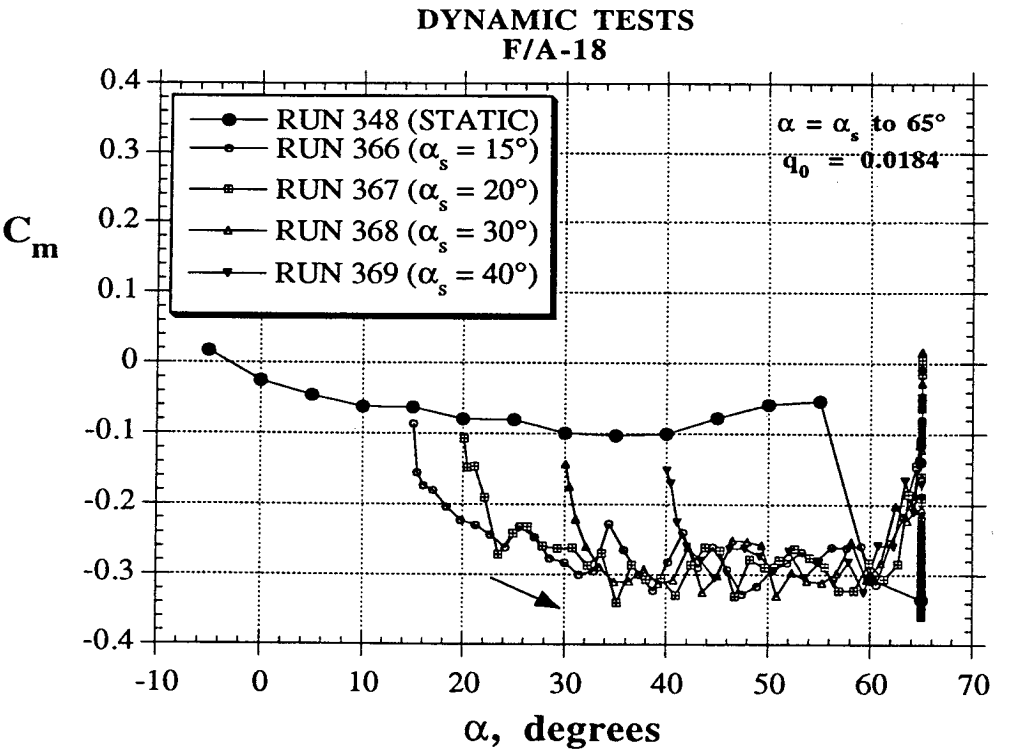

Figure 34 - Effect of Starting Angle of Attack on the Longitudinal Characteristics of the F/A-18 During a Pitch-Up and Hold Maneuver

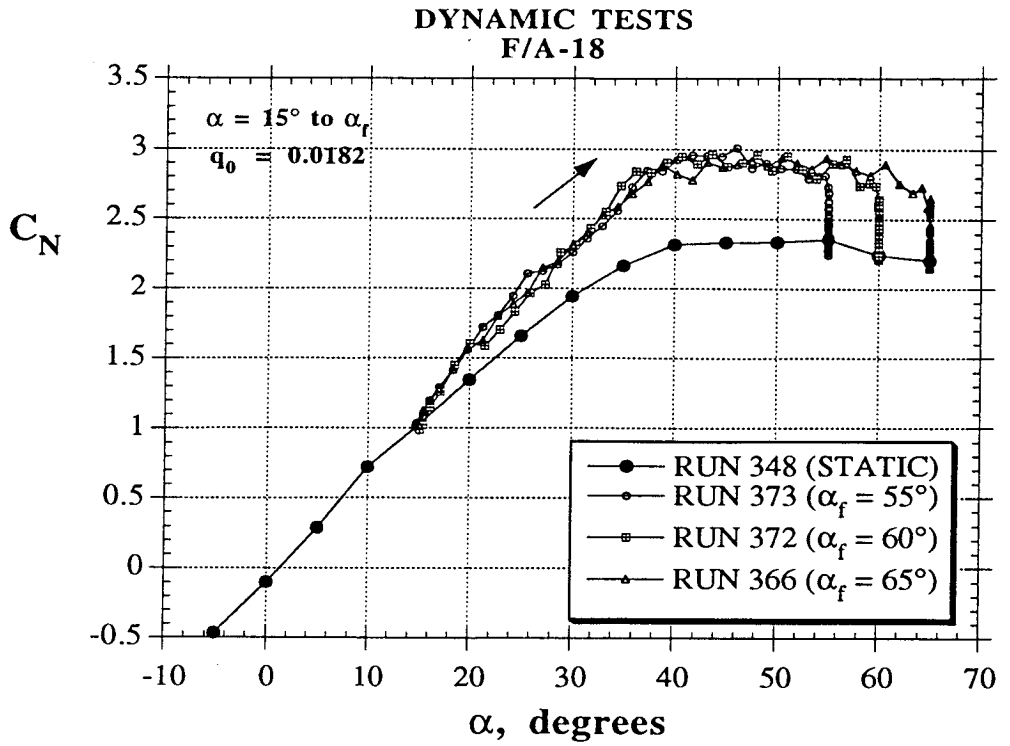

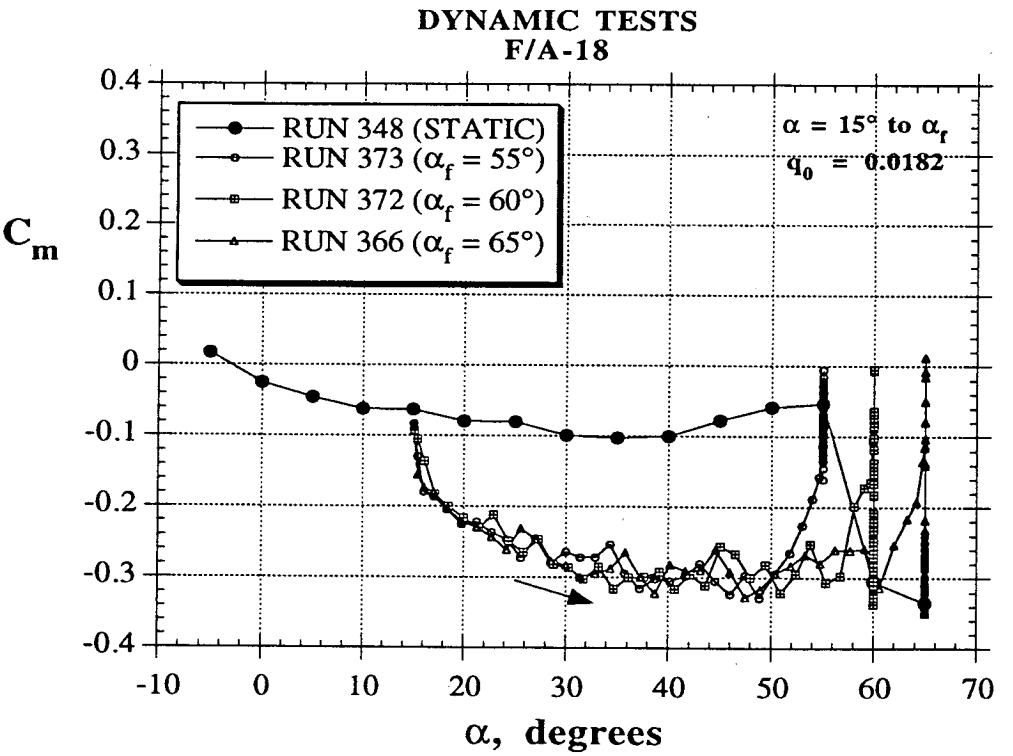

Figure 35 - Effect of Ending Angle of Attack on the Longitudinal Characteristics of the F/A-18 During a Pitch-Up and Hold Maneuver

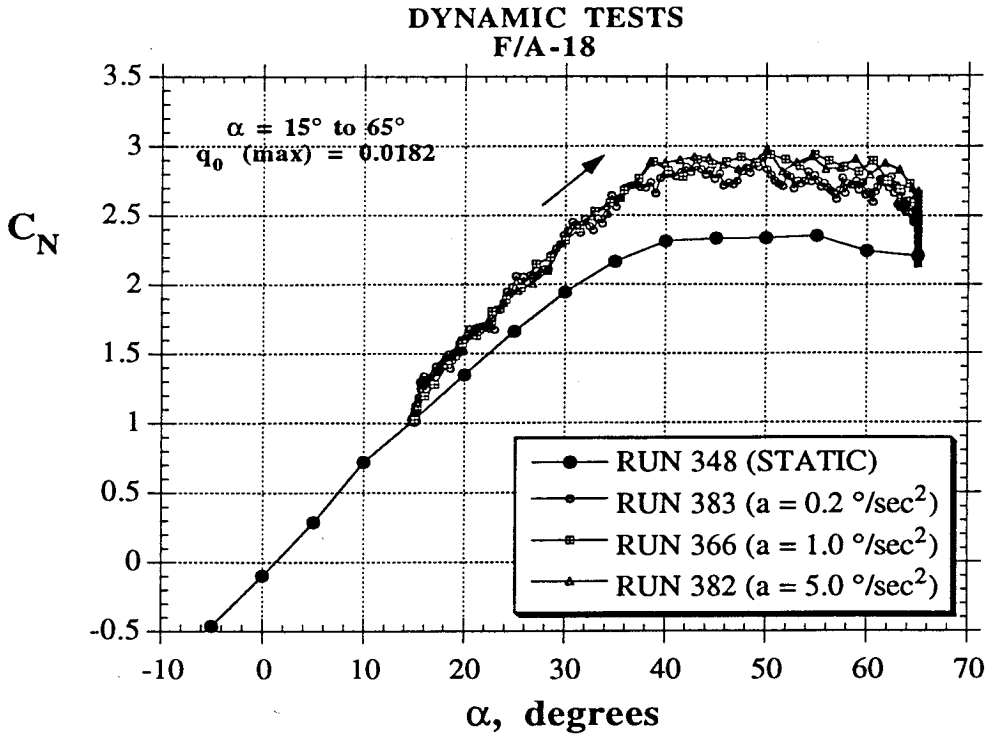

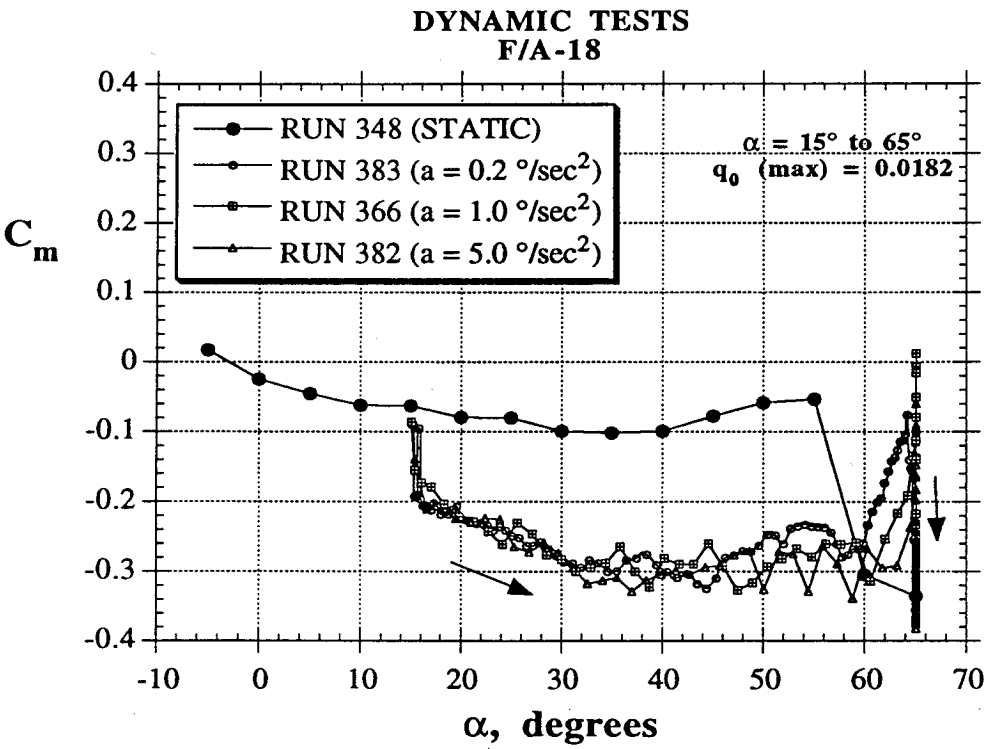

Figure 36 - Effect of Acceleration on the Longitudinal Characteristics of the F/A-18 During a Pitch-Up and Hold Maneuver

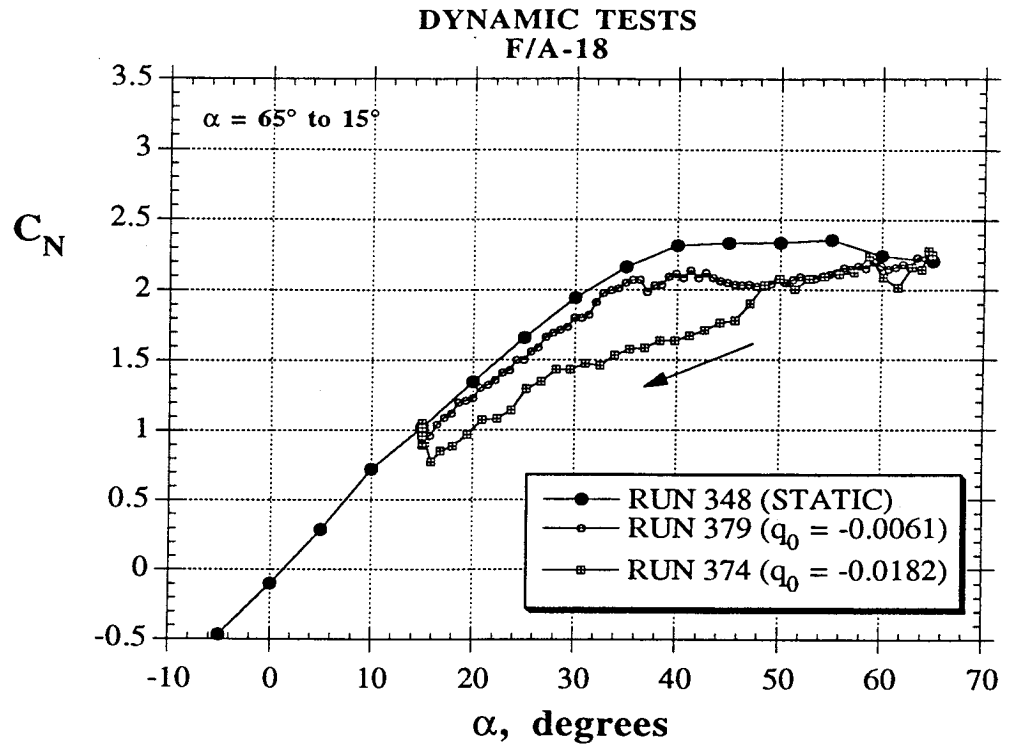

a) C_N Hysteresis Loops

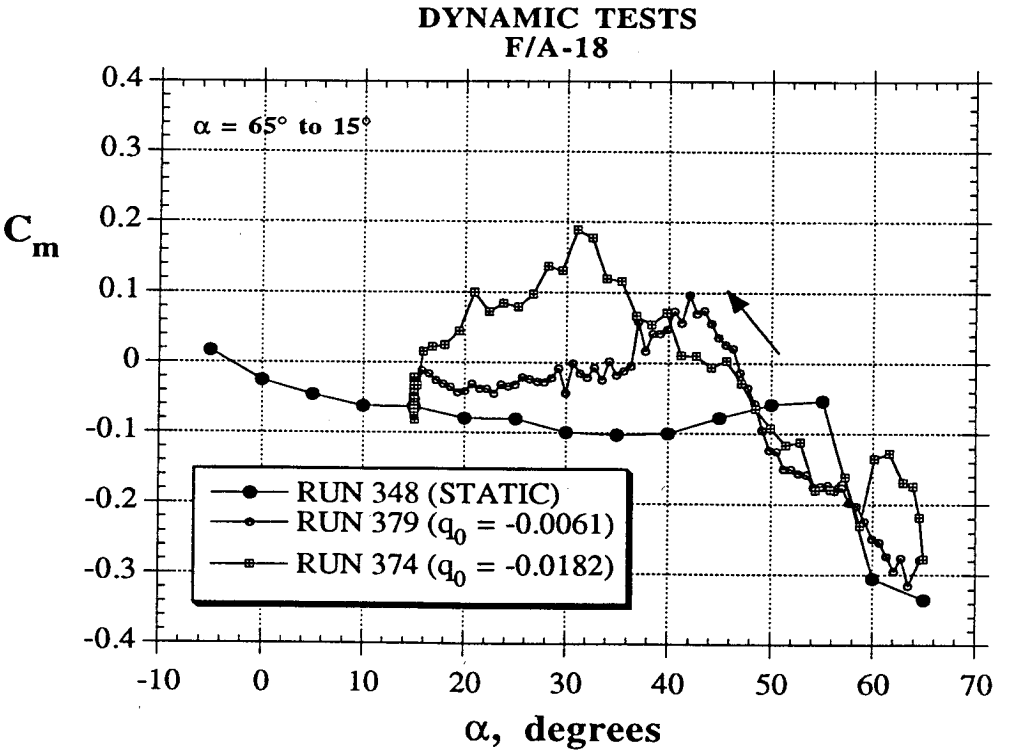

b) C_m Hysteresis Loops

Figure 37 - Effect of Pitch Rate on the Longitudinal Characteristics of the F/A-18 During a Pitch-Down and Hold Maneuver

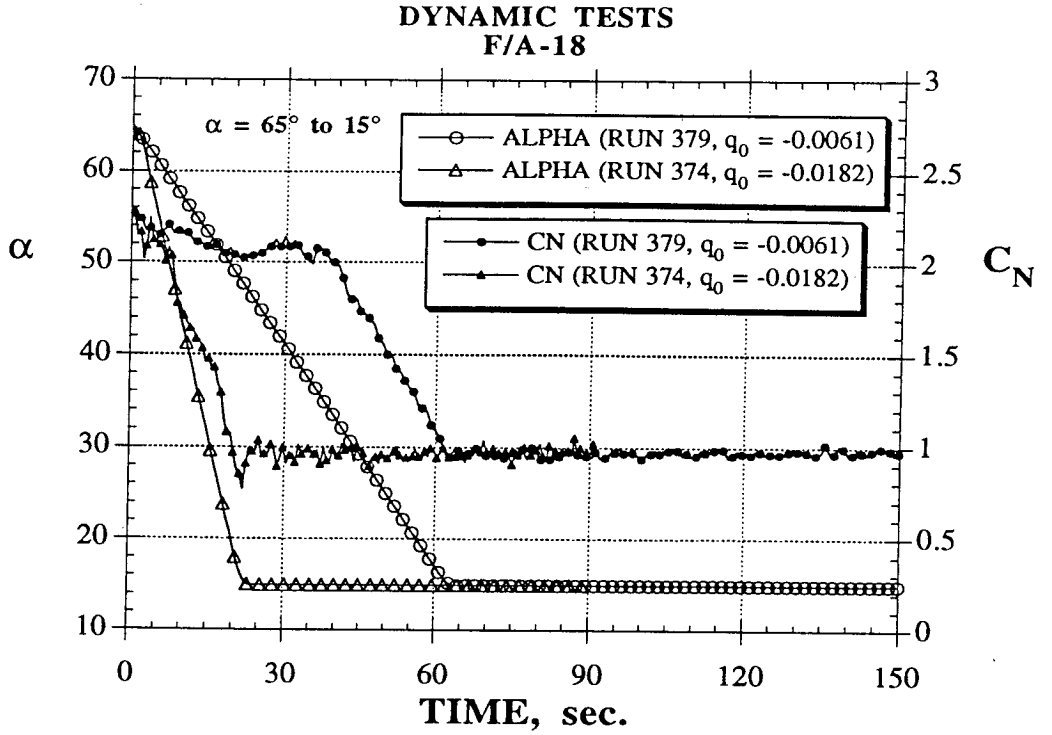

c) Angle of Attack and C_N Time Histories

Figure 37 - Concluded

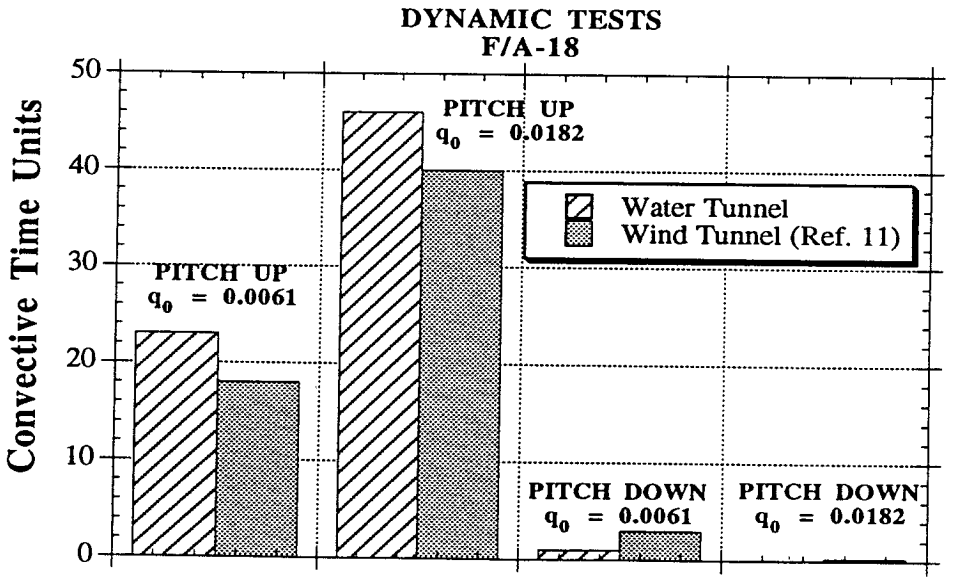

Figure 38 - Persistence of Normal Force During Pitch-Up/Down and Hold Maneuvers (F/A-18, Comparison to Wind Tunnel Test, Ref. 8)

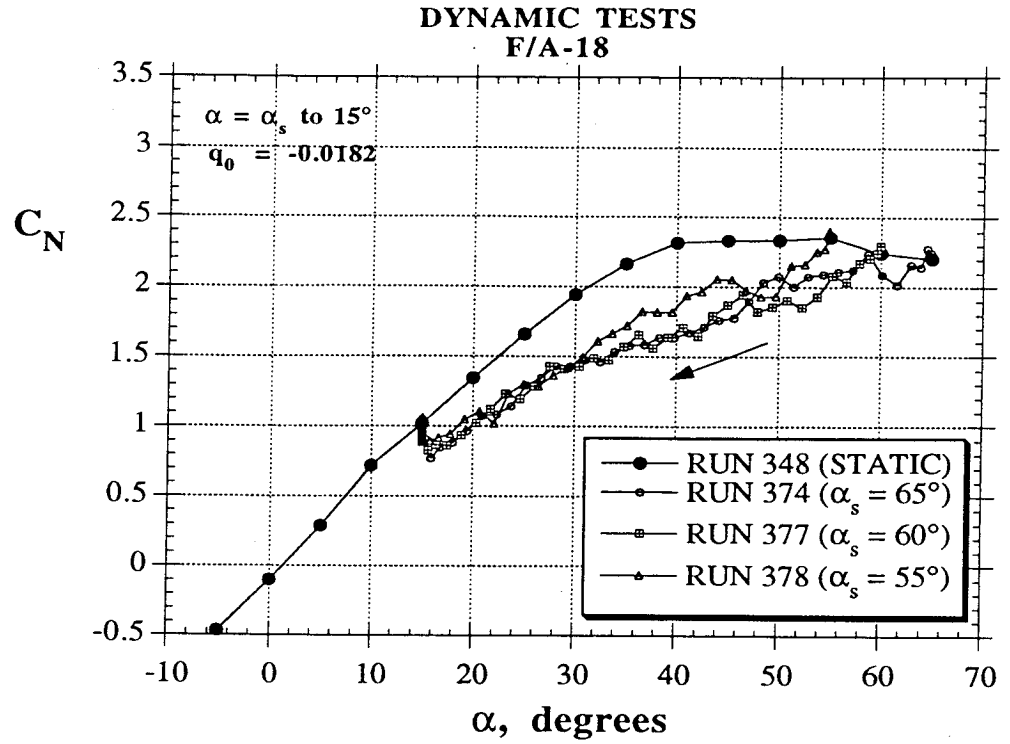

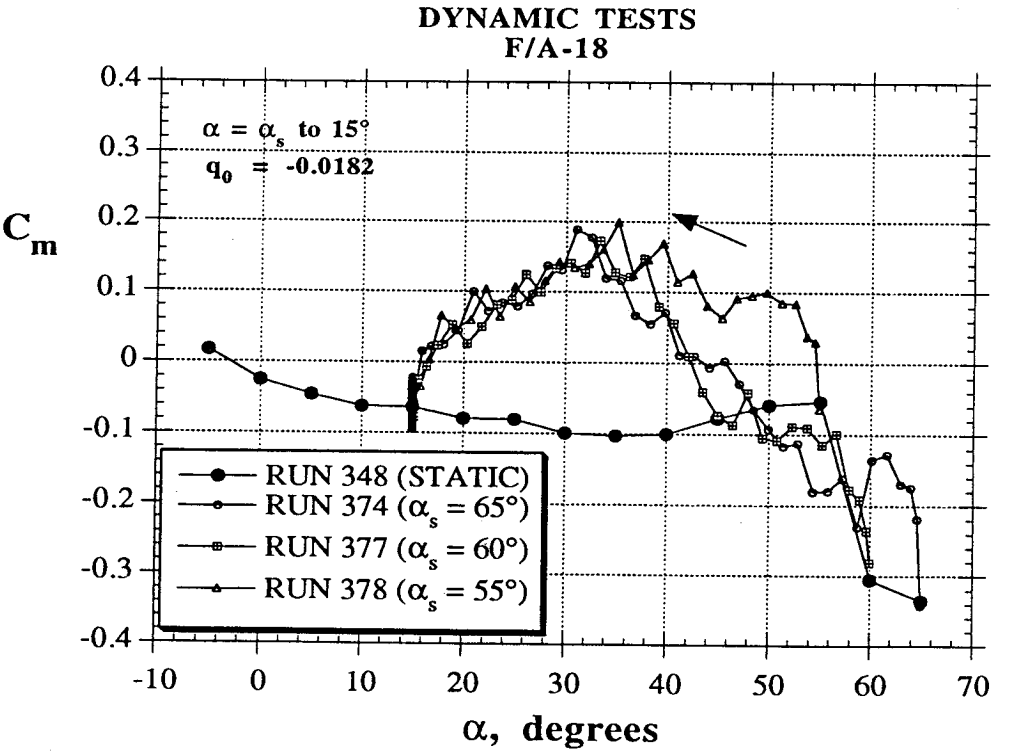

Figure 39 - Effect of Starting Angle of Attack on the Longitudinal Characteristics of the F/A-18 During a Pitch-Down and Hold Maneuver

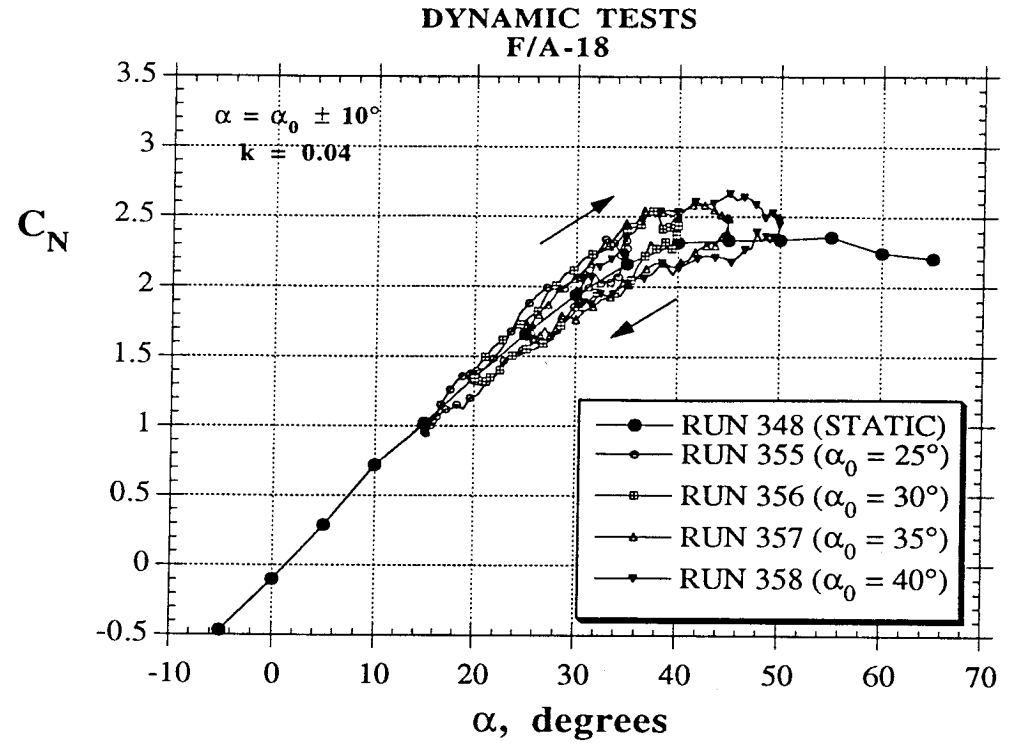

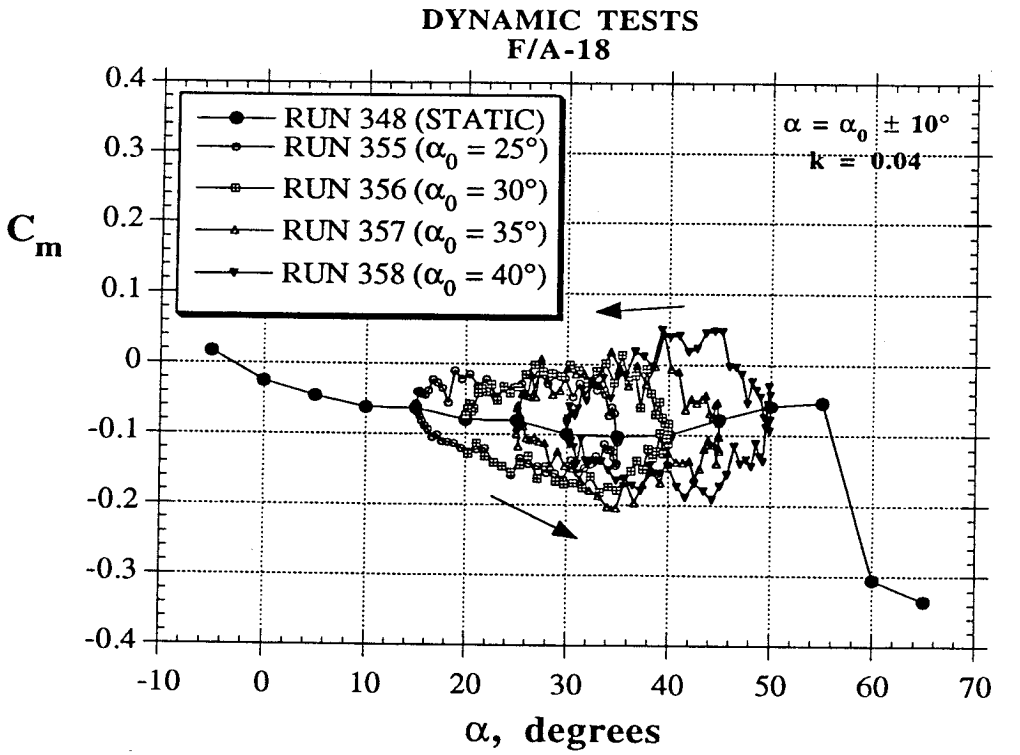

Figure 40 - Pitch Oscillations about Different Mean Angles of Attack α_0 (F/A-18, k = 0.04)

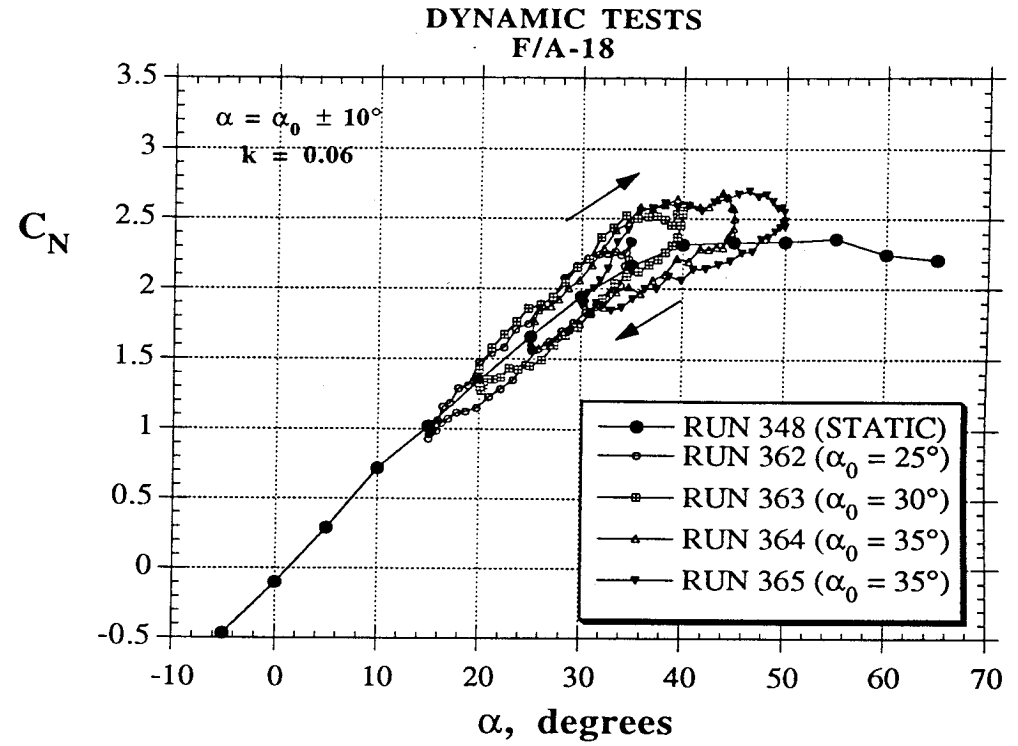

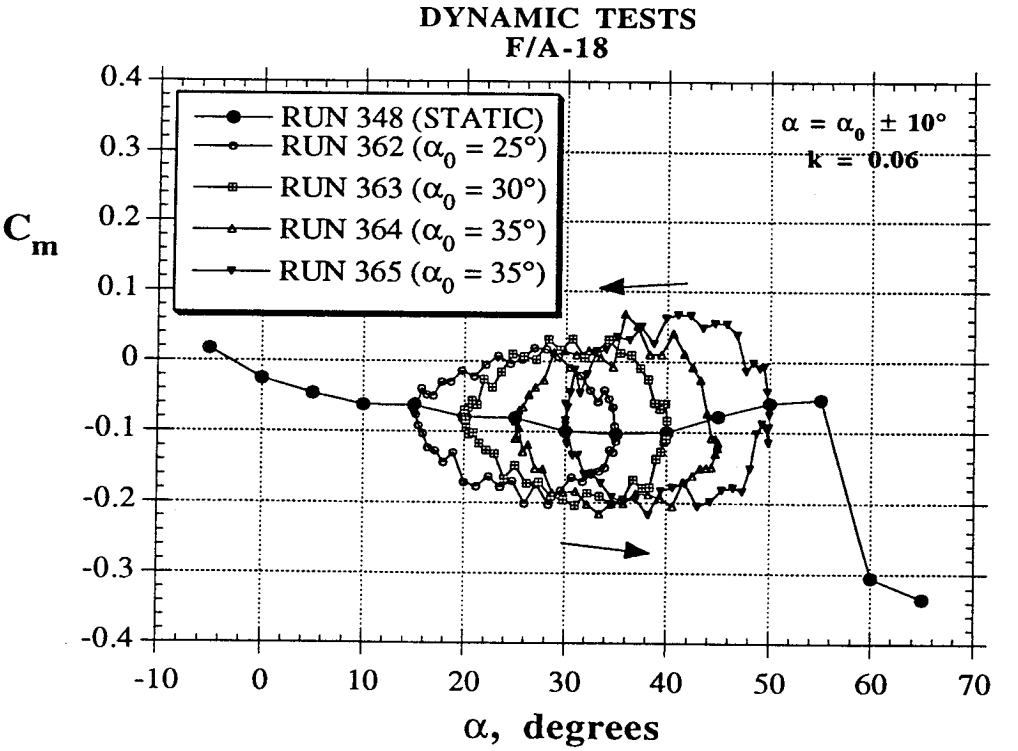

Figure 41 - Pitch Oscillations about Different Mean Angles of Attack α_o (F/A-18, k = 0.06)

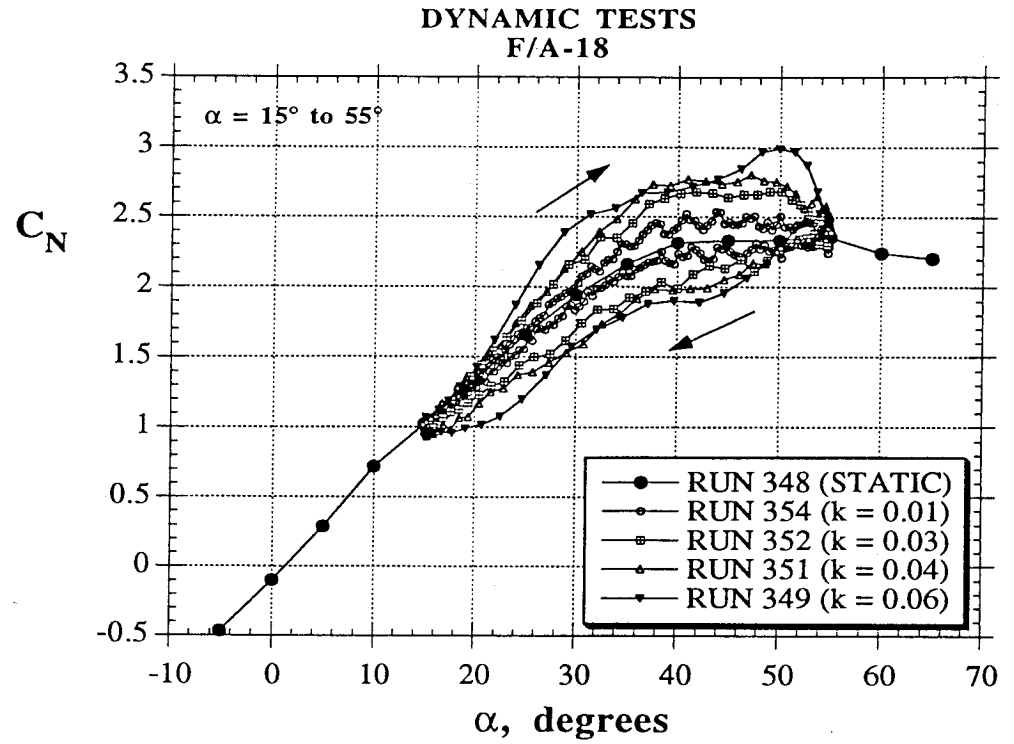

a) C_N Hysteresis Loops

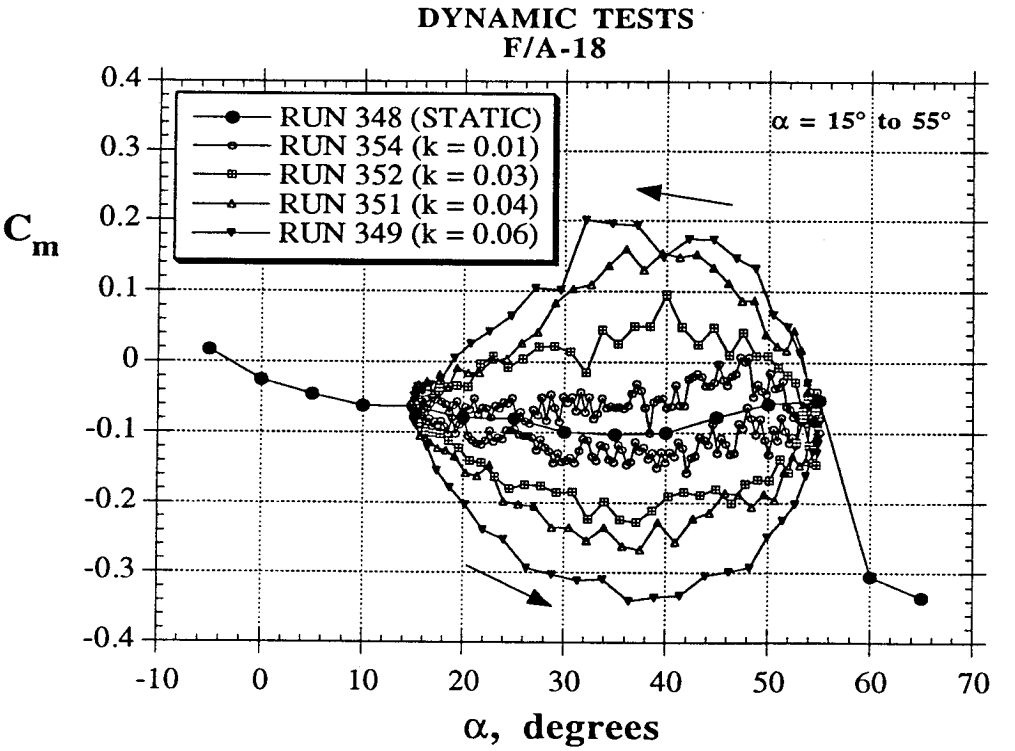

b) C_m Hysteresis Loops

Figure 42 - Effect of Frequency on the Longitudinal Characteristics of the F/A-18 During Pitch Oscillations

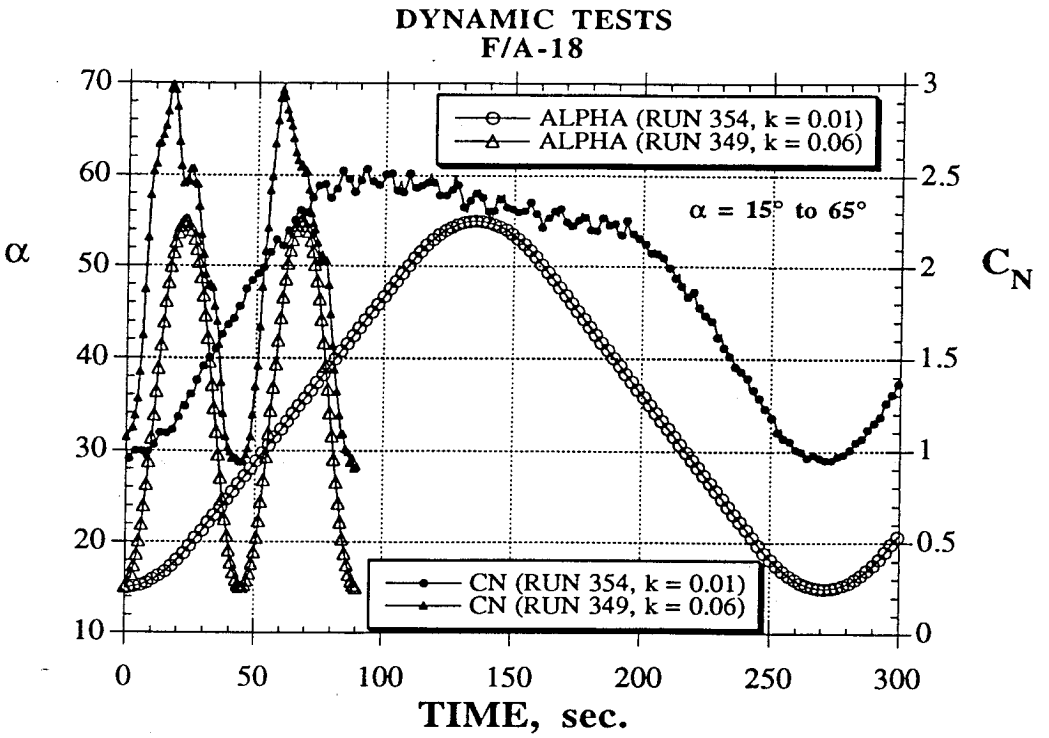

c) Angle of Attack and C_N Time Histories

Figure 42 - Concluded

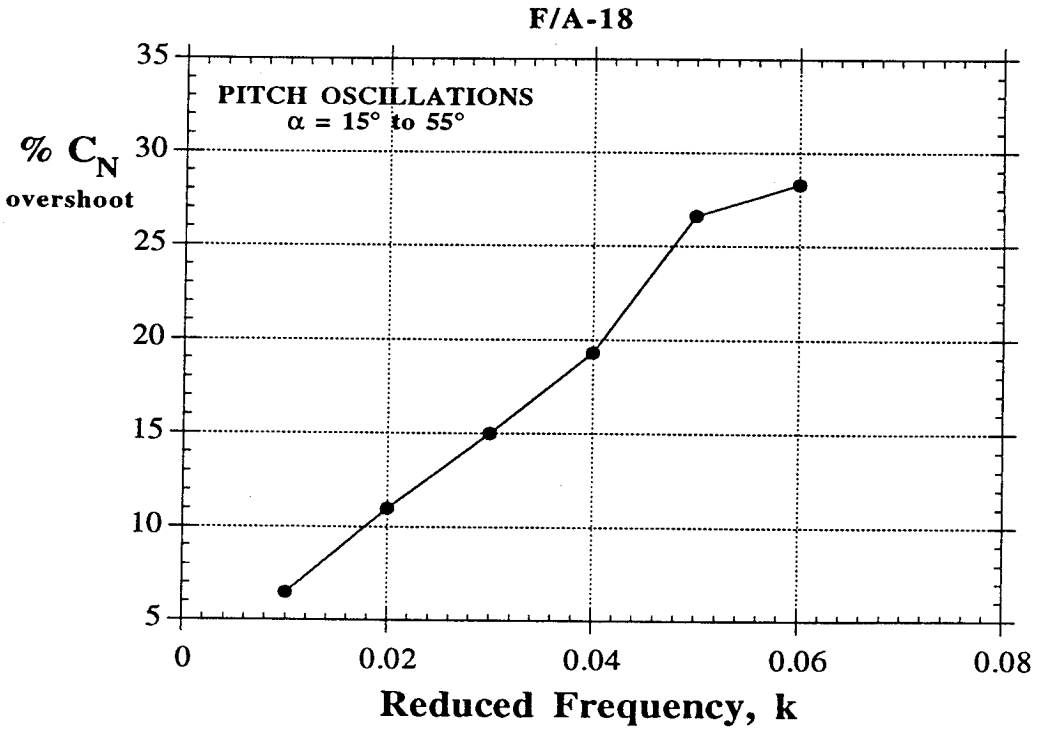

Figure 43 - Percentage of Normal Force Overshoot During Pitch Oscillations at Different Frequencies (F/A-18)

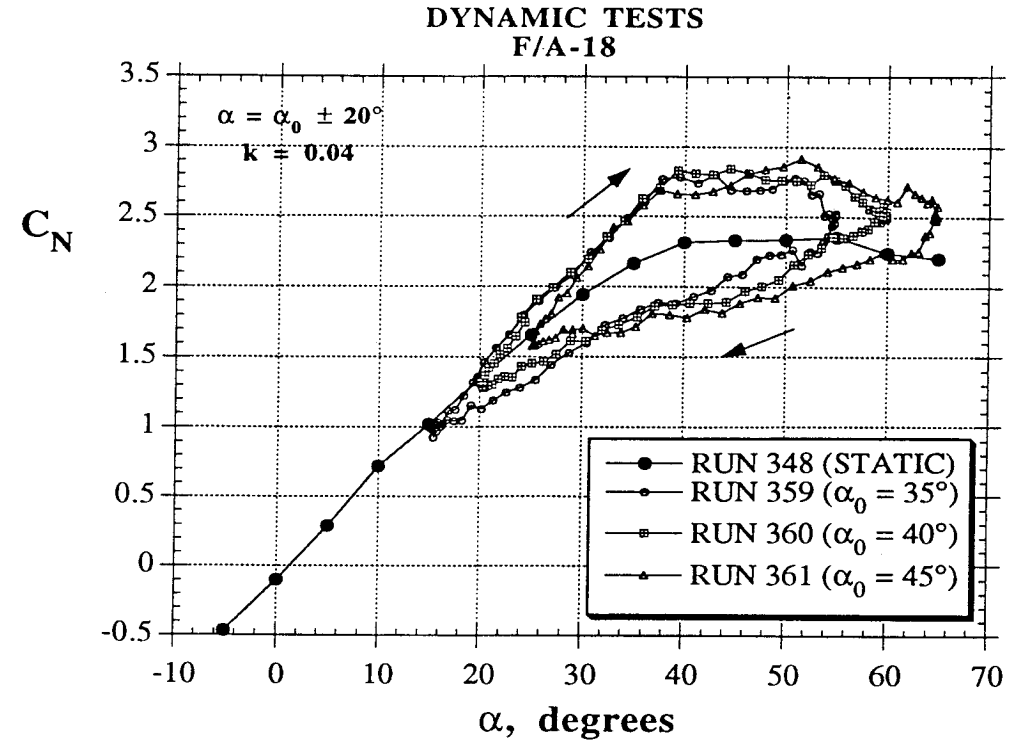

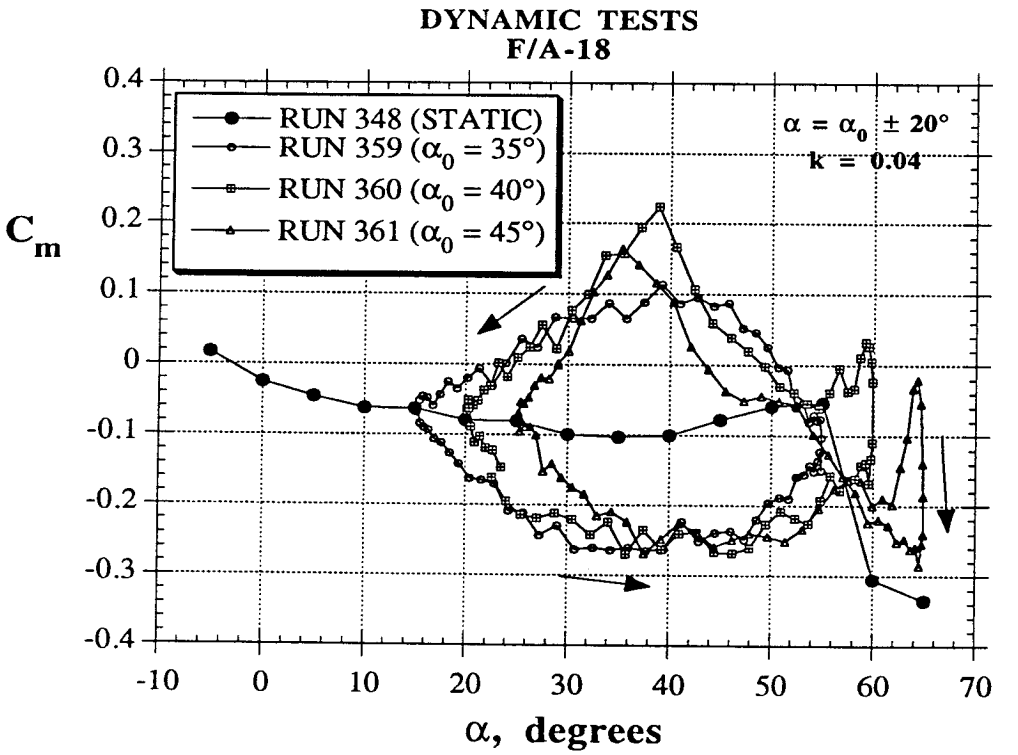

Figure 44 - Large Amplitude Pitch Oscillations about Different Mean Angles of Attack α_0 (F/A-18, k = 0.04)

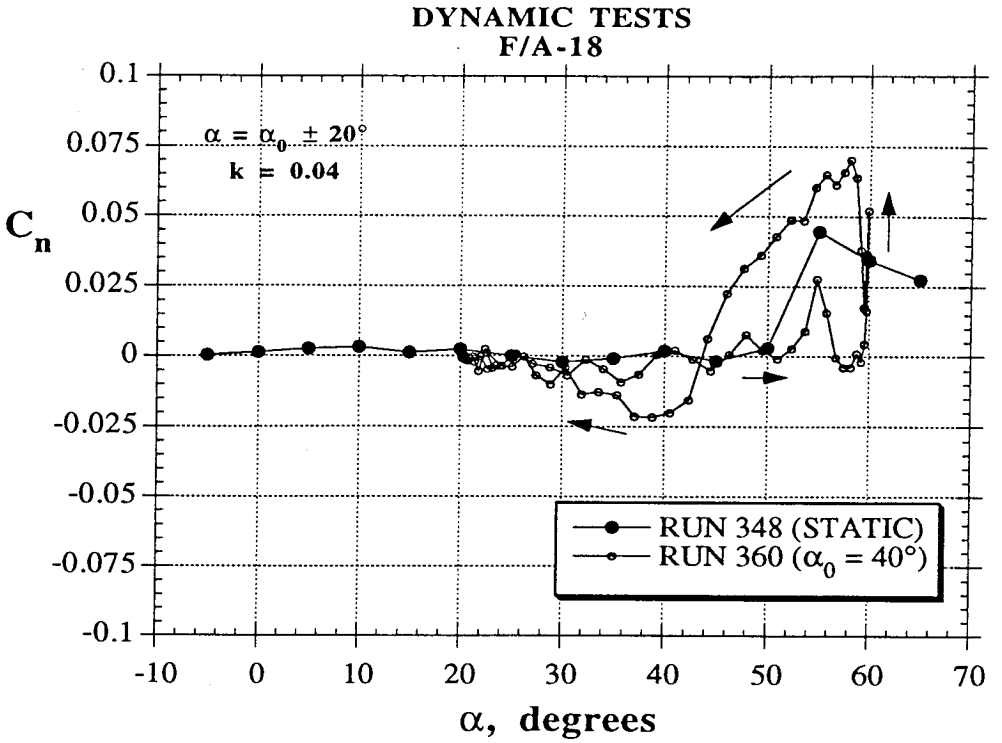

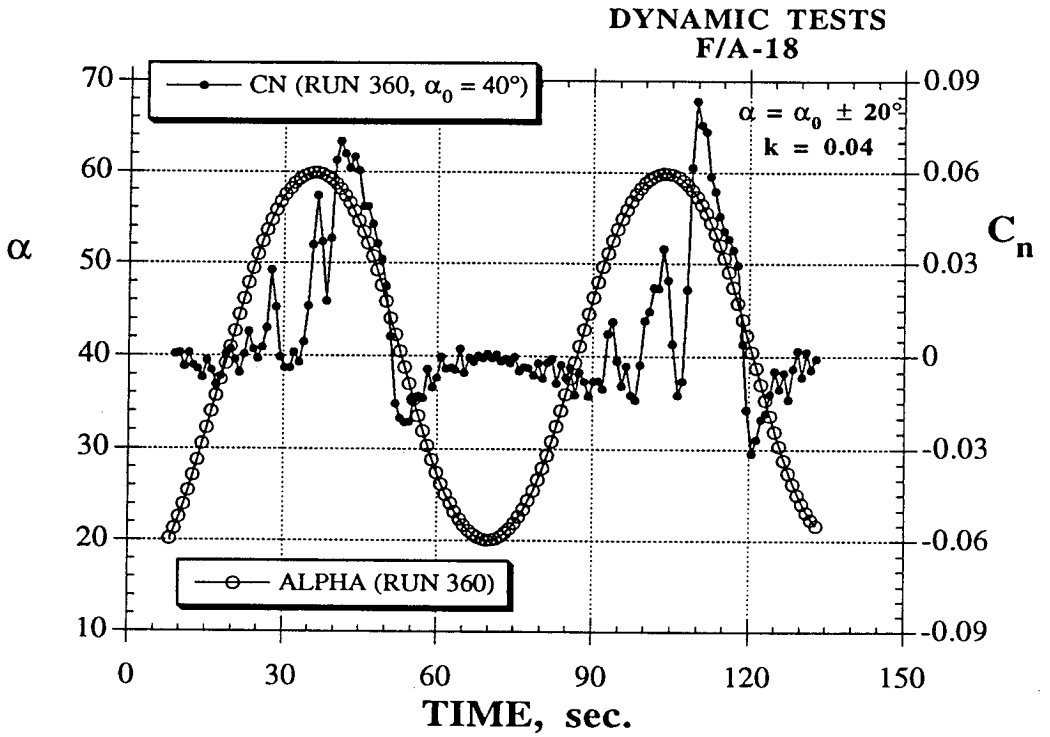

Figure 45 - Yawing Moment Variations During Large Amplitude Pitch Oscillations (F/A-18, k = 0.04)

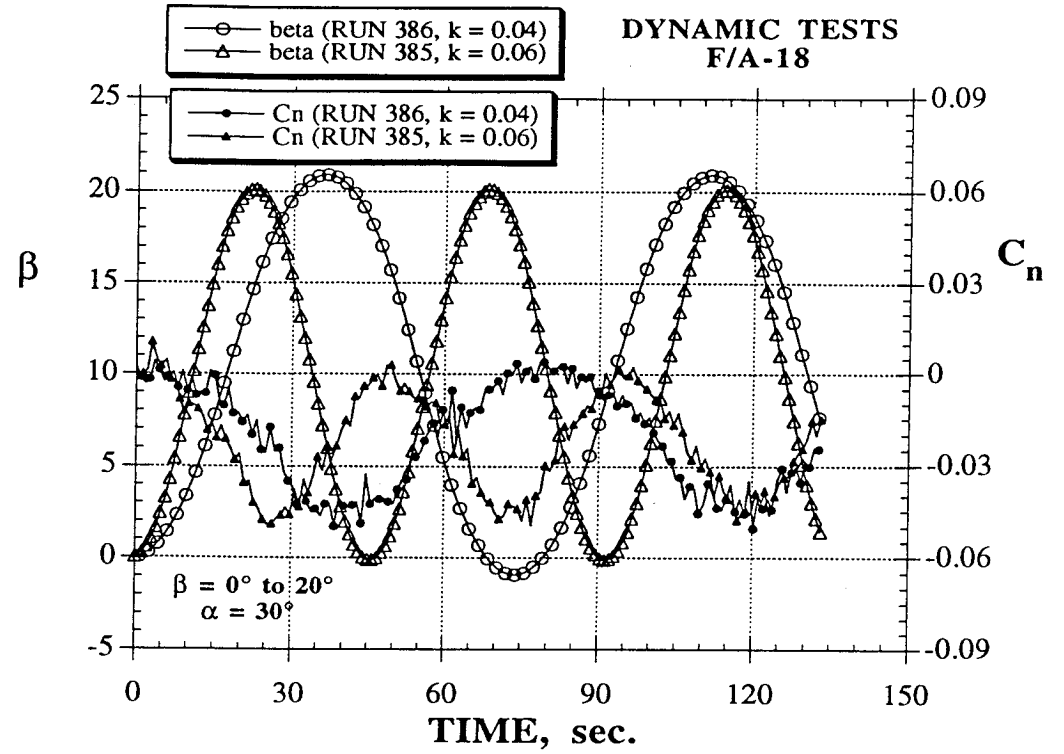

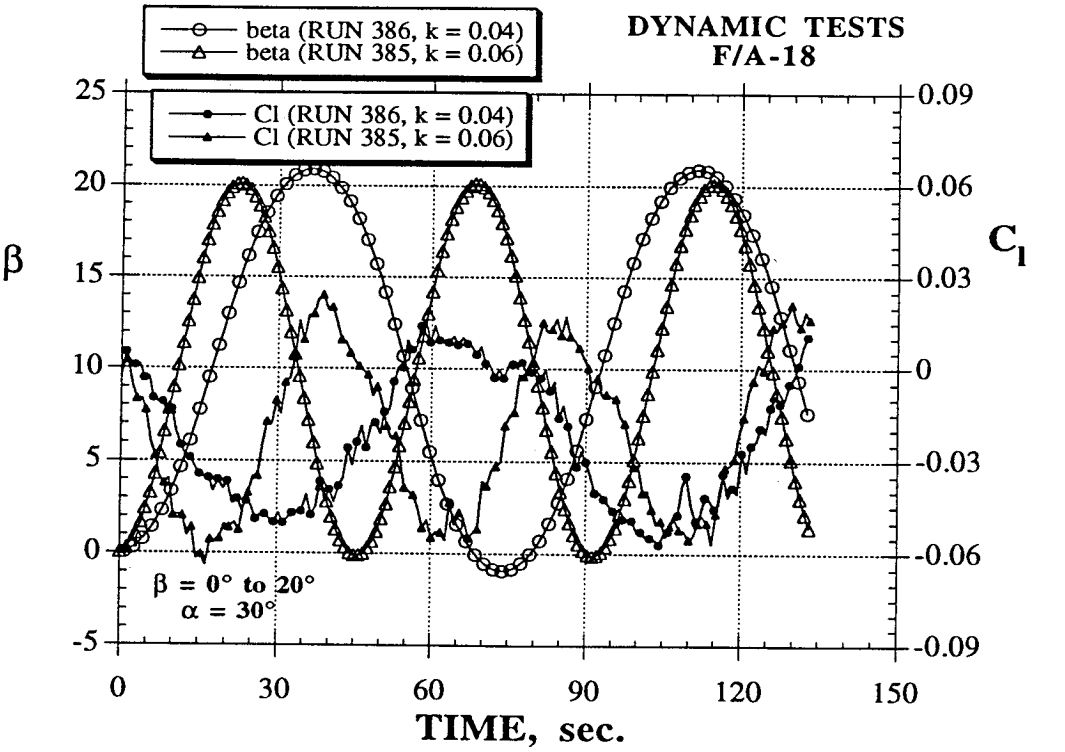

Figure 46 - Sideslip Angle and Yawing and Rolling Moment Time Histories During Yaw Oscillations (F/A-18, $\alpha = 30°$)

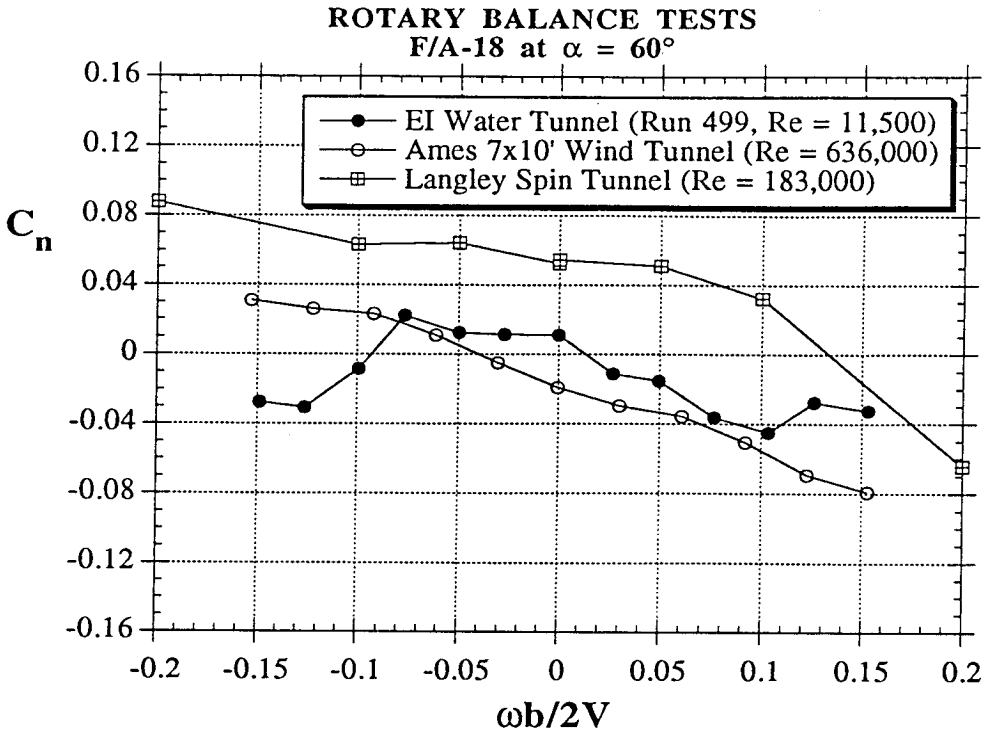

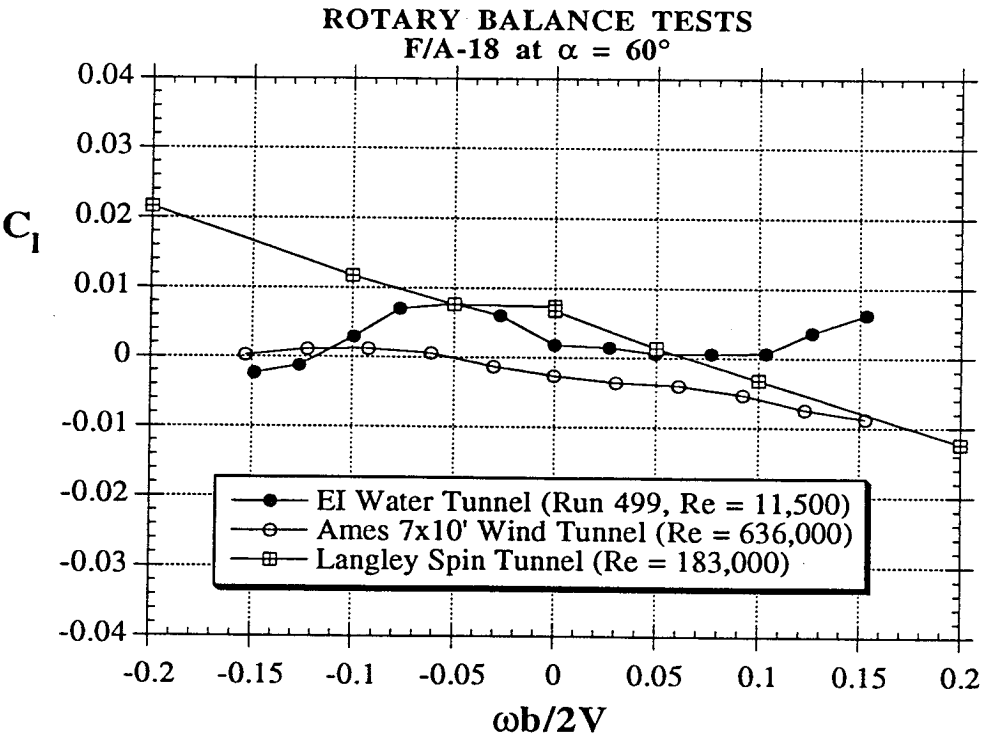

Figure 76 - Concluded

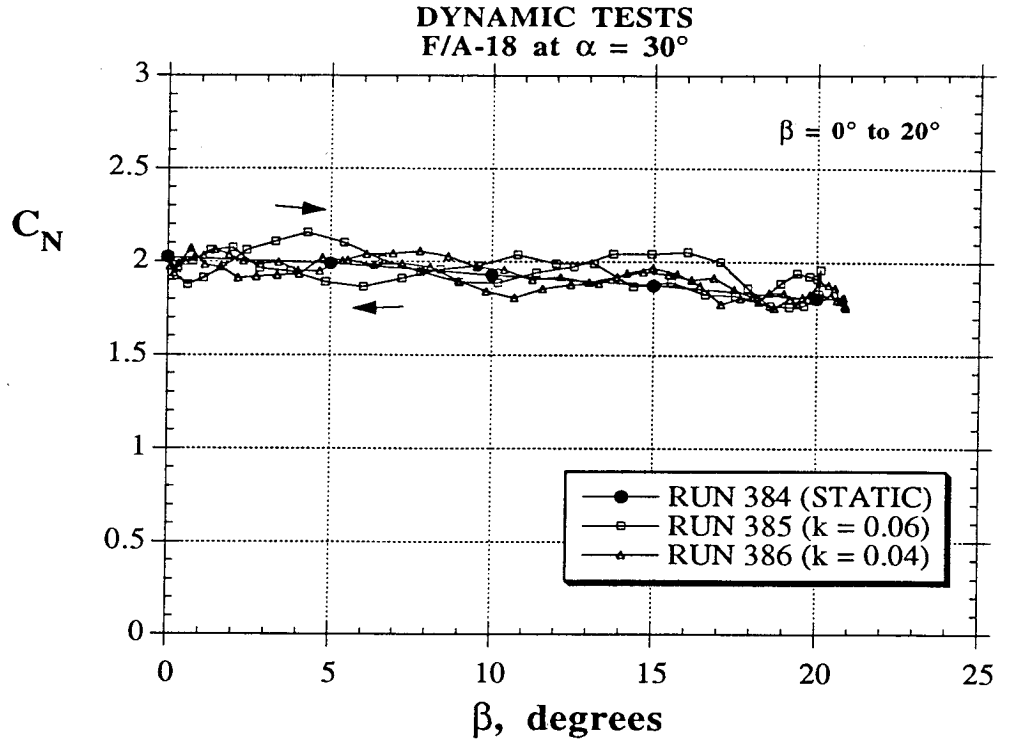

a) C_N Hysteresis Loops

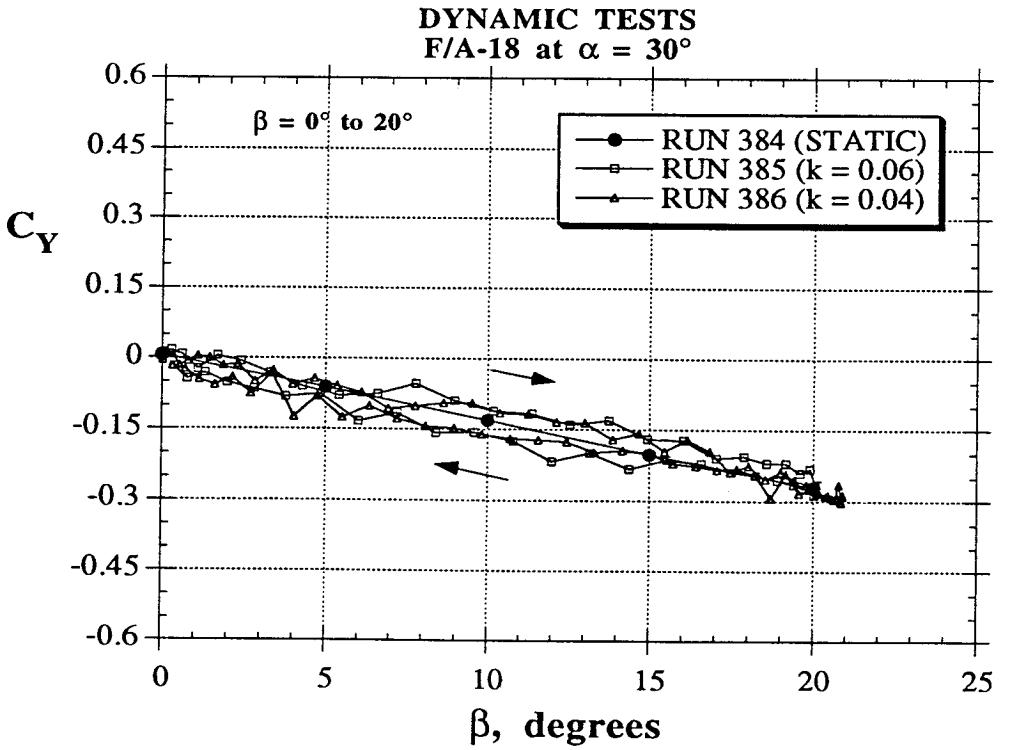

b) C_Y Hysteresis Loops

Figure 47 - Hysteresis Loops During Yaw Oscillations (F/A-18, α = 30°)

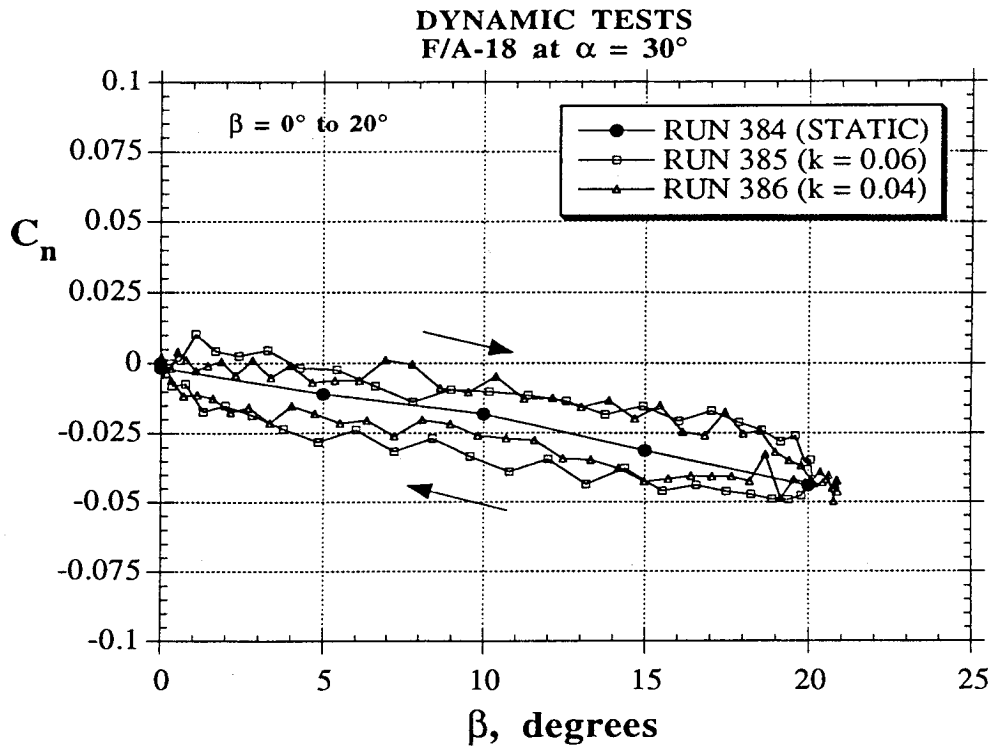

c) C_n Hysteresis Loops

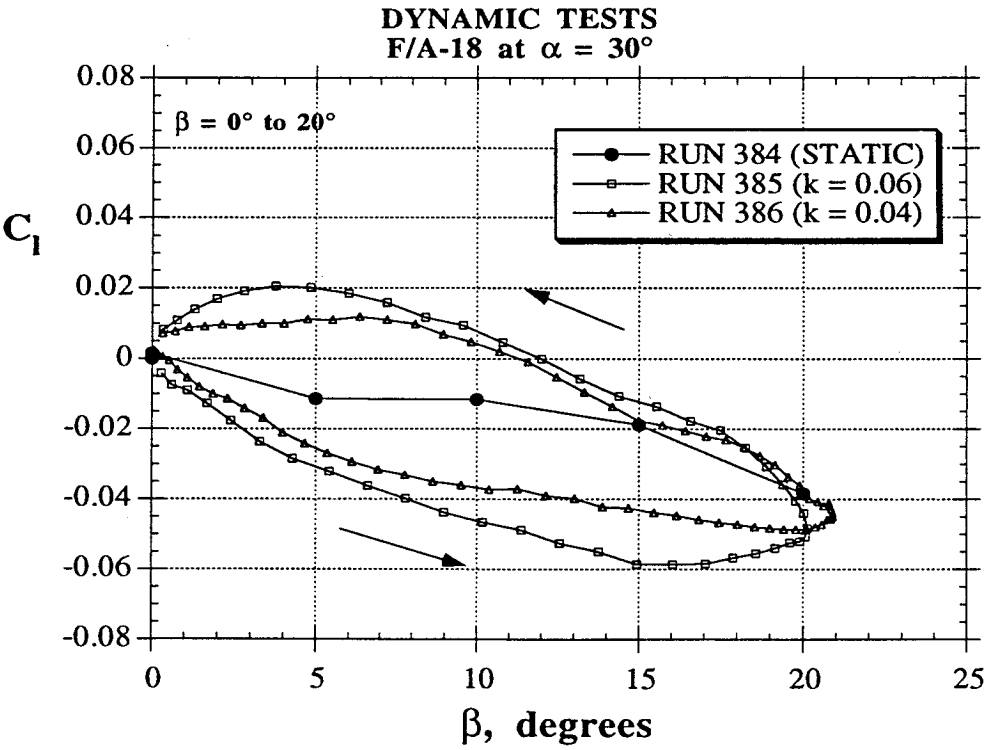

d) C_l Hysteresis Loops

Figure 47 - Concluded

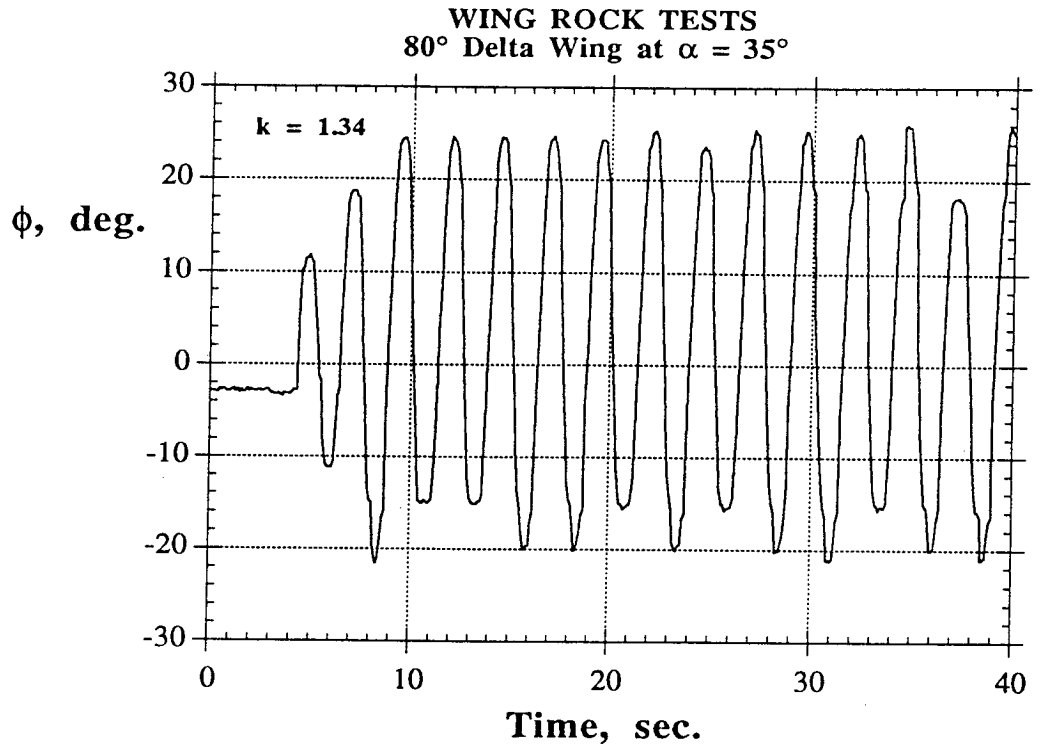

Figure 48 - Roll Angle History of Wing Rock at $\alpha = 35°$ (80° Delta Wing)

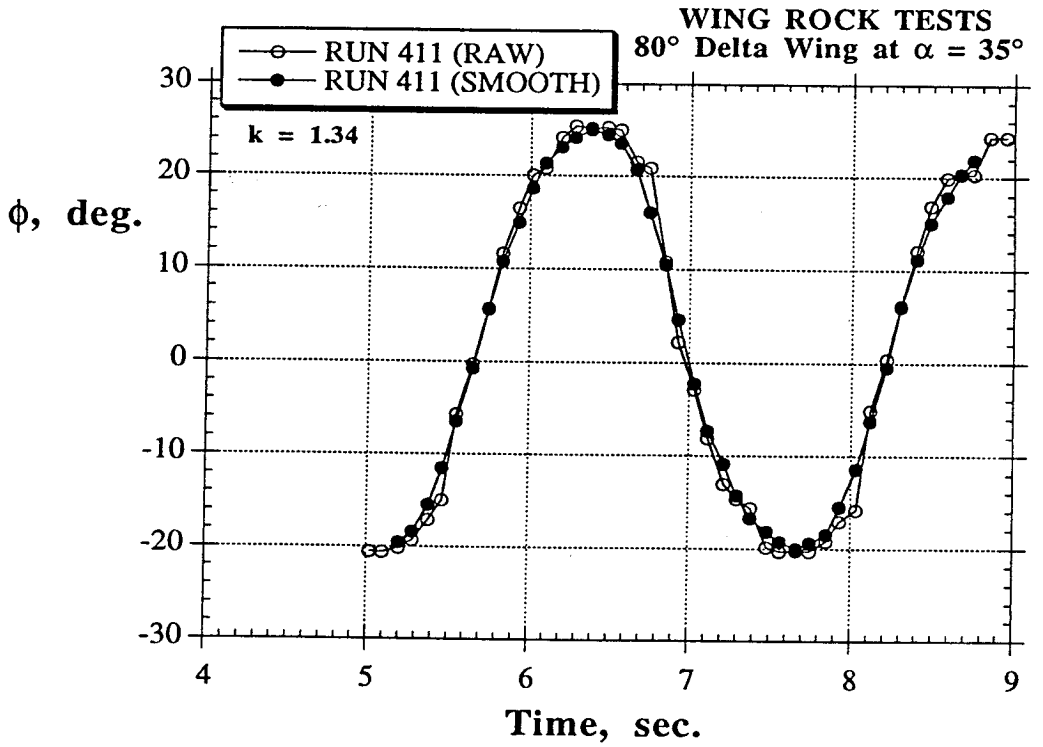

a) Roll Angle

Figure 49 - Time Histories of Roll Angle, Angular Velocity and Angular Acceleration During Wing Rock at $\alpha = 35°$ (80° Delta Wing)

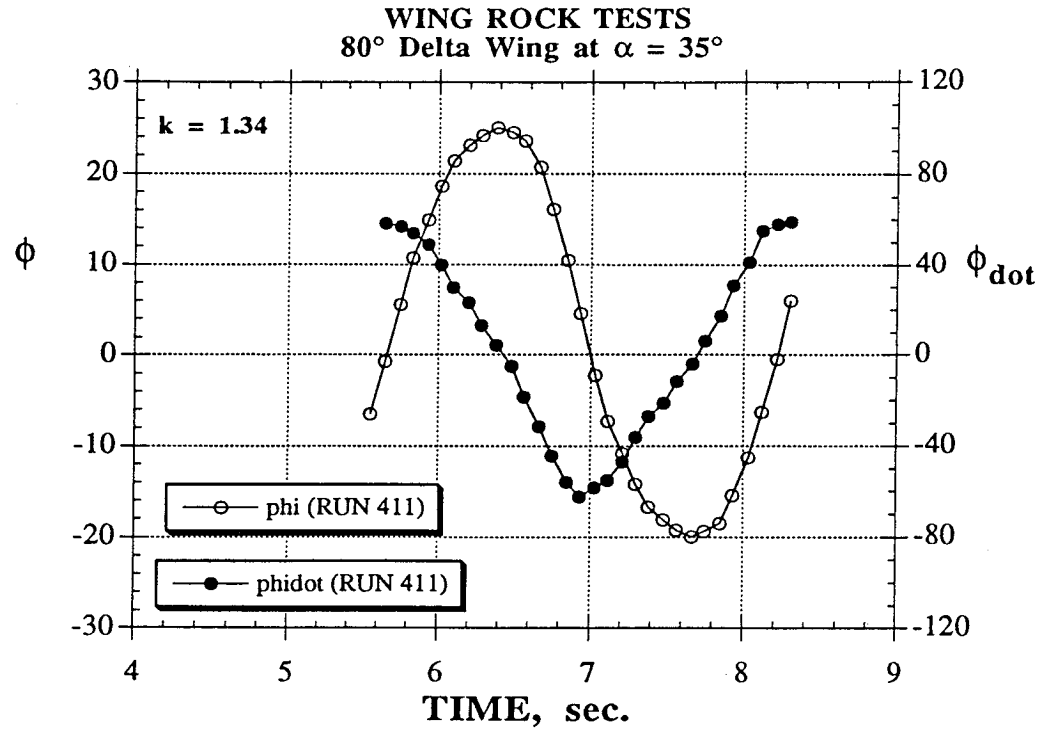

b) Angular Velocity

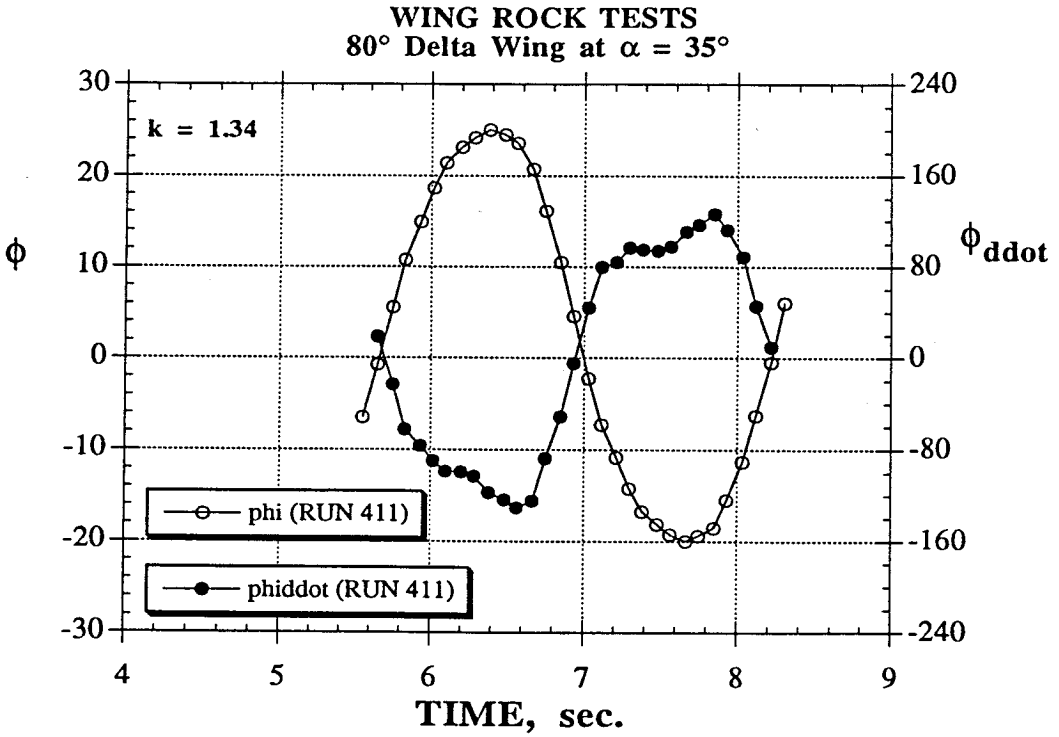

c) Angular Acceleration

Figure 49 - Concluded

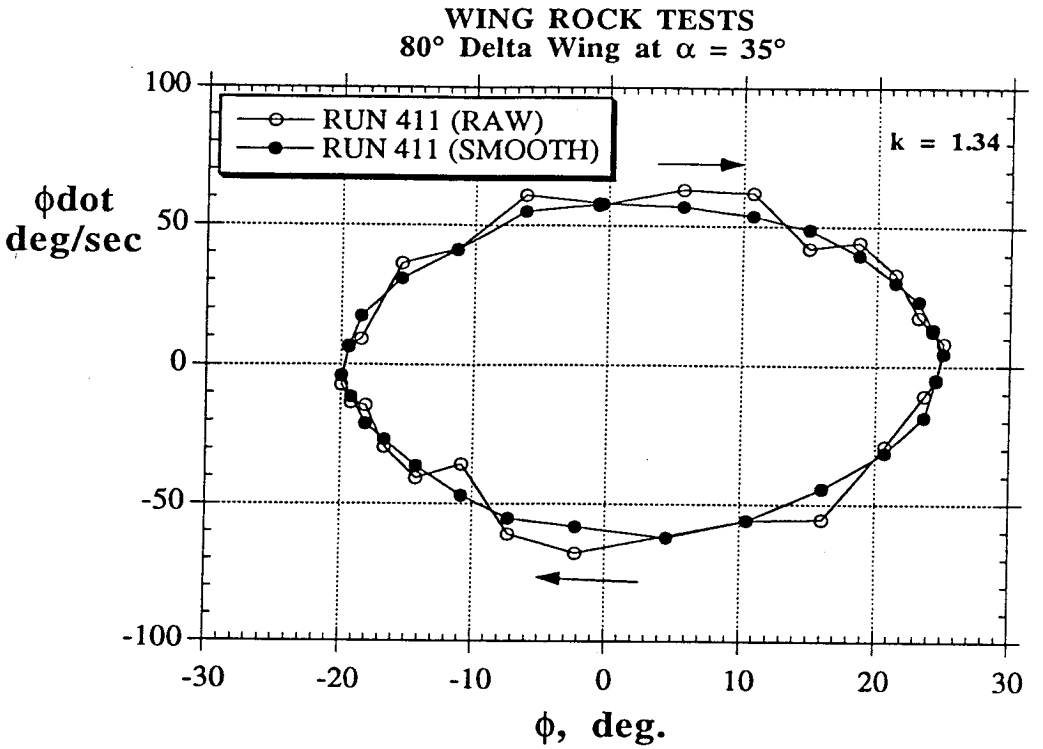

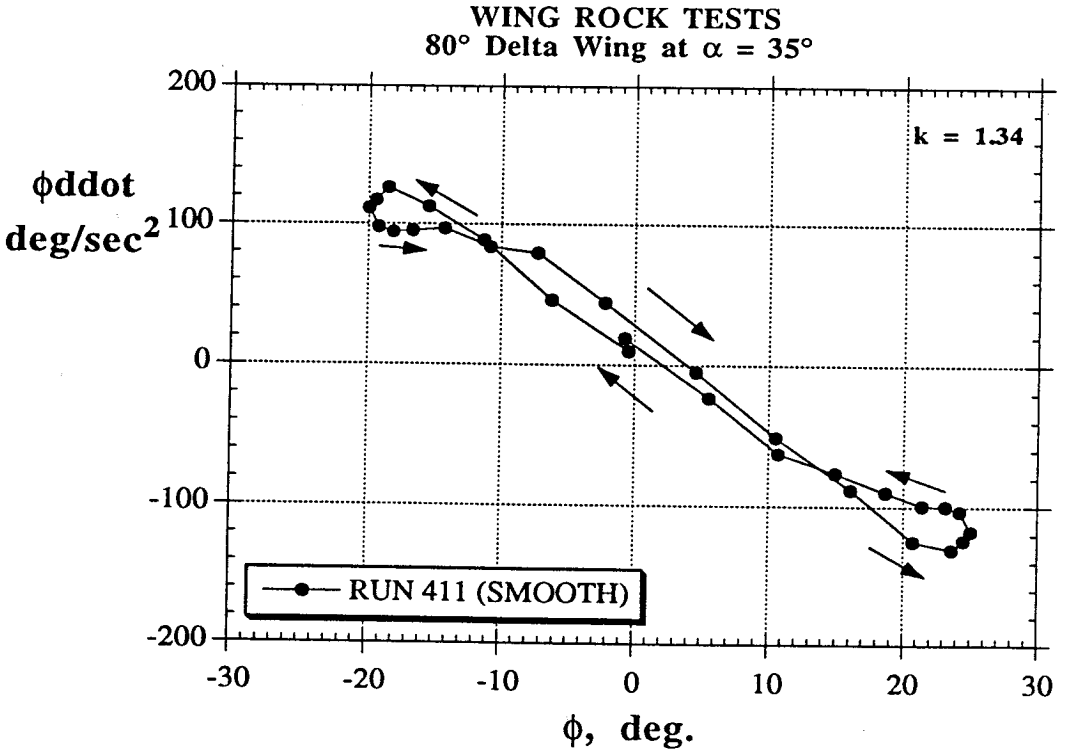

Figure 50 - Phase Plots for One Cycle of Wing Rock at $\alpha = 35°$ (80° Delta Wing)

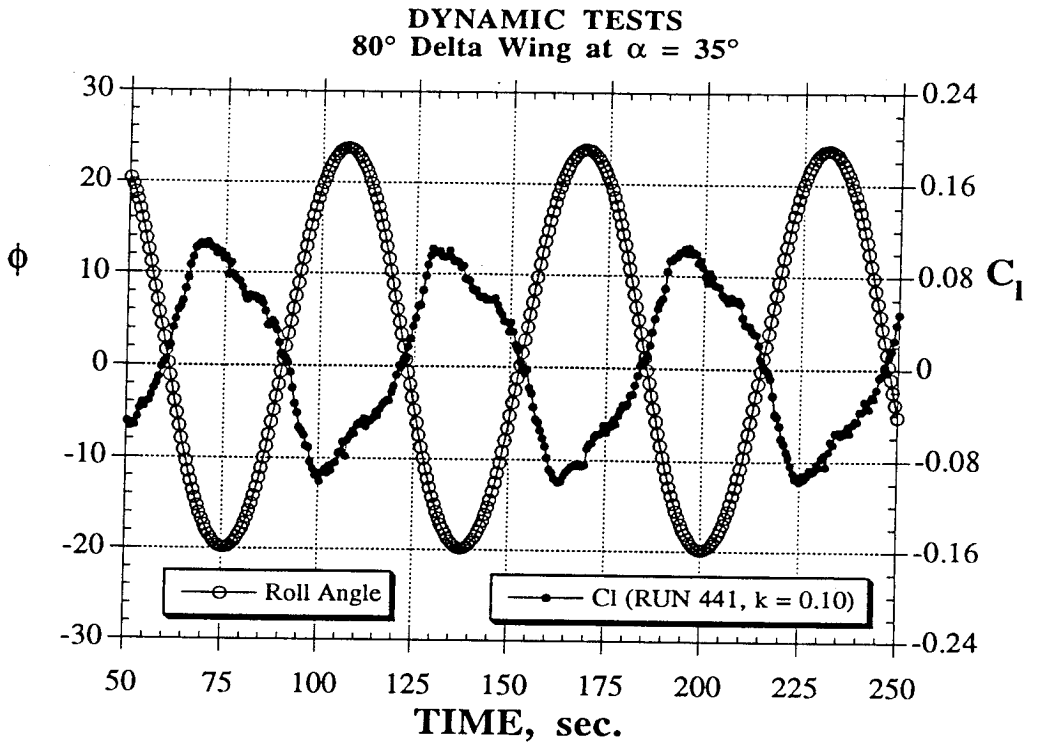

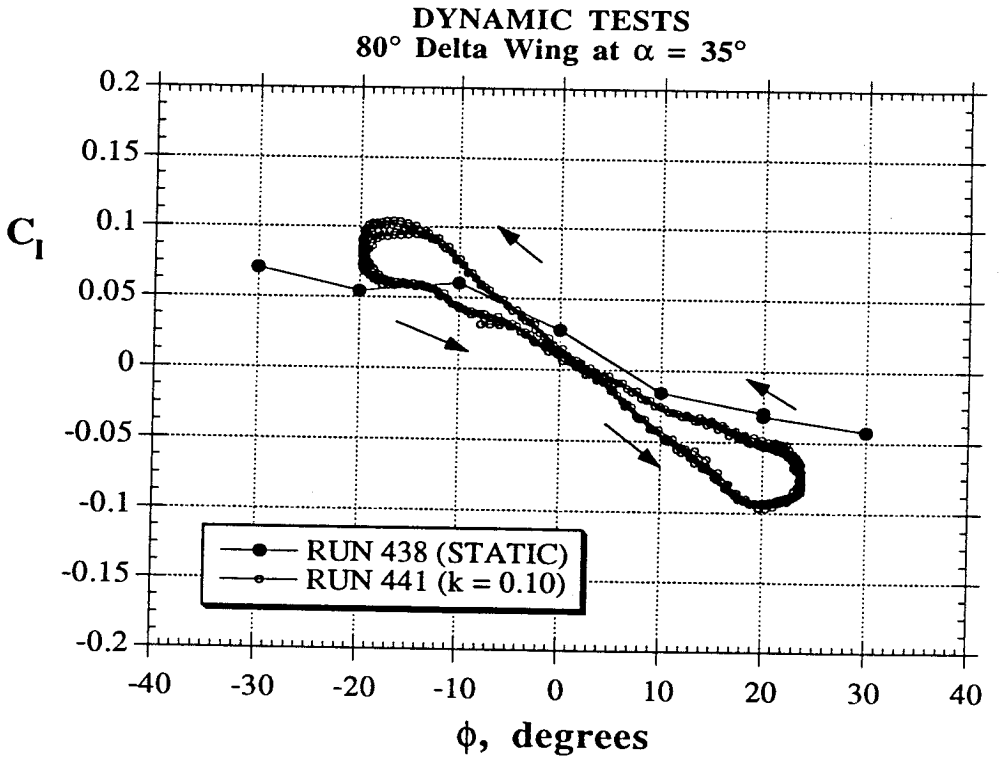

Figure 51 - Rolling Moment Variations During Roll Oscillations (80° Delta Wing, $\alpha = 35°$, $k = 0.1$)

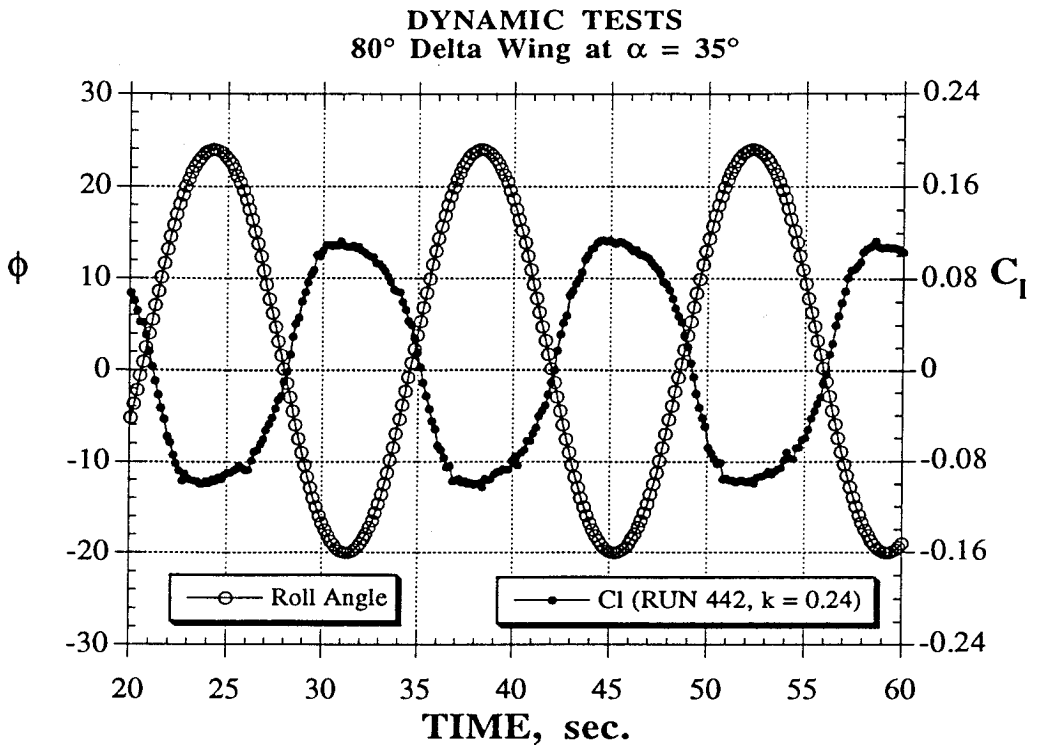

a) Roll Angle and C_l Time Histories

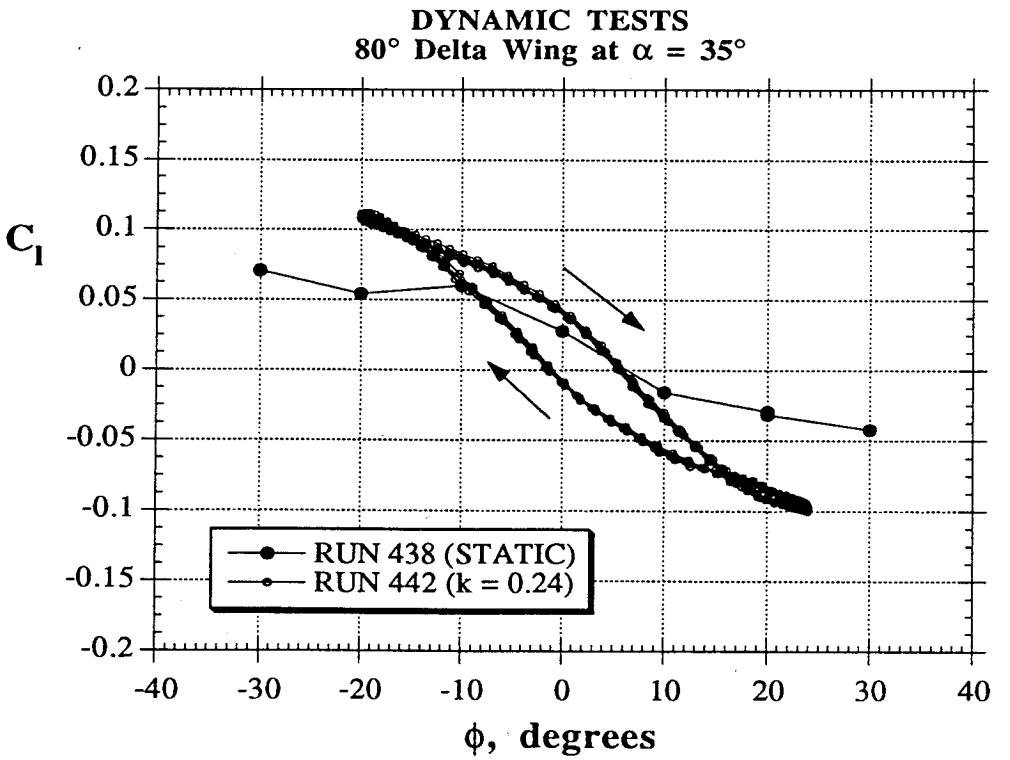

b) C_l Hysteresis Loops

Figure 52 - Rolling Moment Variations During Roll Oscillations (80° Delta Wing, α = 35°, k = 0.24)

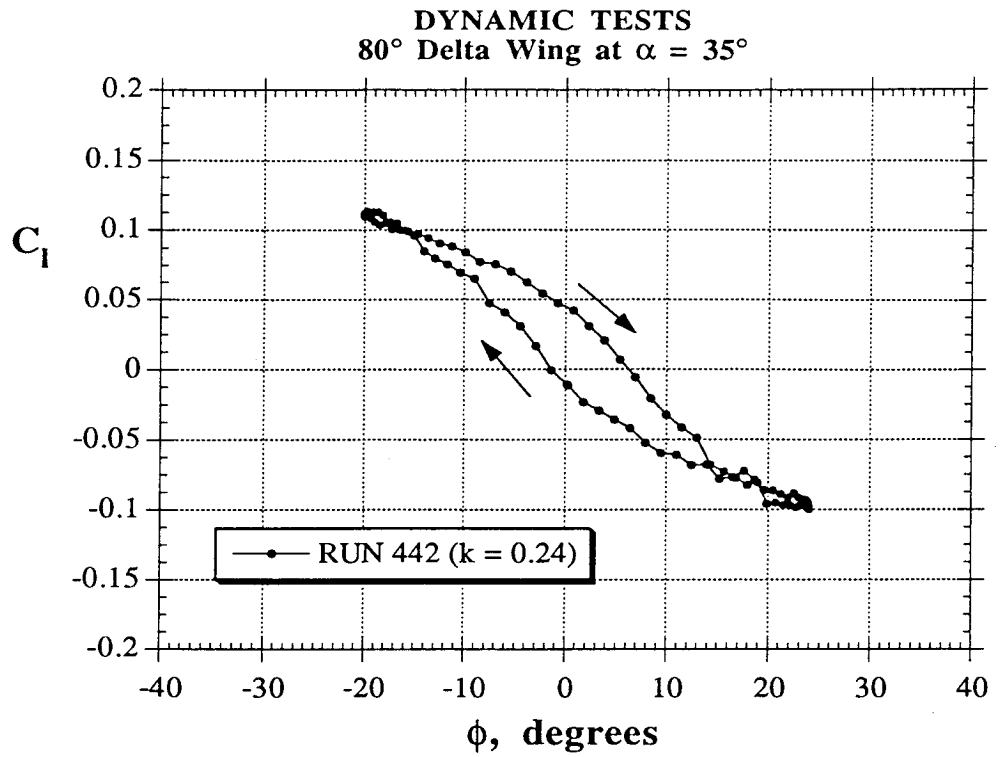

c) C_l Hysteresis Loop (One Cycle)

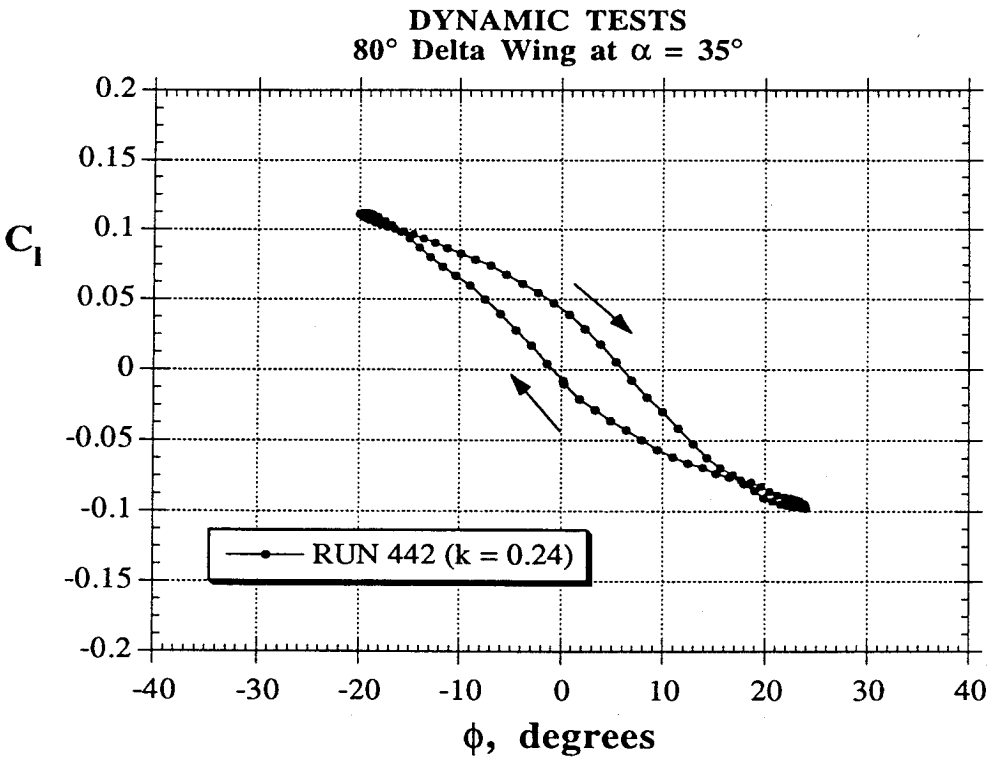

d) C_l Hysteresis Loop (Smooth Data)

Figure 52 - Concluded

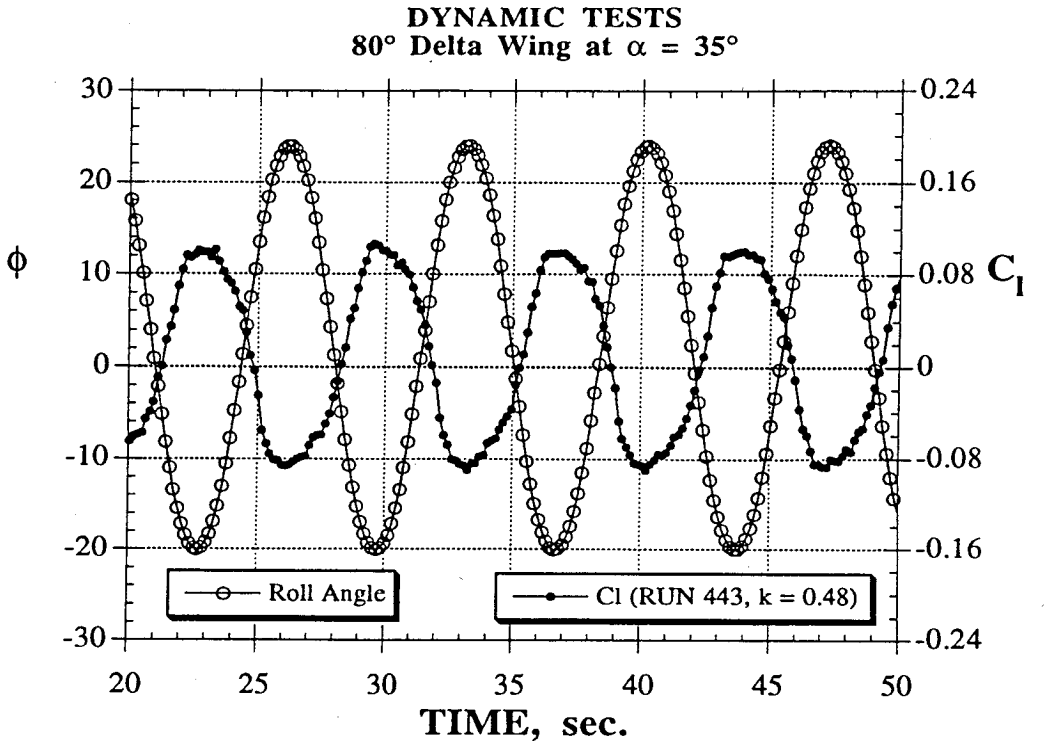

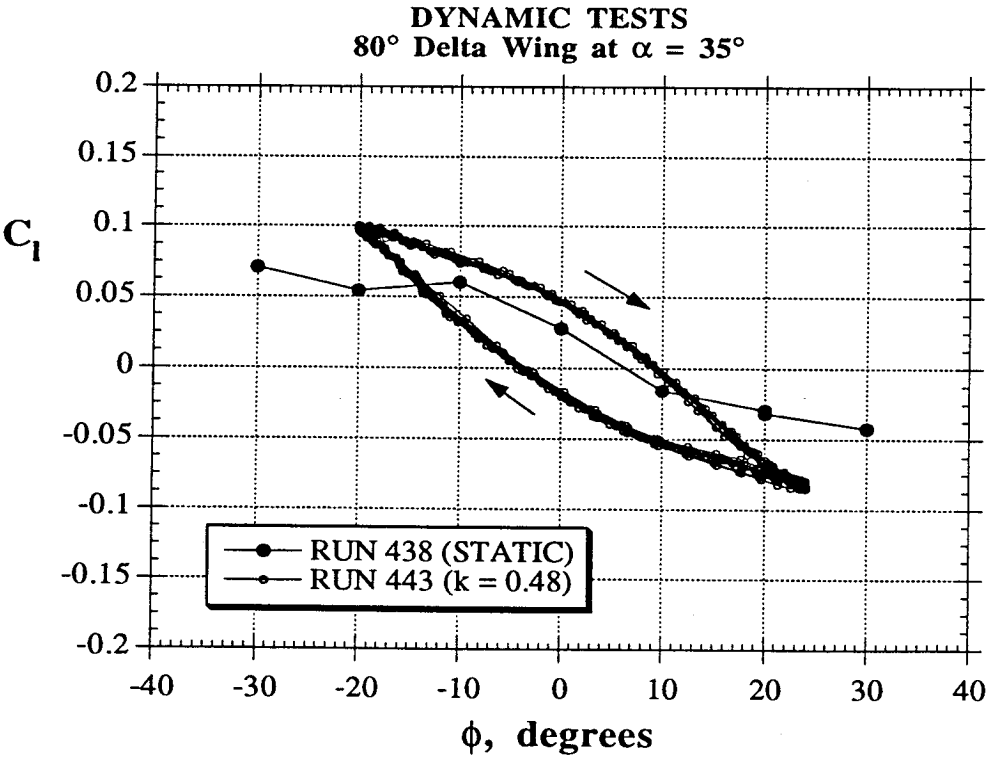

Figure 53 - Rolling Moment Variations During Roll Oscillations (80° Delta Wing, $\alpha = 35°$, $k = 0.48$)

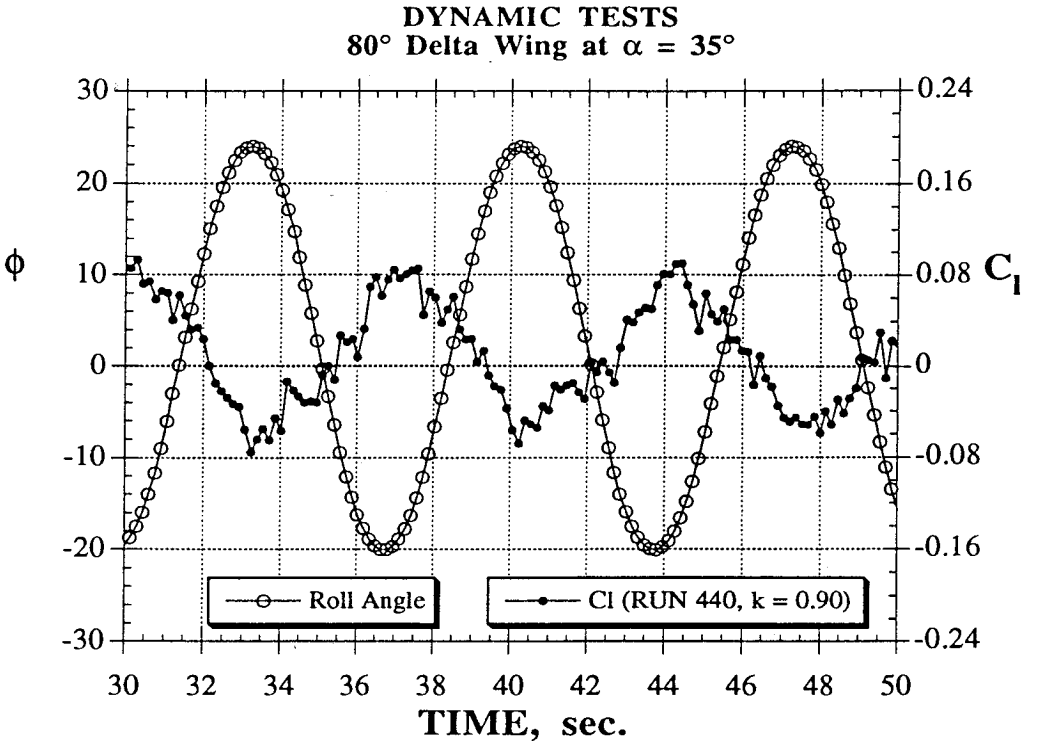

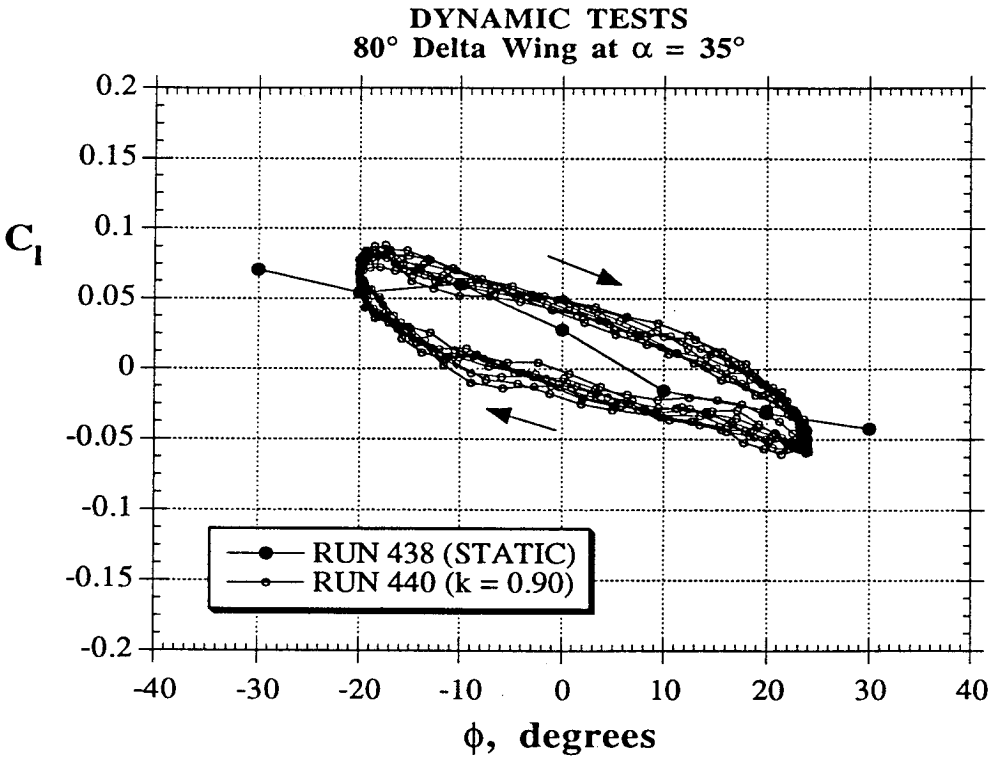

Figure 54 - Rolling Moment Variations During Roll Oscillations (80° Delta Wing, α = 35°, k = 0.9)

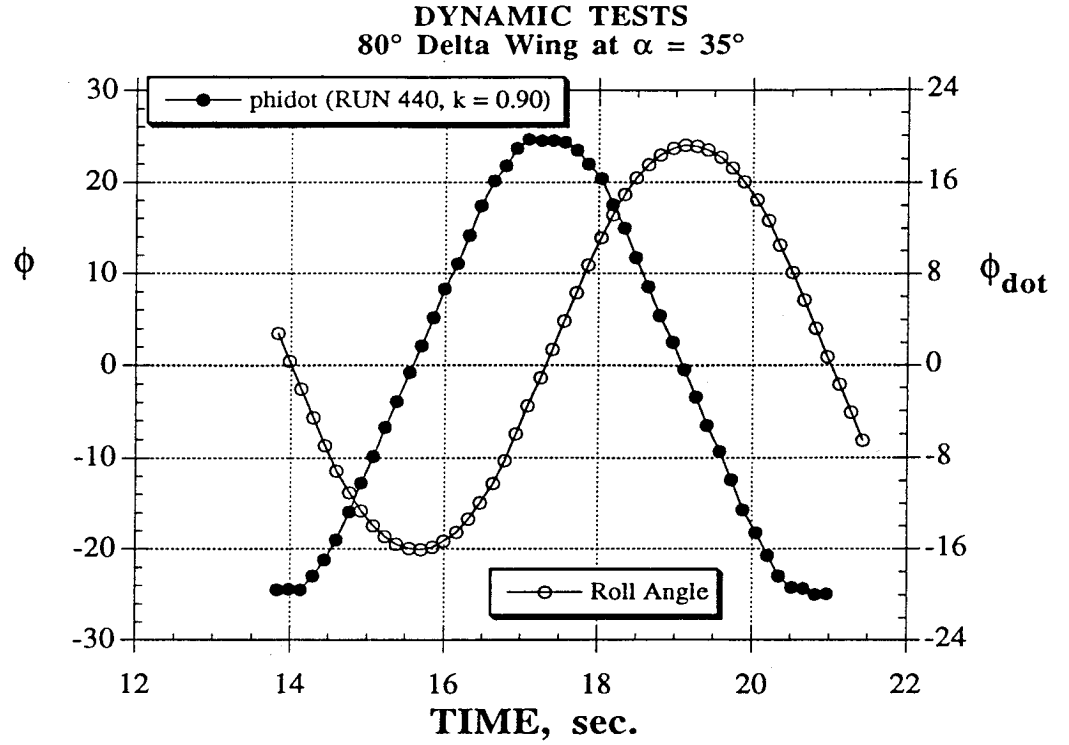

a) Angular Velocity Time History

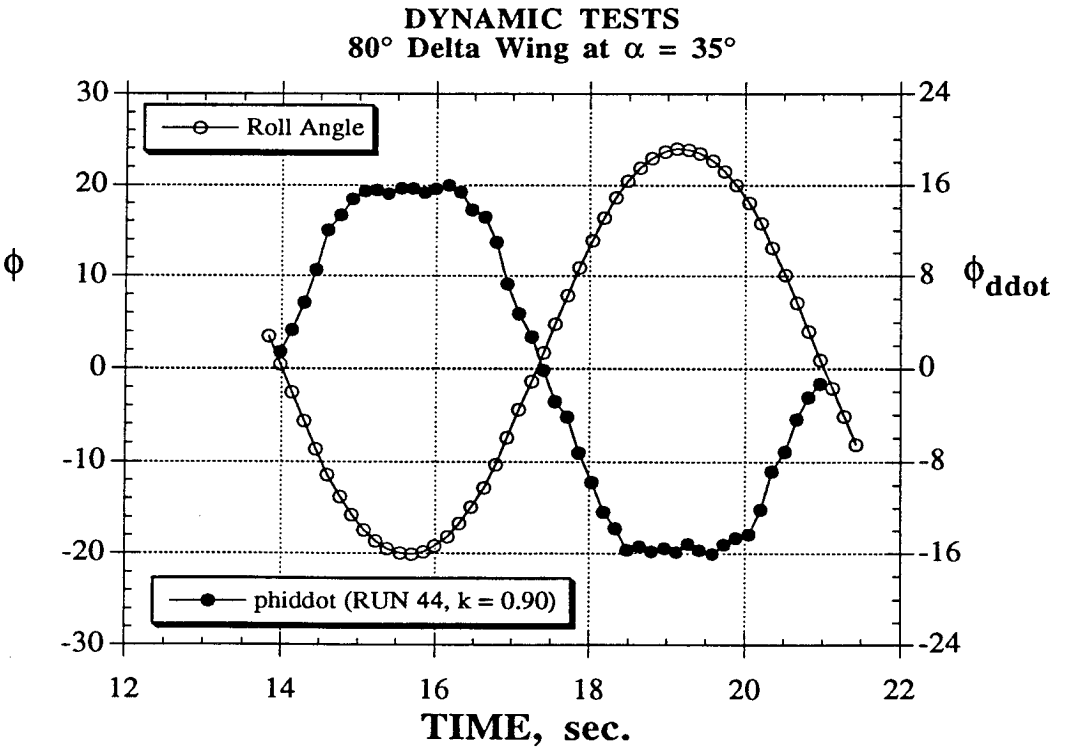

b) Angular Acceleration Time History

Figure 55 - Roll Angle, Angular Velocity and Angular Acceleration Variations During Roll Oscillations (80° Delta Wing, $\alpha = 35°$, $k = 0.9$)

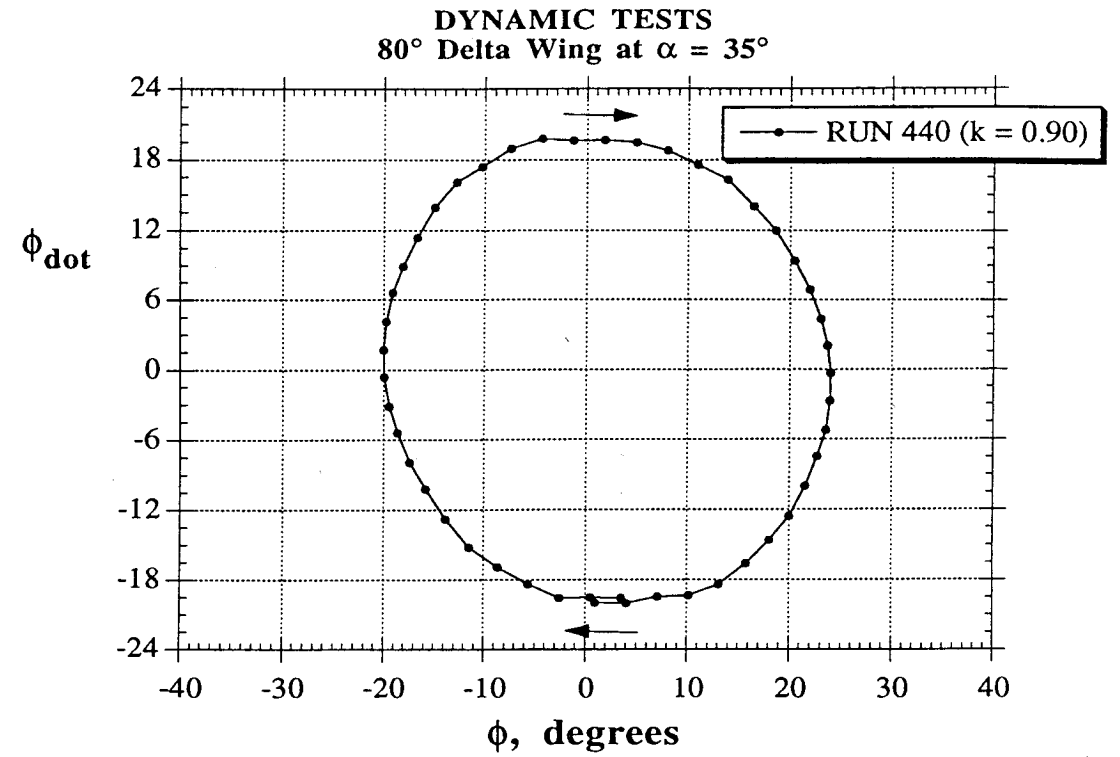

c) Phase Plot (Angular Velocity)

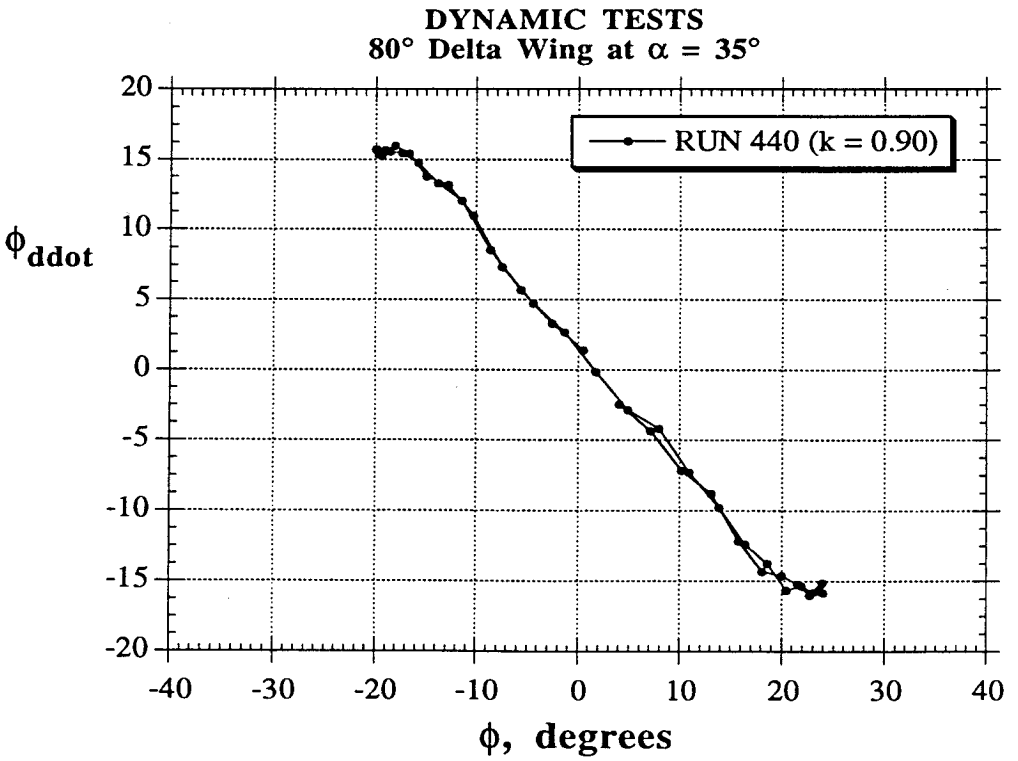

d) Phase Plot (Angular Acceleration)

Figure 55 - Concluded

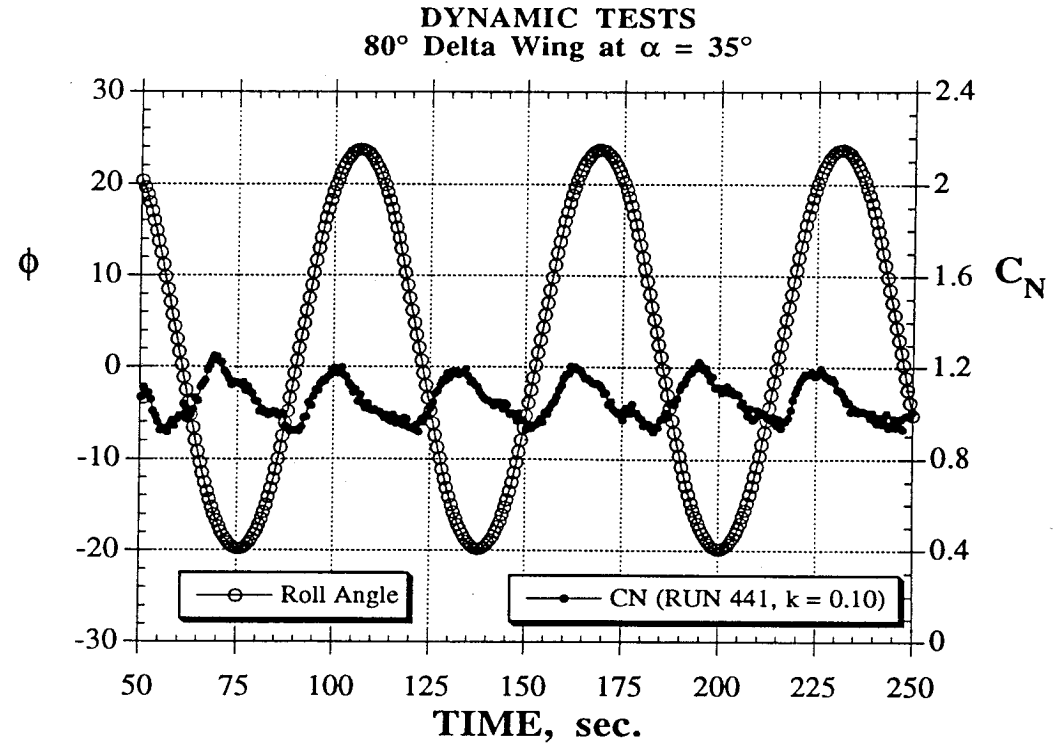

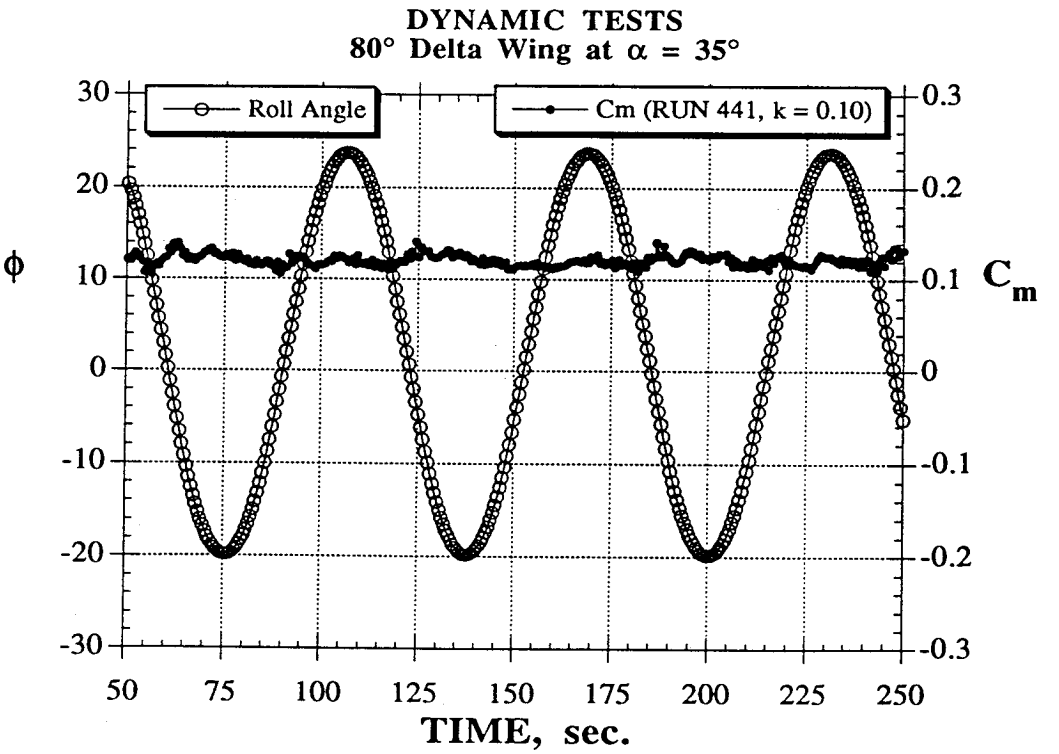

Figure 56 - Longitudinal and Directional Characteristics Variations During Roll Oscillations (80° Delta Wing, $\alpha = 35°$, $k = 0.1$)

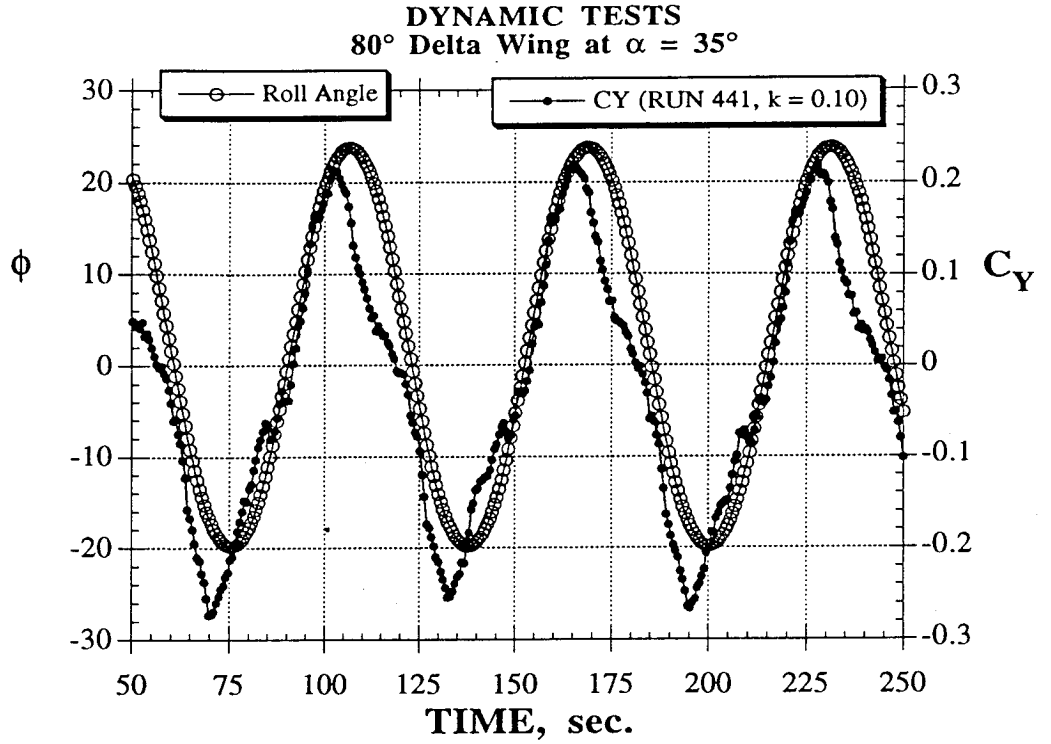

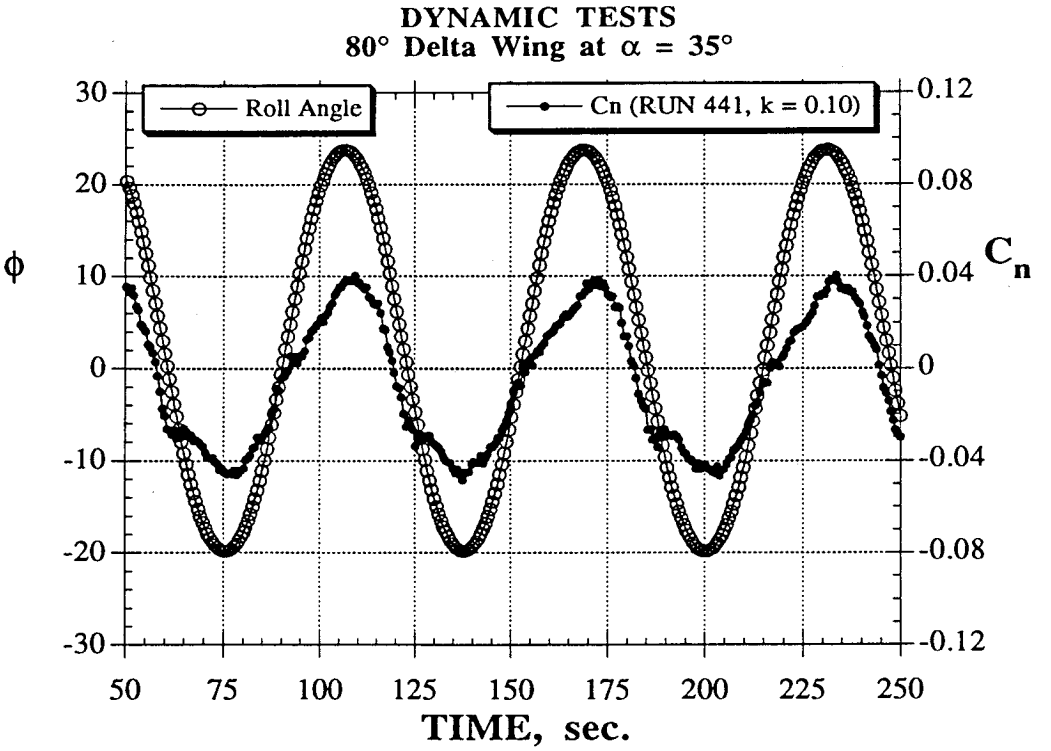

Figure 56 - Concluded

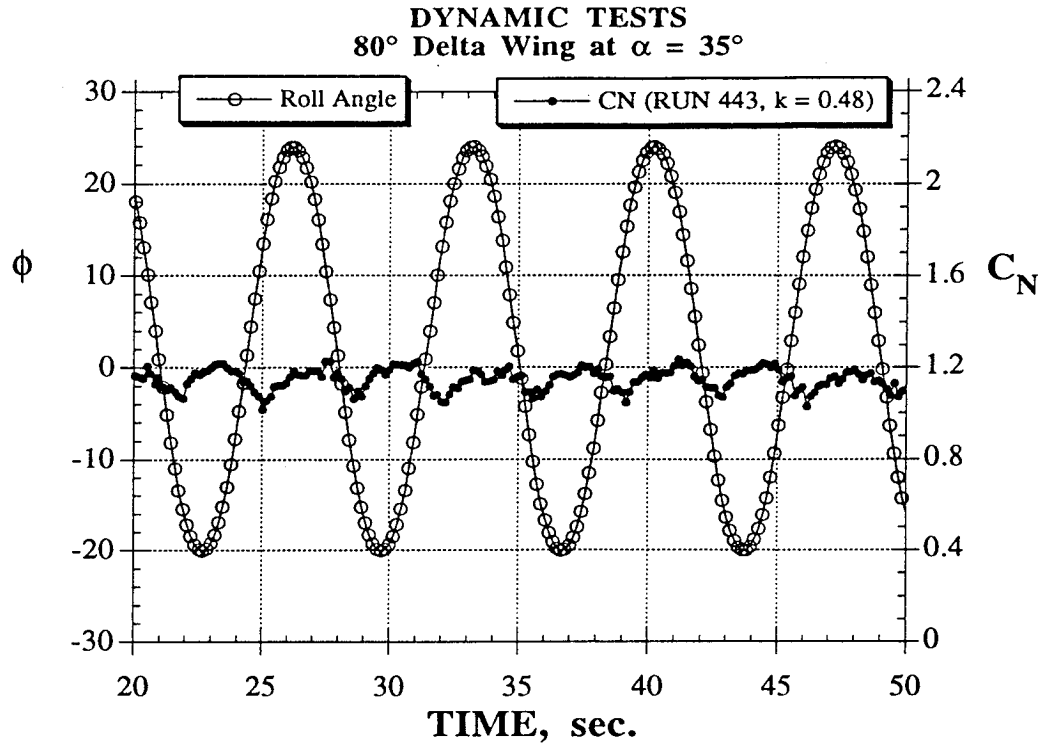

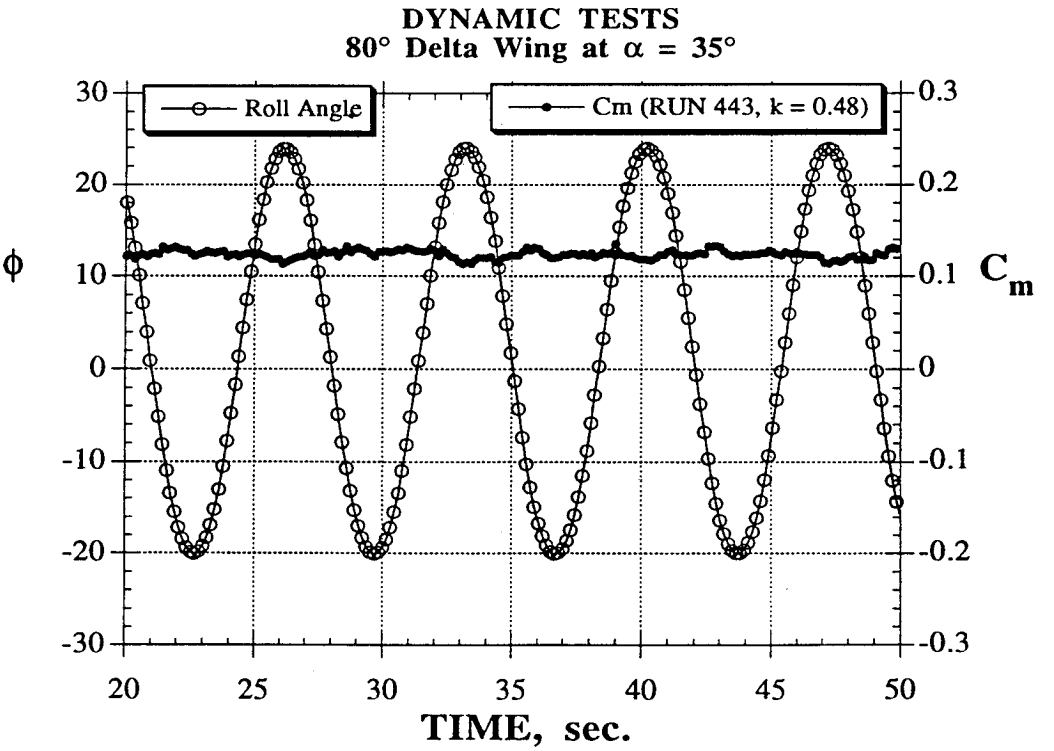

Figure 57 - Longitudinal and Directional Characteristics Variations During Roll Oscillations (80° Delta Wing, $\alpha = 35°$, $k = 0.48$)

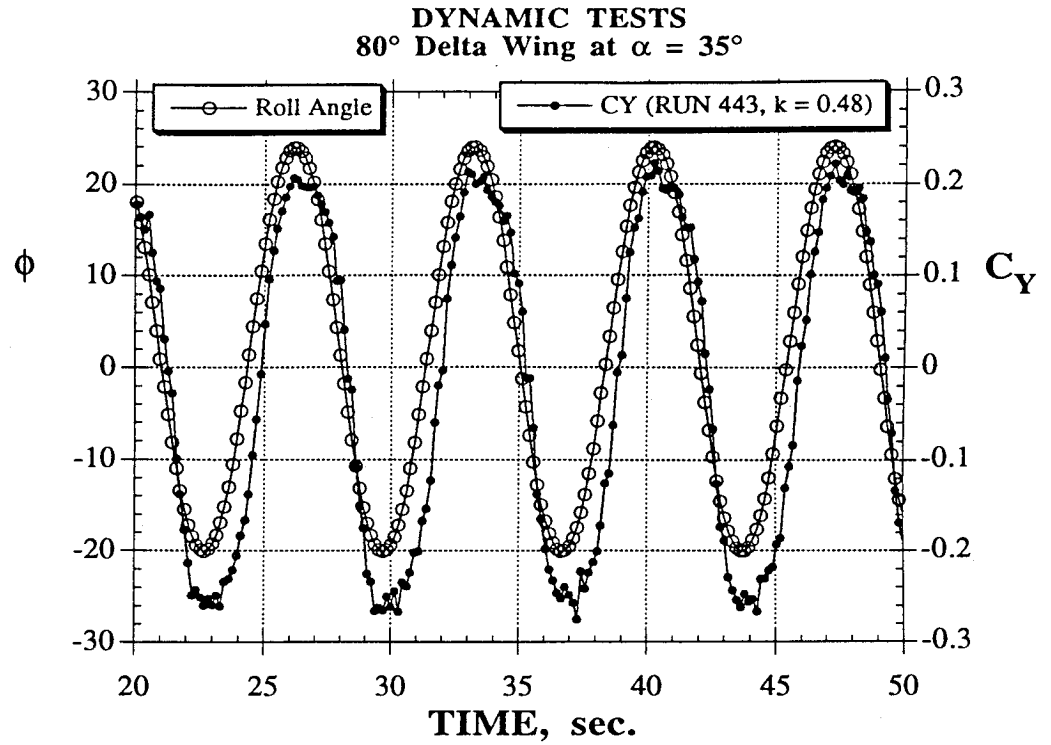

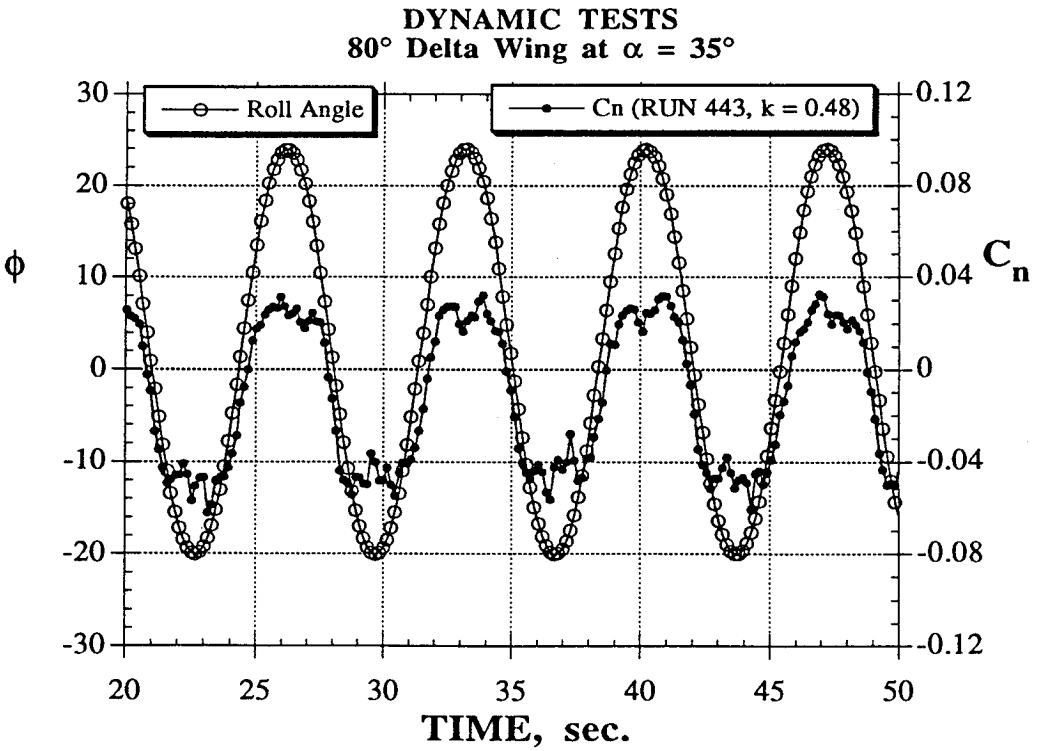

Figure 57 - Concluded

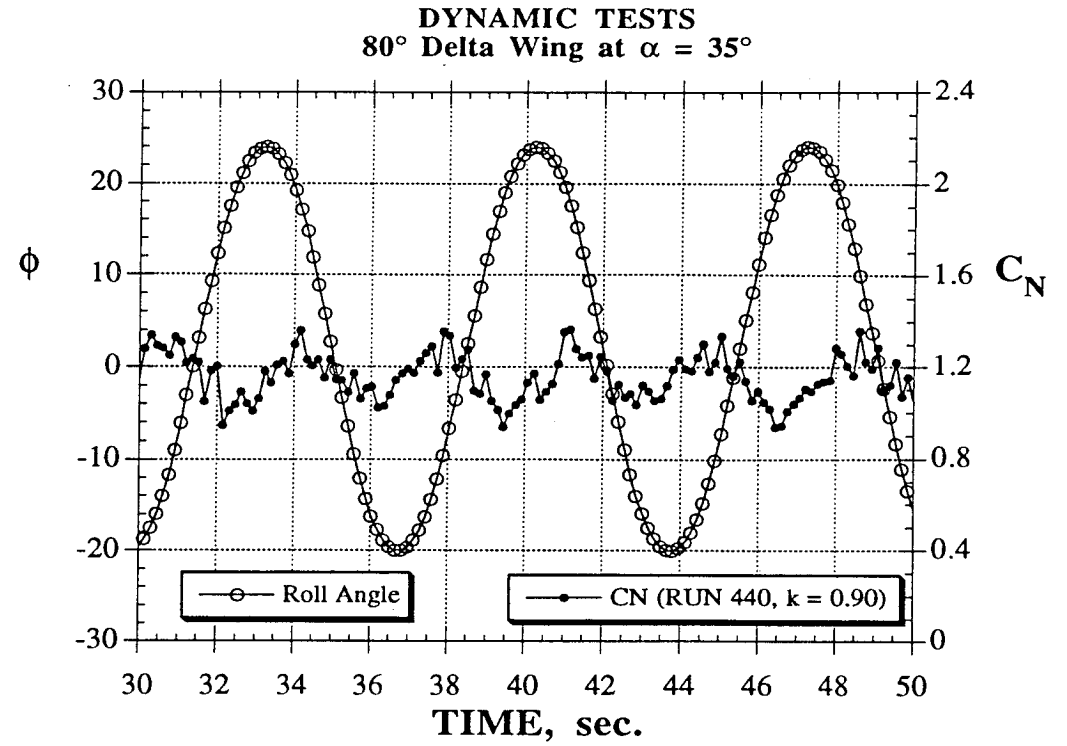

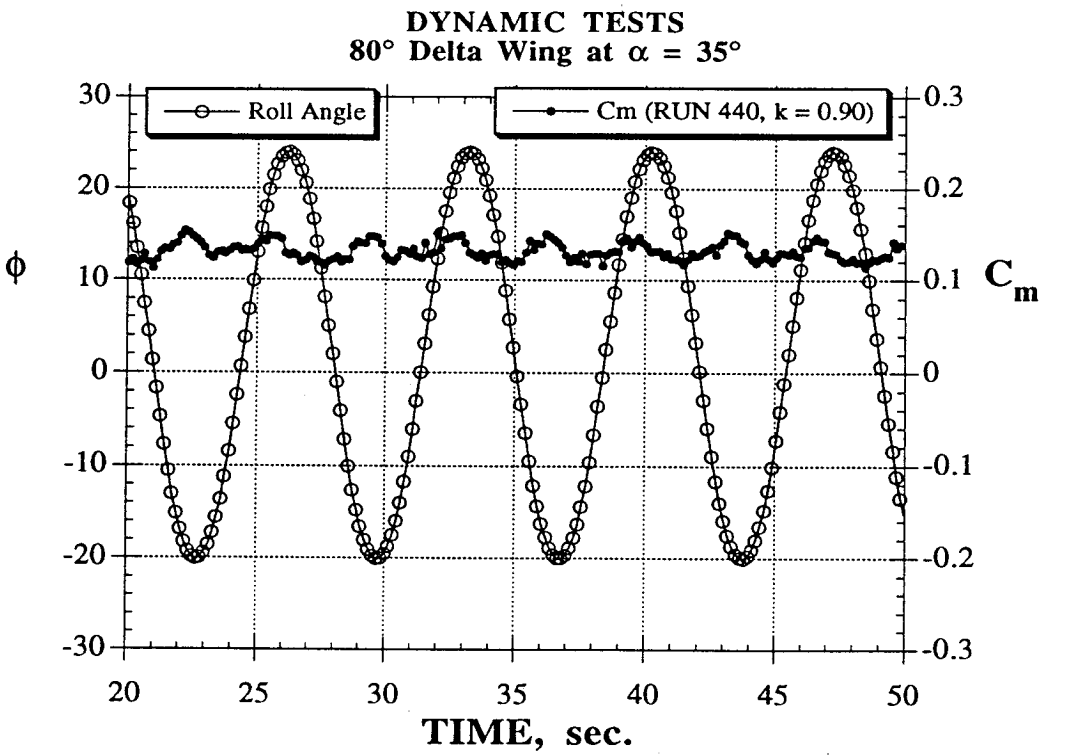

Figure 58 - Longitudinal and Directional Characteristics Variations During Roll Oscillations (80° Delta Wing, $\alpha = 35°$, k = 0.9)

C-2.

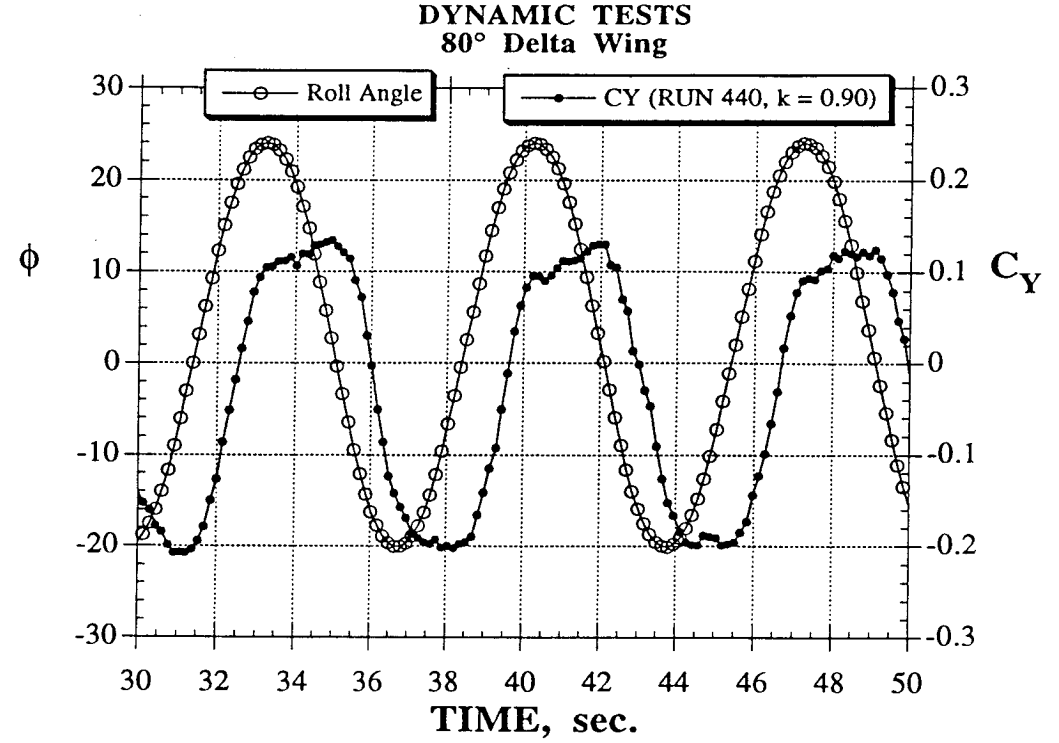

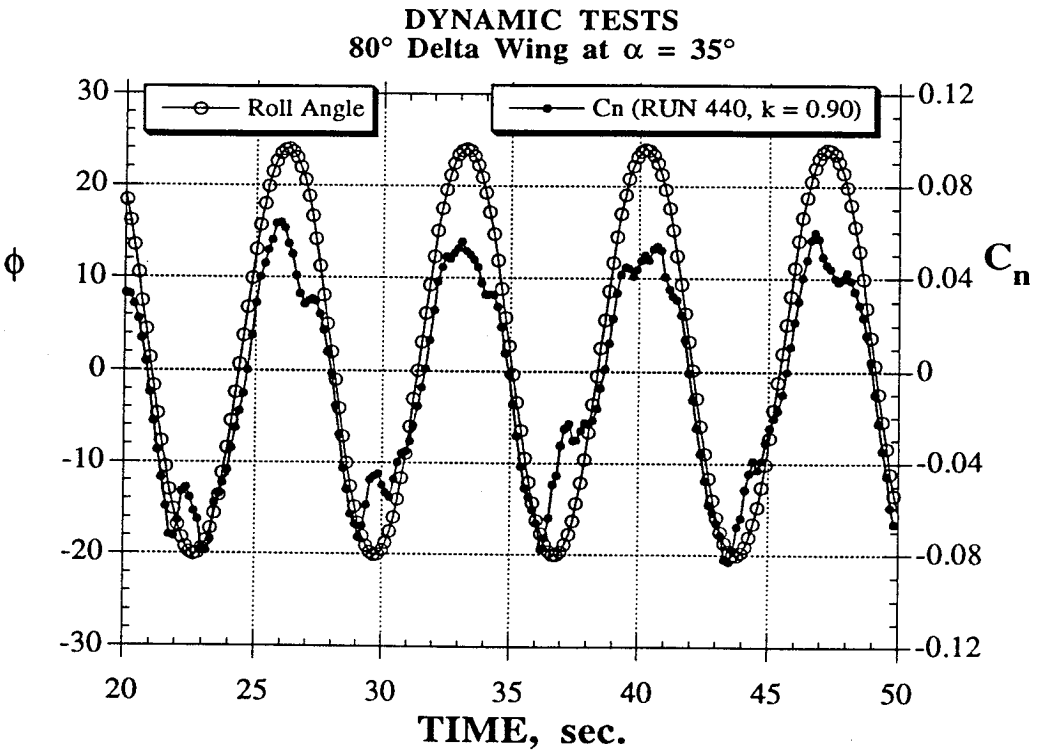

Figure 58 - Concluded

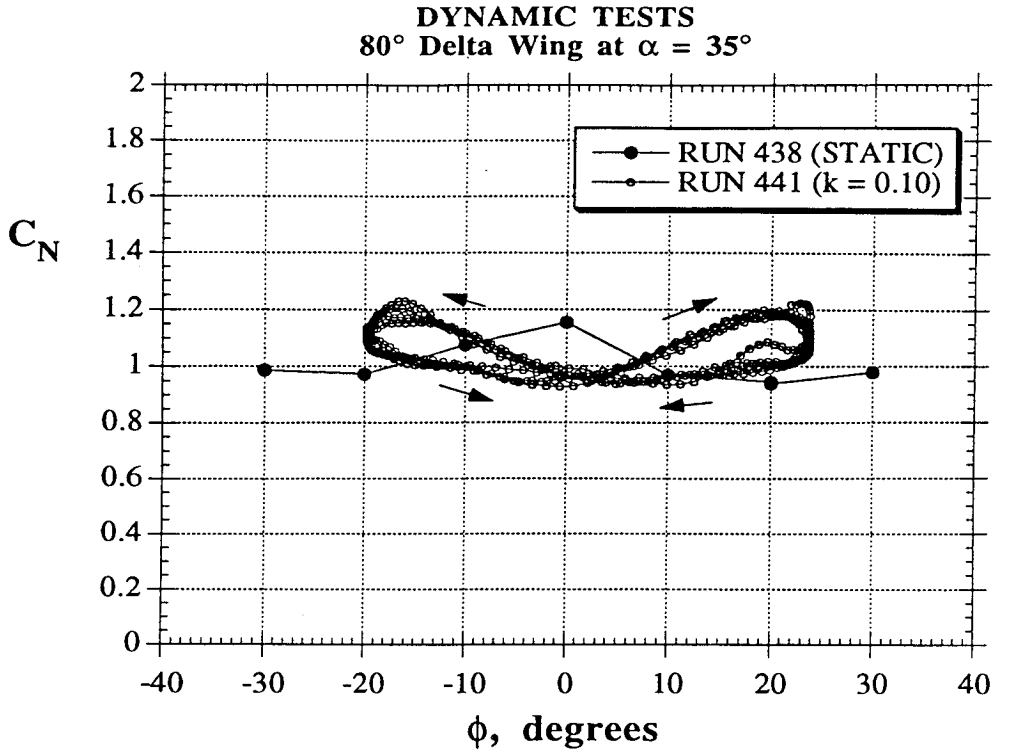

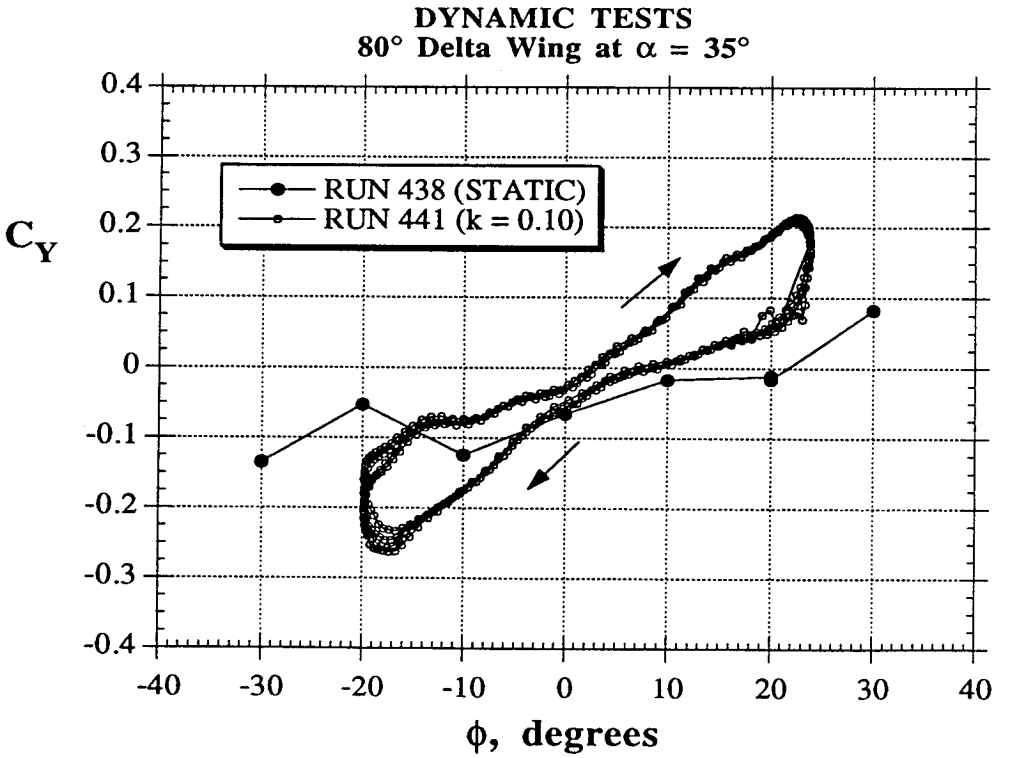

Figure 59 - Normal and Side Force Hysteresis Loops During Roll Oscillations (80° Delta Wing, $\alpha = 35°$, $k = 0.1$)

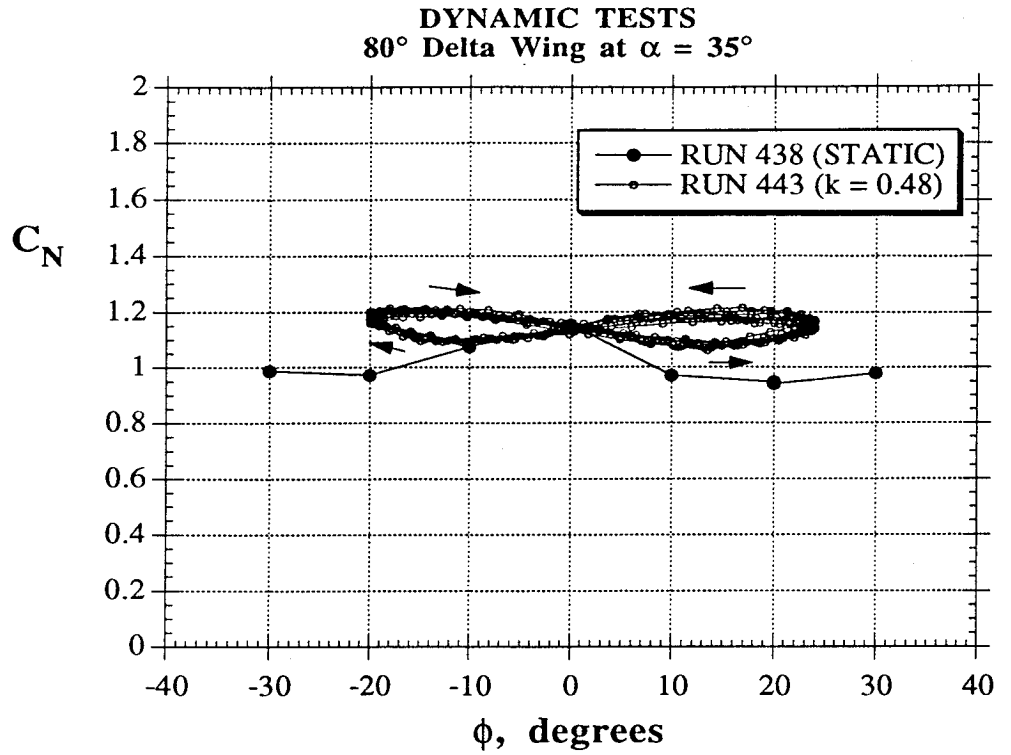

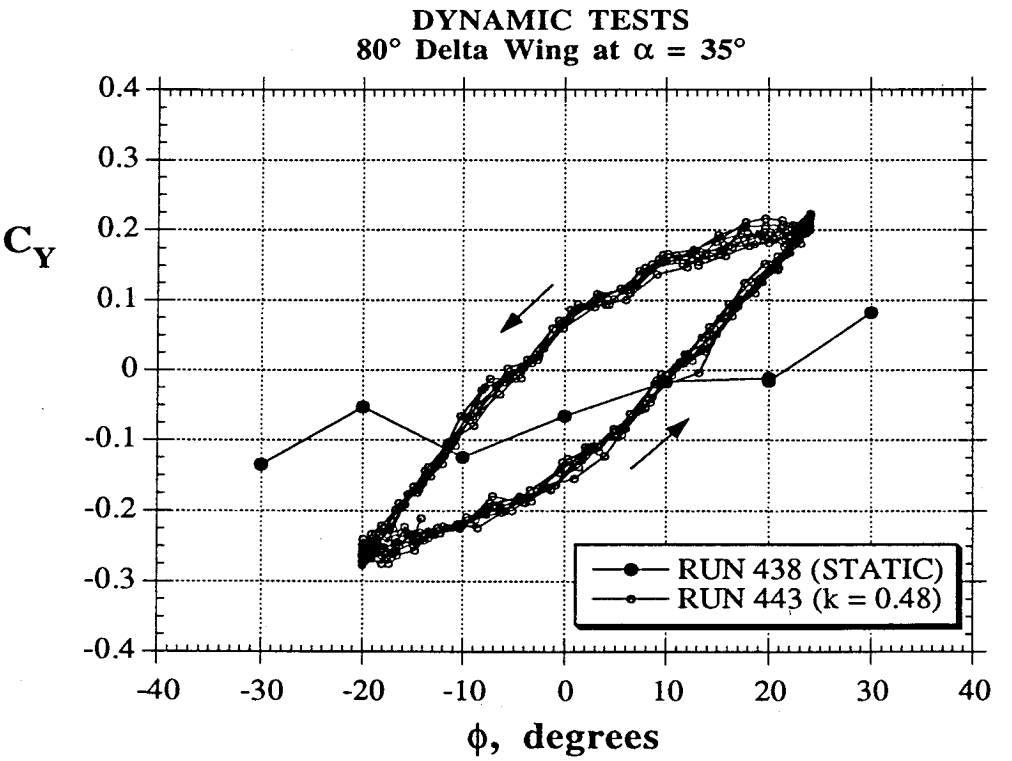

Figure 60 - Normal and Side Force Hysteresis Loops During Roll Oscillations (80° Delta Wing, $\alpha = 35°$, $k = 0.48$)

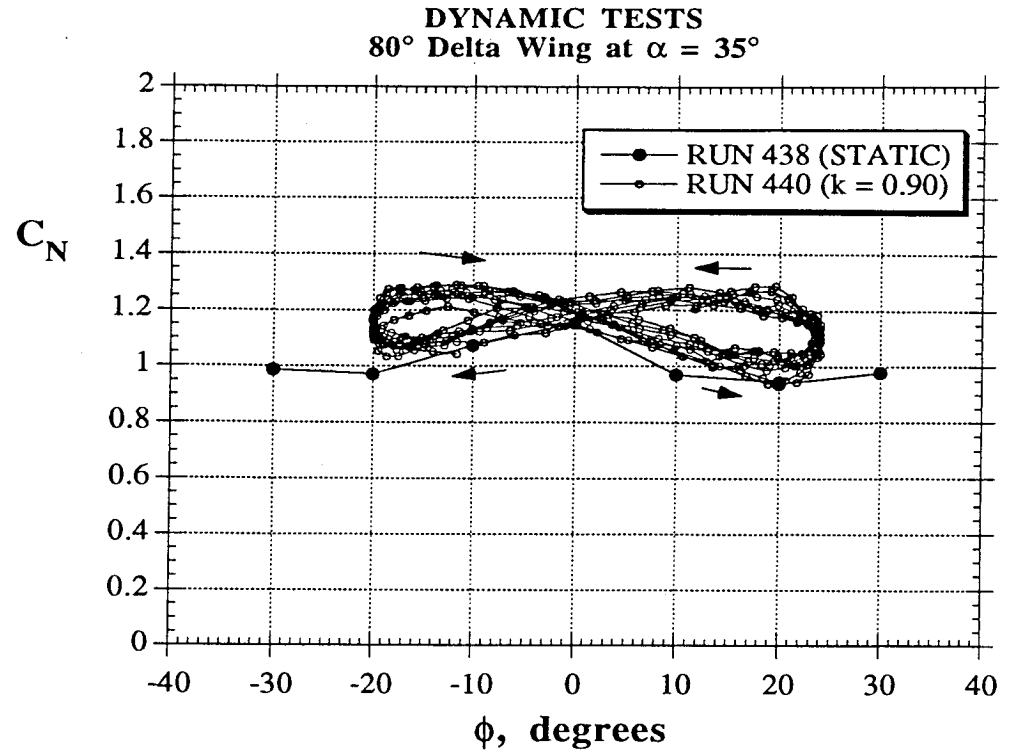

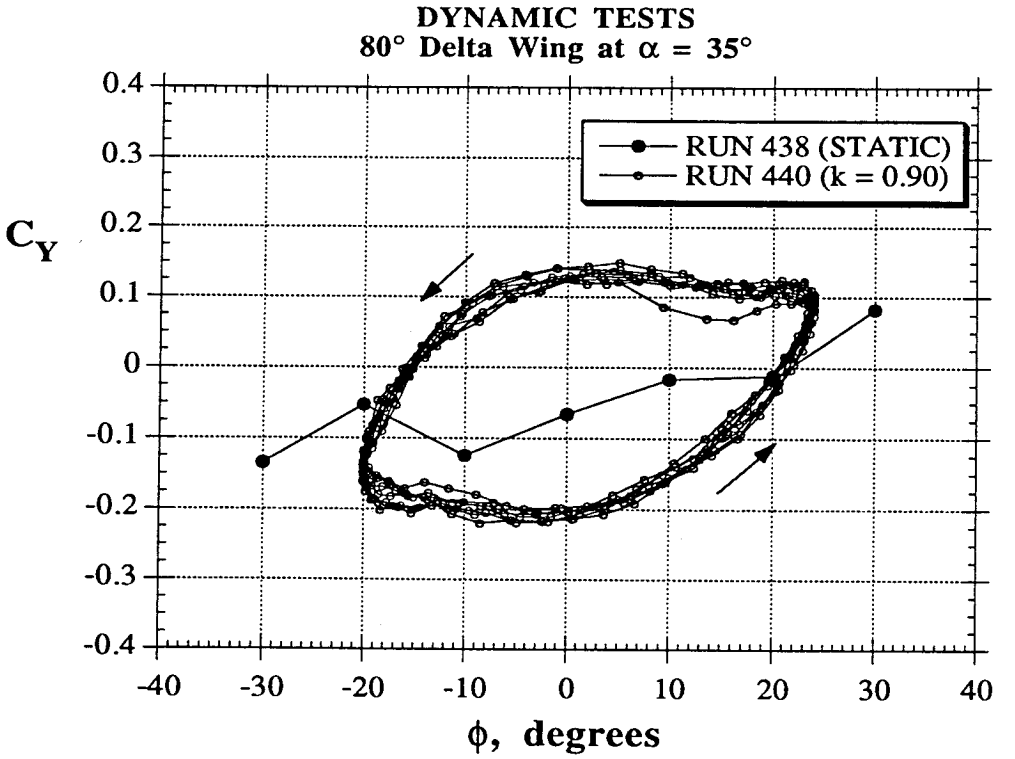

Figure 61 - Normal and Side Force Hysteresis Loops During Roll Oscillations (80° Delta Wing, $\alpha = 35°$, $k = 0.9$)

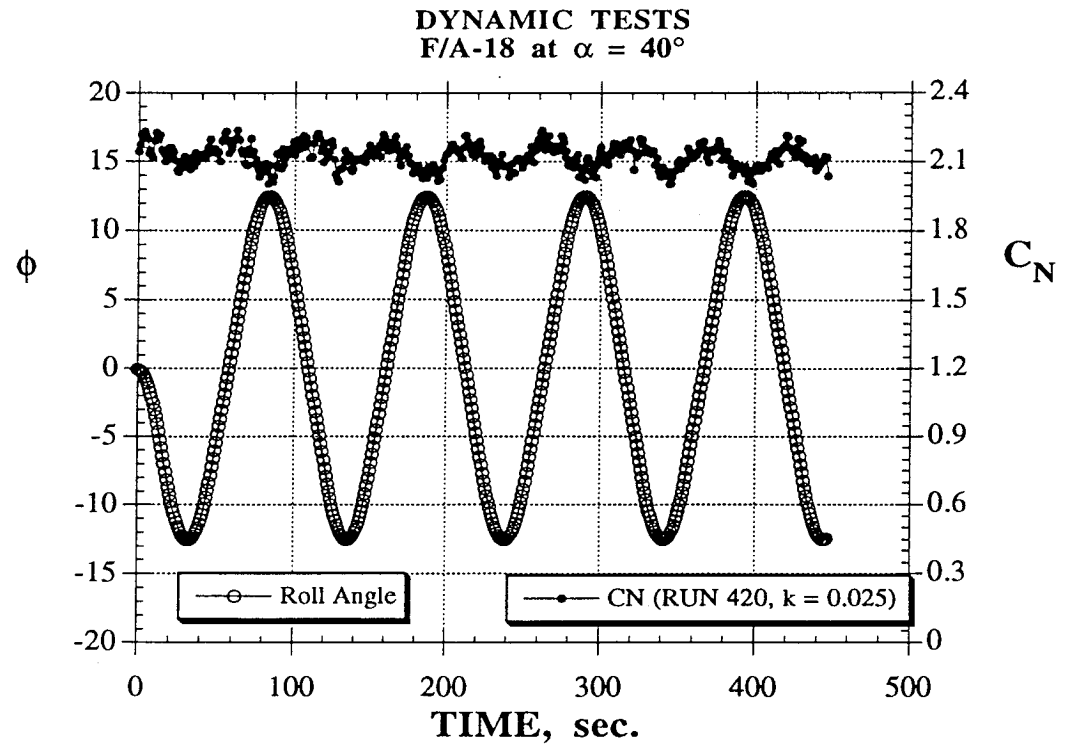

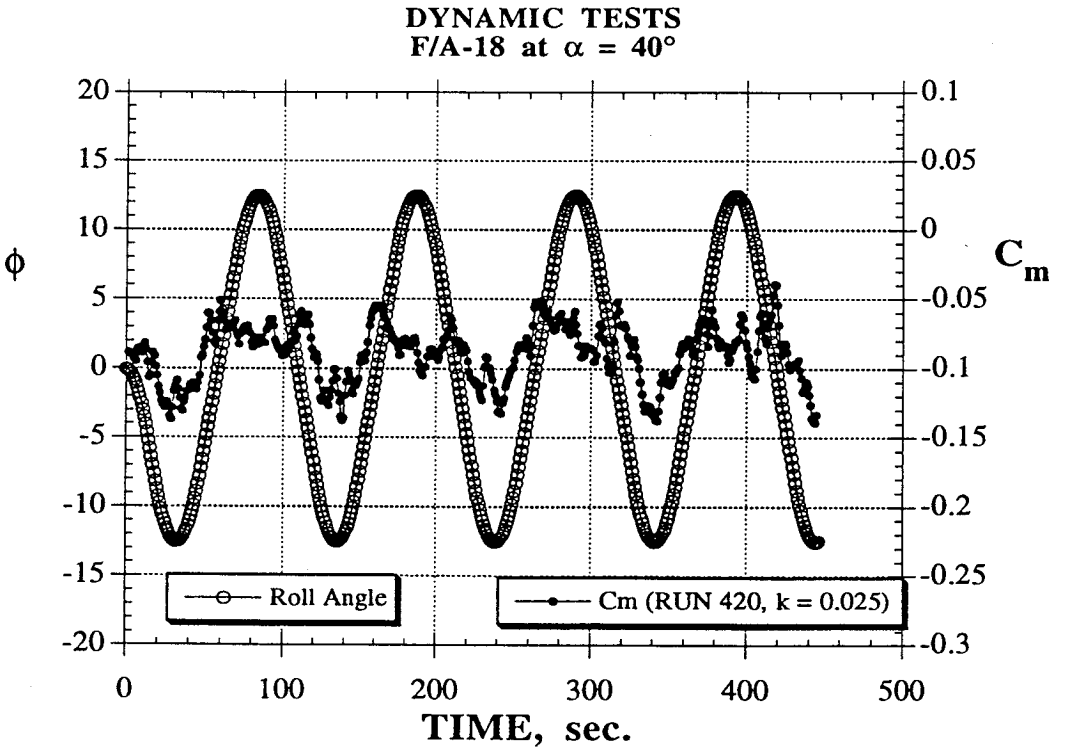

Figure 62 - Roll Angle and Force/Moment Time Histories During Roll Oscillations (F/A-18, $\alpha = 40°$, k = 0.025)

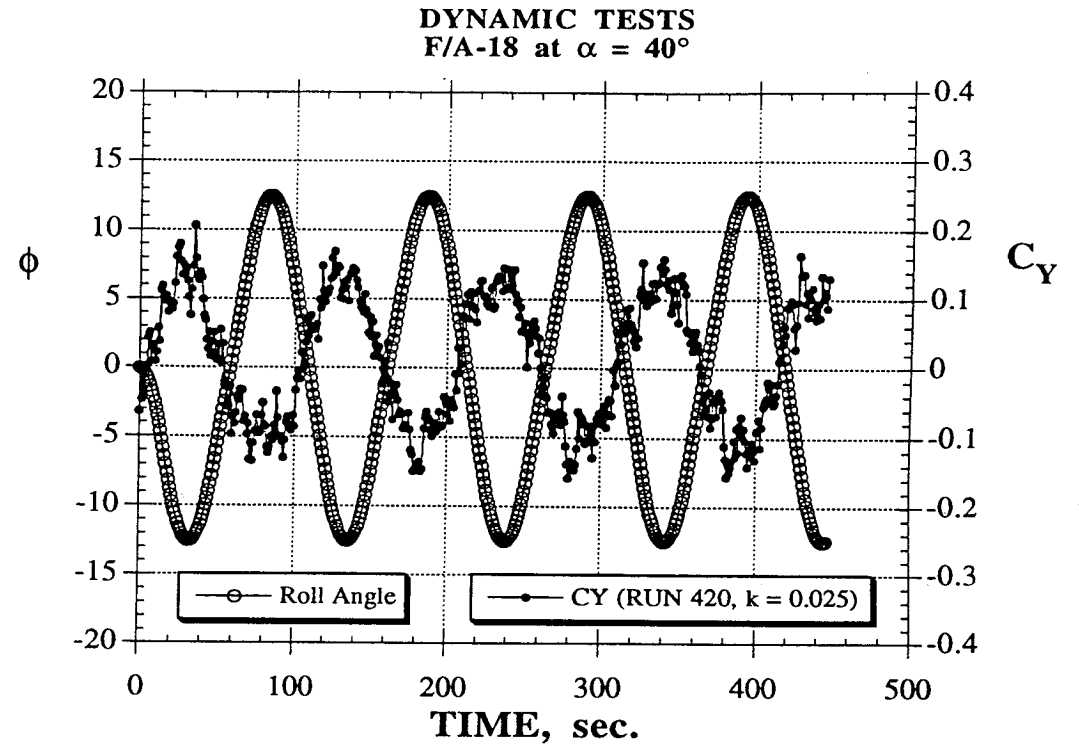

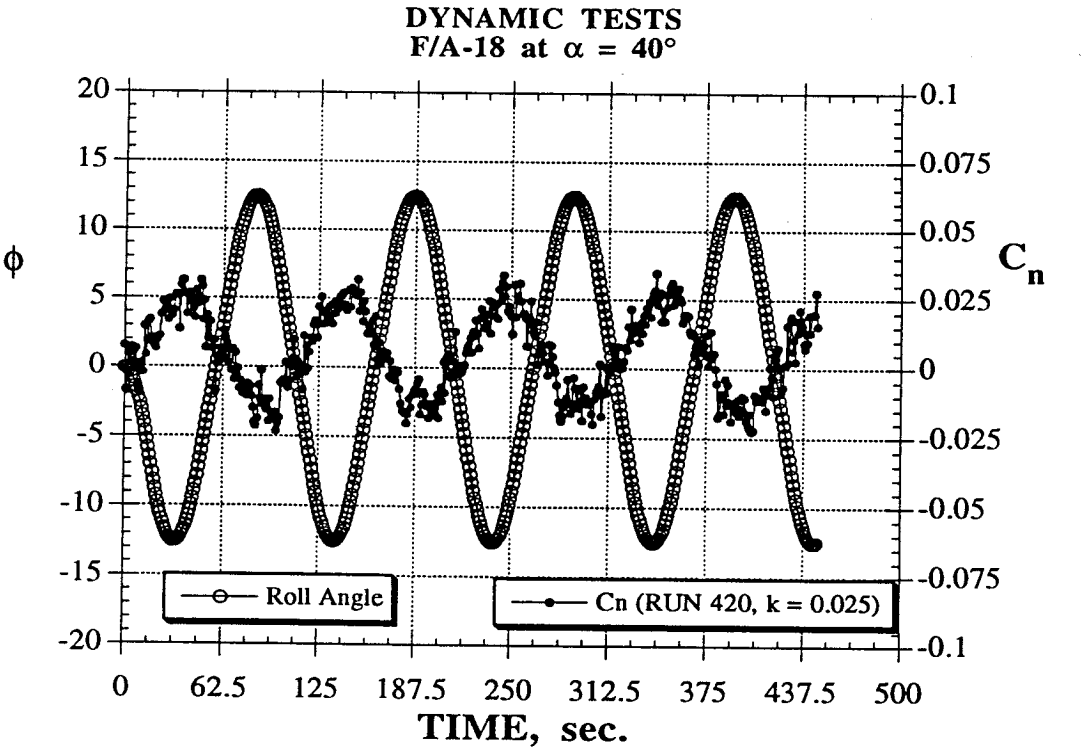

Figure 62 - Continued

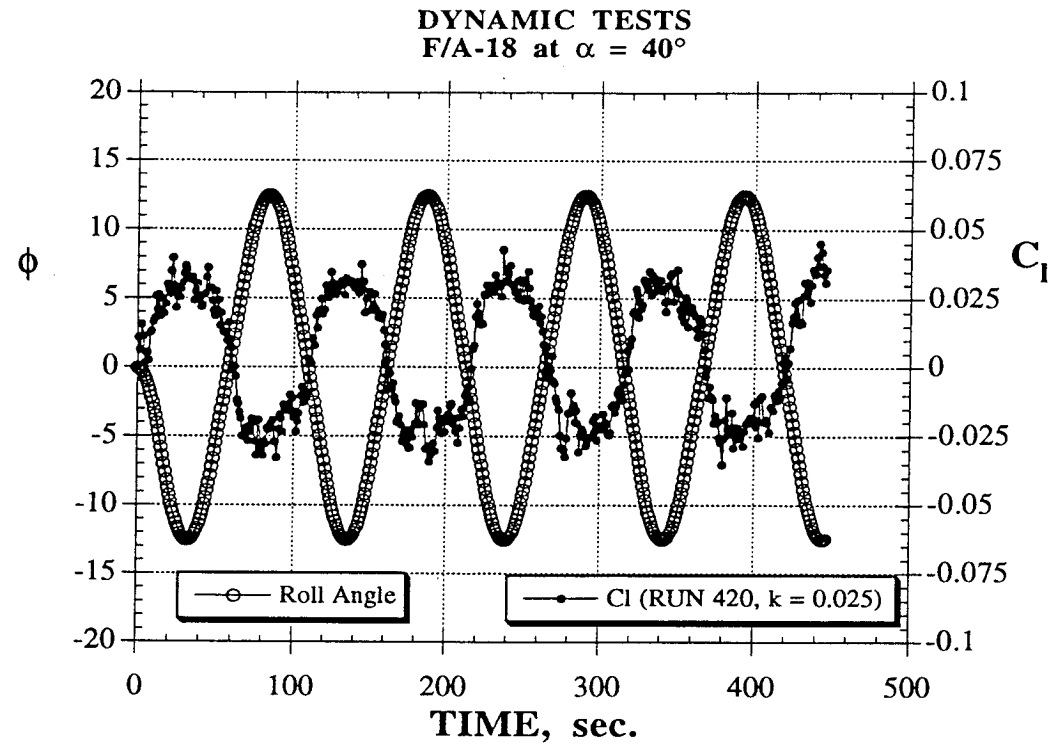

Figure 62 - Concluded

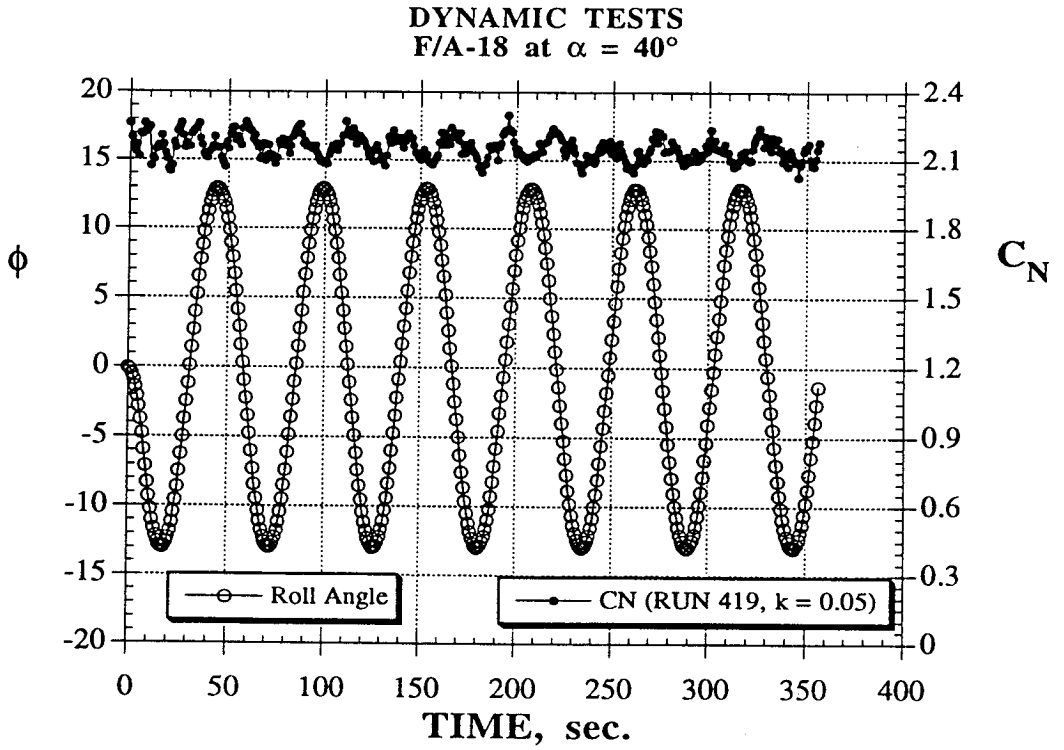

Figure 63 - Roll Angle and Force/Moment Time Histories During Roll Oscillations (F/A-18, $\alpha = 40°$, k = 0.050)

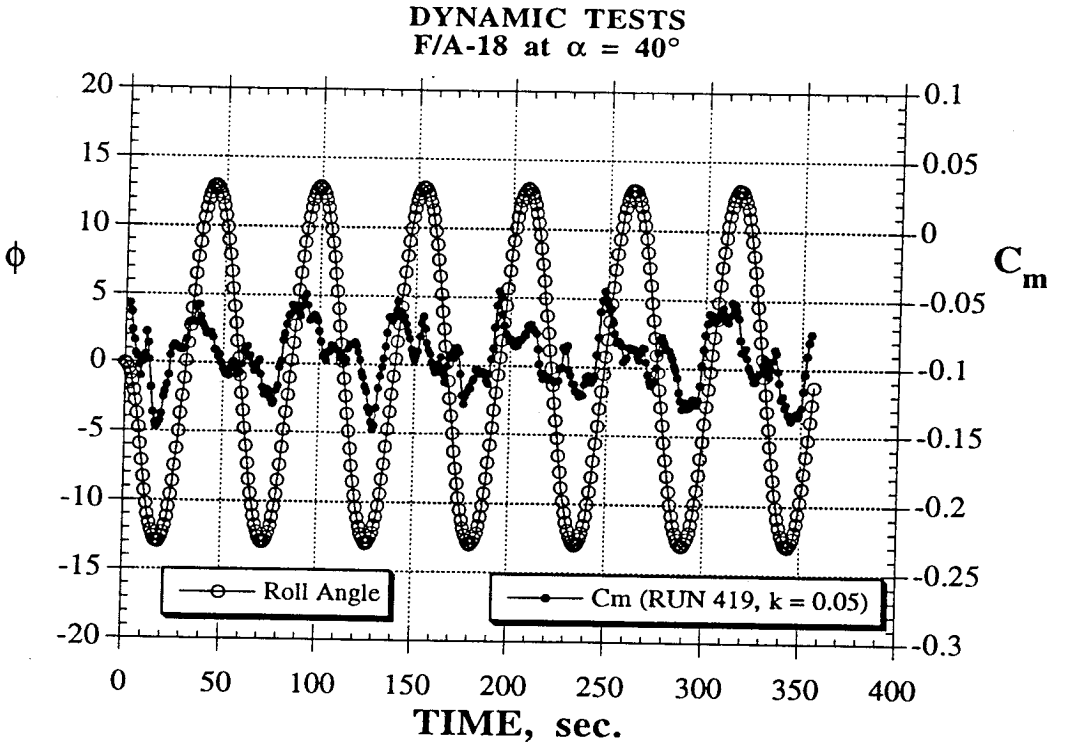

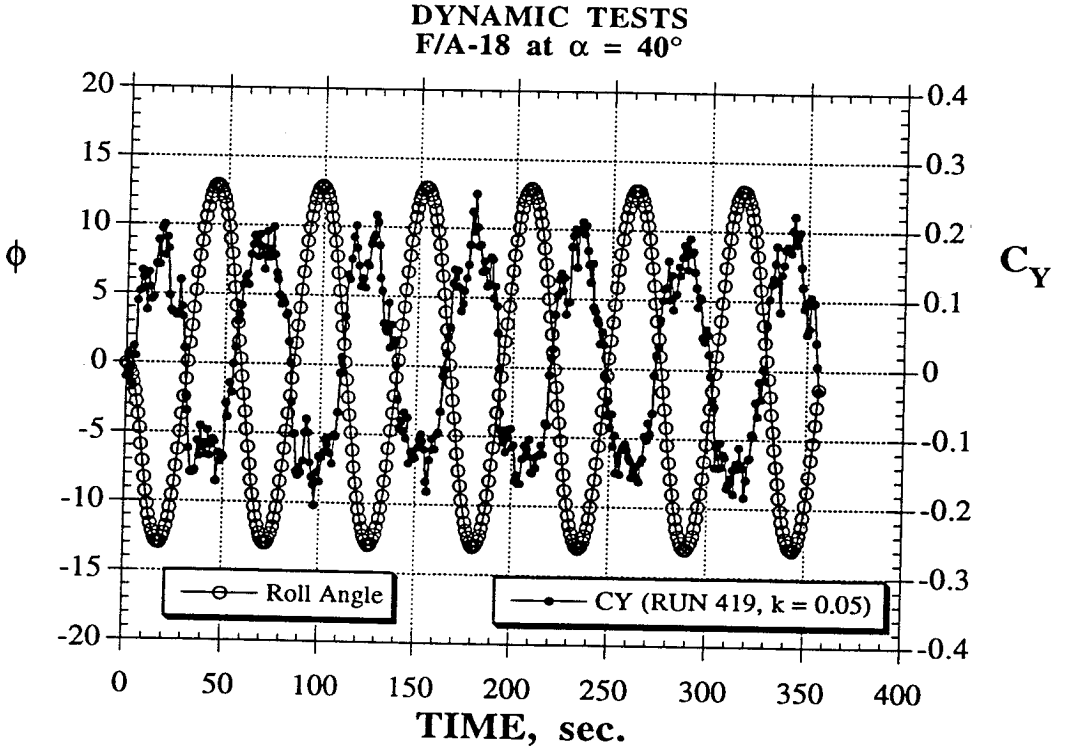

Figure 63 - Continued

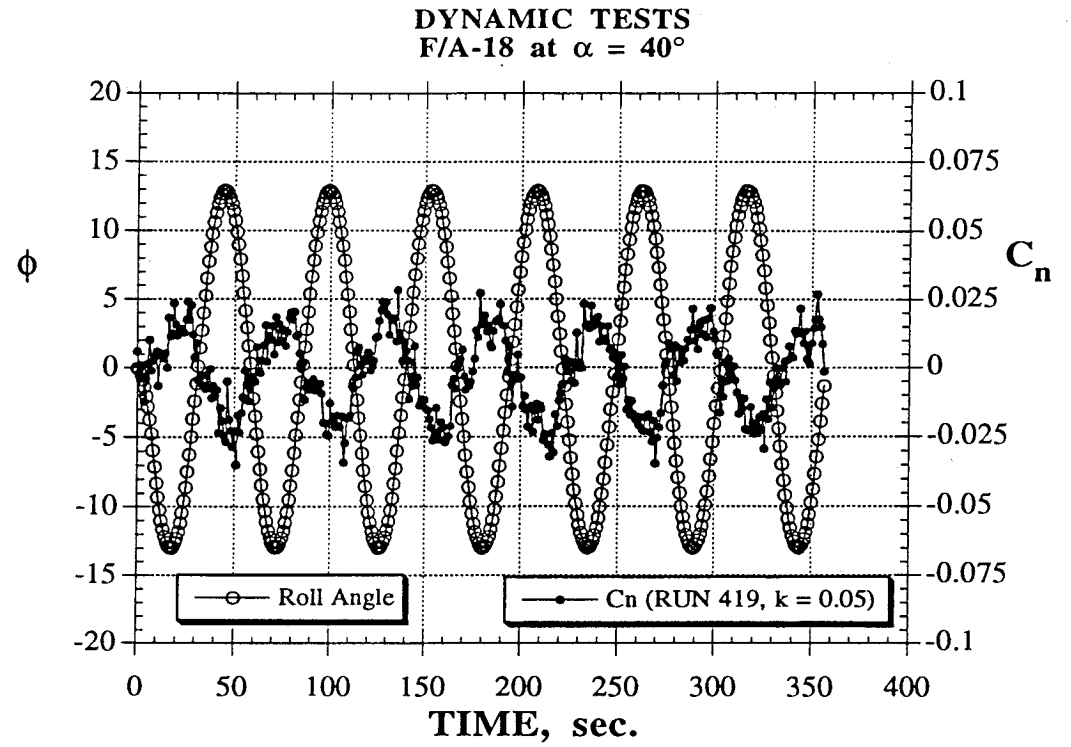

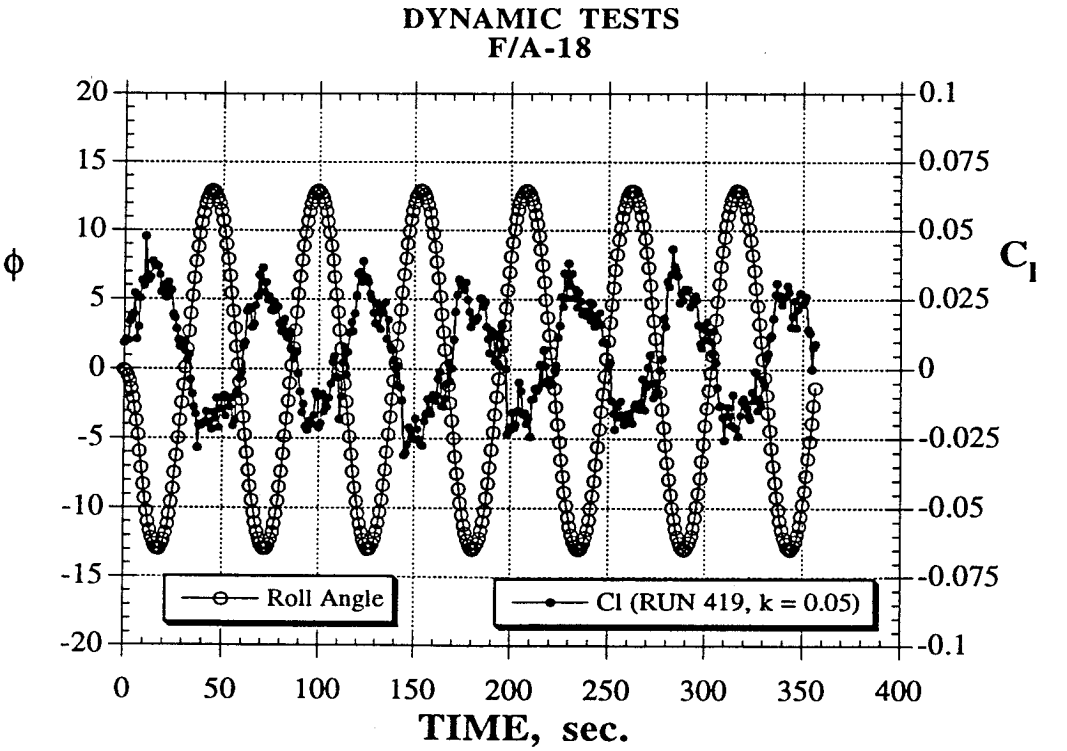

Figure 63 - Concluded

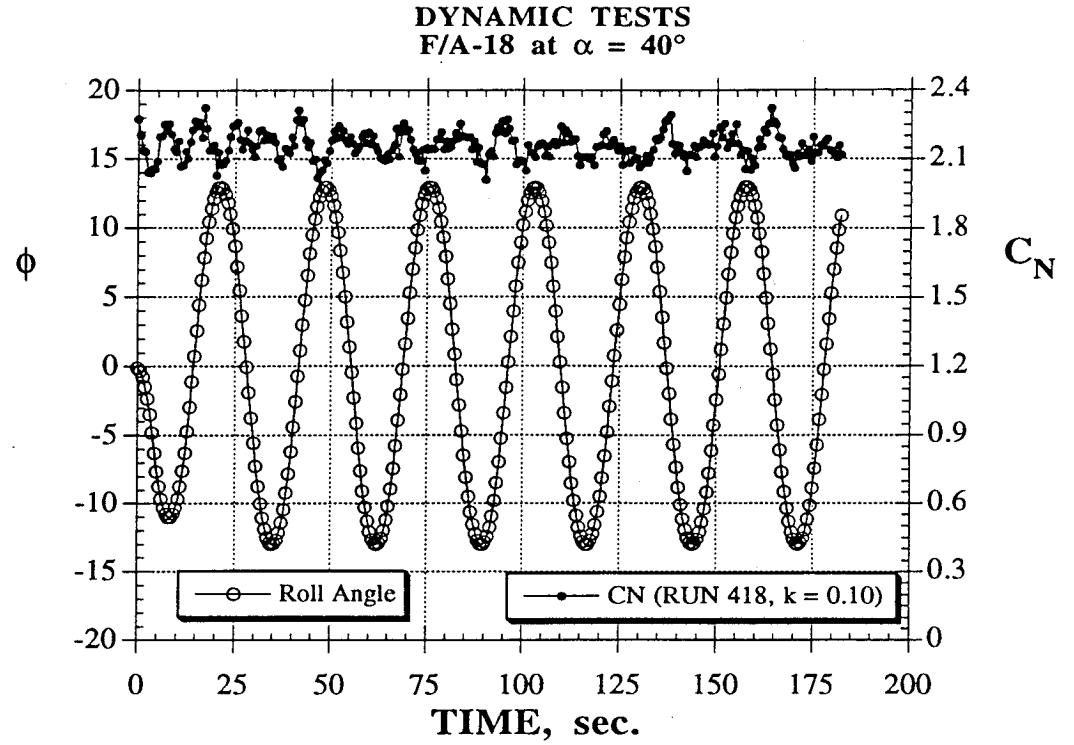

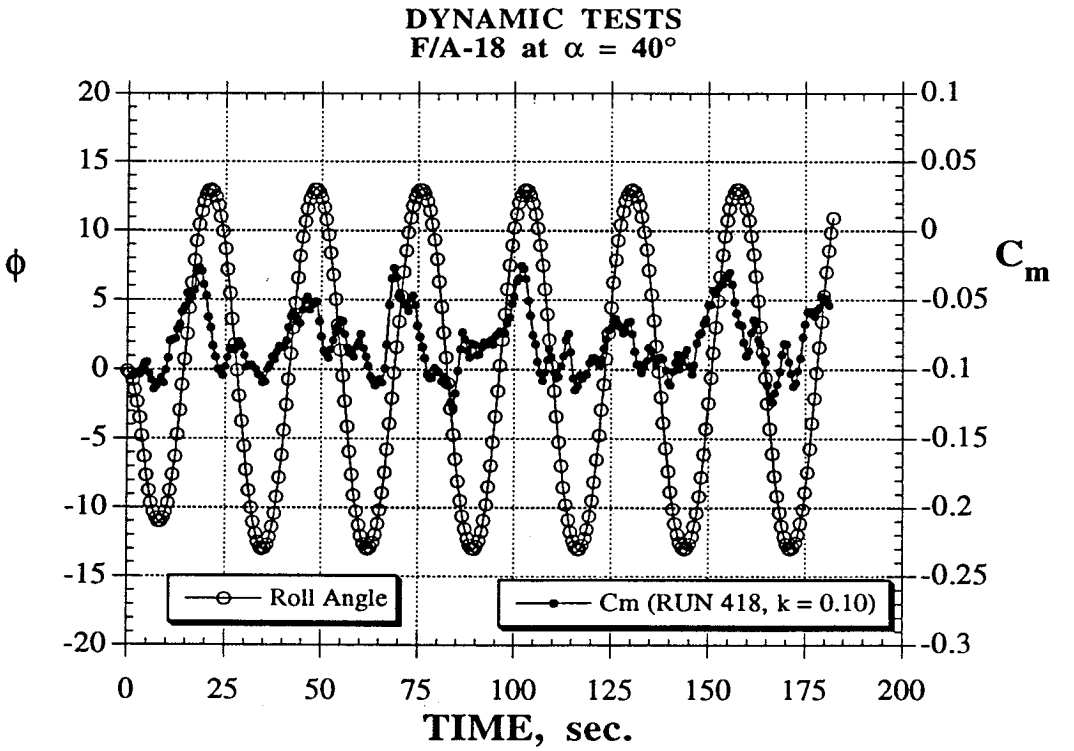

Figure 64 - Roll Angle and Force/Moment Time Histories During Roll Oscillations (F/A-18, $\alpha = 40°$, k = 0.10)

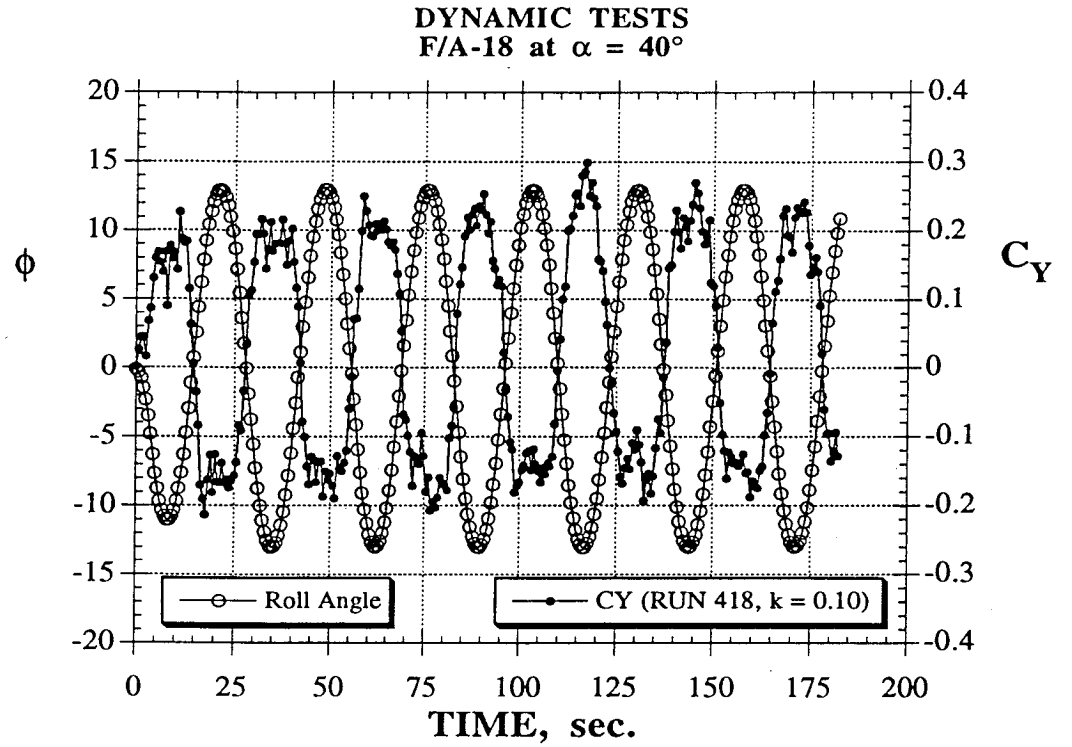

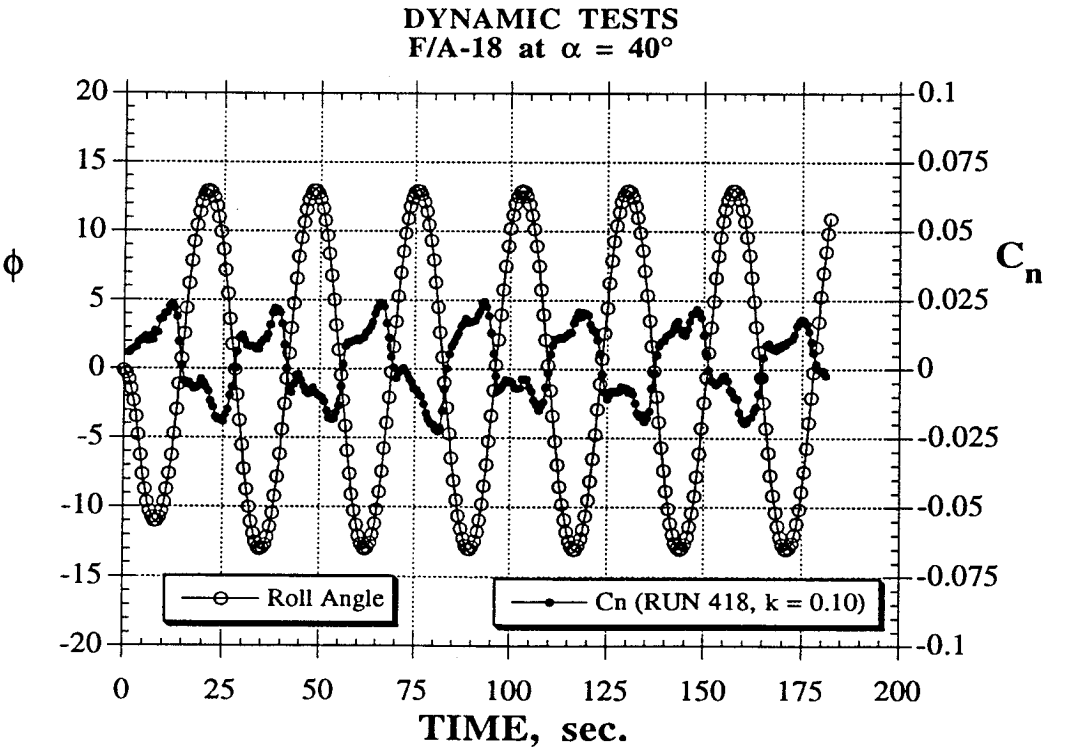

Figure 64 - Continued

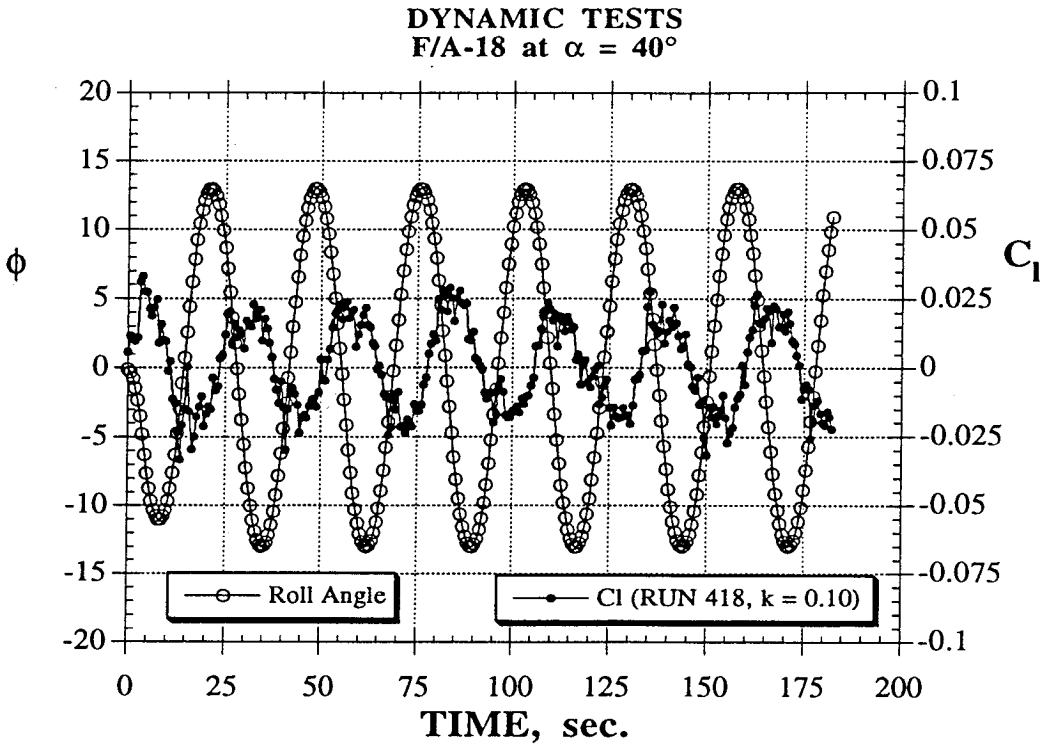

Figure 64 - Concluded

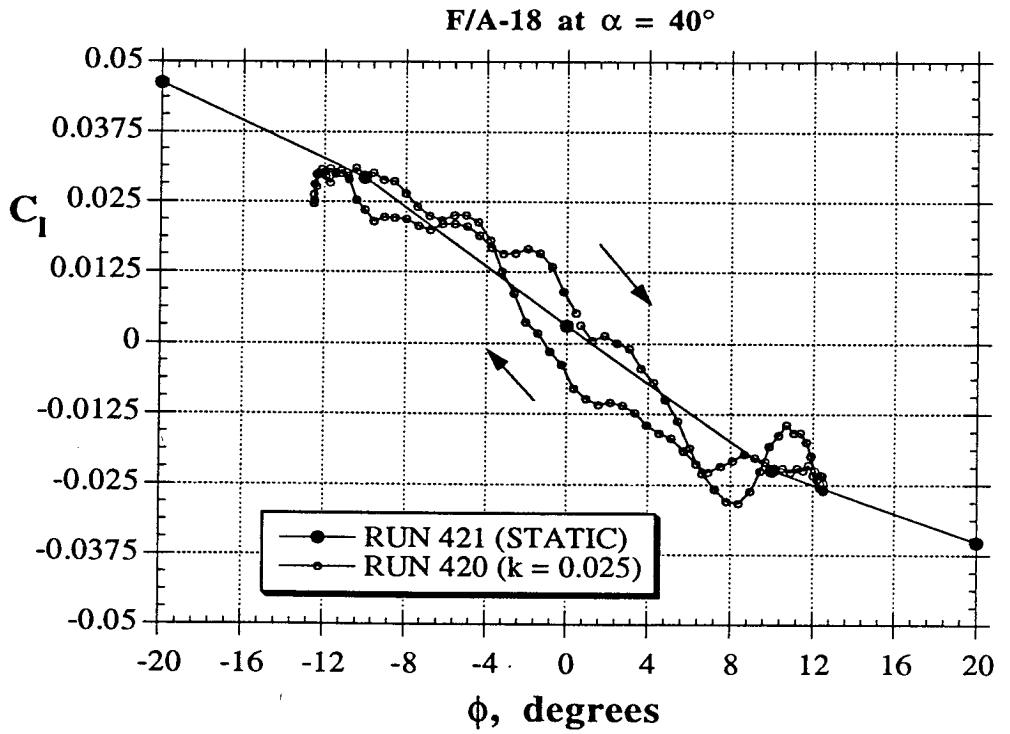

a) k = 0.025

Figure 65 - Rolling Moment Hysteresis Loops During Roll Oscillations (F/A-18, α = 40°)

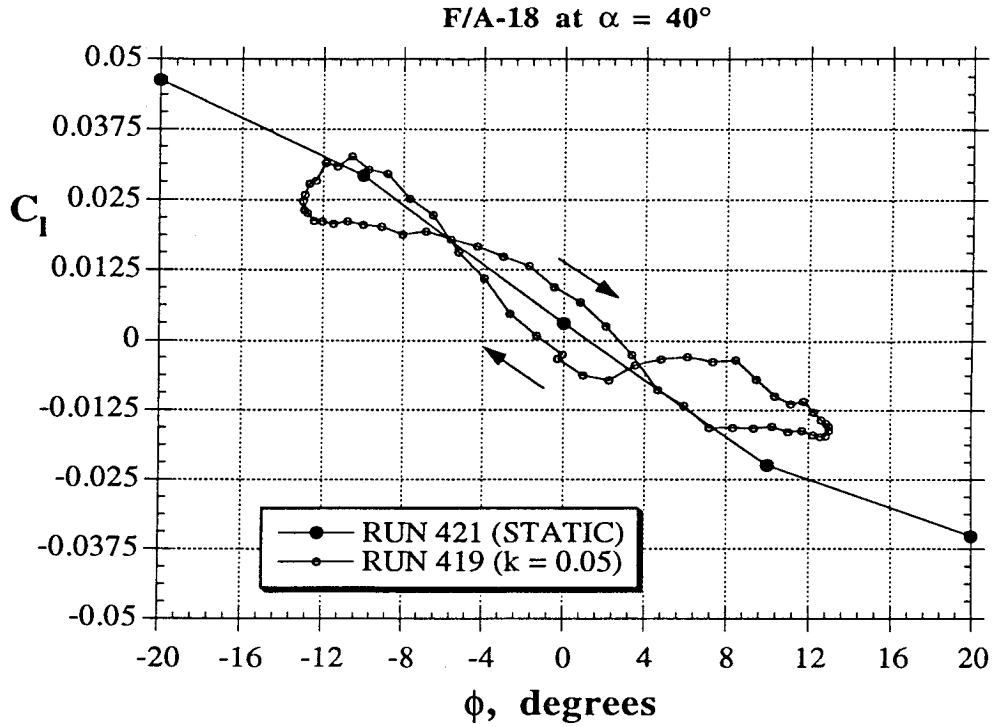

b) k = 0.050

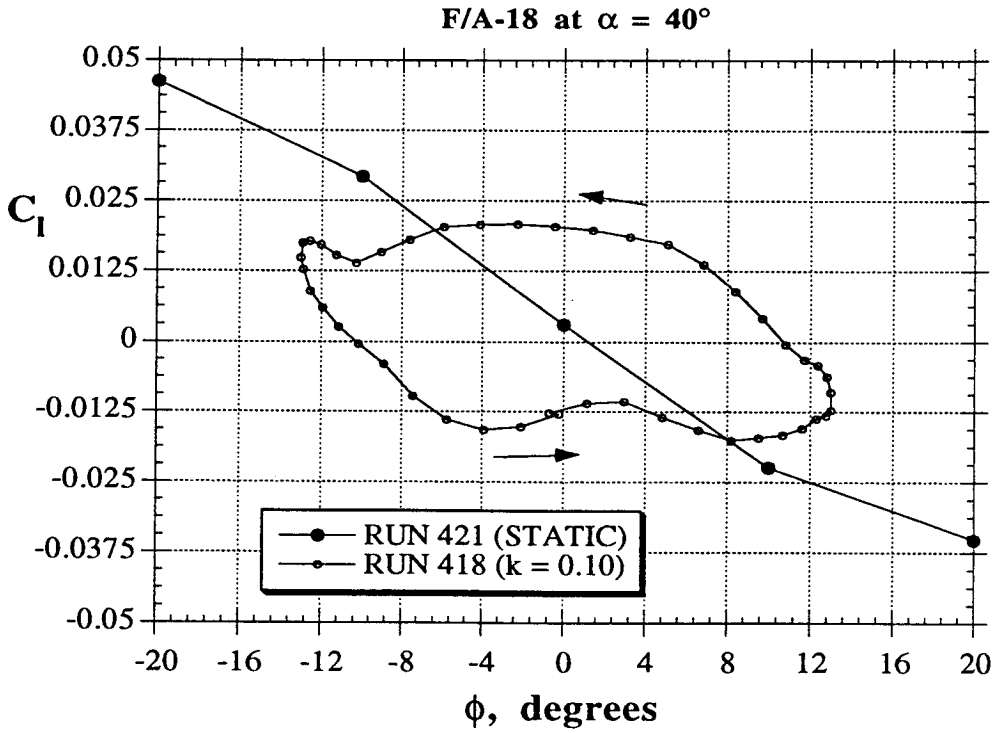

c) k = 0.1

Figure 65 - Concluded

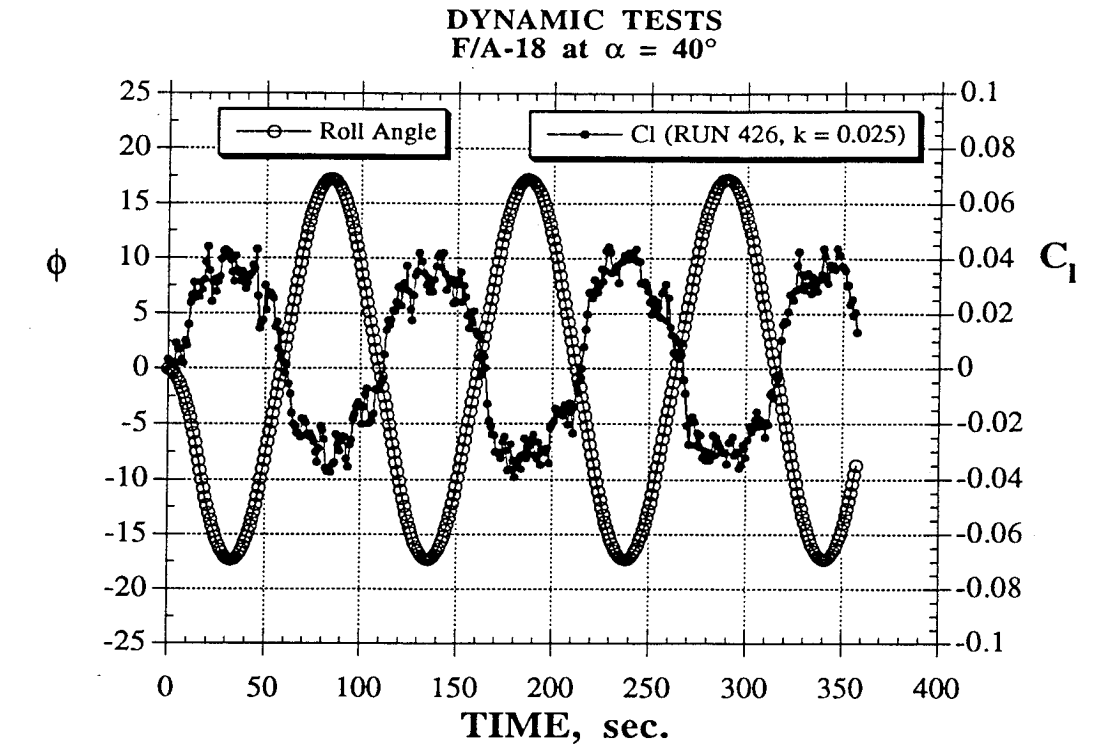

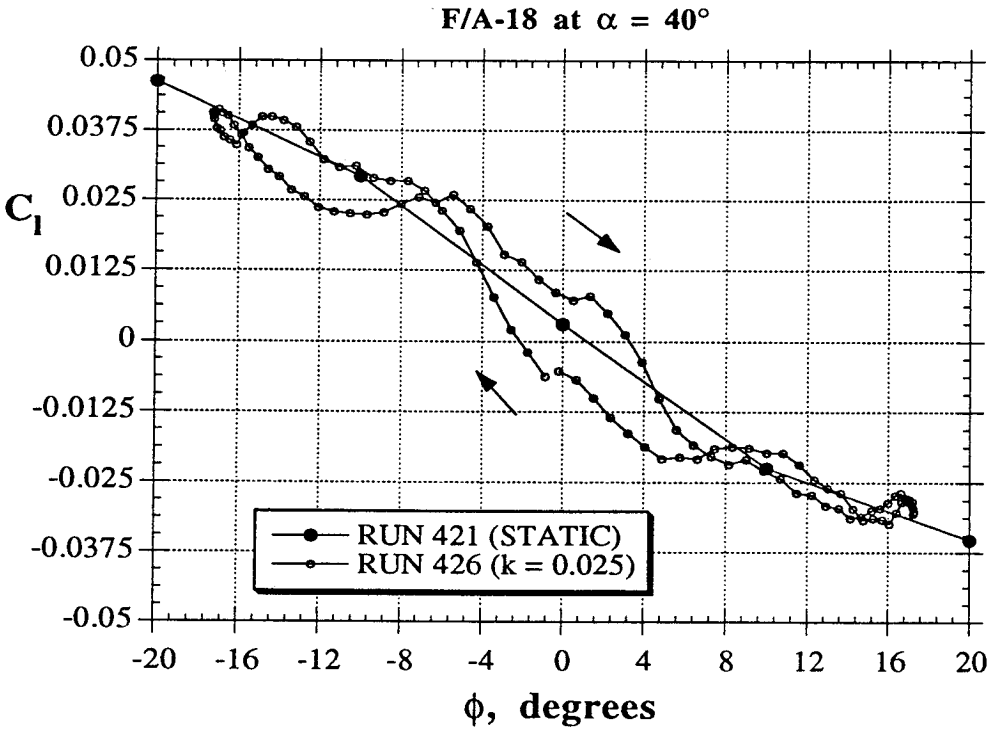

Figure 66 - Rolling Moment Variations During Roll Oscillations (F/A-18, α = 40°, k = 0.025)

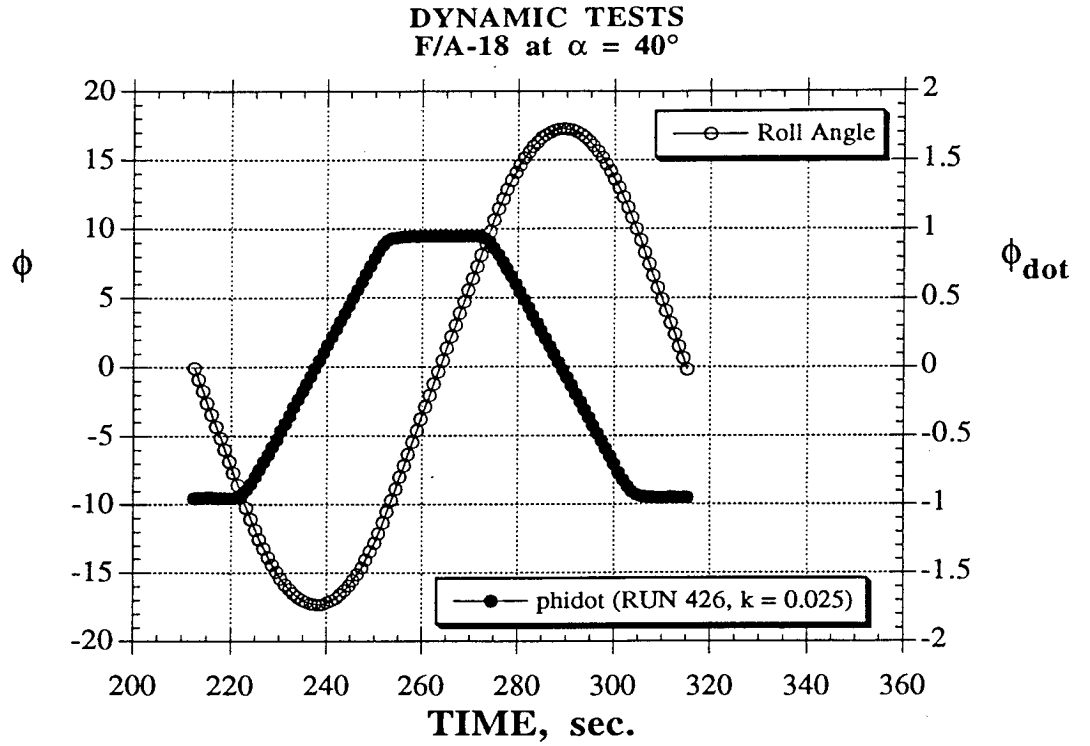

a) Angular Velocity Time History

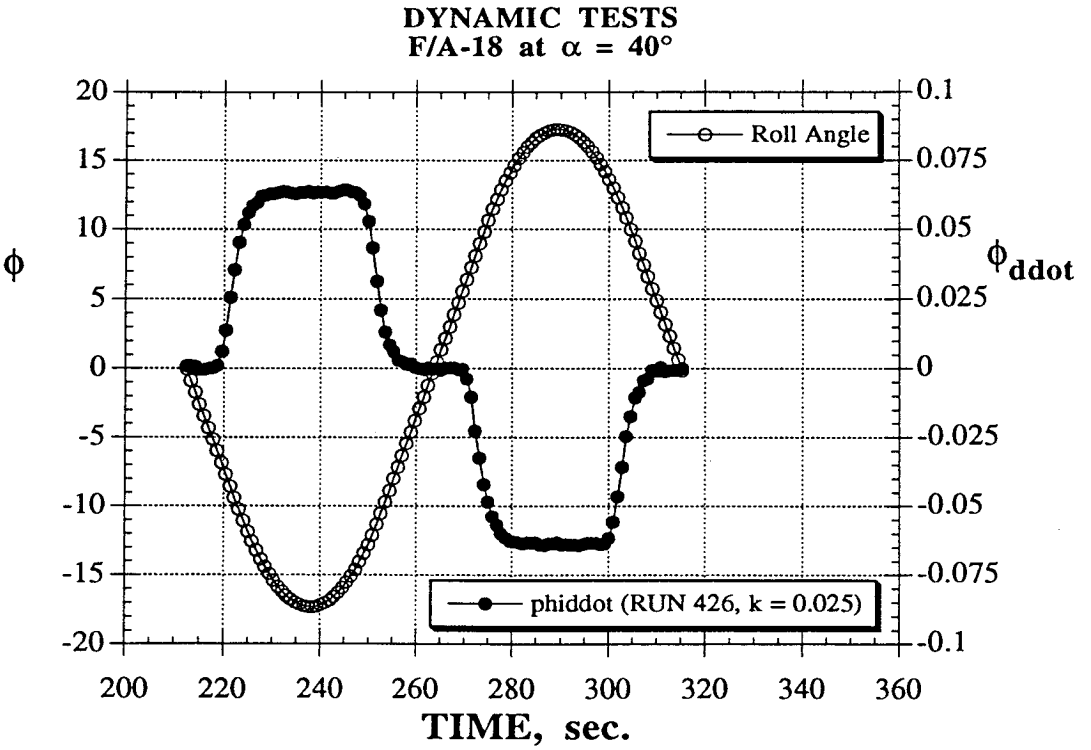

b) Angular Acceleration Time History

Figure 67 - Roll Angle, Angular Velocity and Angular Acceleration Variations During Roll Oscillations (F/A-18, $\alpha = 40°$, $k = 0.025$)

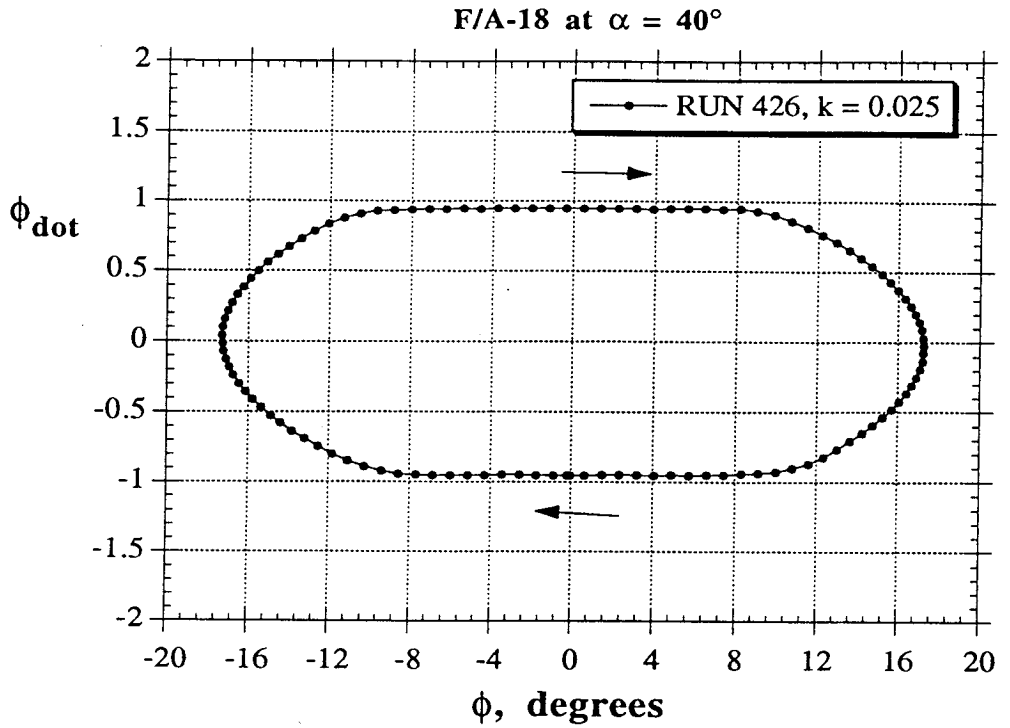

c) Phase Plot (Angular Velocity)

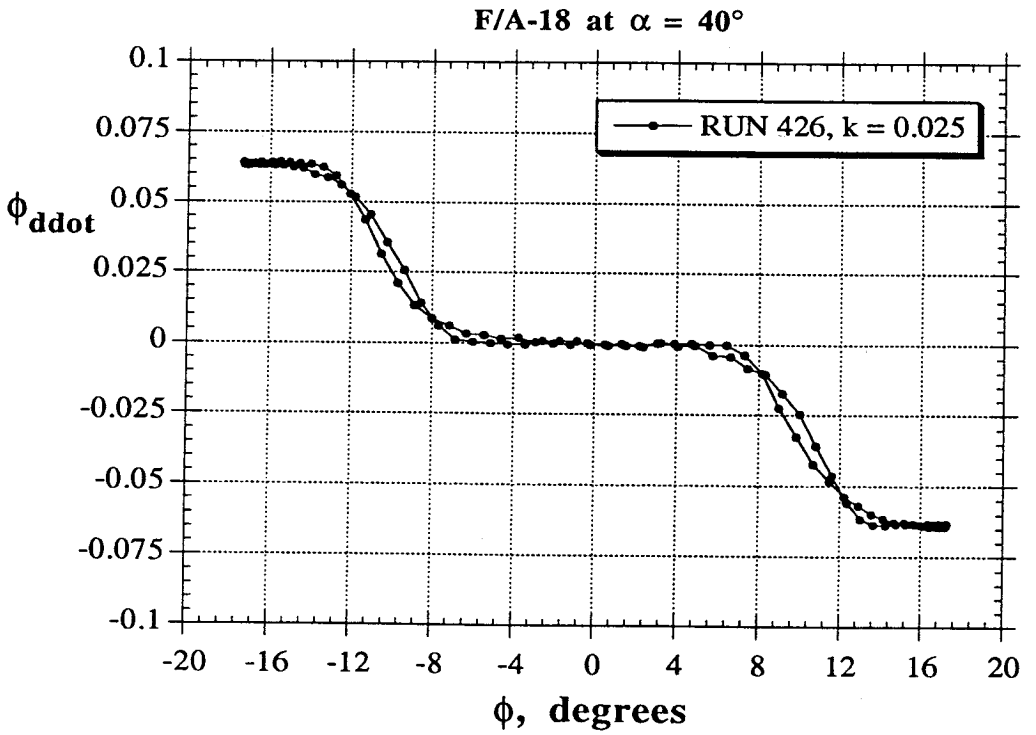

d) Phase Plot (Angular Acceleration)

Figure 67 - Concluded

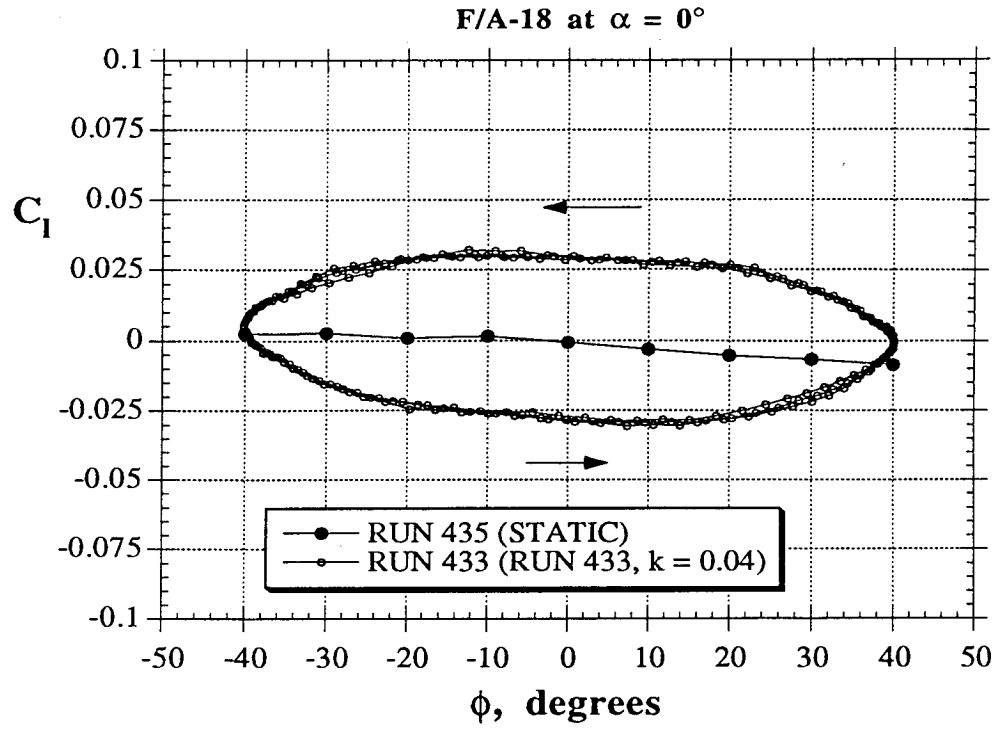

a) α = 0°

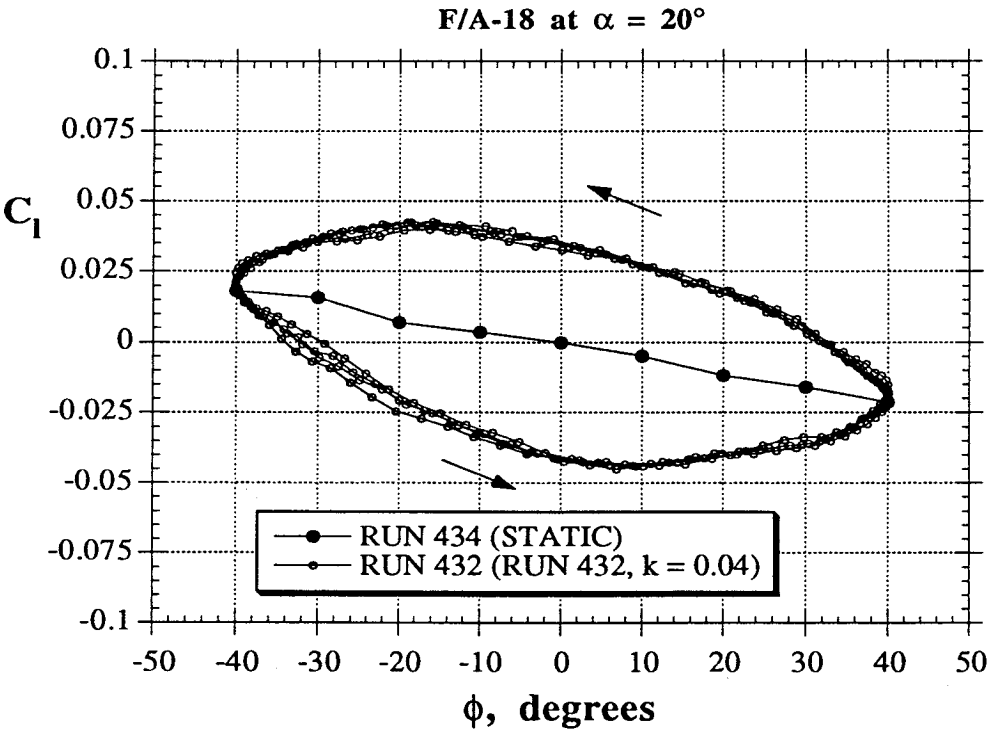

b) α = 20°

Figure 68 - Rolling Moment Variations During Large Amplitude Roll Oscillations at Different Angles of Attack (F/A-18, k = 0.040)

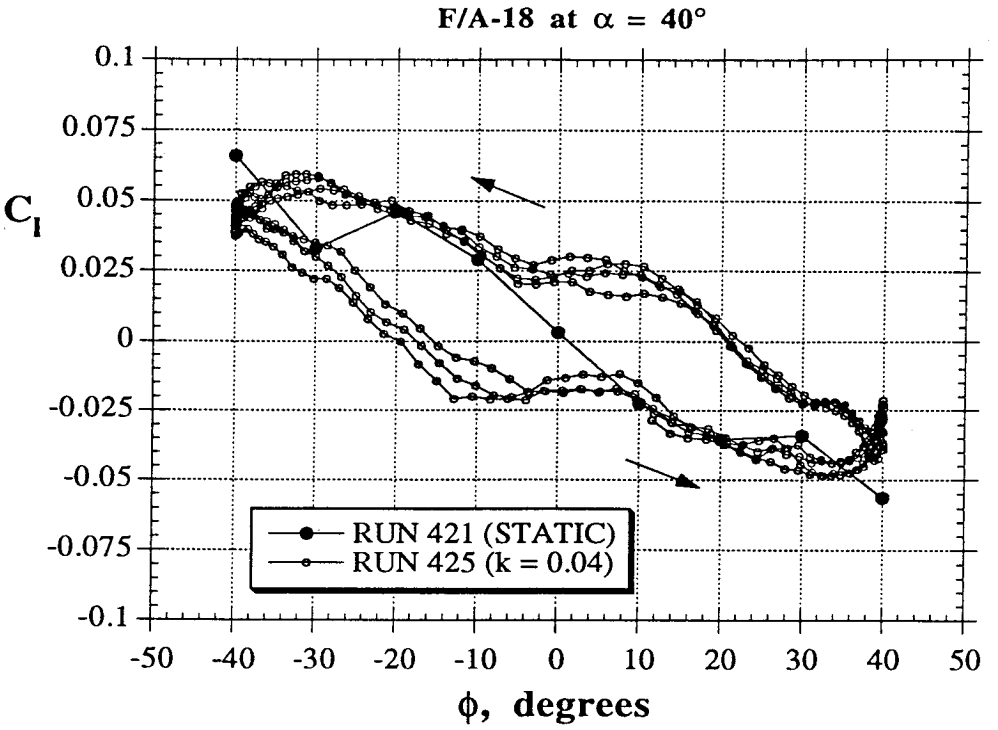

c) α = 40°

Figure 68 - Concluded

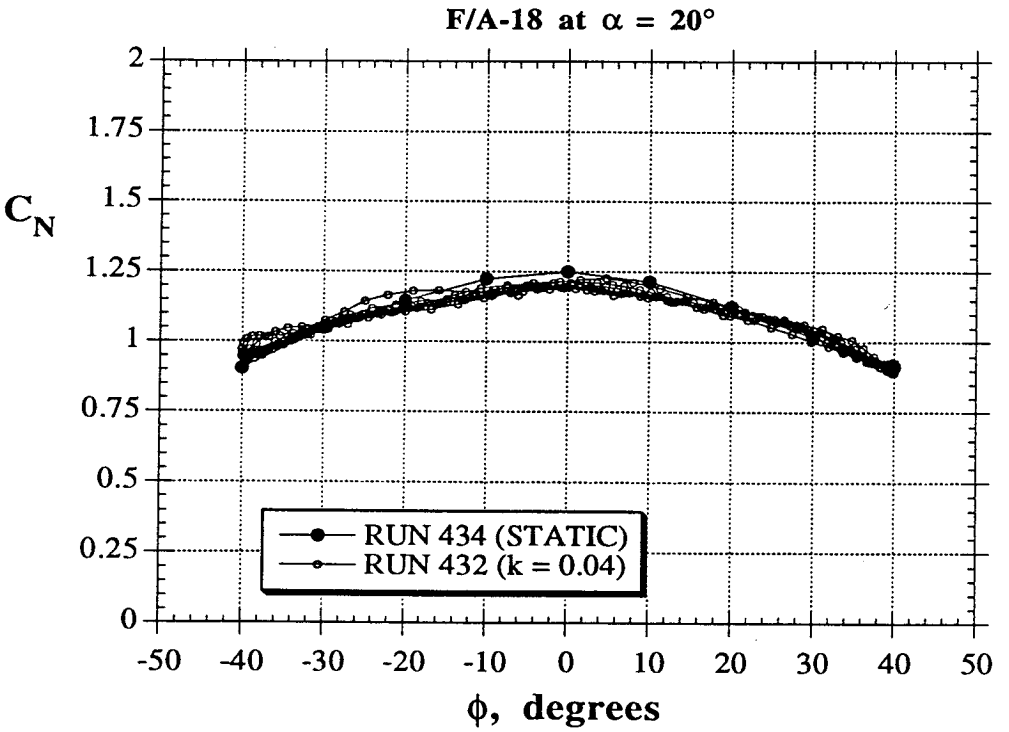

Figure 69 - Hysteresis Loops During Large Amplitude Roll Oscillations (F/A-18, α = 20°, k = 0.040)

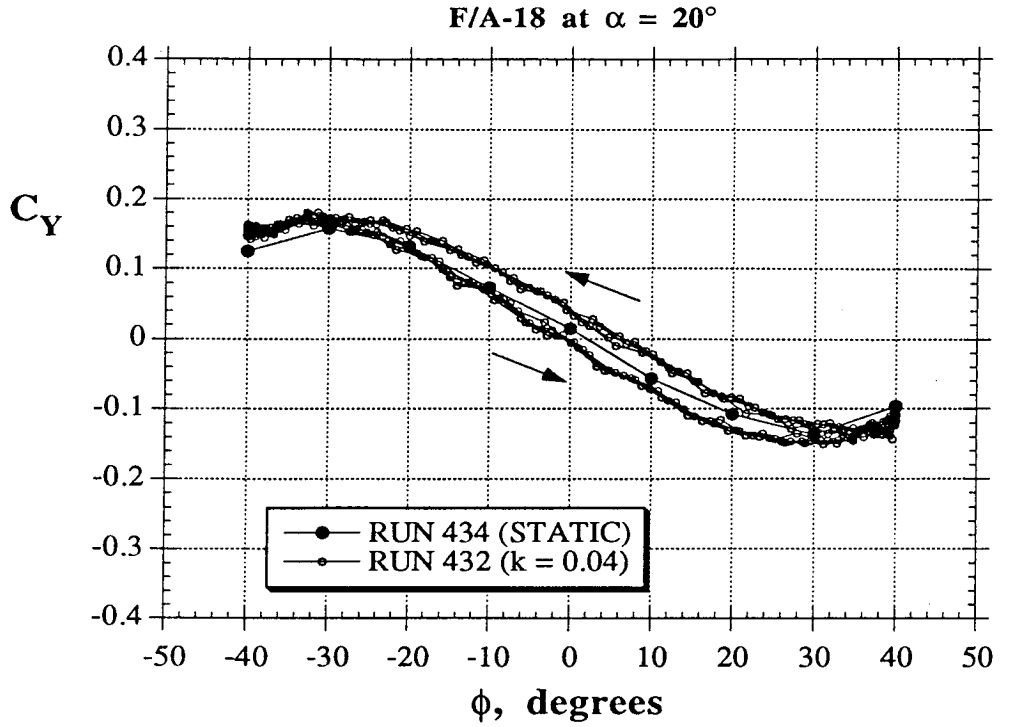

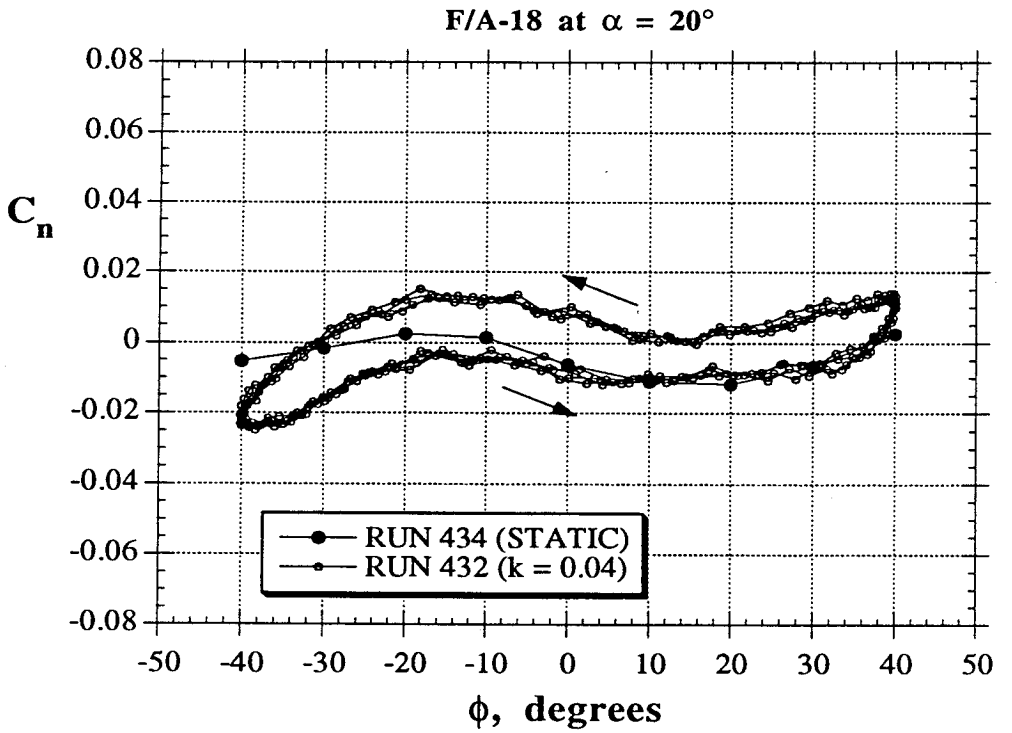

Figure 69 - Concluded

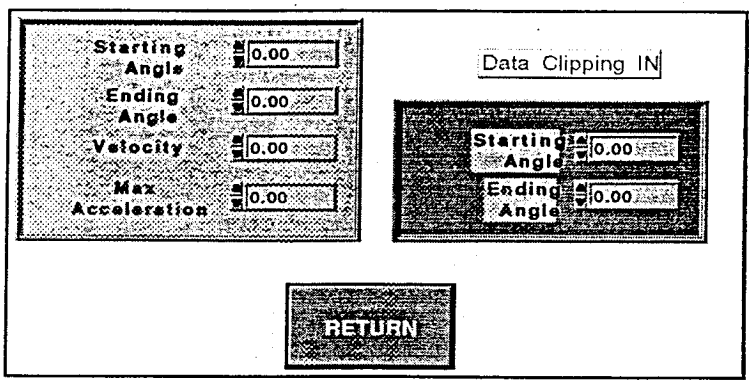

a) Motion Definition and Data Clipping

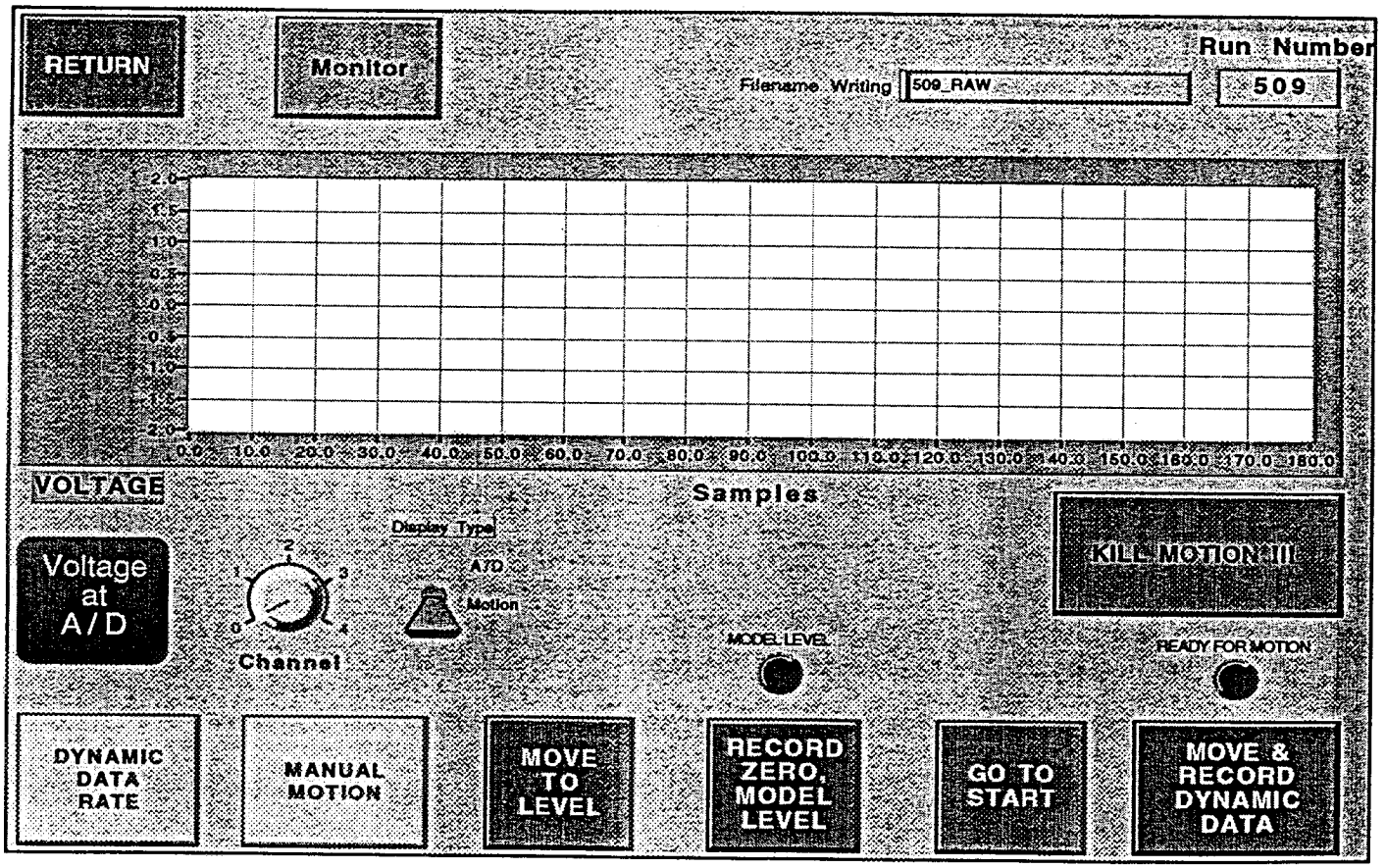

b) "Create New Rotary Tare" Front Panel

Figure 70 - Software Front Panels Used During Rotary-Balance Tests

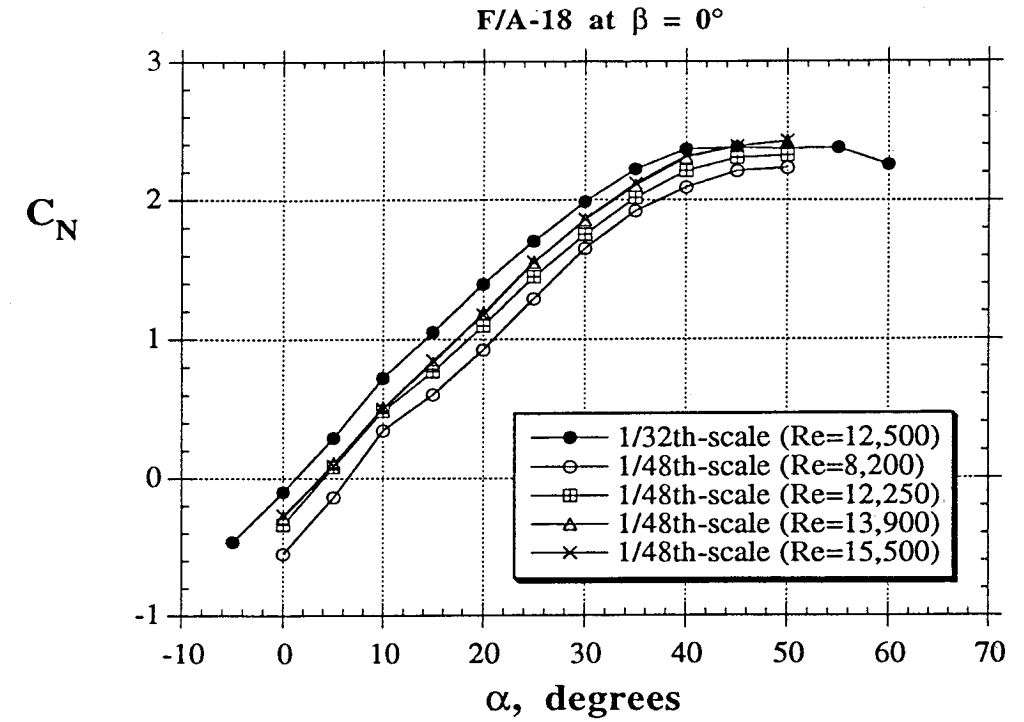

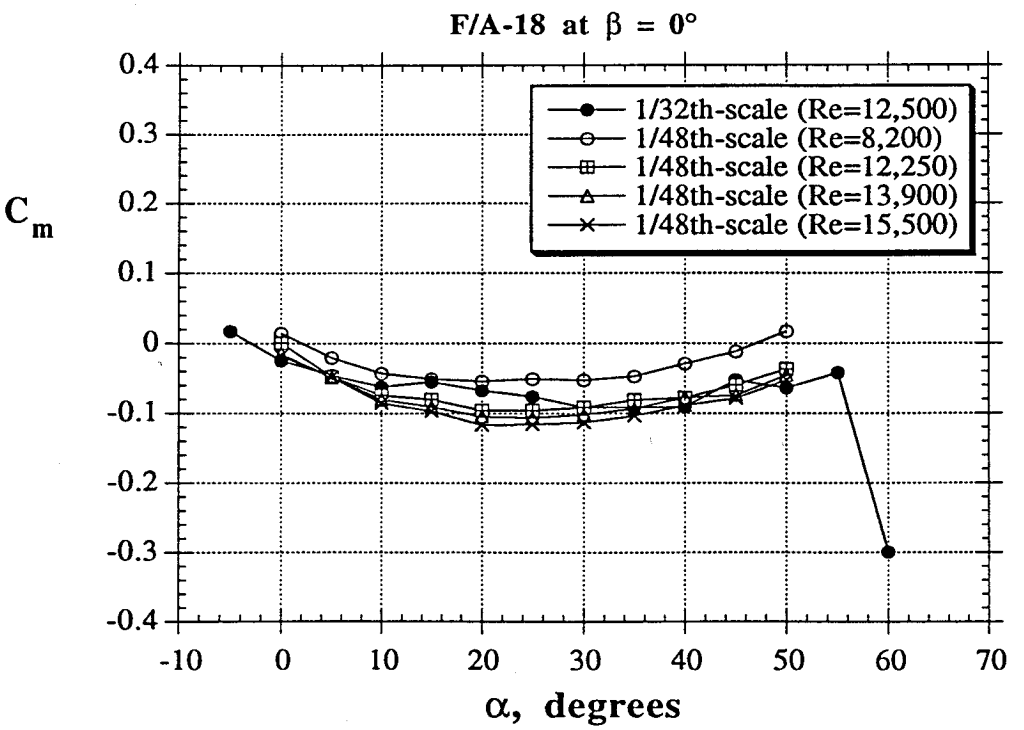

Figure 71 - Results of Static Experiments on the 1/48th-Scale F/A-18 Model

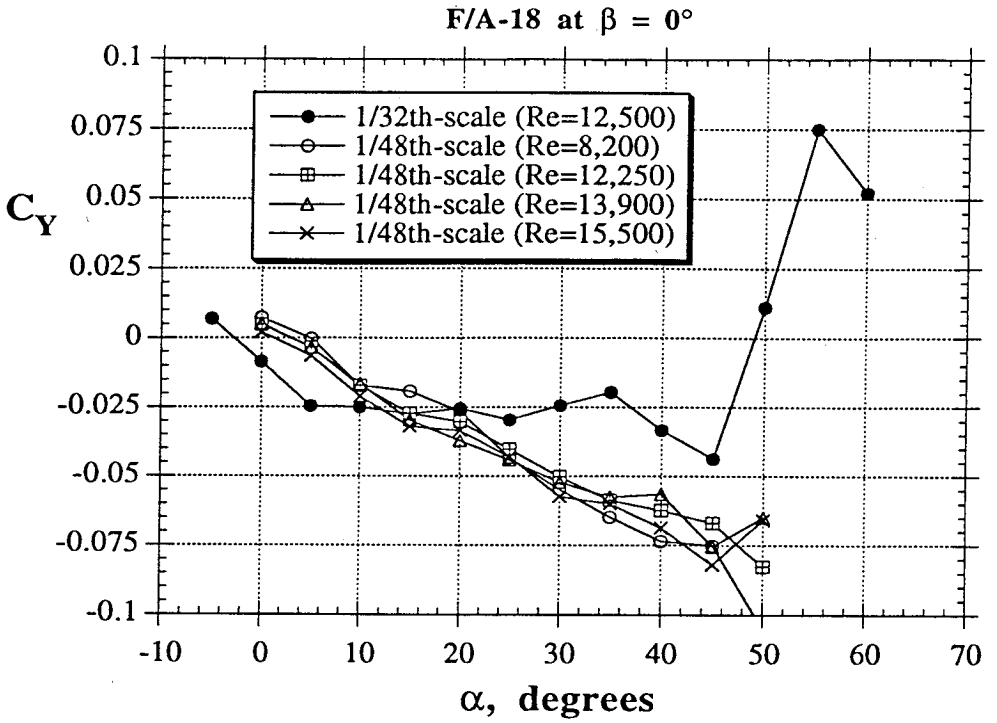

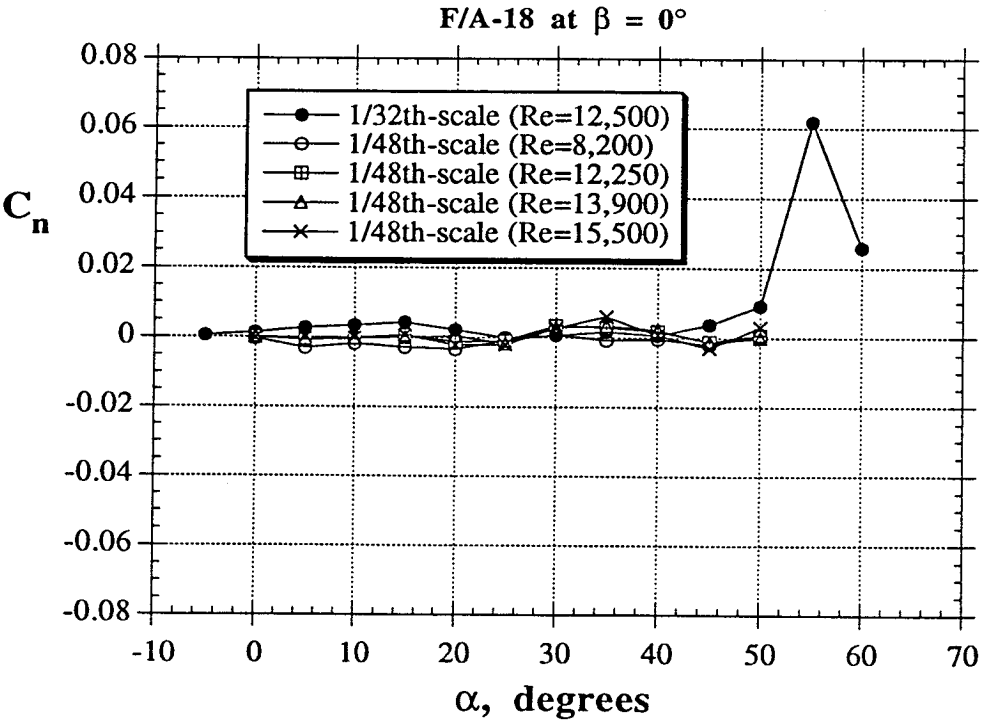

Figure 71 - Continued

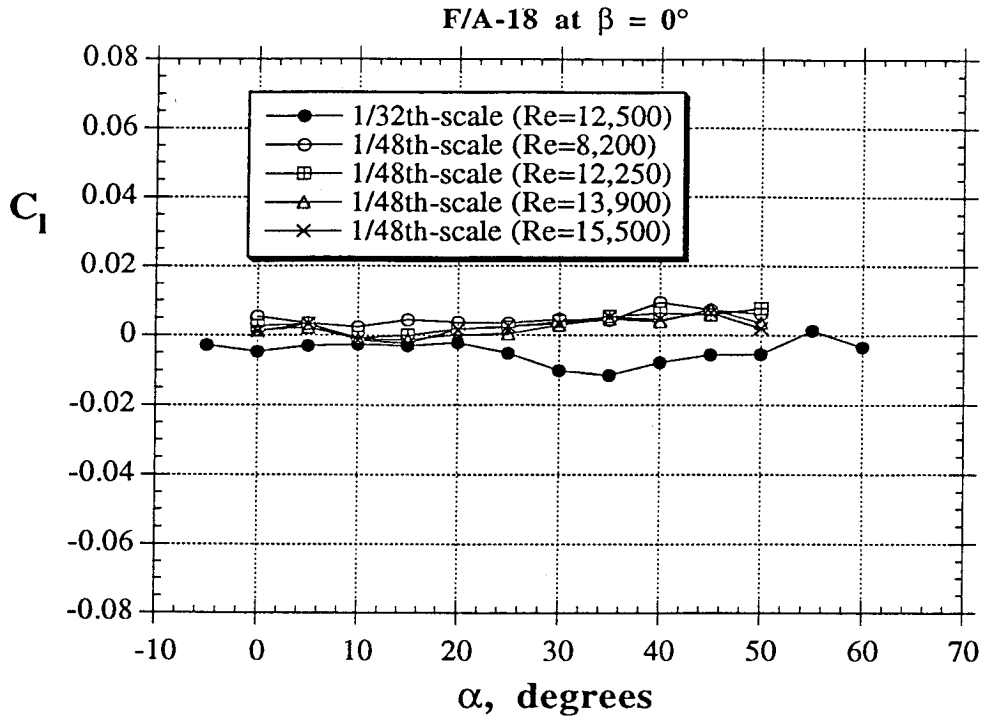

Figure 71 - Concluded

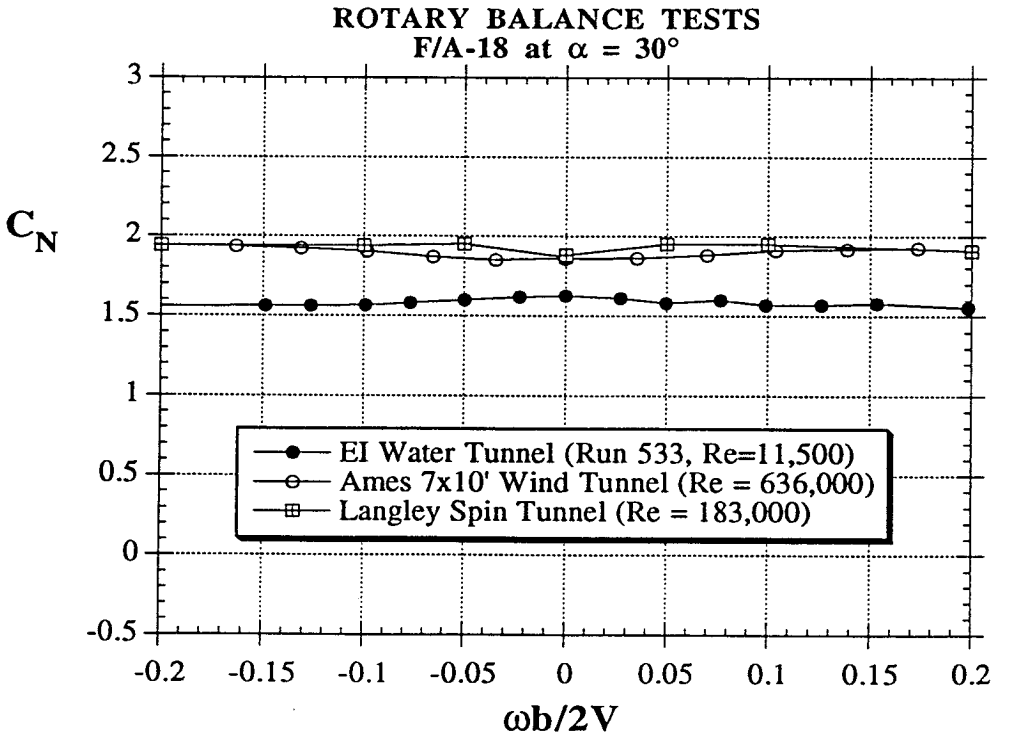

Figure 72 - Results of Rotary-Balance Tests at $\alpha = 30°$ ($1/48^{th}$-Scale F/A-18 Model)

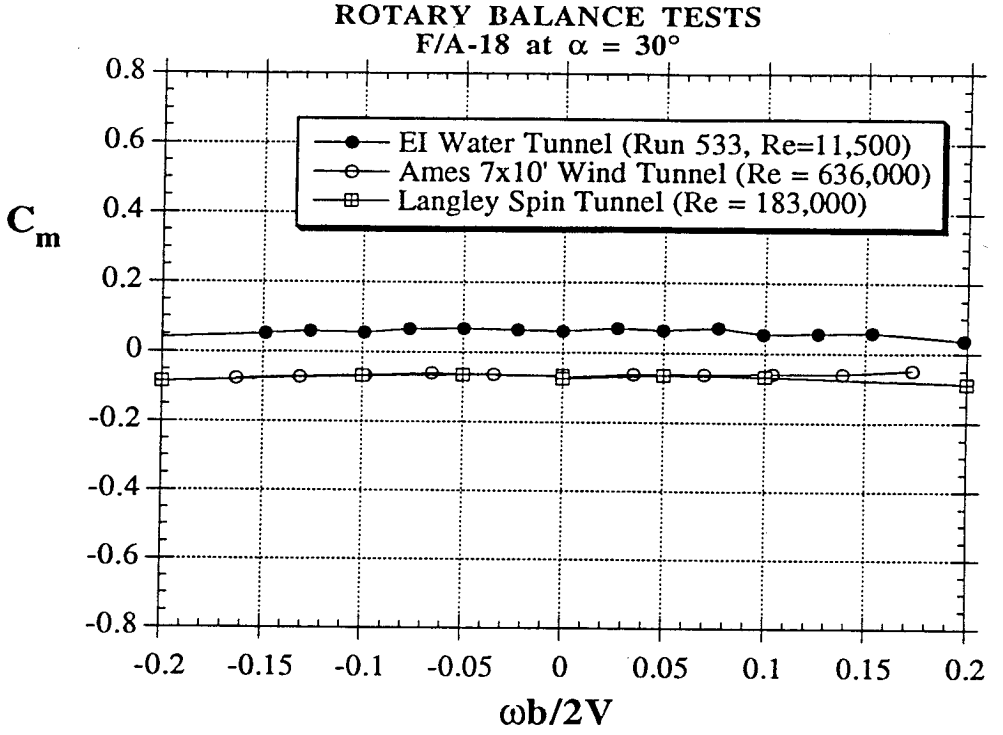

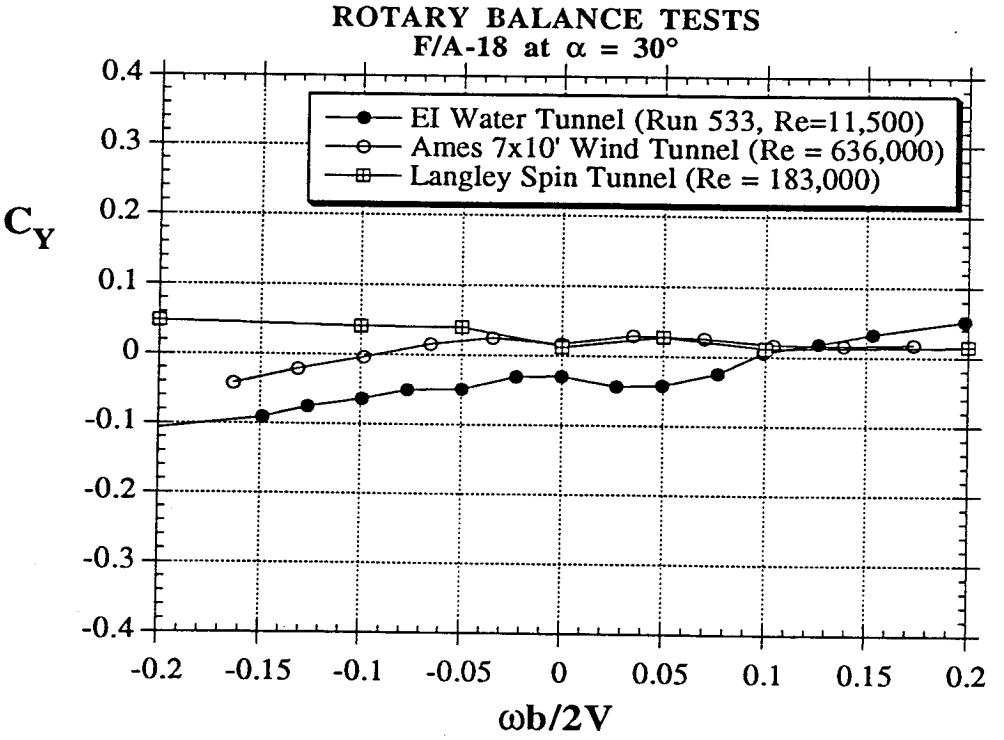

Figure 72 - Continued

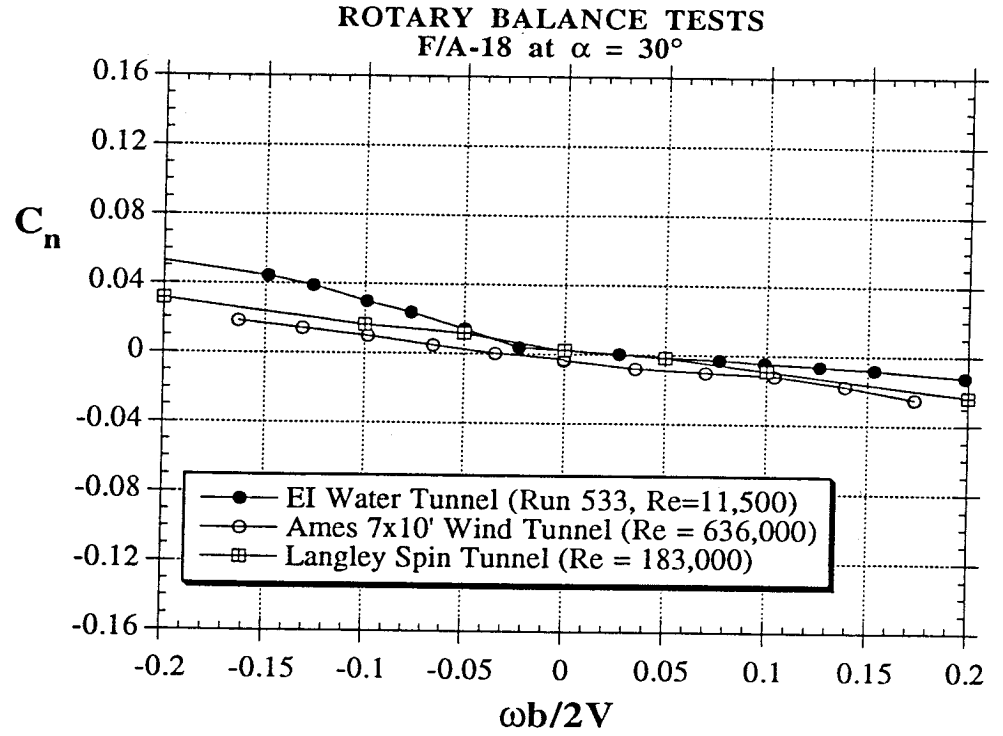

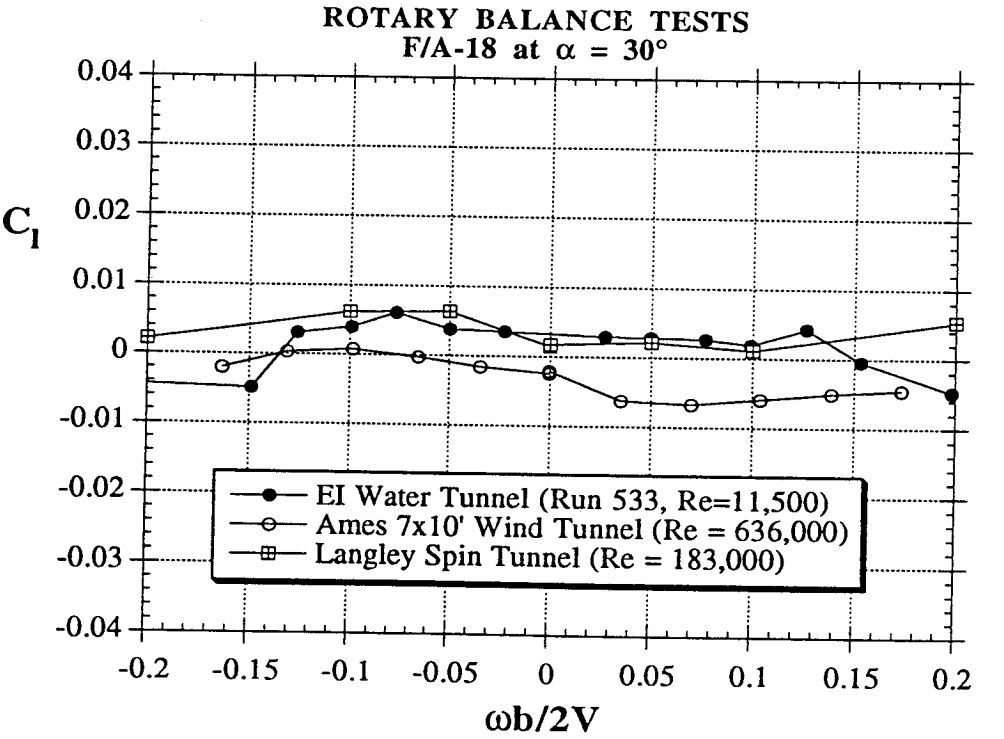

Figure 72 - Concluded

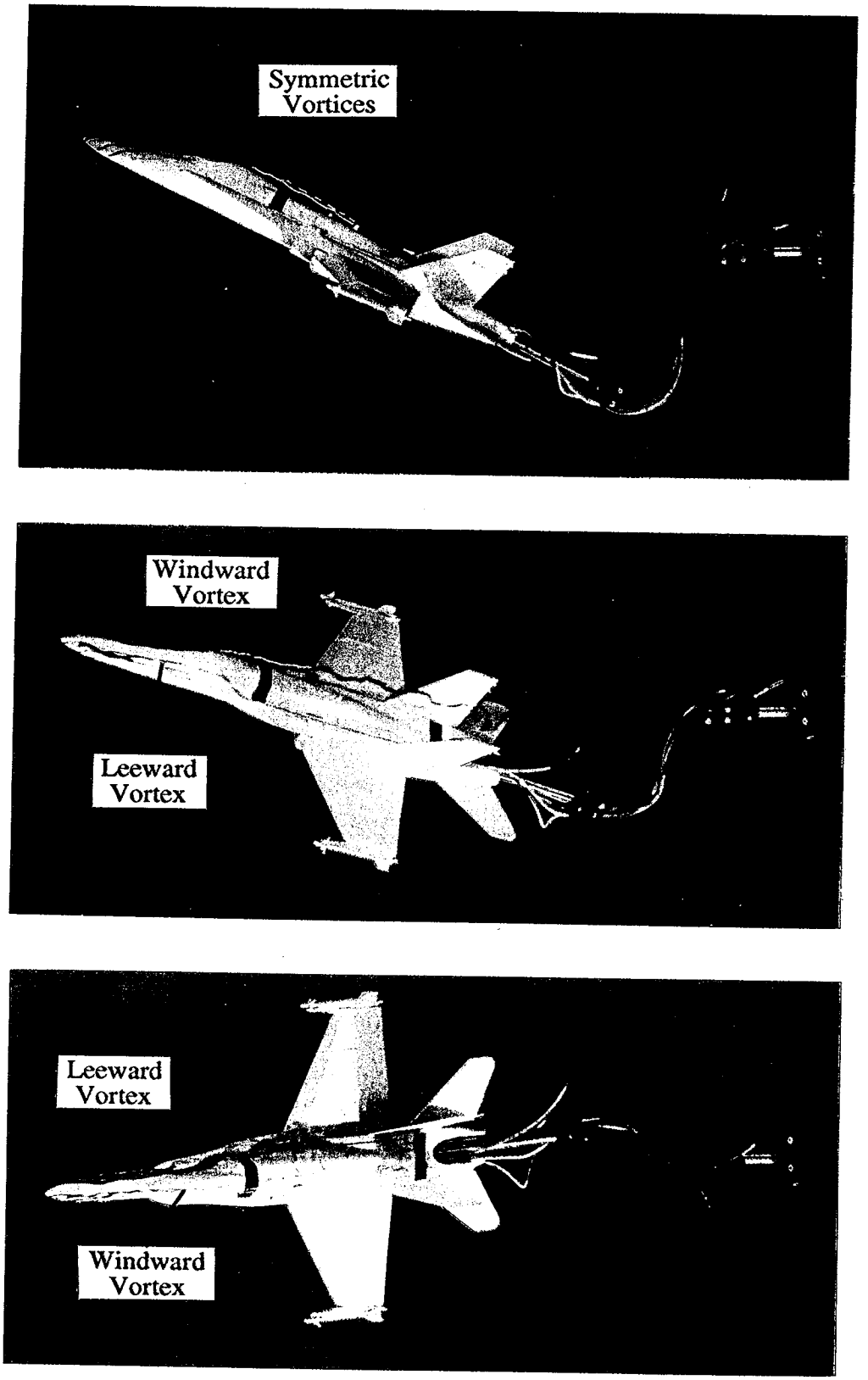

STATIC
$\alpha = 30°$

POSITIVE ROTATION
$\Omega = 0.15$

NEGATIVE ROTATION
$\Omega = -0.15$

Figure 73 - Flow Visualization During Rotary-Balance Tests at $\alpha = 30°$

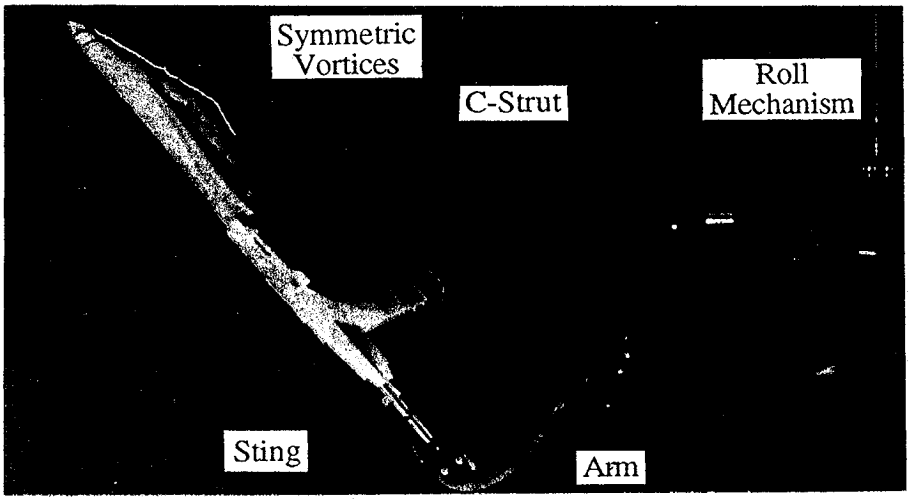

STATIC
α = 50°

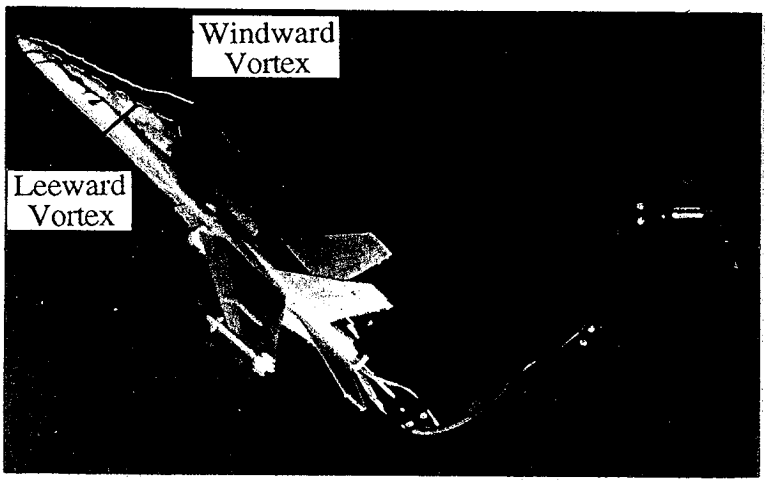

POSITIVE ROTATION
Ω = 0.15

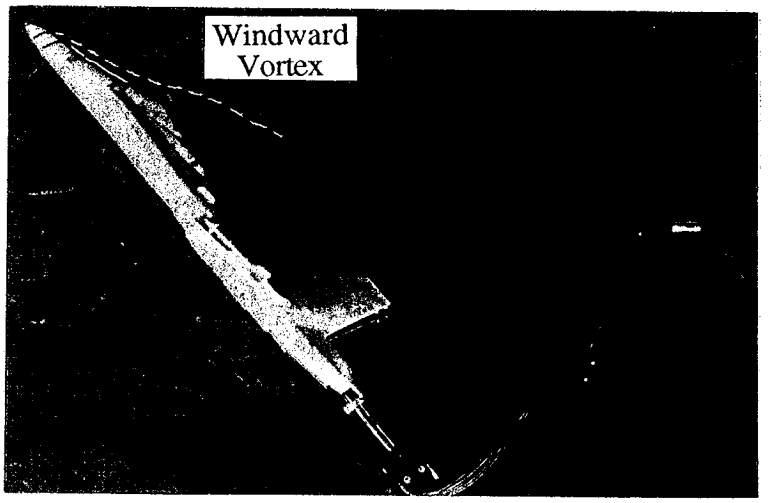

NEGATIVE ROTATION
Ω = -0.15

Figure 74 - Flow Visualization During Rotary-Balance Tests at $\alpha = 50°$

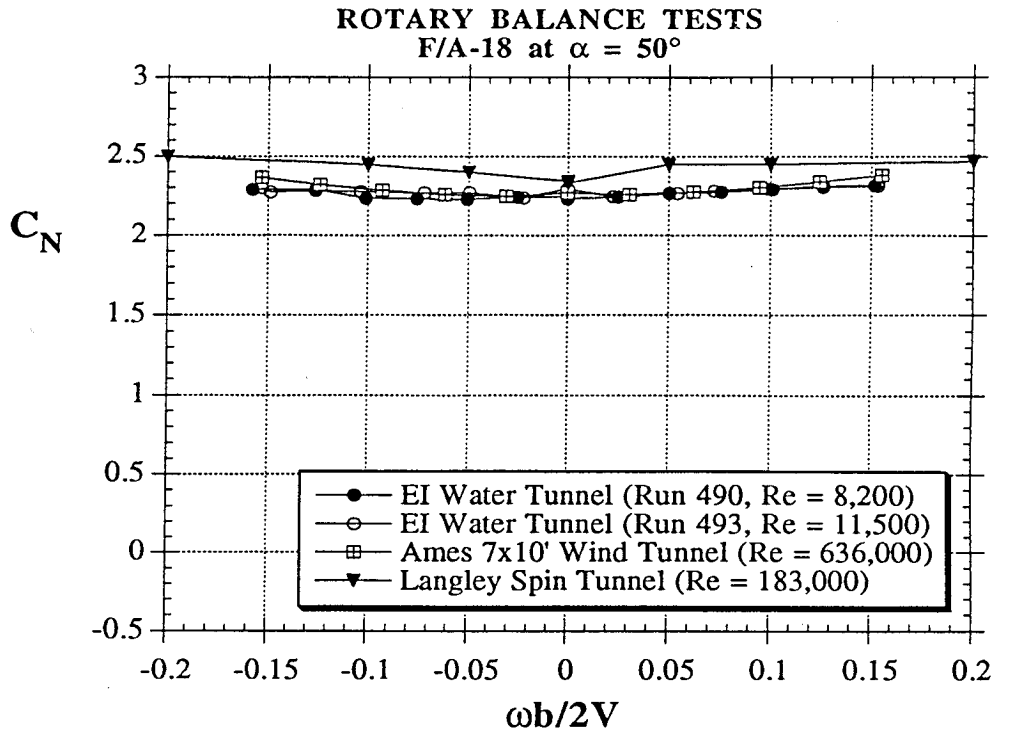

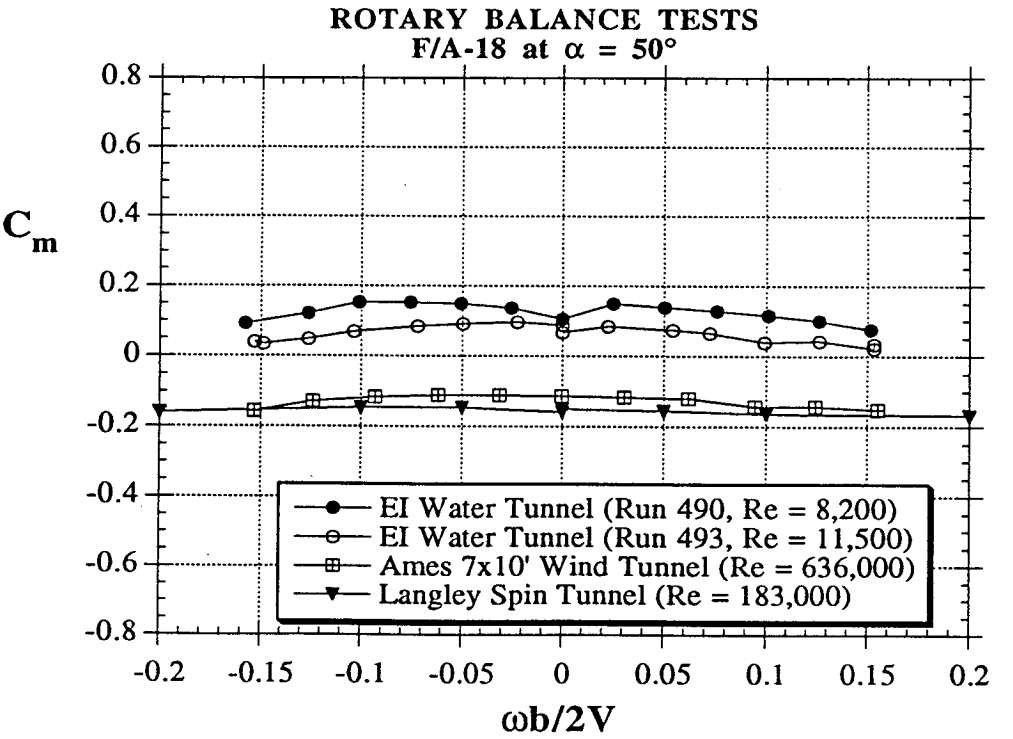

Figure 75 - Results of Rotary-Balance Tests at $\alpha = 50°$ (1/48th-Scale F/A-18 Model)

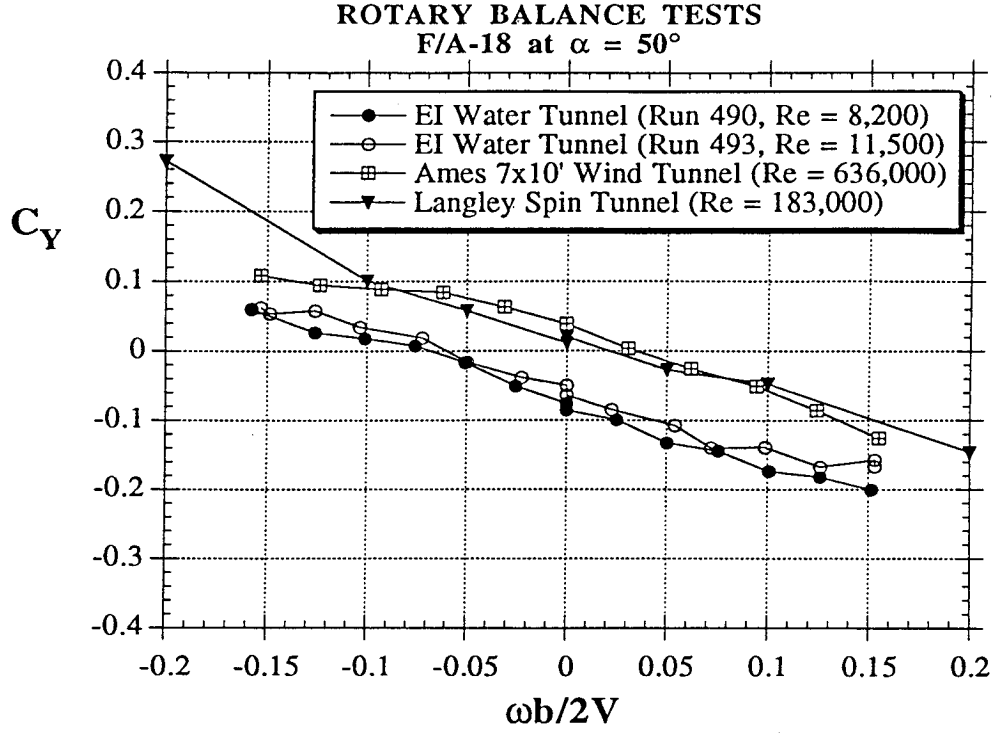

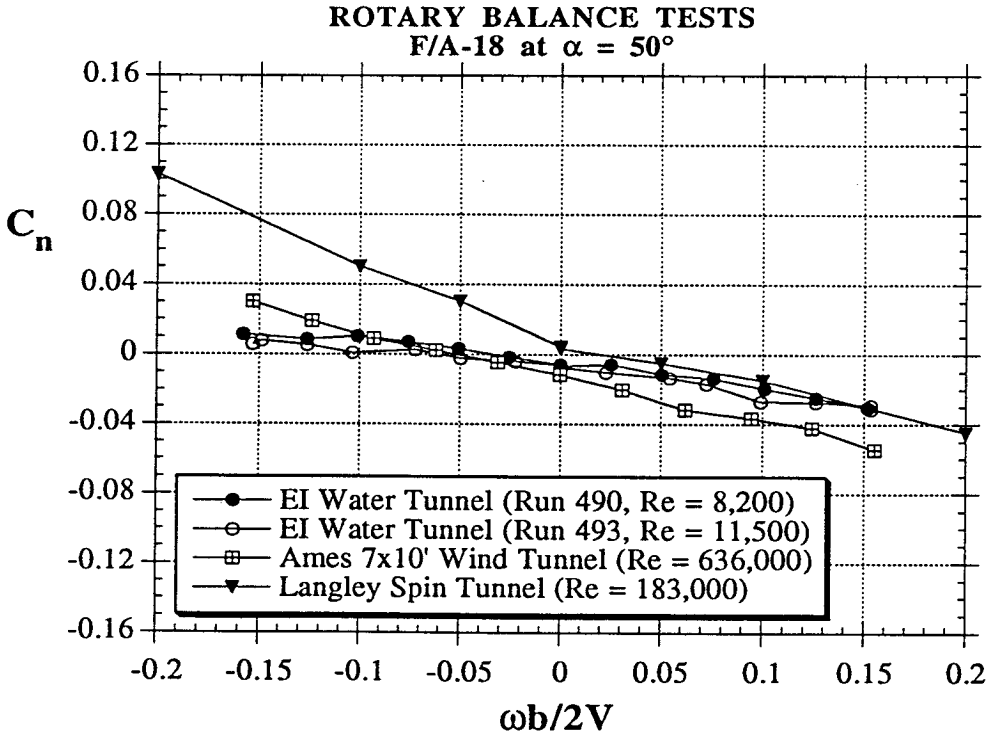

Figure 75 - Continued

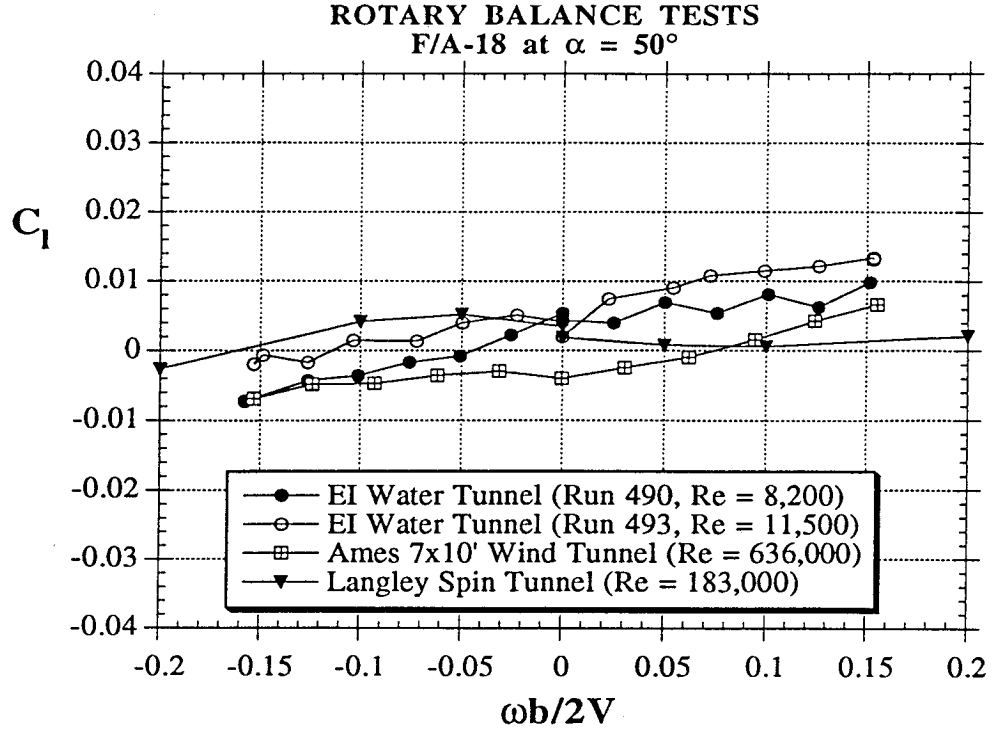

Figure 75 - Concluded

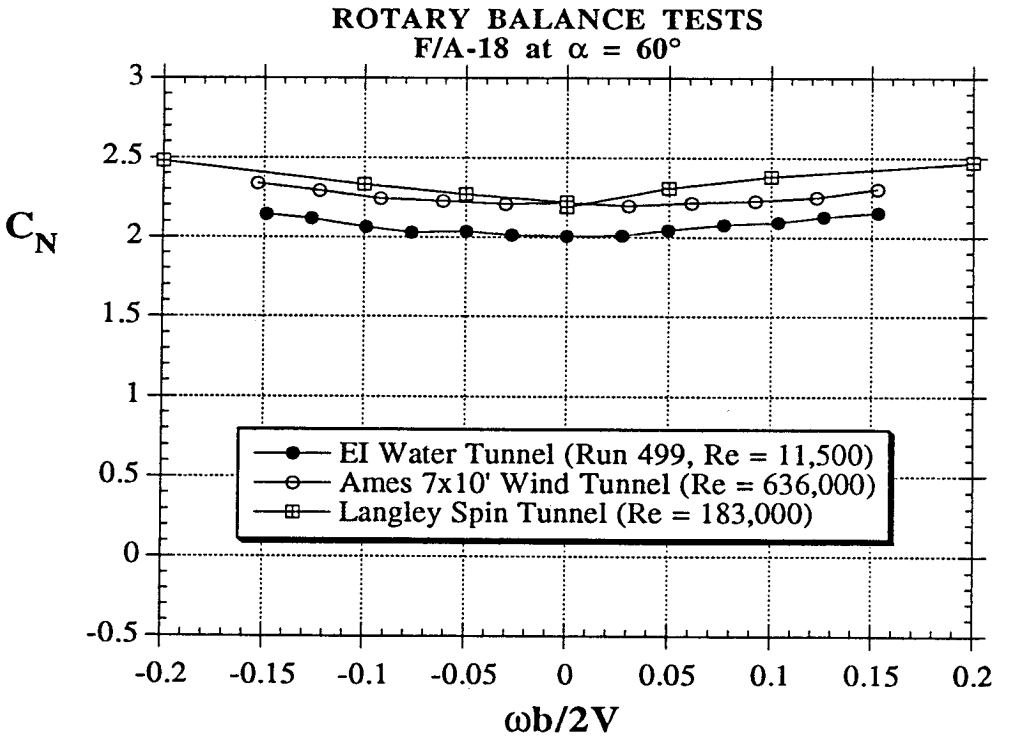

Figure 76 - Results of Rotary-Balance Tests at $\alpha = 50°$ ($1/48^{th}$-Scale F/A-18 Model)

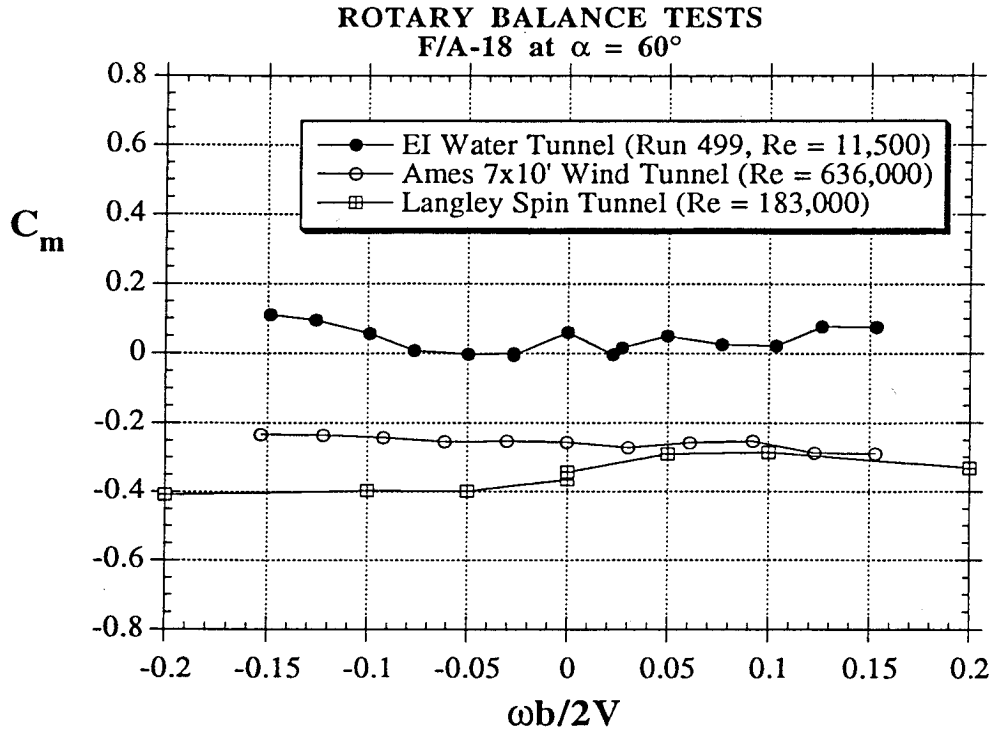

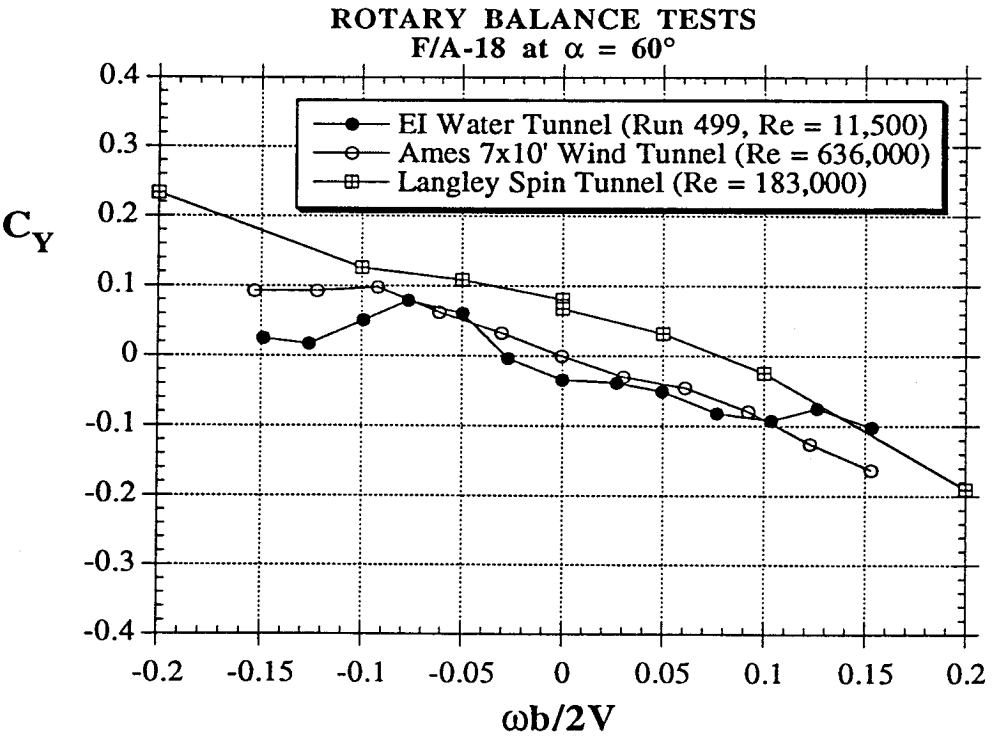

Figure 76 - Continued

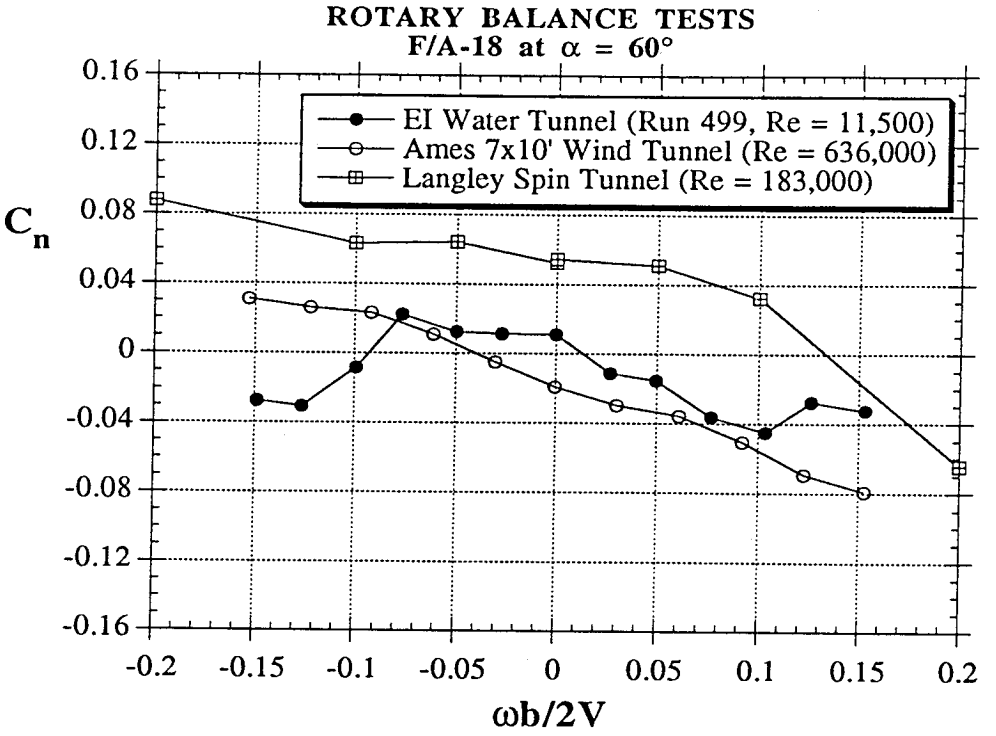

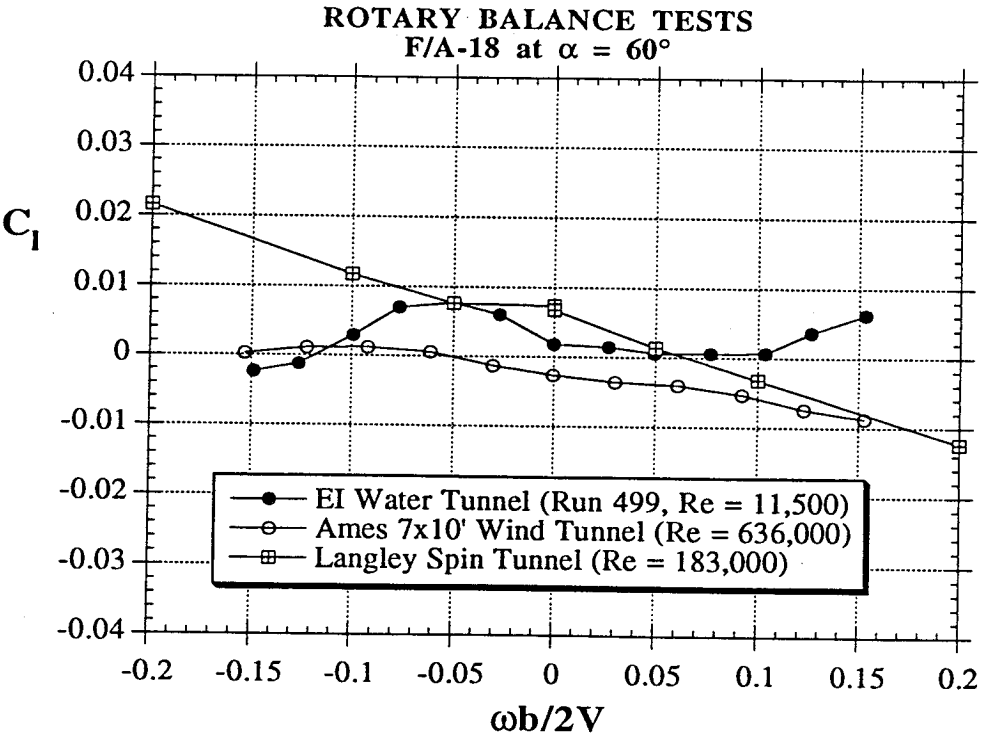

Figure 76 - Concluded

REFERENCES

1. Erickson, G. E., Peake, D. J., Del Frate, J., Skow, A. M. and Malcolm, G. N., "Water Facilities in Retrospect and Prospect - an Illuminating Tool for Vehicle Design," NASA TM 89409, November 1986.

2. Deane, J. R., "Wind and Water Tunnel Investigations of the Interaction of Body Vortices and the Wing Panels of a Missile Configuration," AGARD CP-2467, Jan. 1979.

3. Thompson, D. H., "A Water Tunnel Study of Vortex Breakdown Over Wings with Highly Swept Leading Edges," ARL/A-Note-356, Melbourne, May 1975.

4. Davies, A. G., "A Comparative Study of Vortex Flows in Wind and Water Tunnels," presented at the AGARD Fluid Dynamics Panel Symposium on Aerodynamic and Related Hydrodynamic Studies Using Water Facilities, October 1986.

5. Cunningham, A., "Steady and Unsteady Force Testing of Fighter Aircraft Models in a Water Tunnel," AIAA Paper 90-2815, presented at the AIAA 8th Applied Aerodynamics Conference, Portland, Oregon, Aug. 20-22,1990.

6. Malcolm, G.N. and Nelson, R.C., "Comparison of Water and Wind Tunnel Flow Visualization Results on a Generic Fighter Configuration at High Angles of Attack," AIAA Paper 87-2423, presented at the AIAA Atmospheric Flight Mechanics Conference, Monterey, CA, Aug. 1987.

7. Brandon, J. M. and Shah, G. H., "Effect of Large Amplitude Pitching Motions on the Unsteady Aerodynamic Characteristics of Flat-Plate Wings," AIAA Paper 88-4331, presented at the Atmospheric Flight Mechanics Conference, August 15-17, 1988.

8. Brandon, J. M. and Shah, G. H., "Unsteady Aerodynamic Characteristics of a Fighter Model Undergoing Large-Amplitude Pitching Motions at High Angles of Attack," AIAA Paper 90-0309, 28th Aerospace Sciences Meeting, January, 1990, Reno, Nevada.

9. Ng, T.T., Malcolm, G.N. and Lewis, L.C., "Flow Visualization Study of Delta Wings in Wing-Rock Motion," AIAA Paper 89-2187, 1989.

10. Levin, D. and Katz, J., "Dynamic Load Measurements with Delta Wings Undergoing Self-Induced Roll-Oscillations," AIAA Paper 82-1320, presented at the AIAA 9th Atmospheric Flight Mechanics Conference, 1982.

11. Quast, T., Nelson, R.C. and Fisher, D.F.;"A Study of High Alpha Dynamics and Flow Visualization for a 2.5% Model of the F-18 HARV Undergoing Wing Rock," AIAA Paper 91-3267, presented at the 9th Applied Aerodynamics Conference, Baltimore, MD, 1991.

12. Kramer, B. R., Suárez, C. J., Malcolm, G. N. and James, K. D., "Forebody Vortex Control on an F/A-18 in a Rotary Flow Field," AIAA Paper 94-0619, presented at the 32nd Aerospace Sciences Meeting, Reno, NV, 1994.

13. Hultberg, R., "Low Speed Rotary Aerodynamics of F-18 Configuration for 0° to 90° Angle of Attack - Test Results and Analysis," NASA Contractor Report 3608, August 1984.

REPORT DOCUMENTATION PAGE

Form Approved
OMB No. 0704-0188

1. AGENCY USE ONLY (Leave blank)	2. REPORT DATE	3. REPORT TYPE AND DATES COVERED
	December 1994	Contractor Report

4. TITLE AND SUBTITLE

Development of a Multicomponent Force and Moment Balance for Water Tunnel Applications, Volume II

5. FUNDING NUMBERS

WU 505-5-953
NAS2-13571

6. AUTHOR(S)

Carlos J. Suárez, Gerald N. Malcolm, Brian R. Kramer, Brooke C. Smith, Bert F. Ayers

7. PERFORMING ORGANIZATION NAME(S) AND ADDRESS(ES)

Eidetics International, Inc.
3415 Lomita Blvd.
Torrance, California 90505

8. PERFORMING ORGANIZATION REPORT NUMBER

H-2030

9. SPONSORING/MONOTORING AGENCY NAME(S) AND ADDRESS(ES)

National Aeronautics and Space Administration
Washington, DC 20546-0001

10. SPONSORING/MONITORING AGENCY REPORT NUMBER

NASA CR-4642

11. SUPPLEMENTARY NOTES

NASA Technical Monitor John Del Frate.

12a. DISTRIBUTION/AVAILABILITY STATEMENT

SBIR
Unclassified—Unlimited
Subject Category 34

12b. DISTRIBUTION CODE

13. ABSTRACT (Maximum 200 words)

The principal objective of this research effort was to develop a multicomponent strain gauge balance to measure forces and moments on models tested in flow visualization water tunnels. Static experiments (which are discussed in Volume I of this report) were conducted, and the results showed good agreement with wind tunnel data on similar configurations. Dynamic experiments, which are the main topic of this Volume, were also performed using the balance. Delta wing models and two F/A-18 models were utilized in a variety of dynamic tests. This investigation showed that, as expected, the values of the inertial tares are very small due to the low rotating rates required in a low-speed water tunnel and can, therefore, be ignored. Oscillations in pitch, yaw and roll showed hysteresis loops that compared favorably to data from dynamic wind tunnel experiments. Pitch-up and hold maneuvers revealed the long persistence, or time-lags, of some of the force components in response to the motion. Rotary-balance experiments were also successfully performed. The good results obtained in these dynamic experiments bring a whole new dimension to water tunnel testing and emphasize the importance of having the capability to perform simultaneous flow visualization and force/moment measurements during dynamic situations.

14. SUBJECT TERMS

Dynamic experiments; Static; Water tunnel force/moment balance

15. NUMBER OF PAGES

130

16. PRICE CODE

A07

17. SECURITY CLASSIFICATION OF REPORT	18. SECURITY CLASSIFICATION OF THIS PAGE	19. SECURITY CLASSIFICATION OF ABSTRACT	20. LIMITATION OF ABSTRACT
Unclassified	Unclassified	Unclassified	Unlimited

NSN 7540-01-280-5500

Available from the NASA Center for AeroSpace Information, 800 Elkridge Landing Road, Linthicum Heights, MD 21090; (301)621-0390

Standard Form 298 (Rev. 2-89)
Prescribed by ANSI Std. Z39-18
298-102